From the Sun to the Stars: A Solar Calibrator for the Keck Planet Finder and New Frontiers in Exoplanet Obliquities

Thesis by
Ryan Asa Rubenzahl

In Partial Fulfillment of the Requirements for the
Degree of
Doctor of Philosophy in Astrophysics

Caltech

CALIFORNIA INSTITUTE OF TECHNOLOGY
Pasadena, California

2024
Defended May 13, 2024

Ryan Asa Rubenzahl
ORCID: 0000-0003-3856-3143

ACKNOWLEDGMENTS

This thesis is, first and foremost, for Mom and Dad. Thank you for always feeding my endless curiosity. Thank you for putting me in Space Camp in 2nd grade, obliging me at that museum in Greenwich, buying me that telescope, and giving me everything I needed to chase my dreams. I would not be here without you. This thesis is every bit yours as it is mine. Evan, thank you for keeping me rooted on Earth, and for your incredible Spotify playlists. I love you all.

This thesis is entirely based on work I did with or at W. M. Keck Observatory, which is only possible as the result of the dispossession of Maunakea from Kānaka Maoli. Mahalo to Rich Matsuda for taking the time to have such candid discussions with me. The future of astronomy and community are bright. Thank you to the entire summit crew, but especially Josh Walawender and Grant Hill; SoCal would not have happened without you. Thank you to all of the support astronomers and telescope operators for the many fruitful nights of observing. You make discovery possible.

I have learned a tremendous amount in my time at Caltech, and some of it was scientific. I owe any confidence I have about instrumentation to the incredible mentorship of Sam Halverson. Thank you for teaching me that it is (sometimes) okay to break things. Thank you to Fei Dai for your patience, mentorship, and encyclopedic knowledge of the field. Thank you to my advisor, Andrew Howard, for trusting me to work with hardware, software, and to do exciting science. Thank you to Steve Gibson, Kodi Rider, Arpita Roy, and BJ Fulton for helping me become a better builder, data analyst, and coder.

To Sarah and Aida, thank you for being the best academic siblings and friends I could ask for. Nitika, thank you for the rap battles and pandemic baked goods. To the Sierra Madre Cadre: Sam, Jakob, Ivey, Cannoli, and Nomi, thank you for making home feel like home. Thank you to the Cahill Astronomy Grads past and present, especially Adolfo, Evan, Mia, Max, SamWu, Dee, Jerry, Dillon, Kaew, Kathryn, Jackie, Anna, Chris, Kishalay, Rachael, Jake, Donal, and Scott, for making this department a fun and inclusive place to be. No department runs without amazing staff, and I certainly owe a huge gratitude to Gita Kantiben, for everything you do but especially for making travel so painless. And thank you to Patrick for the homebrew and letting me "borrow" a power supply here and there.

Many thanks to my many wonderful collaborators and conference friends. Thank you to Alex for some of the best Type II outdoors fun I've had. Ashley, Casey, Jared, Jack, Judah, Isabel, Joey, Emily, Daria, Steven, Rae, Emma, Dakotah, Nick, Michael, Arvind, Jacob, Kingsley, Khaled, Ben, and Fede, you are all why EPRV is the best field.

Outreach has been a big part of my time at Caltech, and only because of one person who makes it all happen. I have the utmost admiration for Cameron Hummels, whose tireless efforts have created the most vibrant outreach program I have had the pleasure to take part in.

A special shout-out to my Space Force teammates: Martin, Ryan, Jack, Kevin, Shanks, Chris, Alex, Tori, Billy, and Kingsley–TEAM SPEED!

Thank you to my incredible organizer friends who helped bring C/GPU from a spreadsheet to a NLRB certified labor union. Abdullah, thanks for roping me in. Organizing was the single best unexpected thing I have ever done. Sam, Nadia, Jessica, Jasmine, Korbi, Mike, Ranjani, Alex VW, Ashay, James, Simona, Varun, Quinn, and Fayth–I have so much optimism for the future of Caltech because of all of your hard work and sacrifices. I'm in awe of we did and I can't wait to see how much more you all will win. Solidarity forever!

There is only one person in this universe I would wish to share a planet with. Katherine, thank you for always being by my side, even when we were thousands of miles apart. ILYTTCMBAB.

ABSTRACT

The galactic census is underway. In the thirty years since the discovery of 51-Pegasi b, the first extrasolar planet discovered orbiting a main sequence star, over 5,600 more have been tallied. The known exoplanet population is diverse, yet no extrasolar system observed to date resembles our own. The radial velocity (RV) technique, which works by measuring the reflex motion of a star from a perturbing planet, remains the most capable method for discovering exo-Earths. An exo-Earth would accelerate its star up to 9 cm s^{-1}, Doppler-shifting stellar absorption lines across the detector of a modern spectrograph by 1/10,000th the width of a typical CCD pixel. At this level of precision, every component of the instrument becomes critical to the overall stability. Yet, despite many instruments reaching $<$ 30 cm s^{-1} precision (such as the Keck Planet Finder; KPF), exoplanet discovery has stalled around the 1 m s^{-1} level. The primary limitation is now correlated noise introduced by physical processes on the stellar surface, dubbed "stellar activity," which manifests RV variability up to many m s^{-1} on timescales from minutes to decades.

This thesis has two primary themes. The first is concerned with addressing the stellar activity problem and improving RV instrument performance. Both are well-probed using "Sun-as-a-star" observations, as the Sun is the only star in the universe with all orbiting planets accounted for and its surface resolved at all timescales, wavelengths, and spatial scales. Chapter 3 presents the Solar Calibrator (SoCal), an autonomous system that feeds stable, disc-integrated sunlight to KPF at the W. M. Keck Observatory. With SoCal, KPF acquires 200–800 daily high-resolution ($R = 98{,}000$) optical (445-–870 nm) solar spectra up to a signal-to-noise of 2400, providing a rich and unmatched dataset for developing novel methods for mitigating stellar activity. We also leveraged SoCal to discover, diagnose, and fix a detector issue in KPF, and to develop and optimize the data reduction pipeline. We compared SoCal RVs to solar RVs from the NEID solar feed and found excellent agreement on intra-day timescales at the single-measurement photon-noise level (30—40 cm s^{-1}).

The second theme of this thesis is the precise characterization of extrasolar planets in extremely close-in orbits. These most extreme exoplanets often constrain planet formation theories the most. Chapter 2 presents the discovery and characterization of TOI-1347 b, the most massive rocky ultra-short-

period exoplanet discovered to date. We found tentative evidence for a high mean-molecular-weight atmosphere on the planet, which orbits its star in just 20 hours. An atmosphere on such a highly irradiated world would be unusual, but not impossible, though JWST follow-up measurements are needed to confirm. Chapters 4, 5, 6, and 7 probe the mysterious formation pathways of hot Jupiters from four unique angles. Archeological clues to their dynamical histories remain in their present-day stellar obliquity, the angle between the star's rotation axis and the planet's orbital plane. The first is WASP-107 b, a super-Neptune that must have migrated to explain its ultra-low density and escaping atmosphere. We measured WASP-107 b to be on a polar orbit, an indicator of a history of dynamics with its outer planetary companion WASP-107 c. The second is KELT-18 b, an ultra-hot Jupiter we also found to be on a polar orbit. The mutually misaligned stellar companion in the system may be to blame. The third, Kepler-1656 b, is a highly eccentric sub-Saturn that could plausibly be undergoing migration kick-started by its outer planetary companion. Its orbit may be aligned, atypical of the traditional picture of high-eccentricity migration. The fourth, Kepler-1658 b, is actively experiencing tidal orbital decay around an evolved star, two aspects that strongly constrain orbital realignment timescales. The system either retains its primordial configuration or constrains tidal efficiencies. Unfortunately, our transit observations are contaminated by a massive starspot, which preclude the direct measurement of the obliquity. This chapter instead explores new methods for directly modeling starspots in EPRV spectra.

PUBLISHED CONTENT AND CONTRIBUTIONS

Rubenzahl, R. A. et al. (May 2024a). "KPF Confirms a Polar Orbit for KELT-18 b." In: *Submitted to The Astronomical Journal*.
R.A.R. concieved the projected, collected and reduced the data, performed the analysis, and wrote the manuscript.

Rubenzahl, R. A. et al. (May 2024b). "The Extremely Eccentric Sub-Saturn Kepler-1656 b Has A Low Obliquity." In: *Submitted to The Astrophysical Journal Letters*.
R.A.R. concieved the projected, collected and reduced the data, performed the analysis, and wrote the manuscript.

Rubenzahl, R. A. et al. (Apr. 2024c). "The TESS-Keck Survey. XII. A Dense 1.8 $R_\oplus$ Ultra-short-period Planet Possibly Clinging to a High-mean-molecular-weight Atmosphere after the First Gigayear." In: *The Astronomical Journal* 167.4, 153, p. 153. DOI: `10.3847/1538-3881/ad28bb`. arXiv: `2402.07451 [astro-ph.EP]`.
R.A.R. performed the light curve and radial velocity analyses, optimized the RV scheduling, obtained some of the HIRES observations, and wrote the manuscript. F.D. performed the phase curve and secondary eclipse analysis.

Rubenzahl, R. A. et al. (Dec. 2023). "Staring at the Sun with the Keck Planet Finder: An Autonomous Solar Calibrator for High Signal-to-noise Sun-as-a-star Spectra." In: *Publications of the Astronomical Society of the Pacific* 135.1054, 125002, p. 125002. DOI: `10.1088/1538-3873/ad0b30`. arXiv: `2311.05129 [astro-ph.IM]`.
R.A.R. contributed to the instrument conception and design with input from S.H. and A.W.H., built, tested, and installed the Solar Calibrator hardware and software, collected and analyzed the data, and wrote the manuscript. S.H., J.W., G.H., and A.W.H contributed to the instrument design, installation, and integration at Keck Observatory. M.B. integrated the control software into the Keck Task Library. Other authors assisted with installation at Keck and integration with KPF and the DRP.

Rubenzahl, R. A. et al. (Mar. 2021). "The TESS-Keck Survey. IV. A Retrograde, Polar Orbit for the Ultra-low-density, Hot Super-Neptune WASP-107b." In: *The Astronomical Journal* 161.3, 119, p. 119. DOI: `10.3847/1538-3881/abd177`. arXiv: `2101.09371 [astro-ph.EP]`.
R.A.R. analyzed the data, performed the modeling and n-body simulations, and wrote the manuscript.

TABLE OF CONTENTS

LIST OF ILLUSTRATIONS

LIST OF TABLES

Chapter 1

INTRODUCTION

"The universe is a pretty big place.
If it's just us, seems like an awful waste of space."

— Carl Sagan, *Contact*

1.1 A Brief History of Planet Discovery

For millennia, only our Earth and the five naked-eye visible *planētēs* (Greek for "wanderers")—Mercury, Venus, Mars, Jupiter, and Saturn—were known to humans. Following Galileo's invention of the telescope in 1609, it wasn't until 1781 that William Herschel became the first to observe Uranus (Herschel and Watson, 1781). Over the following decades, subsequent measurements revealed Uranus's path around the Sun was not a perfect ellipse, much unlike the other planets. In 1846, Urbain Le Varrier (and independently, John Couch Adams) hypothesized that an unseen gravitational body was perturbing Uranus' orbit and calculated the position in the sky that such a body must be located to have the observed effect (Le Verrier, 1846; Adams, 1846). Le Varrier mailed his calculation to Johann Galle, who later that night pointed his telescope to the predicted location and found Neptune within 1° (Galle, 1846).

The same principle of inferring the presence of an unseen planet by observing its gravitational perturbation on something we can see is how we discover planets orbiting other stars (exoplanets) today. One hundred years after Neptune's discovery, Otto Struve laid out the foundation for how such a measurement could be made (Struve, 1952). The gravitational influence of an orbiting planet will cause its host star to move in its own smaller and slower orbit. The part of this motion along our line of sight, called the radial velocity, will Doppler-shift the star's spectrum as recorded by an observer with a spectrograph. This method, called the radial velocity (RV) technique (discussed in more detail in Section 1.3), was successfully utilized in 1989 to discover the first sub-stellar companion to a another main sequence star (Latham et al., 1989). Soon after, the first bona-fide explanets were discovered orbiting a neutron star (using pulsar timing variations; Wolszczan and Frail, 1992) and then around a solar-type star (51 Pegasi b, using RVs; Mayor and Queloz, 1995). Curiously, 51 Pegasi b looked nothing like the planets we then knew of. At roughly half the mass of our Jupiter, it takes just 4.2 days to complete a single orbit. Using the RV method, astronomers quickly found many more of these "hot Jupiters" around other nearby, bright stars (e.g., Butler et al., 1997; Butler et al., 1998).

Struve also noted that a planet orbiting its star edge-on to our line-of-sight would appear to transit its star once per orbit, and in doing so would block a fraction of the starlight in proportion to its size. This approach, called the transit method, was successfully used just five years after 51 Pegasi b's discovery to detect HD 209458 b (Charbonneau et al., 2000; Henry et al., 2000). It, too, was a hot Jupiter. Following the launch of the *Kepler* space telescope in 2009 (Borucki et al., 2010) and more recently the *TESS* mission (Ricker et al., 2015) in 2018, the number of known exoplanets has exploded to over 5,600 as of this writing. Around 75% of these (~ 4200) have been discovered by the transit method, primarily from the *Kepler* and *TESS* missions. An additional 7,000 planet candidates from *TESS* still await confirmation (NASA Exoplanet Archive, 2019). The RV method accounts for about 1,100 exoplanets, while other techniques such as direct imaging (Chauvin et al., 2004) and microlensing (Gaudi, 2012) have supplied the remaining $\sim$300.

One conclusion we can already draw is that exoplanets are ubiquitous. Though, due to selection biases, we are still not sensitive to Solar System analogs. The propensity for discovering hot Jupiters in the early days of exoplanet astronomy was not because they are common, but because they are the easiest to detect. Their RV signals (tens to hundreds of m s^{-1}) and transit depths ($> 1\%$) are large, while their short (< 10 day) orbital periods are more readily fully observed. In contrast, it has barely been a single Saturnian year (29.4 Earth years) since the discovery of 51 Pegasi b. As such, we are only just now becoming sensitive to exo-Jupiters and exo-Saturns amongst the systems with the longest observational baselines (Rosenthal et al., 2021; Fulton et al., 2021).

Exo-Earths, on the other hand, present an even greater challenge. Their signals are much smaller; around a Sun-like star, the RV signal is just 9 cm s^{-1}. The likelihood that we would see such a planet transit is about 0.5%, and it would only block 0.01% of its star's light. As we will discuss in Section 1.3, modern and next-generation extreme-precision RV spectrographs are pushing down into the tens of cm s^{-1} stability levels. Though, we must now contend with

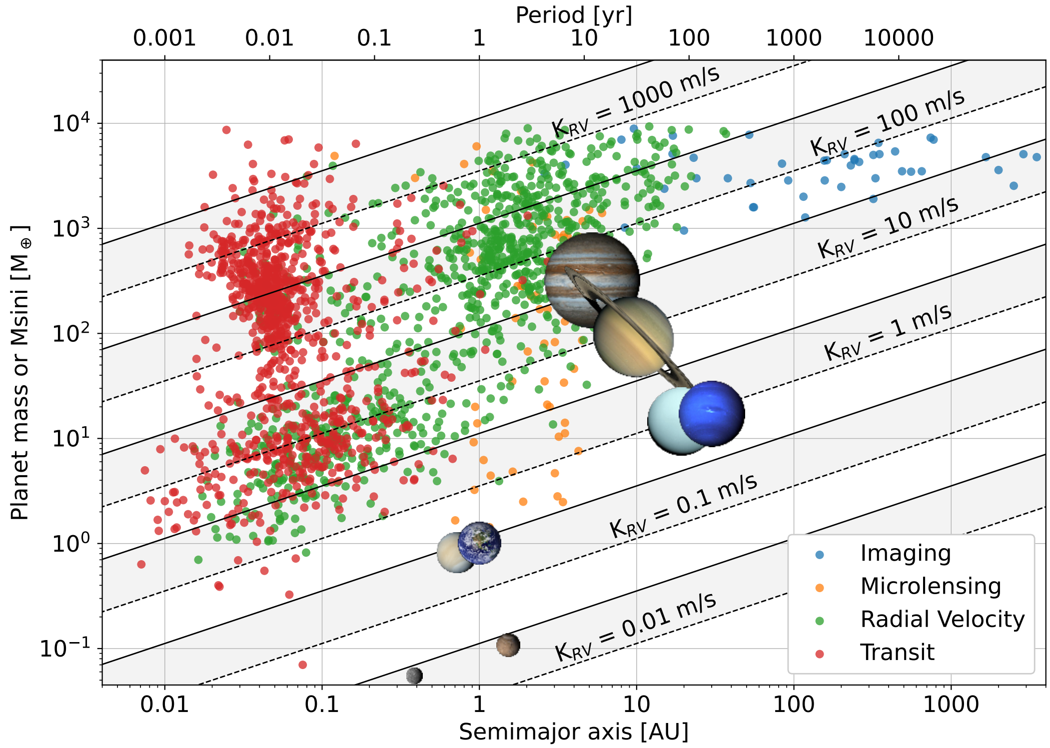

Figure 1.1: Known exoplanets with a mass or $M \sin i$ measured to better than 2σ (2177 of the 5602 exoplanets as of April 1, 2024) as recorded in the NASA Exoplanet Archive. Points are colored according to discovery method for the four primary techniques. The Solar System planets are overplotted for context. The diagonal striped bands correspond to constant RV semiamplitudes for a 0.1 $M_\odot$ host star (dashed line) to a 1 $M_\odot$ host star (solid line).

noise sources arising from magnetic and photospheric activity on the stars themselves (Section 1.5), which can produce RV variability at the m s^{-1} level, swamping or even mimicking small planetary signals.

1.2 The Orbits of Close-In Exoplanets

"But there seems to be no compelling reason why the hypothetical stellar planets should not, in some instances, be much closer to their parent stars than is the case in the solar system. It would be of interest to test whether there are any such objects."

— Otto Struve, *Proposal For A Project Of High-Precision Stellar Radial Velocity Work*, 1952

Indeed, as we just discussed, Struve had correctly predicted the existence of hot Jupiters (HJs). The discovery of 51 Pegasi b had not only marked the beginning of the exoplanet era, it also completely turned upside-down our understanding of planet formation. How can a Jupiter-mass planet form in a 4-day orbit? Shouldn't Jupiter-mass planets live in Jupiter-like orbits? Remarkably, we have yet to reach a consensus on HJ formation to this day.

Formation of Hot Jupiters

The problem begins in the same disk of dust and gas from which a planet forms. In the traditional model of core-accretion (Pollack et al., 1996), a solid core grows (e.g., via pebble accretion or giant impacts) up to a critical mass ($\sim$10 $M_\oplus$). This phase is relatively quick, on the order of 10^5 yr. Then, the core slowly (on the order of $\sim$Myr) accretes a gaseous envelope under hydrostatic equilibrium. When the mass of the gaseous envelope becomes comparable to the mass of the core, the rate of gas accretion becomes exponential. Within 100 kyr the planet accretes enough H/He to grow its mass ten-fold. However, gas in the protoplanetary disk will dissipate after a few to 10 Myr (Fedele et al., 2010; Barenfeld et al., 2016). Giant planet formation is thus a race to assemble a 10 $M_\oplus$ core early enough so that it can achieve runaway gas accretion before the disk dissipates. As a result, one might expect giant planet formation to be more efficient beyond the water-ice line (around 1 AU around solar-type stars) where it is cool enough in the disk for water-ice to condense. This both enriches the solid material budget and fosters an environment where these wide-orbiting (i.e., slower) particles have "stickier" collisions, enhancing core assembly. Indeed, this is where giant planet occurrence peaks; 10–15% of FGK stars host a giant planet in the 2–8 AU range (Cumming et al., 2008; Fulton et al., 2021). HJs are about ten-times more rare, occurring around just 0.5%–1% of FGK stars (Howard et al., 2012; Wright et al., 2012).

At typical HJ orbital distances, the low budget of available solid materials and faster orbital velocities makes growing a massive enough core challenging (Bodenheimer, Hubickyj, and Lissauer 2000, see Dawson and Johnson 2018 for a review). A core could potentially be grown out of successive mergers of super-Earth (1–10 $M_\oplus$) "protocores," at which point core-accretion could proceed to form a HJ *in situ* (Boley, Granados Contreras, and Gladman, 2016; Batygin, Bodenheimer, and Laughlin, 2016). While super-Earths do commonly exist in compact multi-planet systems (Howard et al., 2010b; Rowe et al., 2014), the disk itself will damp orbital excitation, preventing orbit crossings until after the gas disk dissipates (Lee and Chiang, 2016). Gravitational instability is also not an option, as the gas is too hot, too fast, and too low density at HJ orbital distances to self-collapse (Rafikov, 2005).

Consequently, leading theories of HJ formation invoke migration to transport giant planets from more favorable formation locations into close-in orbits. The two plausible migration pathways are *disk migration* (see Baruteau et al. 2014 for a review) and *high-eccentricity migration* (HEM; see Dawson and Johnson 2018 and references therein). The former occurs after a giant planet accretes all the material along its orbital path, opening an annular gap in the protoplanetary disk. An imbalance in tidal and viscous torques between the inner and outer portions of the now-divided disk keeps the planet centered in its gap, which moves inwards as the gas accretes onto the star (Goldreich and Tremaine, 1980; Lin and Papaloizou, 1986; Lin, Bodenheimer, and Richardson, 1996). The migration can be rapid ($\lesssim 10^5$ kyr) and is terminated at the edge of the central magnetospheric cavity at an orbital period of $\sim$3 days (Rice, Armitage, and Hogg, 2008; Batygin, Adams, and Becker, 2023), matching the observed pile-up in HJ occurrence (Wright et al., 2009; Howard et al., 2012). The rate of migration must be fast enough to transport the HJ inward before the disk disperses, but not so fast that the HJ is engulfed by its star.

In the HEM scenario, the HJ instead migrates after the protoplanetary disk has dissipated. If the distant giant planet's eccentricity were perturbed to very high values (e.g., > 0.99) such that the periastron distance becomes very close to the star ($\lesssim$0.04 AU), the extreme change in tidal forces at each periastron passage raises significant tidal distortions on the planet. The planet's orbital angular momentum is converted into heat dissipated into the planet's interior, causing the orbit to shrink and circularize. The excitation of eccentricity could come from planet-planet scattering (Rasio and Ford, 1996), secular chaos (Wu and Lithwick, 2011), or secular interactions with an inclined or eccentric outer companion (Kozai, 1962; Lidov, 1962; Naoz, 2016) which itself could be another planet (Naoz et al., 2011; Teyssandier et al., 2013; Petrovich, 2015a) or a star (Fabrycky and Tremaine, 2007; Petrovich, 2015b). Eccentricity damping during periastron passage may come from tidal friction (Eggleton, Kiseleva, and Hut, 1998; Wu and Murray, 2003; Fabrycky and Tremaine, 2007) or chaotic tides (Wu, 2018; Vick, Lai, and Anderson, 2019). Once the planet migrates far enough, general relativistic precession will decouple the proto-HJ from its outer perturber, quenching any further secular oscillations (Dong, Katz, and Socrates, 2014). The migration continues to transport the HJ to its final semimajor axis with other orbital parameters (e.g., inclination) frozen-in (Anderson, Storch, and Lai, 2016). The typical final semimajor axis is around 0.04 AU, which also corresponds to a 3 day orbit around solar-type stars.

Clues From Stellar Obliquities

A key observable that can distinguish these formation scenarios is the stellar obliquity, sometimes referred to simply as the obliquity, ψ. Defined as the angle between the spin vector of the star and the normal to the planet's orbital plane, the obliquity traces the dynamical history of the star-planet system. In our own solar system, the orbital planes of the planets[1] are all within 0.3–2° of the invariable plane (Souami and Souchay, 2012), the plane normal to the total angular momentum vector passing through the solar system barycenter (dominated by Jupiter's orbit); the inclination of Earth's orbit is 1.57°. The rotation axis of the Sun is inclined about 5.9° (Gomes, Deienno, and Morbidelli, 2017) relative to the invariable plane ($7.155 \pm 0.002°$ relative to Earth's orbital plane, Beck and Giles, 2005). This relatively low stellar obliquity and coplanarity of the planets inspired the nebular hypothesis of planet formation, in which the protoplanetary disk and the central rotating star inherit their angular momenta from the same collapsing cloud of gas and dust (Kant, 1755; Laplace, 1796). The fact that the solar obliquity is nonzero could be due to ongoing processes such as nodal precession from an unseen Planet Nine (Batygin and Brown, 2016; Bailey, Batygin, and Brown, 2016; Lai, 2016; Gomes, Deienno, and Morbidelli, 2017), or arose early in the solar system's history from torques by a stellar flyby on the protoplanetary disk (Heller, 1993) or by solar winds 10-100 Myr after the planets formed (Spalding, 2019).

In extrasolar systems, HJs formed *in-situ* or via disk migration inherit the orbital plane of the protoplanetary disk in which they formed, which itself can be significantly misaligned through magnetic warping by the young star (Lai, Foucart, and Lin, 2011). HJs formed by HEM can obtain any obliquity from aligned (prograde) to anti-aligned (retrograde) (Fabrycky and Tremaine, 2007; Chatterjee et al., 2008; Naoz et al., 2011; Anderson, Storch, and Lai, 2016; Vick, Su, and Lai, 2023). The stellar obliquity is readily measured in extrasolar systems by observing a transit with high-resolution spectroscopy. We discuss

[1]Except Mercury, inclined 6.35°, which is far more susceptible to chaotic evolution away from its initial orbital configuration (e.g., Batygin, Morbidelli, and Holman, 2015).

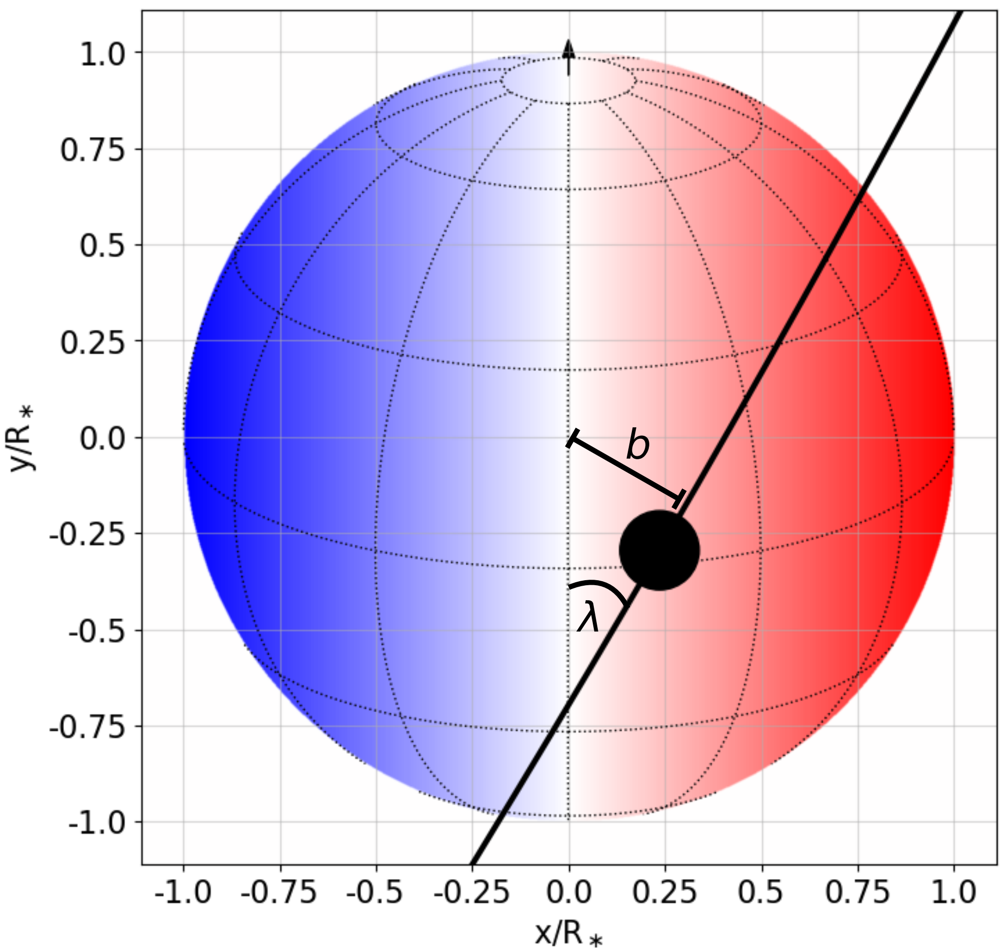

Figure 1.2: 2D sky-plane geometry of a star with a transiting planet (black circle) along its orbit (thick black line). The star is colored according to the projected (solid body) rotational velocity at that point. The coordinate system is defined with the vertical y-axis aligned with the stellar rotation axis and the x-axis horizontal. The planet's orbit is inclined at an angle λ relative to the rotation axis of the star and passes a distance b (the impact parameter) from the center of the star at mid-transit.

the measurement itself in more detail in Section 1.4, but in brief, the planet occults different patches of the rotating stellar surface along its transit chord, removing that patch's contribution to the rotationally broadened line profile. The precise variation across the transit depends on how the transit chord intersects the rotating stellar disk on the sky; in other words, the sky-projected stellar obliquity (λ) is directly measurable (see Figure 1.2).

This technique was applied to HD 209458 b just 18 days after it became the first exoplanet seen to transit (Queloz et al., 2000). Like the solar system planets, HD 209458 b's orbit is aligned with its star, with $\lambda = -4.4 \pm 1.4°$ (Queloz

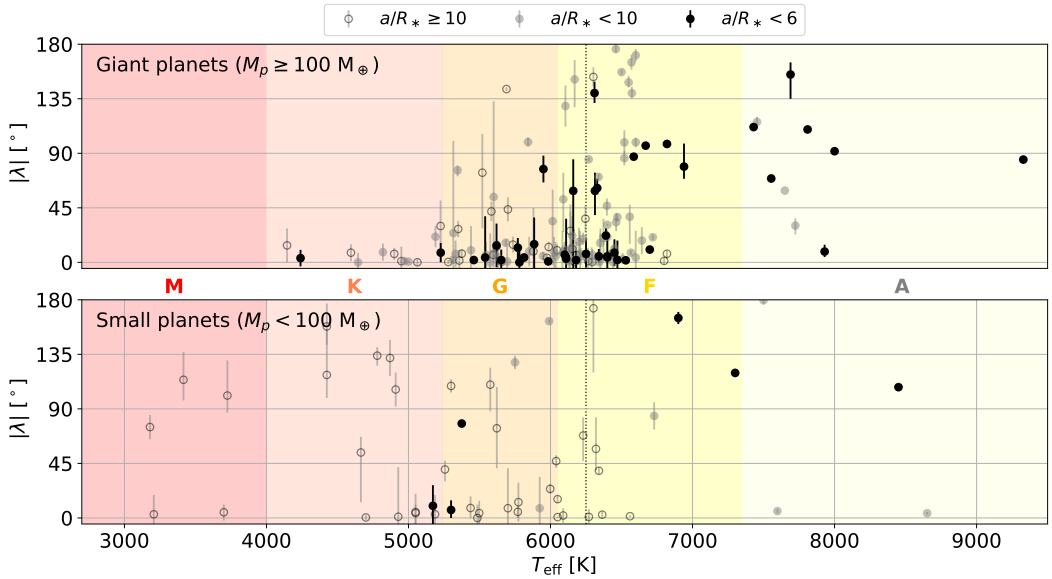

Figure 1.3: Sky-projected stellar obliquities as a function of effective temperature, for giant (≥ 100 M$_\oplus$, top) and small (< 100 M$_\oplus$, bottom) exoplanets. Background shading highlights the stellar spectral types. The Kraft Break at 6250 K is given by the vertical dotted line. Different fills on the scatter points encode the scaled semimajor axis a/R_*. The dataset is the same as Figure 1.1 from the NASA Exoplanet Archive.

et al., 2000; Winn et al., 2005). Over the next eight years, stellar obliquity measurements were made for ten other extrasolar systems; all were aligned. It seemed as if alignment was the norm. Then, Hébrard et al. (2008) measured XO-3 b, an object on the giant-planet-brown-dwarf boundary, and found it to be highly misaligned ($\lambda = 70 \pm 15°$). More misaligned planets were found soon after, including several on retrograde orbits (e.g., Triaud et al., 2010). Winn et al. (2010a) and Schlaufman (2010) noted that it was only the HJs orbiting hot stars which were misaligned, while the cool stars hosted aligned HJs. The top panel of Figure 1.3 plots the current sample of HJ obliquities, in which this pattern can still be clearly seen today. Either obliquity excitation mechanisms only operate around hot stars, or misalignment is a common outcome of HJ formation but orbits are efficiently realigned around cool stars.

The proximity of the transition from alignment to misalignment to the Kraft Break (Kraft, 1967) at 6100–6250 K was immediately suspicious. The Kraft Break corresponds to a change in stellar internal structure, below which (cooler) stars have deep convective envelopes and strong magnetic dynamos, and above which (hotter) stars have radiative envelopes and weak magnetic dynamos.

Magnetic breaking efficiently slows the rotation rates of cool stars, but is unable to affect hotter stars, producing a sharp transition in the $v \sin i_\star$ distribution. Just as stars raise tides on their planets, planets too raise tides on their stars. The tidal potential across the (fluid) stellar interior excites waves that then dissipate into heat, yielding an energy sink that drains angular momentum from the planet's orbit. This damps the orbital inclination, effectively realigning the planet's orbit to the stellar rotation axis (Hut, 1980; Hut, 1981; Winn et al., 2005). Tidal dissipation is more efficient in convective regions, and so cooler stars can more easily realign their planets. The associated timescale for hotter stars far exceeds the ages of those systems (Winn et al., 2010a; Albrecht et al., 2012; Dawson, 2014).

The same tides raised on the star also act to damp the orbital semimajor axis. The tidal bulge raised on the star lags behind a HJ, which orbits its star more quickly than the star rotates. As a result, the bulge torques and slows the orbit of the planet, causing it to inspiral until eventually crossing its Roche boundary and tidally shearing into a stream of particles that fall into the star. In the classical equilibrium tide theory (e.g., Hut, 1980; Rasio et al., 1996), it turns out that semimajor axis decay is more rapid than obliquity damping; in other words, the planet is destroyed before it realigns. Lai (2012) alleviated this problem by showing that the excitation of inertial waves in the convective layers of cool stars leads to the obliquity damping without removing orbital energy, i.e., without orbital decay. Rogers and Lin, 2013 showed that this inertial wave dissipation cannot cannot torque retrograde orbits all the way back to prograde, they either tend towards 90° or 180°. More recent studies which combined both equilibrium tides and inertial wave dissipation (Xue et al., 2014) and the effects of magnetic breaking (Li and Winn, 2016) found that while the obliquity does stall at polar and anti-aligned orientations, close-in giant planets do eventually damp all the way to 0°.

A lingering challenge with inertial wave dissipation is that hot stars would have had convective envelopes pre-main-sequence (Amard et al., 2019), so HJs must form later. Misaligned HJs do tend to orbit older stars, which supports late-arrival theories (Hamer and Schlaufman, 2022). However inertial wave dissipation scales with the rotation rate of the host star, which is likely too slow for cool stars after a few hundred Myr for obliquity damping to occur within typical system ages (Spalding and Winn, 2022). There is also still a problem with initially retrograde systems being torqued into anti-alignment, which is not observed in the exoplanet population (Albrecht, Dawson, and Winn, 2022). Zanazzi, Dewberry, and Chiang (2024) recently showed that resonance locking of the orbital frequency with stellar g-modes in the radiative cores of cool stars can enhance tidal torquing of the stellar spin axis into alignment with the planet's orbit, reproducing the transition at the Kraft Break even for initially retrograde systems while naturally avoiding engulfment.

Suffice it to say, dissipative mechanisms are an ongoing area of theoretical investigation but are likely at play based on observations. Rice, Wang, and Laughlin (2022) showed that the transition in the obliquity distribution at the Kraft Break disappears when selecting only eccentric HJs, which can be explained by dissipative mechanisms which damp eccentricity faster than obliquity. Another clue is the broad tendency for small planets to be misaligned, even around cool stars (bottom panel of Figure 1.3) (Attia et al., 2023). Small planets have longer realignment timescales (which scale as M_p^{-2}) (Albrecht, Dawson, and Winn, 2022) but are also susceptible to ongoing secular interactions with outer perturbers (Yee et al., 2018; Rubenzahl et al., 2021).

If misalignment instead arose during the disk phase, perhaps by an outer stellar perturber torquing the protoplanetary disk (Batygin, 2012), then the strong magnetic dynamos of cool stars could realign their disks through magnetic torquing to produce the observed transition at the Kraft Break (Spalding and Batygin, 2015). HJs like WASP-47 b (Hellier et al., 2012), which have *inner* planetary companions (Becker et al., 2015), are most compatible with disk migration since HEM would have ejected the inner planets. WASP-47 b (Sanchis-Ojeda et al., 2015) and the ~half-dozen similar known systems (Radzom et al., 2024) are well-aligned, hinting at a tendency towards primordial alignment of protoplanetary disks. Additionally, all directly imaged young ($<$ 100 Myr) systems still in the disk phase show alignment (e.g., Hirano et al. 2020; Kraus et al. 2020b, see Albrecht, Dawson, and Winn 2022). Evidence for primordial misalignment exists in systems such as K2-290 A, which has a coplanar planetary system consisting of a HJ and a sub-Neptune, but is highly misaligned (retrograde) (Hjorth et al., 2021). The companion star K2-290 B is at the right distance to have torqued K2-290 A's protoplanetary disk into misalignment, though chaotic evolution as a result of the third star in the system (K2-290 C) could instead have produced the retrograde orbits post-formation

(Best and Petrovich, 2022). Warped disks have also been observed (e.g., Kraus et al., 2020a), and such broken-disk morphologies are expected to further amplify stellar obliquities through resonance crossings (Epstein-Martin, Becker, and Batygin, 2022). Even in isolated single-star systems, the stellar spin direction may randomly tumble due to propagating internal gravity waves in hot stars (Rogers et al., 2013), further blurring the distribution. Overall, observational evidence and theoretical hypotheses exist for both primordial and post-formation obliquity excitation (and subsequent damping), and are compatible with both the disk migration and HEM formation channels.

Another testable prediction is that HJs which underwent HEM should have outer companions which triggered their migration. Distant planetary companions to inner small planets are common ($\sim$50%; Knutson et al., 2014; Bryan et al., 2016) as systems which can form outer giant planets can also likely form smaller inner planets (Bryan and Lee, 2024). A similar fraction of HJs have binary stellar companions between 50–2000 AU, but these companions are weakly coupled to giant planets in the 1–5 AU range and thus unable to induce HEM by the Kozai mechanism (Fabrycky and Tremaine, 2007; Ngo et al., 2016). For close-in smaller planets with outer giant companions, secular interactions driven by resonance crossings during the disk-dispersal stage can also excite large obliquities (Petrovich et al., 2020). The census of distant giant companions is quite incomplete, a consequence of the multi-year observing baselines required to trace out their orbits (e.g., Rosenthal et al., 2021; Van Zandt et al., 2023).

This thesis studies several planetary systems which are each a unique probe of HJ formation pathways. WASP-107 b is a super-inflated Neptune mass exoplanet whose extremely low density is only consistent with a history of migration (Piaulet et al., 2021). In Chapter 4, WASP-107 b's orbit is confirmed to be polar and is likely continuing to be affected by the outer planetary companion WASP-107 c. A number of polar hot Neptunes with escaping atmospheres have now been discovered around cool stars (e.g., Yee et al., 2018; Bourrier et al., 2018; Stefànsson et al., 2022; Attia et al., 2023), suggestive of common formation mechanisms. While the noted preference for polar orbits among HJs (Albrecht et al., 2022) is not yet statistically significant (Dong and Foreman-Mackey, 2023; Siegel, Winn, and Albrecht, 2023), Chapter 5 adds one more polar HJ around a hot star to the population; KELT-18 b is a binary star system, with the binary companion's orbit likely inclined relative to KELT-18 b. As such, it could have triggered HEM via the Kozai-Lidov mechanism so long as KELT-18 b formed well beyond the ice-line. An overabundance of polar orbits within the obliquity distribution would challenge HJ formation theories to explain such a preferred outcome.

Planets caught in the act of HEM would provide direct insight into the process. Chapter 6 provides an obliquity measurement for Kepler-1656 b, a sub-Saturn with an extreme eccentricity consistent with either active tidal migration or ongoing eccentricity oscillations caused by its distant giant companion. Kepler-1656 b, and the one other similar system (TOI-3362; Dong et al., 2021; Espinoza-Retamal et al., 2023) are consistent with aligned orbits. Perhaps HEM and the companions which initiate it are more gentle than previously thought, in which case post-migration dynamics would play a key role in setting the present-day obliquity.

Finally, an especially unique test of realignment mechanisms is to measure planets around evolved stars. In particular, stars more massive than > 1.2 $M_\odot$, which have evolved across the Kraft Break. Such stars have only recently acquired the ability to realign their planets. Chapter 7 investigates a transit of Kepler-1658 b, which is itself an even more powerful laboratory for testing tidal theories as it is also experiencing tidal orbital decay (Vissapragada et al., 2022). Growing this sample will provide new insights into the evolution of exoplanetary orbits (Saunders, N. accepted to AJ).

1.3 Techniques For Measuring the Radial Velocity

"If the mass of this [hypothetical 1 day orbital period] planet were equal to that of Jupiter, it would cause the observed radial velocity of the parent star to oscillate with a range of ± 0.2 km s^{-1}–a quantity that might be just detectable with the most powerful Coudé spectrographs in existence."

— Otto Struve, *Proposal For A Project Of High-Precision Stellar Radial Velocity Work,* 1952

A bound star-planet system will co-orbit their common center-of-mass. The radial velocity (RV) of the star from the observer's line of sight may be calculated from Kepler's laws of motion and Newtonian gravity, which leads to (Lovis and Fischer, 2010)

$$v_r(t) = \gamma + K\left[\cos\left(\omega + f(t)\right) + e\cos\omega\right], \tag{1.1}$$

where

$$K = \frac{M_p}{M_* + M_p} \frac{2\pi a \sin i_{\rm orb}}{P\sqrt{1-e^2}}, \tag{1.2}$$

is the semiamplitude, dependent on the planet mass (M_p), semimajor axis (a), orbital inclination $i_{\rm orb}$, orbital period P, and eccentricity e, as well as the stellar mass M_*. γ is the bulk RV offset while the term in square brackets depends on the argument of periastron (ω) and the true anomaly $f(t)$, which can be computed numerically by solving Kepler's Equation

$$M = E - e \sin E \tag{1.3}$$

for the eccentric anomaly E, given the mean anomaly $M = \frac{2\pi}{P}(t - t_0)$ and the time of periastron passage t_0. Then $\cos f = (\cos E - e)/(1 - e\cos E)$.

The RV (v_r) can be measured thanks to the Doppler effect, which gives the change in wavelength of emitted light due to the (non-relativistic) motion of the source relative to the observer,

$$\frac{v_r}{c} = \frac{\Delta\lambda}{\lambda_0} = \frac{\lambda - \lambda_0}{\lambda_0}, \tag{1.4}$$

where $c \equiv 299,792,458$ m s^{-1} is the speed of light. Thus, we can create a RV time series to search for Keplerian signals of the form in Eq. 1.1 by monitoring the wavelengths λ of the cores of spectral lines, relative to a reference measurement (λ_0). The amplitude of the Keplerian signal constrains the planet's mass while its shape (see Fig 1.4) constrains the planet's orbital properties. Modern spectrometers are able to simultaneously measure thousands of spectral lines from the near-UV to the near-IR at high spectral resolving power $R = \delta\lambda/\lambda_0 \gtrsim 100,000$ using cross-dispersed echelle spectroscopy, a method that neatly formats the high-resolution 1-D spectrum into a 2-D rectangular area that fits conveniently on an imaging array (Gibson, 2013). To isolate the motion of the star from the motion of the observatory along the line of sight, v_r and its associated timestamp t must be transformed into the solar system barycenteric frame (Kanodia and Wright, 2018). With the modern International Celestial Reference System (ICRS) and a precise timing of photon-arrival-times as a function of wavelength, as traced by a chromatic exposure meter (Blackman, Ong, and Fischer, 2019), this "barycentric correction" can be applied to below the 1 cm s^{-1} level.

For a 1 $M_\oplus$ planet in a circular 1 year orbit around a 1 $M_\odot$ star, the RV from Eq. 1.1 is 8.9 cm s^{-1}. This simple fact defines the < 10 cm s^{-1} precision goal

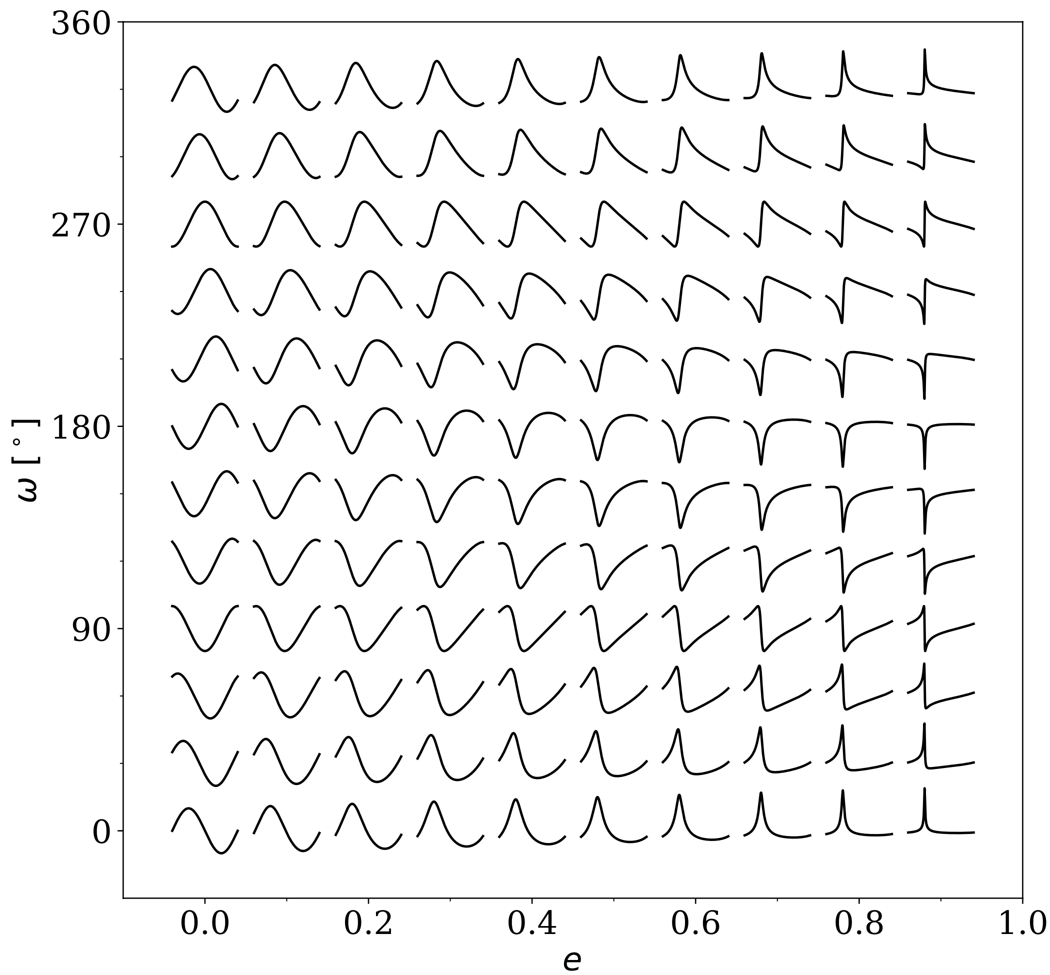

Figure 1.4: Gallery of RV curves (Eq. 1.1) for different eccentricities (e, x-axis) and arguments of periastron (ω, y-axis). Circular orbits produce sinusoidal RV variations. As eccentricity increases, the RV curve becomes more "cuspy" with the bulk of the stellar acceleration occuring near periastron passage. As the orientation (ω) of the orbit changes relative to the observer, the asymmetry of the RV variation around periastron passage changes.

of the Extreme Precision Radial Velocity (EPRV) community (Fischer et al., 2016). In Struve's day, the 1950s state-of-the-art Coudé spectrographs could achieve ~300-500 m s^{-1} stability, at best. Griffin (1973) was the first to point out that this poor precision was primarily due to the wavelength reference, an emission lamp with heated gas such as thorium argon (ThAr), not following the same optical path as the starlight. Griffin (1973) argued that a reference that followed the same optical path already existed: telluric lines from Earth's atmosphere. As such, these lines would move in lockstep with the stellar lines through the spectrometer and could provide ~10 m s^{-1} Doppler precision. Griffin (1973) also pointed out many of the major elements of what we now call the RV "error budget" that would have to be controlled to reach this level: spectral type, wavelength coverage, exposure time, opto-mechanical stability, thermal stability, telluric contamination, and the barycentric correction.

The first dedicated RV searches for exoplanets (Campbell, Walker, and Yang, 1988; Walker et al., 1995) made the next breakthrough by placing a cell of absorptive gas in the optical path, superimposing the gas absorption spectrum on the stellar spectrum (Campbell and Walker, 1979). Absorption lines from the gas provided a wavelength reference that was much more stable than telluric lines. Apart from being extremely poisonous to humans and corrosive to glass, the gas of choice (hydrogen fluoride) had relatively few absorption lines over a narrow wavelength range; the resulting RV prevision was ~15 m s^{-1}. This led Butler et al. (1996) to make the next breakthrough to the ~3 m s^{-1} level by instead using iodine gas, which has a much denser forest of thousands of absorption lines (and did not endanger the observer). When other factors were not limiting, the iodine technique could measure RVs as precise as 1.5 m s^{-1} (e.g., on HIRES after the CCD upgrade in 2004; Vogt et al., 1994).

However, 1.5 m s^{-1} is about where the iodine technique bottoms-out. The iodine spectrum still covers a narrow wavelength range (510–620 nm), limiting the usable portion of the stellar spectrum from which the RV can be derived. A complex forward model is required to convolve the instrument line-spread function (LSF) with the product of a lab-measured iodine spectrum (with $R = 10^6$ from a Fourier Transform Spectrograph; FTS) and an iodine-free template stellar spectrum (itself deconvolved by the LSF) Doppler shifted by some amount $\Delta\lambda$, which can then be fit to the observed star+iodine spectrum. As a result, high signal-to-noise (S/N) is needed (200 per pixel for 1.8 m s^{-1}

performance) as well as a detailed understanding of the LSF (to $< 1\%$, which can be measured from the same FTS iodine spectrum and observations of B stars with iodine; Valenti, Butler, and Marcy, 1995).

At the same time that the iodine technique was being developed at Lick Observatory (Vogt, 1987; Vogt et al., 2014) and Keck Observatory (Vogt et al., 1994), an alternative technique was being developed in Europe. Baranne et al. (1996) built the ELODIE spectrograph, which was fiber-fed (rather than slit-fed at Lick and Keck), held in a temperature-controlled room, and relied on its intrinsic stability rather than a simultaneous wavelength reference (Brown, 1990). ELODIE achieved $\sim$7 m s^{-1} precision, good enough for the Nobel Prize winning discovery of 51 Pegasi b (Mayor and Queloz, 1995). The lessons learned from ELODIE led to the conception of HARPS (Mayor et al., 2003), the first purpose-built Doppler spectrometer for planet hunting. HARPS combined the fiber-fed stability of ELODIE with the principle of simultaneous wavelength reference from the iodine technique by using a second fiber to measure a ThAr spectrum directly adjacent to the stellar spectrum (Rupprecht et al., 2004). With the full wavelength coverage of the spectrometer now available for computing RVs, along with other innovations that further improved stability (e.g., fiber scrambling; Avila and Singh, 2008), HARPS became the first instrument to break the m s^{-1} precision barrier by achieving 0.5–0.8 m s^{-1} performance at S/N $\geq$ 200 (Fischer et al., 2016).

A comprehensive accounting of the RV error budget (e.g., Podgorski et al., 2014; Fischer et al., 2016; Halverson et al., 2016; Blackman et al., 2020) has led to the current generation of fiber-fed spectrometers built on highly stabilized optical platforms, inside precisely thermally controlled vacuum chambers, with fiber scrambling (agitation) for spatial (modal) noise suppression (Halverson et al., 2015). A laser frequency comb (LFC; Murphy et al., 2007; Ycas et al., 2012; Phillips et al., 2012) or a Fabry-Perot etalon (Wildi et al., 2010; Halverson et al., 2014) now serves as the idealized wavelength reference, thanks to their full wavelength coverage and regularly (and precisely) spaced emission lines of homogeneous intensity. Still, it is impossible to hold an instrument perfectly still, so in practice the instrumental drift must be monitored. Generally, a ThAr (or Uranium Neon, UNe) lamp is used to obtain a reference absolute wavelength solution, since the emission line positions are both known from quantum mechanical transitions and empirically measured using FTS spectra

(Redman, Nave, and Sansonetti, 2014). LFC spectra can then be tied to this absolute scale, and since the spacing between lines is both precisely known and regular, the wavelength corresponding to any given pixel on the detector can be traced based on how much the apparent LFC line positions deviate over time (e.g., due to thermal expansion). LFCs are extremely expensive, highly complex optomechanically, and come with high operating costs, so a (significantly cheaper but less long-term stable) etalon is used as the workhorse simultaneous reference taken alongside stellar observations to "connect the dots" between daily LFC and ThAr calibration sets (Bauer, Zechmeister, and Reiners, 2015). Currently, LFCs used in EPRV systems do not provide light bluer than ~490 nm, so another source (e.g., ThAr) must supplement for full wavelength coverage. The modern generation of EPRV systems, which includes (in the optical) HARPS-N (Cosentino et al., 2012), ESPRESSO (Pepe et al., 2013), EXPRES (Jurgenson et al., 2016), NEID (Schwab et al., 2016), MAROON-X (Seifahrt et al., 2018), and KPF (Gibson et al., 2020), is pushing to 10–30 cm s^{-1} precision (Pepe, F. et al., 2021). Concurrently, instruments like HPF (Mahadevan et al., 2012) and PARVI (Gibson, 2023) are overcoming challenges to instrumental stability in the near-infrared (NIR).

With such stable, high-resolution spectra across a broad wavelength range, uncontaminated by a superimposed gas spectrum, new methods of extracting the RV are being actively developed. The RV is traditionally computed by cross-correlating the stellar spectrum with a spectral line mask, optimized for the particular stellar spectral type (Baranne et al., 1996; Pepe et al., 2002), and measuring the location of the peak. Originally done optically in the focal plane by a physical mask with holes cut-out at the locations of spectral lines (Fellgett, 1955; Griffin, 1967; Baranne, Mayor, and Poncet, 1979), nowadays this is done numerically. The cross-correlation function (CCF) is effectively the averaged spectral line across the detector, which also smears across noise properties which may themselves vary across the detector. New methods that derive RVs at the line-by-line (LBL) level (Dumusque, X., 2018) are opening the way to characterizing instrumental drift across the detector (Cretignier et al., 2021; Cretignier et al., 2023). Improved modeling of telluric contamination (Bedell et al., 2019) and wavelength calibration (Zhao et al., 2021) lead the way to optimized spectral extraction. As we will discuss in Section 1.5, the now-primary (and perhaps fundamental) limit to the RV technique is stellar variability at the 0.1–1 m s^{-1} level from phenomena on the stellar surface.

1.4 Techniques For Measuring the Stellar Obliquity

Perhaps the first measurement of a stellar obliquity was performed on our Sun by Christoph Scheiner, a Jesuit astronomer who geometrically determined the inclination of the Sun's rotation axis relative to the ecliptic by tracing the path of thousands of sunspots (Casanovas, 1997). While we cannot directly observe the motion of a starspot, a transiting planet may in some cases obscure a starspot, producing a detectable "bump" in the light curve. The next time the stellar rotation period and planetary orbital period conspire to rotate the starspot into the visible hemisphere during a transit, whether or not the transit chord intersects the spot again depends on the projected spin-orbit angle λ. This "spot-crossing" technique (Sanchis-Ojeda et al., 2011) has been used to measure the stellar obliquity for heavily spotted stars. Rapidly rotating stars have enhanced brightness at their poles as a result of their oblate figure reducing the surface gravity at high latitudes, a feature that also enables obliquity measurements ("gravity darkening," Barnes, 2009). Asteroseismology has also been used to determine stellar inclinations, and thus obliquities, for several transiting planets (Huber et al., 2013). Statistical studies at the population level can leverage stellar rotation rates to infer the parent obliquity distribution for transiting planets (e.g. Louden et al., 2021; Louden et al., 2024). This thesis utilizes the spectroscopic transit technique, which is more broadly applicable to all stellar types and transiting geometries.

The Rossiter-McLaughlin Technique

As alluded to in Chapter 1.2, the stellar obliquity can be measured by observing an exoplanet transit its star with a RV spectrograph. This possibility was first noted by J. R. Holt (Holt, 1893) and was observed for the first time (on binary star systems) independently by Rossiter (Rossiter, 1924) and McLaughlin (McLaughlin, 1924). The Rossiter-McLaughlin (RM) effect, which bears their names, refers to the anomalous Doppler-shift recorded by a RV spectrograph due to a transiting object occulting the rotating stellar disk, altering the rotationally broadened line profile of the star. A planet on a prograde orbit would first transit the approaching (blueshifted) hemisphere of the star, thereby causing the observer to measure a disk-integrated line profile that is distorted slightly red. The opposite effect happens after the planet crosses the stellar rotation axis. If the planet were instead orbiting retrograde, this effect would play out in reverse. The shape and asymmetry of the RV variation

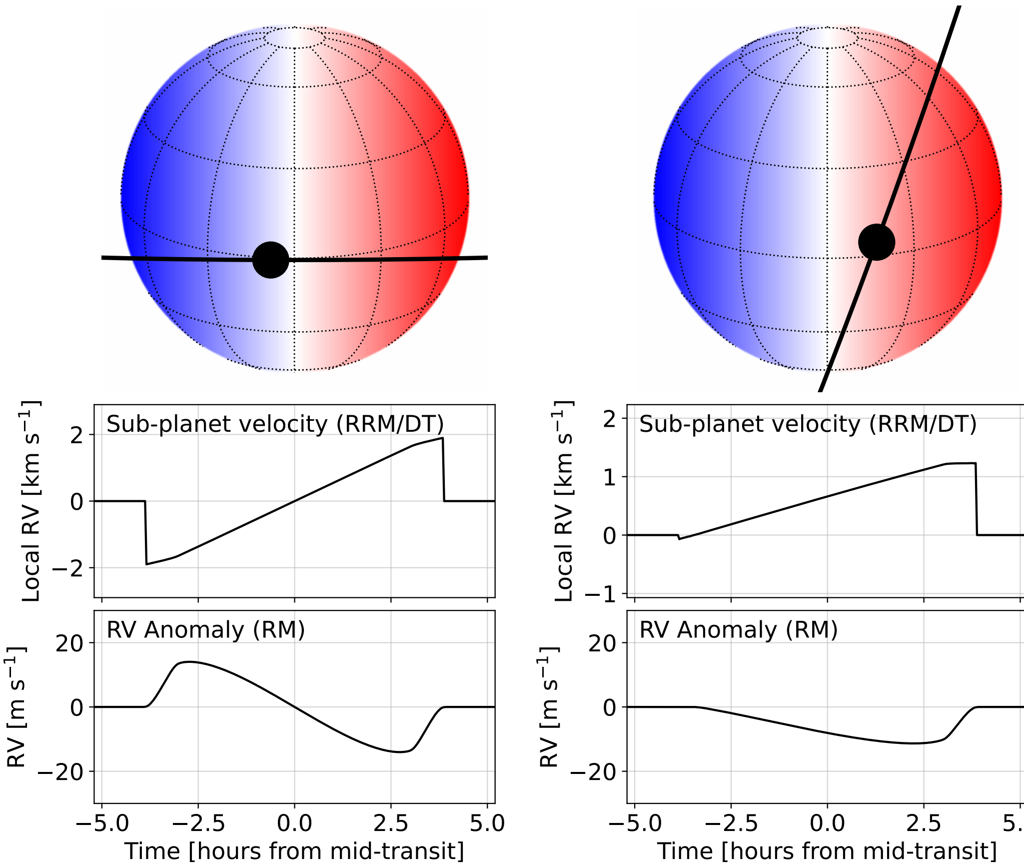

Figure 1.5: Example orbital geometries for an aligned (left) and misaligned (right) 1 $R_{\rm Jup}$ exoplanet in a 3.8 d orbit (with $i_{\rm orb} = 85°$) around a 1 $R_\odot$ star with $v \sin i_\star = 2$ km s^{-1}. The star has lines of latitude and longitude drawn to visualize its orientation in space; the star is slightly inclined towards the observer ($i_\star = 70°$) and has its rotation axis aligned with the vertical axis of the plot. The middle row plots the subplanet velocity, also called the local RV, defined in the text. The bottom row plots the corresponding RV anomaly that a Doppler spectrometer would measure.

throughout the transit depend on the projected obliquity and the transit impact parameter. Figure 1.5 plots an example geometry and corresponding RV variation for an aligned and misaligned planet. All the possible "RM curves" are plotted in Figure 1.6.

Theoretical modeling of the RM effect has grown in complexity as RV precision has pushed to the m s^{-1} level and below (Kopal, 1942; Hosokawa, 1953; Hirano et al., 2011). The anomalous RV is the intensity-weighted velocity of the stellar photosphere within the planet shadow (the "subplanet velocity," middle row in Figure 1.5), normalized by the fraction of the total flux obscured by the planet

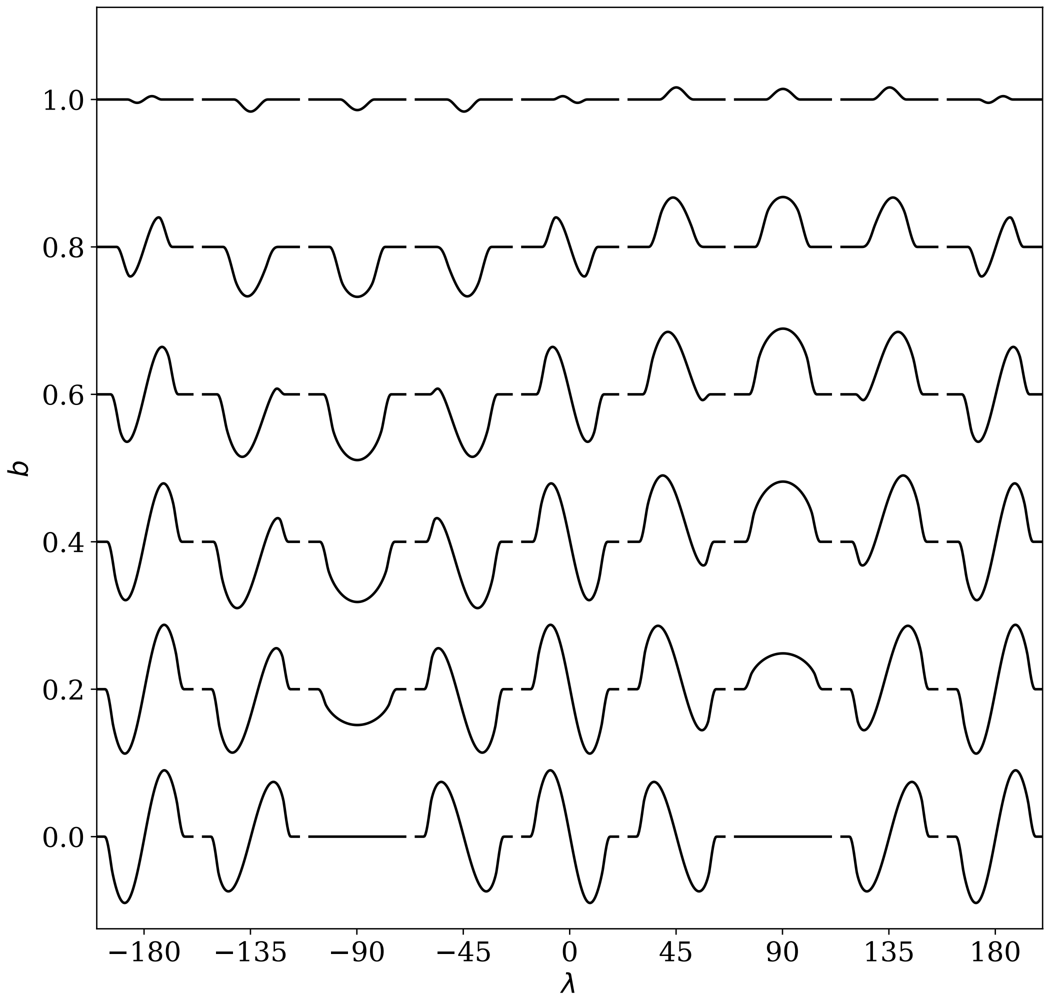

Figure 1.6: Gallery of RV variations due to the RM effect for different projected obliquities (λ, x-axis) and transit impact parameter (b, y-axis). Prograde ($|\lambda| < 90°$) orbits are characterized by an up-then-down (red-then-blue) pattern, while retrograde orbits ($|\lambda| > 90°$) show the opposite effect. The degree of asymmetry increases as λ deviates from fully aligned/polar/antialigned ($0°/90°/180°$) orbits. To detect a polar orbit, the transit impact parameter must be $b > 0$. As b increases, the transit chord approaches the limb of the star. The resulting RM curve for misaligned orbits will generally only occult either the approaching or receding hemisphere, rather than transiting both.

(lower panel in Figure 1.5, see Albrecht, Dawson, and Winn 2022 for more details). The subplanet velocity is affected not just by rotation, but also by convection (Beckers and Nelson, 1978; Shporer and Brown, 2011; Cegla et al., 2016a) which itself can be impacted by active regions (Haywood et al., 2016). A useful quantity is the expected amplitude of the RM signal (i.e., anomaly at ingress or egress) from the rotational effect alone (Albrecht, Dawson, and Winn, 2022),

$$\Delta \mathrm{RV}_{\mathrm{max}} \approx 15 \mathrm{~m~s}^{-1} \left(\frac{R_p/R_{\mathrm{Jup}}}{R_*/R_\odot} \right)^2 \left(\frac{v \sin i_\star}{2 \mathrm{~km~s}^{-1}} \right) \sqrt{1-b^2}. \tag{1.5}$$

While the RM signal scales with $v \sin i_\star$, Doppler precision is degraded at high $v \sin i_\star$ due to broadened lines having more centroid uncertainty than steeper, narrower lines, as well as uncertainty introduced from line blending (Bouchy, Pepe, and Queloz, 2001). Stars with $v \sin i_\star \gtrsim 10$ km s^{-1} are generally not amenable to precise RVs, but are instead more amenable to directly resolving perturbation from the transiting planet to the line profile itself.

The Reloaded Rossiter-McLaughlin Technique

The RM effect manifests in RV time series from the act of measuring the centroid of a spectral line, for example with the CCF technique (see Chapter 1.3). Physically, the planet's shadow removes that patch of the photosphere's contribution to the stellar spectrum, and thus the CCF, which biases the measured RV. In cases where $v \sin i_\star$ is large enough, the distortion can be directly resolved in the CCF. The toy model shown in Figure 1.7 shows that both a transiting planet and a starspot will have this effect. In practice, the contribution of the starspot is not simply a reduced-intensity copy of the stellar photosphere, but is itself a cooler photosphere with its own intrinsic spectrum.

The Doppler Tomography (DT; Donati et al., 1997; Collier Cameron et al., 2010) technique directly models this distortion by fitting a combination of two Gaussians to the CCF; one Gaussian represents the unperturbed CCF ("star" in Figure 1.7) and the other represents the bump from the planet ("planet" in Figure 1.7), also called the "Doppler shadow." The amplitude of the Doppler shadow (A_{shadow}) depends on how much of that particular velocity is removed by the planet. Said another way, it is related to the amplitude of the stellar CCF (A_{star}) by the ratio of the the planet's area to the area on the stellar disk

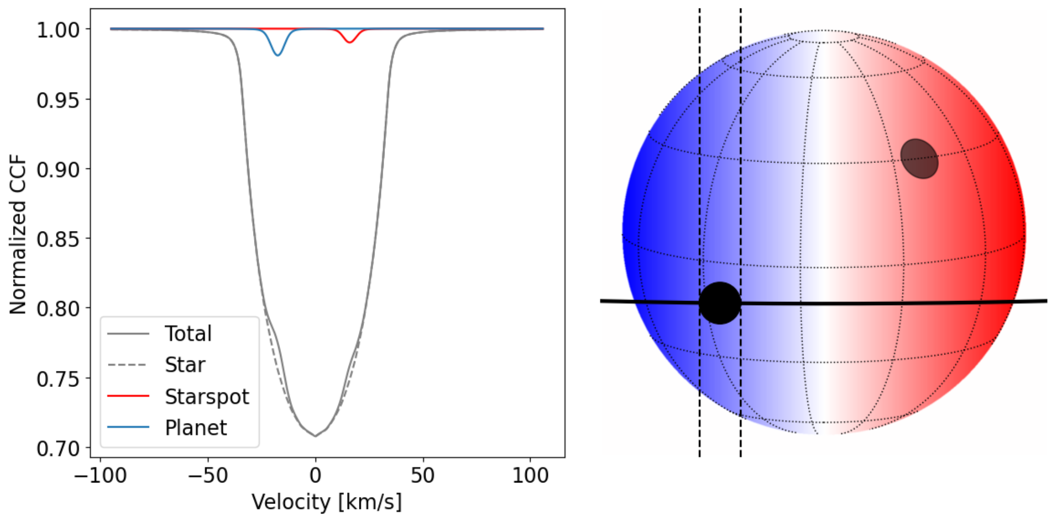

Figure 1.7: **Left:** Synthetic CCF (described in Chapter 7) consisting of an unperturbed stellar line profile broadened by $v \sin i_\star = 34$ km s^{-1} (grey dashed), the local CCF from the patch of star within the planet shadow (blue) as well as within a starspot (red), and the total (observed) CCF (grey solid) which is equal to the stellar CCF minus that beneath/within the planet/spot. **Right:** The on-sky geometry (same style as Figure 1.2) at the same timestamp that the CCFs are computed at, showing the planet occulting blueshifted light and a spot at +30° latitude with an intensity 30% that of the photosphere.

within the vertical strip in Figure 1.7 (Albrecht, Dawson, and Winn, 2022),

$$\frac{A_{\mathrm{shadow}}(t)}{A_{\mathrm{star}}} \approx \frac{1}{4}\left(\frac{R_p}{R_*}\right)\frac{1}{\sqrt{1-x(t)^2}}. \tag{1.6}$$

The width of the Doppler shadow is determined by the amount of broadening that occurs within the shadow, i.e. the local RV gradient across the shadow $2(R_p/R_*)v \sin i_\star$. The centroid of the Doppler shadow in velocity space is the subplanet velocity, defined in the previous section. The Doppler shadow's dependence on (R_p/R_*) rather than $(R_p/R_*)^2$ makes it more amenable to characterizing smaller planets, so long as rotational broadening is the dominant broadening mechanism. From Eq. 1.6, characterization of terrestrial-size exoplanets requires LSF stability at the 100 ppm level.

The Reloaded RM (RRM) method, developed by Cegla et al. (2016b), expands upon the DT technique. For rapidly rotating stars, the stellar line profile is not a Gaussian, but a rotation profile (Gray, 2005). The RRM method directly measures this by constructing a template CCF, $\mathrm{CCF}_{\mathrm{out}}$, by averaging all the observations taken outside the planet transit. This template is then subtracted from each in-transit CCF, yielding

$$\text{CCF}_{\text{loc}} = \text{CCF}_{\text{out}} - \text{CCF}_{\text{in}} = (\text{star}) - (\text{star} - \text{shadow}) = \text{shadow}. \qquad (1.7)$$

Thus, the CCF_{loc} are a direct measurement of the Doppler shadow itself. The RRM prescription fits these CCF_{loc} with Gaussian profiles and extracts their centroid, RV_{loc}, which are modelled by the subplanet velocity. Computing the model is relatively cheap, as only a few coordinate rotations are needed to identify the patch of star beneath a given point (x, y) on the sky and project the rotational velocity at that point along the line of sight. Adding the effects of center-to-limb variations can be accomplished by a simple polynomial model (Cegla et al., 2016b). Thus, the RRM technique effectively constructs a 1-D velocity time series that is efficiently fit. If the planet traverse multiple stellar latitudes, then this method also becomes sensitive to the stellar differential rotation (Roguet-Kern, Cegla, and Bourrier, 2022).

Generally, the presence of stellar activity produces only a linear trend in the classical RM time series, since the rotation period (days–weeks) is typically many times the typical transit duration (hours). However, line distortions (e.g., Figure 1.7) can blur the planet shadow if they overlap, making measurements of the obliquity more difficult.

1.5 Stellar Activity: Why Stare at the Sun?

The 1 m s^{-1} Stellar Activity Barrier

Despite EPRV instruments, facilities, and survey architectures maturing to the technical capability needed for measuring exo-Earths (Crass et al., 2021; Newman et al., 2023), exoplanet mass measurements with the RV technique have bottomed-out around 1 m s^{-1} (see Figure 1.8). At the sub-m s^{-1} level, phenomena on the surfaces of stars become the limiting noise source across all timescales (See Fig 1.9):

- On minutes timescales, acoustic oscillations restored by pressure (p-mode) in a star's convective zone cause the stellar radius to pulsate (Brown et al., 1991; Kjeldsen and Bedding, 1995; Kjeldsen et al., 2008), inducing m s^{-1} level Doppler shifts. While there are many oscillation modes with overlapping frequencies, this noise source can be efficiently binned down by tuning exposure times (or better, taking sequences of fast exposures) to average over the characteristic frequency ν_{max} (Chap-

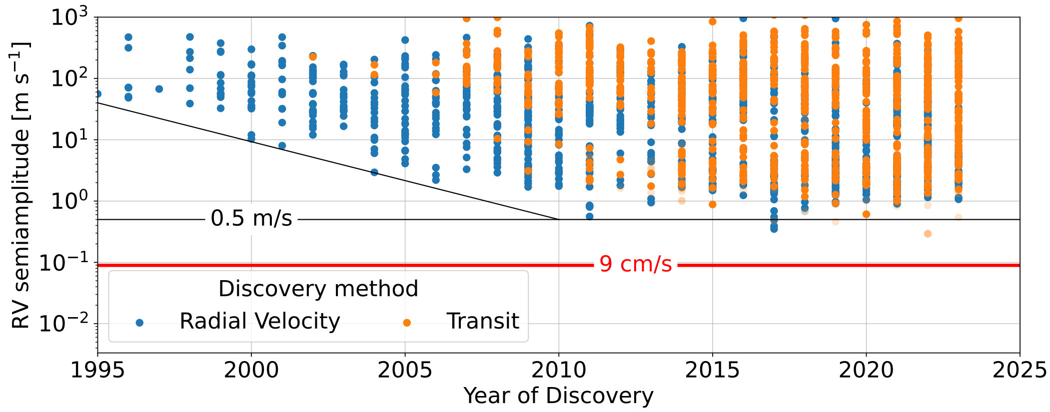

Figure 1.8: Measured RV semiampiltude as a function of year for exoplanets discovered by RVs (blue) or the transit method (orange). Since ~2010, RVs have been unable to characterize exoplanets below about 0.5–1 m s^{-1}. Stellar activity remains the greatest challenge to breaking this barrier to reach the 9 cm s^{-1} amplitude of an exo-Earth (red line). Data from the NASA Exoplanet Archive (as of Oct 4, 2023).

lin et al., 2019; Gupta and Bedell, 2023). This corresponds to ~5 min for solar type stars, but can be hours for hotter or evolved stars.

- Evolving convective patterns on small (granulation, hours) and large (supergranulation, tens of hours, see Rincon and Rieutord 2018) spatial scales distort spectral line shapes and positions, producing m s^{-1} level Doppler shifts when fitting line centroids (Dravins, Lindegren, and Nordlund, 1981; Del Moro, 2004). Like p-modes, granulation can be partially binned down by averaging exposures taken several hours apart within a given night (Dumusque, X. et al., 2011a). However, longer timescale supergranulation is difficult to resolve given the day-night cycle of Earth. 3D magnetohydrodynamical simulations have been the primary method for modeling granulation effects in spectra (Meunier, N. et al., 2015; Cegla et al., 2018; Palumbo et al., 2022).

- Magnetic activity manifesting as active regions (e.g. starspots, faculae, plage) are modulated by the star's rotation period, producing RV variability up to many m s^{-1} on weeks–months timescales. While active regions break the flux-symmetry across the star's rotational velocity profile (Saar and Donahue, 1997; Meunier, Desort, and Lagrange, 2010; Boisse, I. et al., 2011; Dumusque, X. et al., 2011b), a larger effect is the suppression of the convective blueshift within active regions (dominant

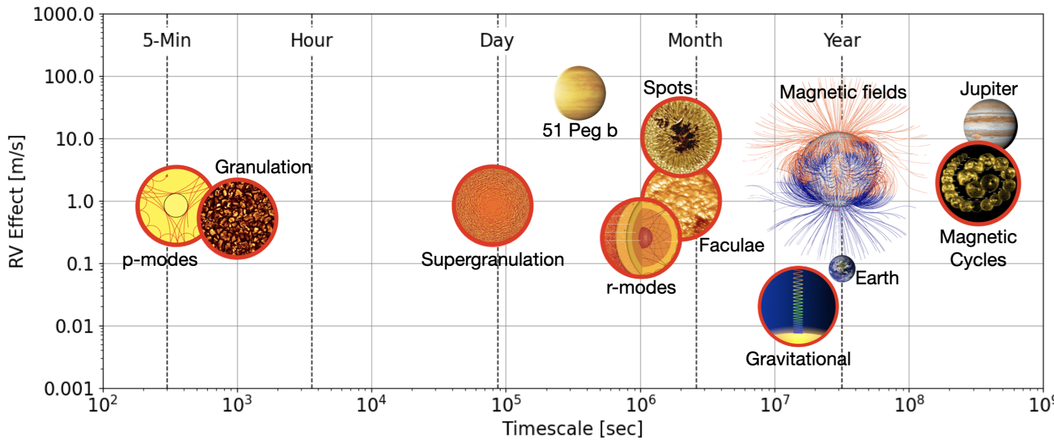

Figure 1.9: RV landscape of stellar activity for Sun-like stars. The confluence of multiple phenomena with different temporal and spectral characteristics at similar RV amplitudes nets a complex RV signal. The signals of 51 Pegasi b, Jupiter, and the Earth are shown for context. Nearly all types stellar activity become relevant at the > 10 cm s^{-1} level and span the full range of timescales from minutes to decades.

source in the Sun; Meunier, N., Lagrange, A.-M., and Desort, M., 2010a; Meunier, N. and Lagrange, A.-M., 2013; Haywood et al., 2016; Milbourne et al., 2019). Both produce quasi-periodic noise as active regions, grow, shrink, and move across the stellar disk. A common strategy is to use Gaussian Process (GP) regression in the time domain, often by training the GP on activity indicators (Haywood et al., 2014; Rajpaul et al., 2015; Aigrain and Foreman-Mackey, 2023). However, GPs are susceptible to overfitting and/or absorbing planetary signals (Blunt et al., 2023).

- Long-term magnetic activity cycles can produce RV variations on decades timescales (Baliunas et al., 1995; Meunier, N., Lagrange, A.-M., and Desort, M., 2010b; Lovis et al., 2011; Luhn et al., 2022) as a star increases and decreases in activity level (11 years for the Sun).

Stellar activity does not just bury the small signals of exoplanets. The quasi-periodic nature of active regions can also masquerade as exoplanet signals, yielding false positive detections (e.g., Lubin et al., 2021). Even with decades long surveys and thousands of observations per star, stellar activity remains the fundamental limit in our ability to detect exo-Earths (Langellier et al., 2021; Luhn et al., 2023; Gupta and Bedell, 2023). To detect true positive exo-Earths to characterize with next-generation NASA flagship missions like the Habitable Worlds Observatory (HWO), we must develop pipelines which derive RV time series unaffected by activity.

Traditional methods compute the RV by fitting the centroid of the cross correlation function (CCF) of a line mask with the observed spectrum. The RV time series is then detrended against a so-called "activity indicator," a metric which is highly correlated with stellar activity. Common indices use the chromospheric magnetically sensitive Ca H&K lines (S-index, $\log R'_{\mathrm{HK}}$) (Isaacson and Fischer, 2010a), Hα (Kürster et al., 2003), or line shape changes traced by the full width at half maximum (FWHM) or the bisector inverse slope (BIS) of the CCF (Queloz, D. et al., 2009). These have the advantage of being computed from the same spectrum as the RVs, but do not correlate perfectly with the activity-related component of the full-spectrum CCF RV. Aigrain, Pont, and Zucker (2012) developed a spot model to predict RVs in a similar way based on observed photometric variability (FF'). Troublingly, even photometrically quiet stars can exhibit unaccounted RV noise up to tens of m s^{-1} (likely granulation, Bastien et al., 2014).

Dumusque, X. (2018) took a different approach. By computing RVs at the individual line level (line-by-line, or LBL), they could combine only activity-insensitive lines (i.e. lines whose individual RVs were uncorrelated with activity indicators) for a more robust CCF RV, though at the cost of degraded precision (due to fewer lines being used). A followup study showed that the depth of individual spectral lines is strongly correlated with activity (Cretignier et al., 2020). Siegel et al. (2022) built upon this work to combine the LBL technique with FF' and GPs using a novel activity indicator based on line depth, the "depth metric." This method reduced the root-mean-square (RMS) of HARPS RVs of α Cen B from 2.67 to 1.02 m s^{-1} and could recover injected planetary signals as small as 1 m s^{-1}. Another promising novel activity indicator is $\Delta\alpha B^2$, a proxy for unsigned magnetic flux (Lienhard et al., 2023). While these approaches are superior to traditional detrending methods when strictly comparing the RMS reduction, Zhao et al. (2022) showed that methods often don't agree on distinguishing planetary signals from activity. On stars, the residual RMS is an unknown combination of both.

New methods which utilize the full wealth of spectral information are needed to make progress. While the spectral fingerprint of activity is a change in line shape, an exoplanet induces an achromatic Doppler shift. This fundamental difference may be leveraged to extract activity-invariant RVs. A promising approach used the principle components of the CCF to recover injected planet signals down to 40 cm s^{-1} (Collier Cameron et al., 2021). A more granular LBL approach could utilize all spectral information to push this even further.

Staring at the Sun

Observations of our Sun are unequivocally our best laboratory for directly connecting active processes to EPRV measurements, because we have the "answer in the back of the book." Utilizing the precise JPL ephemerides of the solar system planets, all planetary signals can be removed to below the mm s^{-1} level (Wright and Kanodia, 2020). Surface features are resolved in exquisite detail from the ground (e.g. DKIST; Rimmele et al., 2020) and from space (e.g. NASA Solar Dynamics Observatory, SDO; Schou et al., 2012).

As such, there is a growing network of instruments that feed disc-integrated sunlight into EPRV spectrographs. The Low Cost Solar Telescope (LCST; Phillips et al., 2016) for HARPS-N was the first, beginning operations in 2015. In 2018, a similar instrument (HELIOS) was added to HARPS. The current generation of EPRV spectrometers have begun to include solar feeds during their development stages, as they are particularly helpful for developing and testing various aspects of the instrument (e.g., optical alignment, data reduction pipeline) and assessing overall performance during the commissioning stage without requiring expensive nighttime allocations on the telescope. The NEID Solar Feed (Lin et al., 2022) and Lowell Observatory Solar Telescope (LOST; Llama in prep) both began operations in 2020 and have proven valuable in these regards. EPRV facilities which do not currently have solar feeds either have one planned, such as PoET for ESPRESSO (Leite et al., 2022) and ABORAS for HARPS-3 (Jentink et al., 2022), or are actively being installed (e.g., MAROON-X, PARVI, NIRPS). Each of these facilities utilize the same principle: an autonomous solar tracker on the roof of the observatory acquires the Sun, focuses sunlight into an integrating sphere which spatially scrambles the input sunlight, and long optical fiber run transports the homogenized sunlight to the spectrograph within the observatory. Chapter 3 presents the solar feed for KPF, the Solar Calibrator (SoCal). Figure 1.10 compares SoCal to other EPRV solar feeds.

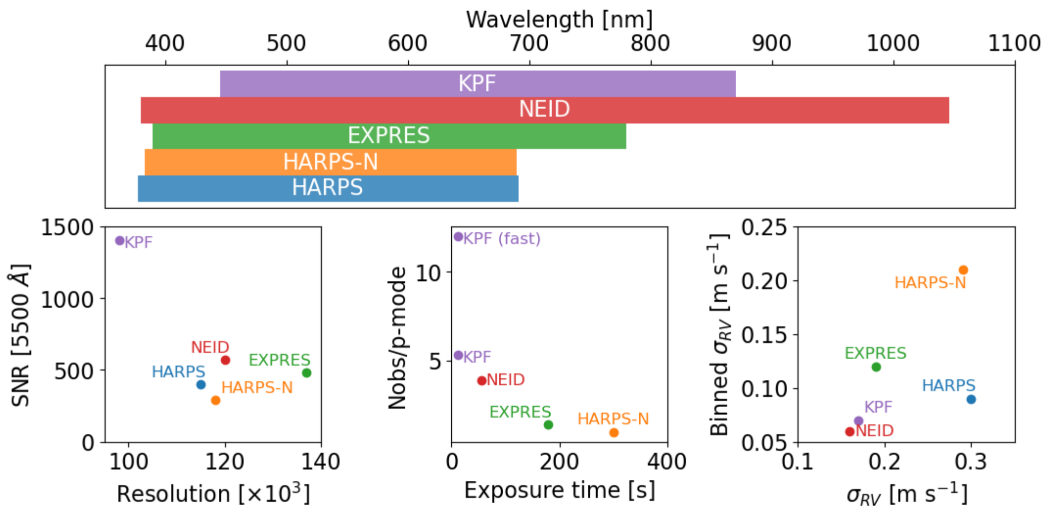

Figure 1.10: Comparison between the HARPS (blue), HARPS-N (orange), EXPRES (green), NEID (red), and KPF (purple) solar feeds. **Top:** wavelength coverage of each instrument. **Bottom-Left:** single-exposure S/N (at 5500 Å) vs. spectral resolution. KPF stands out at S/N > 1000 in the green channel (> 2000 in the red channel). **Bottom-Middle:** Number of obsevations per p-mode oscillation (5.5 minute interval) as a function of exposure time. KPF utilizes fast exposure times to obtain fast cadence, which is further sped-up in the fast-readout mode. **Bottom-Right:** Single-measurement photon-limited uncertainty σRV vs. the same quantity binned over 5.5 minutes worth of exposures (y-axis).

The only cross-instrument solar comparison study to date was recently conducted by Zhao et al. (2023b). The authors compared one month of solar data between HARPS, HARPS-N, EXPRES, and NEID, focusing on the agreement between instruments. They found an exceptional 15–30 cm s^{-1} RMS on intra-day timescales. On inter-day timescales, a larger 50–60 cm s^{-1} RMS was observed. The difference was attributed to unshared observing conditions (e.g. differential extinction due to variable airmass and solar disk position at each site at a given time). The authors noted qualitative agreement in quasi-periodic variability on the solar rotation period, but left a quantitative assessment to future work. At the moment, such studies suffer from a data availability problem. Only the first three years of HARPS-N solar data (2015–2018) have been published (Collier Cameron et al., 2019; Dumusque et al., 2021), but recent data is proprietary. A public database for EXPRES solar data is also still in-development (J. Llama, private communication). Only the NEID and KPF solar data are immediately available on a public archive. Improved data availability will yield massive, rich training datasets for developing novel methods for mitigating stellar activity.

By correlating synthetic RVs from the active and quiet parts of the Sun (computed using the SDO Helioseismic and Magnetic Imager (HMI) maps with `SolAster`, Ervin et al., 2022) to observed line shape changes, the source of activity may be identified. Lakeland et al. (2024) showed that synthetic RVs from the quiet part of the solar surface (i.e., not in a spot/faculae/plage) show a stable 1 m s^{-1} variability over their entire 7 yr baseline, with no correlation to known activity indicators. This granulation and supergranulation noise may be discernible by line bisector changes (Palumbo and Ford, 2024), though this requires very high spectral resolution and S/N to resolve individual line shape changes. Line-shape distortions from active regions likewise require ultra-high spectral S/N (Dravins and Ludwig, 2024). Machine learning methods such as neural networks (de Beurs et al., 2022) and auto-encoders (Liang, Winn, and Melchior, 2024) may be able to learn the difference between line shape changes and achromatic Doppler shifts, but require immense (and accurate) training sets to be reliably deployed for planet-hunting.

The KPF Solar Calibrator (SoCal), presented in Chapter 3, was built to fill this niche. SoCal spectra reach a maximum S/N of 2400, compared to ∼400 of existing EPRV solar feeds, though at lower resolution (see Figure 1.10). The fast cadence of SoCal additionally enables more effective binning over p-modes (binning noise described in Zhao et al., 2023b) to better isolate other noise sources. In a typical 6–8 hour day, EPRV solar feeds collect hundreds of spectra. The longitudinal coverage of HARPS, HARPS-N, EXPRES/NEID, and KPF yields 20 hours of continuous solar observations in the summer months and ∼17 hours in the winter, opening the door to studying intermediate timescale phenomena such as granulation. Critically, common variability in such multi-instrument contemporaneous datasets can be uniquely attributed to astrophysical processes on the Sun, while variability seen in only one instrument can be diagnosed as internal systematic errors. Both need to be better understood to usher in the era of exo-Earth discovery and characterization.

1.6 Thesis Outline

This thesis centers around the Keck Planet Finder (KPF), a newly commissioned EPRV spectrograph at W. M. Keck Observatory, but begins pre-KPF with the confirmation and mass measurement of the largest rocky ultra-short-period planet discovered to date, TOI-1347 b, in Chapter 2. This measurement highlights the importance of mitigating stellar activity in RV datasets. Chapter 3 presents the Solar Calibrator, an instrument for Sun-as-a-star observing with KPF. SoCal spectra are the highest S/N of their kind and will serve as a rich, public dataset for developing novel methodologies for mitigating stellar activity. SoCal gives us confidence in the immediate short-term stability (hardware and software) of KPF, which permits measurements of exoplanet stellar obliquities via spectroscopic transits.

The remaining chapters concern stellar obliquity measurements of four exoplanets, each of which provides a unique lens on HJ formation. The first is WASP-107 b, a super-Neptune that requires migration (via interactions with its outer companion) to explain its ultra-low density and extraordinarily large envelope mass fraction. Chapter 4 adds WASP-107 b to the growing population of polar hot Neptunes around cooler stars with escaping atmospheres, suggestive of common formation mechanisms.

Chapters 5, 6, and 7 present obliquity measurements made with KPF. The first is KELT-18 b, a proof of concept for KPF and another definitive "polar planet" with a stellar companion. The second, Kepler-1656 b, is a highly eccentric sub-Saturn that could plausibly be undergoing migration kick-started by its outer planetary companion. Curiously, its orbit may be aligned, atypical of the traditional picture of high-eccentricity migration. Lastly, in Chapter 7, is Kepler-1658 b, an exoplanet undergoing active orbital decay around a star that evolved across the Kraft Break, making it a unique dynamical laboratory for constraining tidal efficiencies. However, the transit we observed is contaminated by a massive starspot, which precludes the direct measurement of the obliquity and thus a dynamical interpretation. However, the starspot signal opens a new window into probing the effect of starspots on EPRV spectra. This dataset is thus an exciting union of the two primary themes in this thesis: stellar activity and the orbits of close-in exoplanets.

Finally, Chapter 8 concludes and looks to the exciting future of RV exoplanet astronomy.

Chapter 2

A DENSE ULTRA-SHORT-PERIOD PLANET POSSIBLY CLINGING TO A HIGH-MEAN-MOLECULAR-WEIGHT ATMOSPHERE

Rubenzahl, R. A. et al. (Apr. 2024). "The TESS-Keck Survey. XII. A Dense 1.8 R $_\oplus$ Ultra-short-period Planet Possibly Clinging to a High-mean-molecular-weight Atmosphere after the First Gigayear." In: *The Astronomical Journal* 167.4, 153, p. 153. DOI: 10.3847/1538-3881/ad28bb. arXiv: 2402.07451 [astro-ph.EP].

2.1 Introduction

Ultra-short-period planets, or USPs, are exoplanets that orbit their stars with short orbital period (< 1 day). USPs tend to not exceed 2 $R_\oplus$ in size, save for the closest of the hot Jupiter (HJ) population. This "hot-Neptune desert" (Mazeh, Holczer, and Faigler, 2016) has been hypothesized to be sculpted by mass loss mechanisms, such as photoevaporation (Owen and Wu, 2017) or core-powered mass loss (Gupta and Schlichting, 2019). Such mechanisms destroy the atmospheres of smaller planets, whereas giant planets can better resist mass loss (in fact, HJ atmospheres can become inflated; Batygin, Stevenson, and Bodenheimer, 2011; Grunblatt et al., 2017). The *Kepler* mission (Borucki et al., 2010) took the first steps to map out the demographics of close-in transiting planets and revealed that USPs exist around ∼0.5–0.8% of GK stars (Sanchis-Ojeda et al., 2014). Another key discovery from *Kepler* was the "radius gap" around 1.7–1.9 $R_\oplus$, which separated the bimodal peaks corresponding to the smaller super-Earth population (no atmosphere) and the larger sub-Neptunes ($\gtrsim$1% H/He atmosphere) (Fulton et al., 2017; Fulton and Petigura, 2018).

To date, only two non-giant USPs have been discovered with radii larger than 2 $R_\oplus$. TOI-849 b (Armstrong et al., 2020) is a massive (∼40 $M_\oplus$) rocky world that is likely the stripped core of a giant planet (perhaps via giant collisions). LTT-9779 b (29 $M_\oplus$, 0.79 days; Jenkins et al., 2020) defies its environment with a substantial (9% by mass) H/He atmosphere and a 4.6 $R_\oplus$ radius. This suggests some USPs can retain atmospheres. If so, where is the boundary between bare rocky cores and those with residual (or secondary) atmospheres?

A close-in orbiting planet will reflect starlight and emit thermal radiation, causing the observed brightness of the system to vary with the planet's orbital position. This variation, called the phase curve, depends on the planet's albedo and day-night temperature contrast. Phase curve variations have been used to directly probe the surfaces of several USPs, finding some to be bare rock (LHS 3844 b; Kreidberg et al., 2019; Kane et al., 2020) and others to perhaps possess high mean-molecular weight atmospheres (55 Cnc e; Demory et al., 2016).

Unlike *Kepler*, which observed a single patch of sky for four years, the Transiting Exoplanet Survey Satellite (*TESS*; Ricker et al., 2015) is an all-sky transit survey that has discovered thousands of close-in planets around nearby bright stars that are amenable to radial velocity (RV) follow-up measurements. RVs provide key insight into the existence of exoplanetary atmospheres by measuring the planet's mass, thereby constraining the bulk density, planet surface gravity (which is related to atmospheric scale height), and its ability to resist photoevaporation. Our collaboration, the *TESS*-Keck Survey (TKS; Chontos et al., 2022), has been monitoring 86 *TESS* systems with RV follow-up using the HIgh Resolution Echelle Spectrometer (HIRES; Vogt et al., 1994) at the Keck-I Telescope. As part of TKS, we have measured the masses of several USPs, such as TOI-561 b (Weiss et al., 2021) and TOI-1444 b (Dai et al., 2021), both of which have rocky compositions. In this paper, we present the discovery and mass measurement of the USP TOI-1347 b. The heaviest of the non-giant USPs[1] to date, TOI-1347 b shows hints of phase curve variability and a secondary eclipse in its *TESS* photometry, which may indicate the presence of a high mean-molecular-weight atmosphere. We also detected a second transiting planet in the system at 4.84 d, TOI-1347 c, in line with the common trend for USPs to have nearby outer companions which can shepherd the migrations of their USPs into their present sub-day orbits (Millholland and Spalding, 2020).

This paper is structured as follows. In Section 2.2 we characterize the host star using spectroscopy. We rule out stellar companions using speckle imaging

[1]Other than the exceptional LTT-9779 b and TOI-849 b, which likely belong to a separate class of planets than the $\lesssim 10$ $M_\oplus$ USPs (Dai et al., 2021).

in Section 2.3. In Section 2.4 we analyze the *TESS* light curve to measure the stellar rotation period, planetary transits, and tentative phase-curve variability and secondary eclipse. In Section 2.5 we present our RV measurements and the resulting mass constraints for both planets. Finally, we discuss the implications of our observations for the TOI-1347 system in Section 2.6.

2.2 Host Star Properties

Spectroscopic Properties

TOI-1347 (TIC 229747848) is a late G type ($T_{\mathrm{eff}} = 5464 \pm 100$ K) star that is relatively active ($\log R'_{\mathrm{HK}} = -4.66$), showing strong variability in both photometry (see Section 2.4) and RVs (see Section 2.5).

We obtained high-resolution spectra of TOI-1347 with HIRES (with the B3 decker, $R = 67,000$) and HARPS-N ($R = 115,000$); see Section 2.5 for details. We applied the `SpecMatch-Synthetic` (Petigura, 2015) algorithm to the HIRES spectrum to measure T_{eff}, $M_\star$, Fe/H, and $\log g$. These parameters, as well as the J and K magnitudes from the TICv8 catalog (Paegert et al., 2021) and the *Gaia* parallax (Gaia Collaboration et al., 2023), were input into *isoclassify* (Huber et al., 2017a; Berger et al., 2020) to constrain $R_\star$. We also used `KeckSpec` (Polanski in prep) to compute alpha elemental abundances. Stellar parameters for TOI-1347 are included in the catalog of MacDougall et al. (2023). We verified that our values agree with the values therein to within 1σ.

We similarly derived spectroscopic parameters from the co-added HARPS-N spectra of TOI-1347 using the FASMA spectral synthesis package (Tsantaki et al., 2018; Tsantaki, Andreasen, and Teixeira, 2020). We verified that all derived quantities were in agreement with the HIRES values. In particular, the HARPS-N data are of sufficient resolution to detect $v \sin i_\star$, whereas with HIRES we only obtain an upper limit. Table 2.1 lists our adopted stellar parameters.

Age

We constrained the age of the host star using several methods. Using a stellar rotation period of 16.1 ± 0.3 days (see Section 2.4 for details), we estimated the gyrochronological age of the star. The scaling relation of Mamajek and Hillenbrand (2008) gives an age of 1.33 ± 0.06 Gyr. Using the latest empirical relations of Bouma, Palumbo, and Hillenbrand (2023a), the

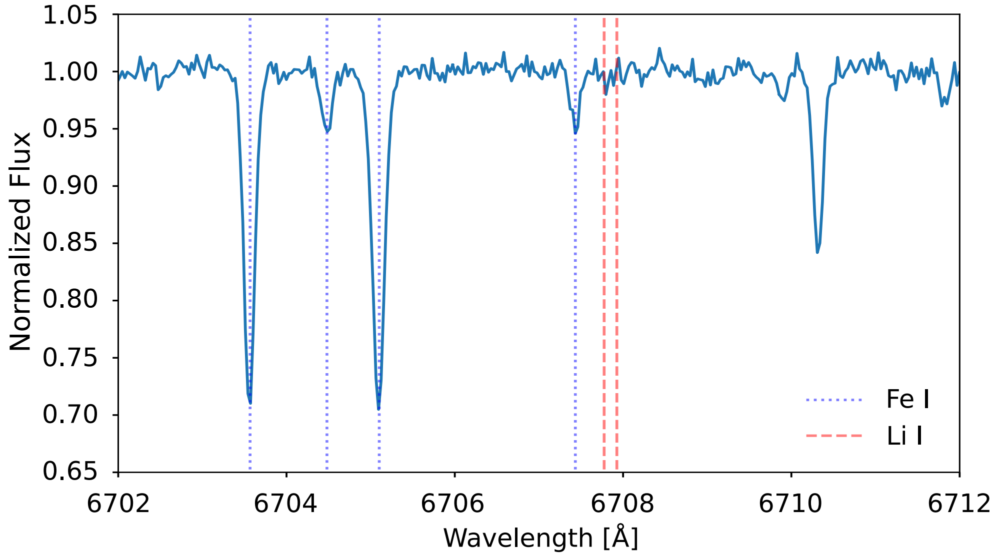

Figure 2.1: HIRES spectrum of TOI-1347 in the neighborhood of the lithium doublet. Nearby Fe I lines are labelled. No absorption attributed to lithium was detected.

age is 1.7 ± 0.1 Gyr. We also obtained an age estimate using chromospheric activity in the Ca II H & K lines from our HIRES spectra. We measured $\log R'_{\mathrm{HK}} = -4.66 \pm 0.05$ using the method of Isaacson and Fischer (2010b). Combining with the calibration of Mamajek and Hillenbrand (2008), the corresponding age is 1.6 ± 0.4 Gyr. We also looked for the lithium doublet in our HIRES spectra, but were unable to detect the lithium doublet above the noise floor in the continuum (see Fig. 2.1). We placed an upper limit of 2 mÅ (95% confidence) on the equivalent width. According to Berger, Howard, and Boesgaard (2018), the star is consistent with field stars and is most likely older than the Hyades cluster (∼650 Myr). Lastly, MacDougall et al. (2023) derived an age of $0.8^{+1.1}_{-0.6}$ Gyr from isochronal fitting.

The age uncertainties above do not account for systematic errors. Therefore, we combined age indicators with an unweighted mean. We adopted a wide age uncertainty of 0.4 Gyr to reflect the systematic uncertainties between the different age estimators. Our best age estimate for TOI-1347 is thus 1.4 ± 0.4 Gyr. Importantly, this age is longer than the timescale on which photoevaporation operates, which is typically confined to the first few hundred Myr when the star is active in X-rays and extreme UV (Ribas et al., 2005; Tu et al., 2015).

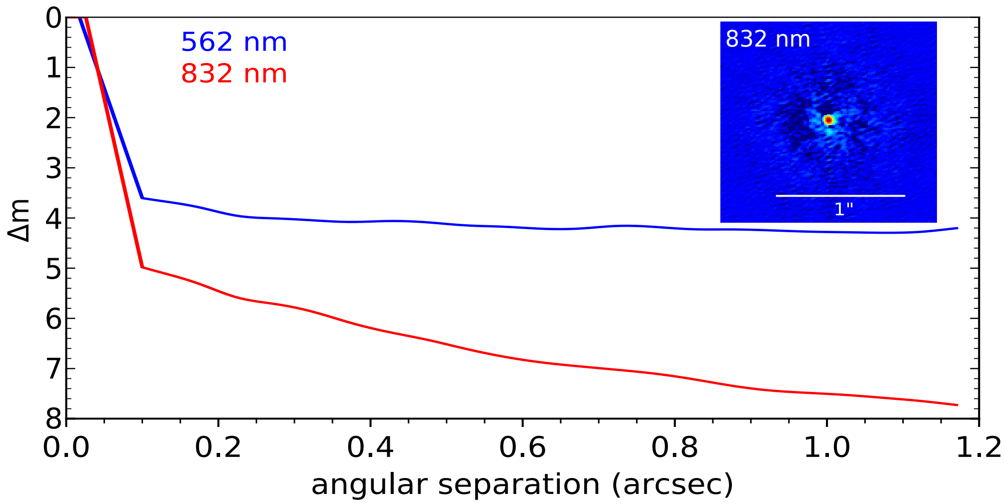

Figure 2.2: Contrast curves around TOI-1347 from Gemini/'Alopeke; the inset shows the reconstructed image at 832 nm. No companions are detected.

2.3 High Resolution Imaging

To help validate the transiting planets, we observed TOI-1347 with the 'Alopeke (Scott et al., 2021) dual-channel speckle imaging instrument on Gemini-N (PI: Crossfield) with a pixel scale of 0.01 arcsec/pixel and a full width at half maximum resolution of 0.02 arcsec. With 'Alopeke we obtained simultaneous speckle imaging at 562 and 832 nm, with a total of seven observing blocks each consisting of one thousand 60 ms exposures.

We processed these images with the speckle pipeline of Howell et al. (2011), which yielded the 5-sigma sensitivity curves and reconstructed image shown in Fig. 2.2. The curves do not show companions at angular separations of 0.5 arcsec or greater at a contrast of 4.12 mag at 562 nm and 6.52 mag at 832 nm (Fig. 2.2).

2.4 *TESS* Photometry

TOI-1347 was observed by *TESS* in sectors 14–26, 40, 41, and 47–60, which span UT Jul 18 2019 to Jan 18 2023. The Science Processing Operations Center (SPOC; Jenkins et al., 2016) detected two transiting planet candidates which were subsequently diagnosed and vetted as *TESS* Objects of Interest (TOIs) 1347.01 (b) and 1347.02 (c) (Guerrero et al., 2021).

We downloaded the 20 s and 120 s cadence SPOC light curves using `lightkurve` (Lightkurve Collaboration et al., 2018). We removed all data points with a non-zero Quality Flag, i.e. those suffering from cosmic rays or other known

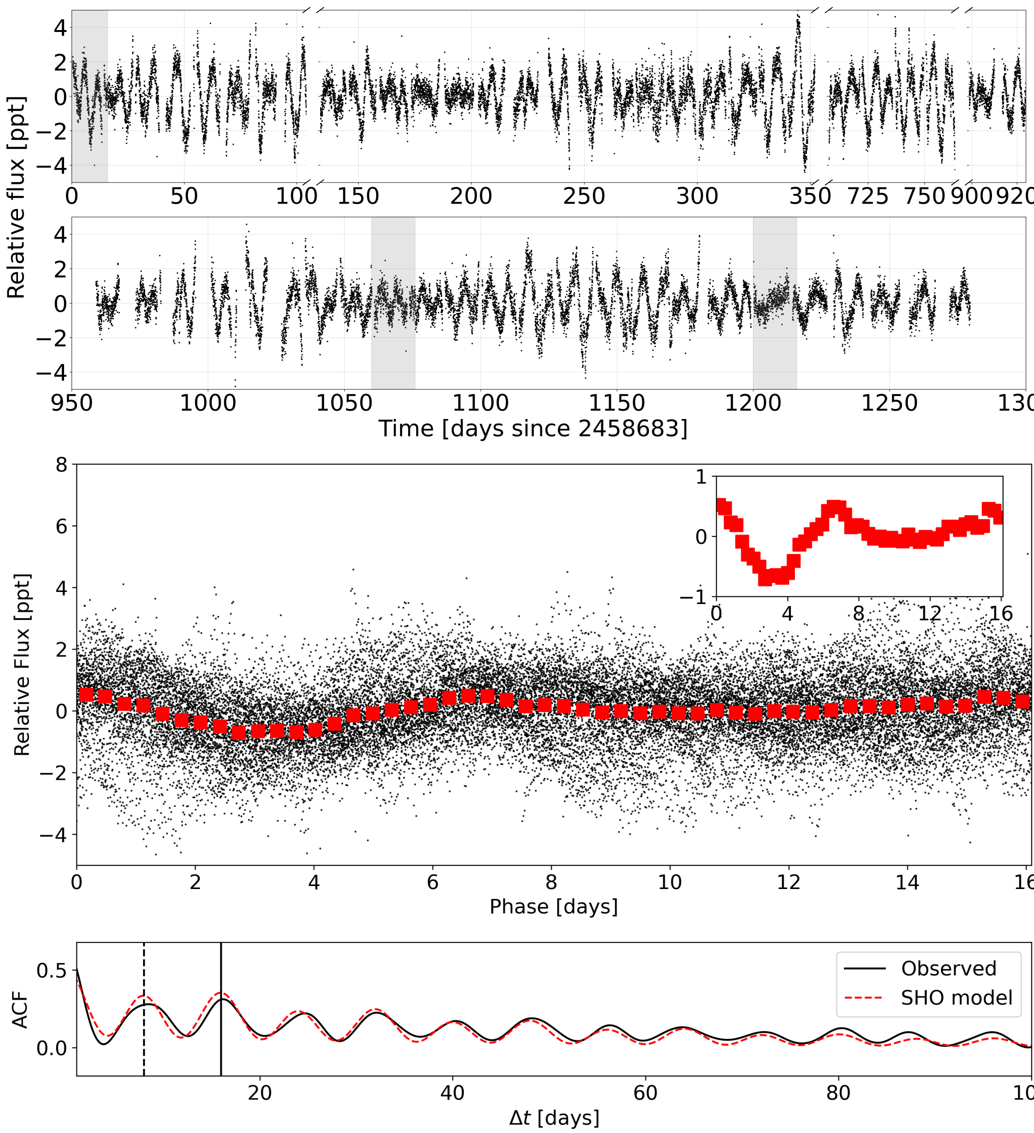

Figure 2.3: **Top:** The full 120 s cadence SPOC *TESS* light curve, binned to 30 min. Rotationally modulated variability is strong and evolves over time; the three shaded regions highlight example 16 day windows in which different numbers of maxima/minima are observed. **Middle:** The 30-min light curve phased to the 16.1 day rotation period. The red points further bin the folded data to ~ 8 hour bins. The inset zooms in on these binned phased data and highlights the tendency for every other set of maximum/minimum to repeat in amplitude. **Bottom:** The ACF of the photometry, showing regular peaks at all multiples of 8 days (dashed line) with the highest peak at 16 days (dark line). The red dashed line shows the best-fit SHO model described in Section 2.4.

Table 2.1: Stellar Parameters of TOI-1347

Parameter	Value	Unit	Source
TIC ID	TIC 229747848		[a]
Right Ascension	18:41:18.4	hh:mm:ss	[a]
Declination	+70:17:24.19	dd:mm:ss	[a]
V magnitude	11.168 ± 0.013		[a]
TESS magnitude	10.7157 ± 0.0066		[a]
J magnitude	10.011 ± 0.02		[a]
K magnitude	9.616 ± 0.015		[a]
Gaia magnitude	11.2076 ± 0.0005		[b]
Parallax	6.7803 ± 0.0112	mas	[b]
RA proper motion	-6.0883 ± 0.0150	mas yr^{-1}	[b]
Dec proper motion	26.1020 ± 0.0150	mas yr^{-1}	[b]
Galactic U	-5.31 ± 0.09	km s^{-1}	[c]
Galactic V	-7.72 ± 0.46	km s^{-1}	[c]
Galactic W	4.91 ± 0.23	km s^{-1}	[c]
Luminosity	0.55 ± 0.02	$L_\odot$	[d]
Radius	0.83 ± 0.03	$R_\odot$	[d]
Mass	0.913 ± 0.033	$M_\odot$	[e]
$T_{\rm eff}$	5464 ± 100	K	[e]
$\log g$	4.64 ± 0.10		[e]
[Fe/H]	0.04 ± 0.06	dex	[e]
[α/Fe]	-0.03 ± 0.06	dex	[f]
$v \sin i_\star$	< 3	km s^{-1}	[e]
$v \sin i_\star$	2.9 ± 0.1	km s^{-1}	[g]
v_{eq}	2.61 ± 0.11	km s^{-1}	This work
$\log R'_{\rm HK}$	-4.66 ± 0.05		This work
$P_{\rm rot}$	16.1 ± 0.3	days	This work[h]
$P_{\rm rot}$	16.3 ± 0.6	days	This work[i]
$P_{\rm rot}$	16.2 ± 0.3	days	This work[j]
Age	1.7 ± 0.1	Gyr	This work[k]
Age	1.33 ± 0.06	Gyr	This work[l]
Age	1.6 ± 0.4	Gyr	This work[m]
Age	$0.8^{+1.1}_{-0.6}$	Gyr	[n]
Age	> 650	Myr	This work[o]
Age	1.4 ± 0.4	Gyr	Adopted value

[a]TIC v8.2 (Paegert et al., 2021). [b]*Gaia* DR3 (Gaia Collaboration et al., 2023). [c]Derived from *Gaia* DR3 astrometry, using the local standard of rest from Coşkunoğlu et al. 2011 as implemented in `PyAstronomy.pyasl.gal_uvw` (Czesla et al., 2019). [d]Isoclassify (Huber et al., 2017a), using the SpecMatch-Synthetic results from a HIRES spectrum. Uncertainties are random errors for the adopted model grid. To account for systematic errors, see Tayar et al. (2022). [e]SpecMatch-Synthetic (Petigura, 2015), using a HIRES spectrum taken at $R \sim 67000$ with no iodine. [f]KeckSpec (Polanski in prep), using a HIRES spectrum taken at $R \sim 67000$ with no iodine. [g]FASMA (Tsantaki et al., 2018; Tsantaki, Andreasen, and Teixeira, 2020), using the co-added HARPS-N spectra. [h]From ACF of TESS photometry (Section 2.4). [i]From `TESS-SIP` with TESS photometry (Section 2.4). [j]From GP fit to RVs (Section 2.5). [k]From $P_{\rm rot}$ using empirical relations of Bouma, Palumbo, and Hillenbrand (2023a). [l]From $P_{\rm rot}$ using empirical relations of Mamajek and Hillenbrand (2008). [m]From $\log R'_{\rm HK}$ using empirical relations of Mamajek and Hillenbrand (2008). [n]From isochronal fitting by MacDougall et al. (2023). [o]From Li and comparison to Hyades (Berger, Howard, and Boesgaard, 2018).

systematic issues. We then stitched and normalized the multi-sector data using `lightkurve` and applied a 5-σ sigma-clipping. `lightkurve` also provides the correction for scattered light (2% contamination reported by ExoFOP). The resulting light curve, shown in Figure 2.3, exhibits significant but coherent periodic variability corresponding to rotationally modulated surface inhomogeneities on the stellar disk.

Stellar Rotation Period

The effect of a starspot on photometry is to reduce the observed (integrated) intensity when on the visible hemisphere. The net effect of many spots is quasiperiodic variability that can be treated as time-correlated noise (Haywood et al., 2014; Rajpaul et al., 2015; Aigrain and Foreman-Mackey, 2023). The *TESS* photometry of TOI-1347 shows strong rotational variability with maxima/minima occurring roughly every ~ 8 days (see the top panel in Figure 2.3). A Lomb-Scargle periodogram of the photometry shows a strong peak at 8 days (Fig 2.4). However, a closer examination of the light curve reveals that the depths of adjacent maxima/minima are dissimilar. In fact, the depths of alternating maxima/minima tend to have similar amplitudes. This can be explained if the star has a 16 day rotation period and multiple spot groups concentrated on opposite hemispheres of the star, an effect noted for a number of other stars (Holcomb et al., 2022). In fact, a periodogram analysis of the RV dataset shows a strong peak at 16 days (Fig 2.4). Spots affect RVs in much the same way as photometry by breaking the flux balance across star's rotational velocity profile (Saar and Donahue, 1997), in addition to suppressing the convective blueshift (Haywood et al., 2016).

While the periodogram is essentially a Fourier decomposition showing the amplitude of the best-fitting sine wave at all possible periods, the autocorrelation function (ACF) measures the self-similarity of a time series as a function of time delay. Thus, if the variability in a time series is not sinusoidal (asymmetric, more complex shape), then the ACF will give a better estimate of the periodicity than the periodogram. The ACF of the *TESS* photometry has its highest peak at $\sim$16 days (Fig 2.3) with adjacent ACF peaks alternating between high and low amplitude. An analysis of the ACF using `spinspotter` (Holcomb et al., 2022) successfully identified the half-period effect by checking that the odd peaks are less than 10% the height of the even peaks. `spinspotter` returns a rotation period of $P_{\rm rot} = 16.1 \pm 0.3$ days by averaging the locations of the even-numbered peaks only. We also measured the stellar rotation period using the TESS Systematics Insensitive Periodogram algorithm (TESS-SIP Hedges et al., 2020). `TESS-SIP` simultaneously corrects for instrument systematics while performing the periodogram search on the TESS Simple Aperture Photometry. Using `TESS-SIP` for sectors 14-26 for TOI-1347, we measured a stellar rotation period of 16.34 ± 0.57 days.

With all of this considered, we adopt the ∼16 day solution as the rotation period of TOI-1347 and explain the Lomb-Scargle periodogram peak at $P_{\rm rot}/2$ as arising from antipodal spot groups. The persistence of repeated peaks every 8 days in the ACF, even out to beyond 100 days, can be explained if the starspots on TOI-1347 live for many rotation periods. Following the prescription of Giles, Collier Cameron, and Haywood (2017), we fit the observed ACF with an underdamped simple harmonic oscillator (uSHO), including a second component with power at $P/2$:

$$y = e^{-\Delta t/\tau}\left[A\cos\left(\frac{2\pi\Delta t}{P}\right) + B\cos\left(\frac{2\pi\Delta t}{P/2}\right) + y_0,\right]. \tag{2.1}$$

In Eq. 2.1, y is the ACF strength and the coefficients A and B give the relative strengths of the antipodal spot groups. We used `scipy.optimize` (Virtanen et al., 2020) to find the maximum a-posteriori (MAP) solution, then used that as a seed for a Markov-chain Monte Carlo (MCMC) analysis using `emcee` (Foreman-Mackey et al., 2013). The fit recovered $P = 16.0$ d, and the best-fit exponential decay timescale was $\tau = 45$ days, roughly three times the rotation period. Both coefficients $A = 0.05$ and $B = 0.18$ were constrained to nonzero values, again supporting the multiple spot group hypothesis.

Lastly, our `SpecMatch-Synthetic` analysis of the HIRES spectrum in Section 2.2 yielded only an upper limit corresponding to the line spread function of HIRES (roughly 2.2 km s^{-1}). Masuda, Petigura, and Hall (2022) recently showed that on the population level, such nondetections of $v \sin i_\star$ are most consistent with a $<$ 3 km s^{-1} upper-limit. Combining $P_{\rm rot} = 16.1$ d with the stellar radius from Section 2.2, we get an equatorial rotational velocity of $v_{eq} = 2.6 \pm 0.1$ km s^{-1}. This is consistent with a $<$ 3 km s^{-1} upper-bound for HIRES, though it is slightly smaller than the measured HARPS-N value. Were the rotation period 8 d, we would instead have $v_{eq} \sim 5$ km s^{-1}, which (barring a misaligned stellar inclination of $\lesssim 30°$) would be detectable in the HIRES spectrum and inconsistent with the HARPS-N measurement. If astro-

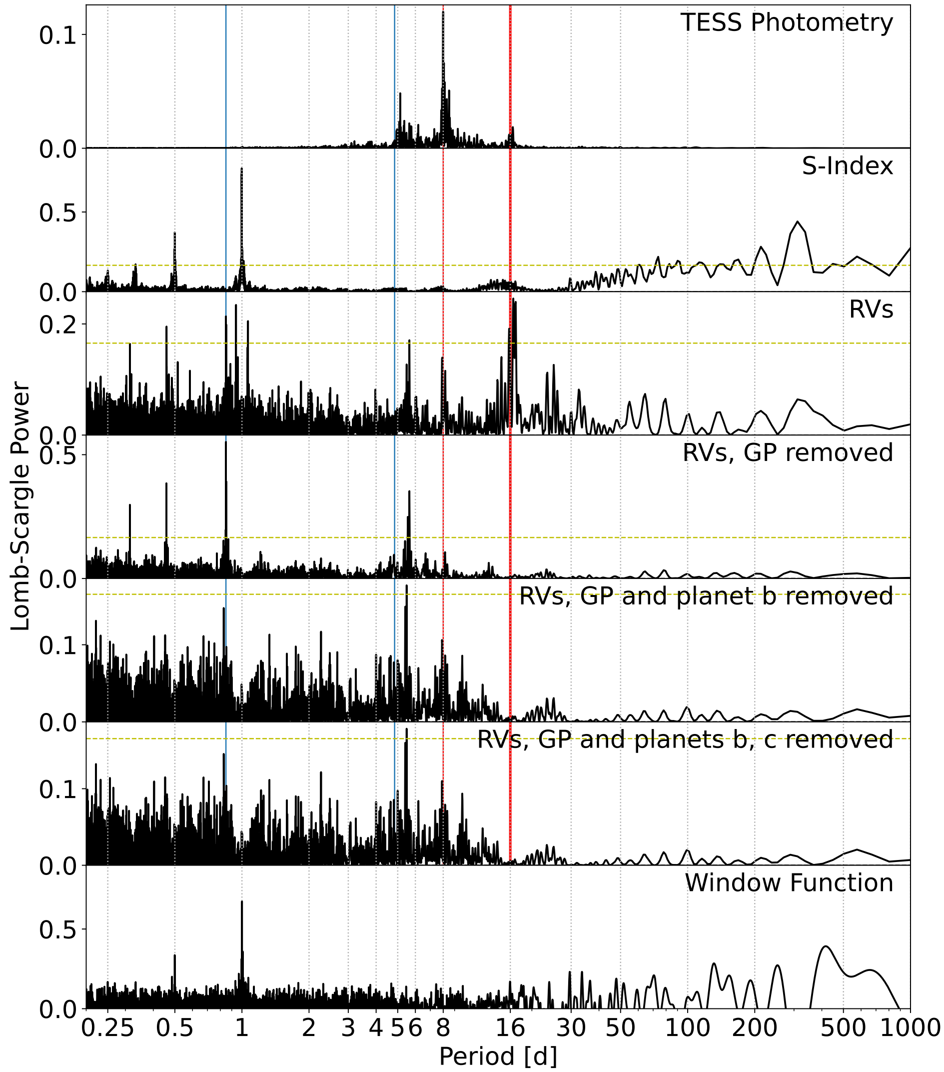

Figure 2.4: Lomb-Scargle periodograms of, from top to bottom, the *TESS* photometry, S-Indices, RVs, RVs with the GP model (Section 2.5) removed, the GP-corrected RVs with the Keplerian model for the USP subtracted, the GP-corrected RVs with both planets subtracted, and the window function (Dawson and Fabrycky, 2010) of the RV time series. The periodograms are computed using `astropy.timeseries.LombScargle` (Astropy Collaboration et al., 2022). The blue dashed lines correspond to the orbital periods of TOI-1347 b and c, and the two dark red lines are drawn at 8 days (thin) and 16 days (thick). The horizontal yellow line is the 1% false alarm probability.

physical, the slightly larger $v \sin i_\star$ could be explained by differential rotation and long-lived starspots at higher latitudes.

Additional Transiting Planets?

We searched the *TESS* light curve for planetary transits with a Box-Least-Squares algorithm (BLS, Kovács, Zucker, and Mazeh, 2002) as described in Dai et al. (2021). We recovered the two planet candidates reported by ExoFOP at 0.84 and 4.84 days. We did not find any other transit signals with SNR > 6.5.

Transit Modeling

Our transit analysis closely follows that described in (Dai et al., 2021). Briefly, we generated transit signals using the `Python` package `Batman` (Kreidberg, 2015), parameterized with the stellar density (ρ_*) to break the degeneracy between the scaled semimajor axes (a/R_*) and impact parameters (b) of the transiting planets (Seager and Mallén-Ornelas, 2003). We imposed a prior using the best-fit stellar density from our adopted M_* and R_* of $\rho_* = 2.25 \pm 0.26$ g cm^{-3}. For the limb darkening coefficients, we used the prior and parameterization scheme of Kipping (2013) for a quadratic limb darkening law (q_1 and q_2). The other transit parameters included the orbital period ($P_{\rm orb}$), time of conjunction ($T_{\rm c}$), planet-to-star radius ratios ($R_{\rm p}/R_\star$), scaled orbital distances ($a/R_\star$, computed from stellar density and orbital period), orbital inclinations ($\cos i$), orbital eccentricities (e), and the arguments of pericenter (ω). We initially allowed non-zero eccentricities for both TOI-1347 b and c; however, the posterior distributions are fully consistent with circular orbits. Neither the existing transit nor RV data (Section 2.5) support the detection of nonzero eccentricities. In our final fits, we chose to restrict both planets to circular orbits to reduce model complexity.

Our transit fitting pipeline takes the following steps:

1. Fit a global model of all transit epochs, assuming no transit timing variations (TTVs). This model is found by maximizing the likelihood with the `Levenberg-Marquardt` method implemented in `Python` package `lmfit` (Newville et al., 2014).

2. Search for TTVs: We held the transit shape parameters fixed and fit for the mid-transit times of each transit epoch. We removed out-of-transit variations with a quadratic model. We did not detect significant TTVs for either planet, so we continued with fixed orbital periods.

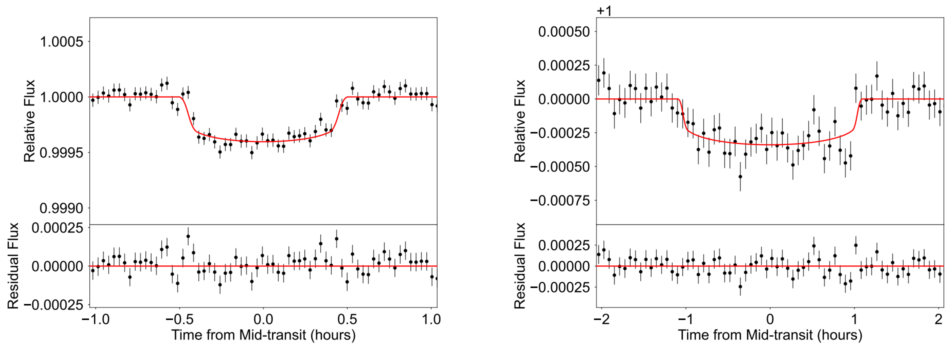

Figure 2.5: The 2 min *TESS* light curves phase-folded and binned using the orbital periods of TOI-1347 b (top) and c (bottom). The best-fit transit models are shown with red solid lines.

3. Full model. We sampled the posterior distributions of both planets jointly using the MCMC framework implemented in *emcee* (Foreman-Mackey et al., 2013) with 128 walkers initialized near the MAP solution. We ran `emcee` for 50000 steps, ensuring that this was many times longer than the autocorrelation of various parameters (typically 100s of steps).

Fig. 2.5 shows the phase-folded and binned transits of TOI-1347 b and c with the MAP model. Using the stellar radius derived in Section 2.2, we derived $R_{p,b} = 1.8 \pm 0.1$ $R_\oplus$ and $R_{p,c} = 1.6 \pm 0.1$ $R_\oplus$, in agreement with the radii measured by MacDougall et al. (2023) ($R_{p,b} = 1.81^{+0.09}_{-0.06}$ $R_\oplus$ and $R_{p,c} = 1.68^{+0.09}_{-0.07}$).

Phase Curve

We searched the *TESS* light curve for phase curve variations and secondary eclipses of TOI-1347 b. First, we masked the in-transit data and removed long-term variability (stellar and/or instrumental) using the method of Sanchis-Ojeda et al. (2013b). This involves fitting a linear function of time to the out-of-transit data points within a window of 2× the orbital period, then dividing the best-fit function within that window, repeating for every data point in the light curve. This detrended light curve is then phase-folded to the orbital period of TOI-1347 b.

The resultant phase curve is shown in Figure 2.6. We were able to detect a tentative phase curve variation (3σ) and a secondary eclipse (2σ) using a joint model. To model the secondary eclipse, we simply modified the best-fit

Table 2.2: Transit and RV Parameters of the TOI-1347 System

Parameter	Symbol	Posterior Distribution	Unit
TOI-1347 b			
Planet/Star Radius Ratio	$R_p/R_\star$	0.02039 ± 0.00072	
Time of Conjunction	T_c	1682.71214 ± 0.00060	(BJD-2457000)
Orbital Period	$P_{\rm orb}$	$0.84742346 \pm 0.00000061$	days
Orbital Inclination	$i_{\rm orb}$	deg	
Orbital Eccentricity	e	0 (fixed)	
Impact Parameter	b	0.82 ± 0.03	
Scaled Semi-major Axis	$a/R_\star$	4.43 ± 0.21	
RV Semi-amplitude	K	$7.74^{+0.80}_{-0.79}$	m s^{-1}
Planetary Radius	R_p	1.8 ± 0.1	$R_\oplus$
Planetary Mass	M_p	11.1 ± 1.2	$M_\oplus$
Bulk Density	ρ	$9.9^{+2.1}_{-1.7}$	g cm^{-3}
Equilibrium Temperature	T_{eq}	1400 ± 40	K
TOI-1347 c			
Planet/Star Radius Ratio	$R_p/R_\star$	0.0179 ± 0.0010	
Time of Conjunction	T_c	1678.5059 ± 0.0021	(BJD-2457000)
Orbital Period	$P_{\rm orb}$	4.841962 ± 0.000012	days
Orbital Inclination	i	87.5 ± 0.4	deg
Orbital Eccentricity	e	0 (fixed)	
Impact Parameter	b	0.73 ± 0.08	
Scaled Semi-major Axis	$a/R_\star$	14.18 ± 0.49	
RV Semi-amplitude	K	$1.08^{+0.91}_{-0.92}$ (< 2.59 at 95%)	m s^{-1}
Planetary Radius	R_p	1.6 ± 0.1	$R_\oplus$
Planetary Mass	M_p	2.8 ± 2.3 (< 6.4 at 95%)	$M_\oplus$
Bulk Density	ρ	$3.6^{+3.3}_{-3.0}$ (< 4.1 at 95%)	g cm^{-3}
Equilibrium Temperature	T_{eq}	1000 ± 25	K
Stellar Parameters			
Stellar Density	$\rho_\star$	2.30 ± 0.24	g cm^{-3}
Limb Darkening	q_1	0.28 ± 0.20	
Limb Darkening	q_2	0.35 ± 0.28	
HIRES RV Jitter	$\sigma_{\rm HIRES}$	$4.05^{+0.73}_{-0.67}$	m s^{-1}
HARPS-N RV Jitter	$\sigma_{\rm HARPS}$	$8.20^{+2.67}_{-1.98}$	m s^{-1}
GP Amplitude	$A_{\rm GP}$	$9.70^{+1.16}_{-1.06}$	m s^{-1}
Rotation Period	$P_{\rm GP}$	$16.16^{+0.35}_{-0.35}$	days
Oscillator Quality Factor	Q_0	$1.49^{+0.74}_{-0.91}$	
Quality Factor Difference	ΔQ	$1.71^{+1.32}_{-2.33}$	
Fractional Amplitude	f	$0.73^{+0.19}_{-0.24}$	
Instrumental RV Parameters			
RV Offset (HIRES)	$\gamma_{\rm HIRES}$	$-2.12^{+0.90}_{-0.87}$	m s^{-1}
RV Offset (HARPS-N)	$\gamma_{\rm HARPS}$	$6.29^{+3.35}_{-3.41}$	m s^{-1}

transit model by shifting the mid-transit times by half the orbital period (i.e., assuming $e = 0$) and turning off limb darkening ($q_1 = q_2 = 0$). The secondary eclipse depth ($\delta_{\rm sec}$) is allowed to vary freely to account for a combined effect of reflected stellar light and thermal emission from the planet's night side. For the phase curve, we used a Lambertian disk model (see e.g. Demory et al., 2016) parameterized by an amplitude A and phase offset of the peak θ. We sampled the posterior distribution with a MCMC analysis similar to that described in Section 2.4. We found a secondary eclipse depth of $\delta_{\rm sec} = 26 \pm 12$ ppm and a phase curve amplitude of $A = 28 \pm 9$ ppm. The peak of the phase curve variation is shifted by $33 \pm 14°$ to the west of the planet.

The lower panel of Figure 2.6 compares the amount of thermal emission vs. reflected light as a function of the planet's Bond albedo (A_B). At high albedo, the planet is more reflective and the equilibrium temperature will be lower. In this case, the phase curve will be dominated by reflected stellar light rather than thermal emission. This is necessary to explain the large secondary eclipse depth measured in the *TESS* band. Moreover, we marginally detected a phase offset of 33$\pm$14° to the west of the planet. Both of these effects can be explained if TOI-1347 b is retaining a high-mean-molecular-weight atmosphere. Silicate clouds in this atmosphere could produce a high albedo, while partial cloud coverage may produce the observed phase offset to the West (see e.g. Kepler-7 b, Demory et al., 2013). However, the data in hand are insufficient to definitively confirm the presence of an atmosphere on TOI-1347 b. Higher SNR follow-up observations with JWST are required.

2.5 Radial Velocities

We collected 120 high-resolution optical spectra of TOI-1347 between UT November 28, 2019 and UT July 26, 2022 with HIRES on the Keck-I telescope as part of TKS (Chontos et al., 2022). We took exposures using the "C2" decker ($R = 45,000$) and integrated until the exposure meter reached 60,000 counts (signal-to-noise ratio (S/N) $\sim$ 100 per reduced pixel) which resulted in a typical exposure time of 648 sec. We used the standard procedures of the California Planet Search (CPS; Howard et al., 2010a) to reduce the HIRES spectra and extract precise RVs using the iodine cell for wavelength calibration (Butler et al., 1996). The average Doppler precision per measurement was 1.83 m s^{-1}.

We also obtained 14 spectra with the High-Accuracy Radial-velocity Planet Searcher in the North, installed at the Telescopio Nazionale Galileo (HARPS-N; Cosentino et al., 2012). Observations were taken with 1800 s exposure times (average S/N is 42.3 in order 50) with simultaneous wavelength calibration provided by the Fabry-Perot etalon. Cross-correlation functions (CCFs) were created using the ESPRESSO G2 mask, and RVs were extracted by fitting for the CCF centroid (Dumusque et al., 2021). Before jointly fitting with the HIRES RVs, we subtracted the median RV from the HARPS-N dataset.

See Table 2.3 for the full RV dataset, which includes Mount Wilson S-Index values derived from the Ca II H& K lines (Duncan et al., 1991) for the HIRES

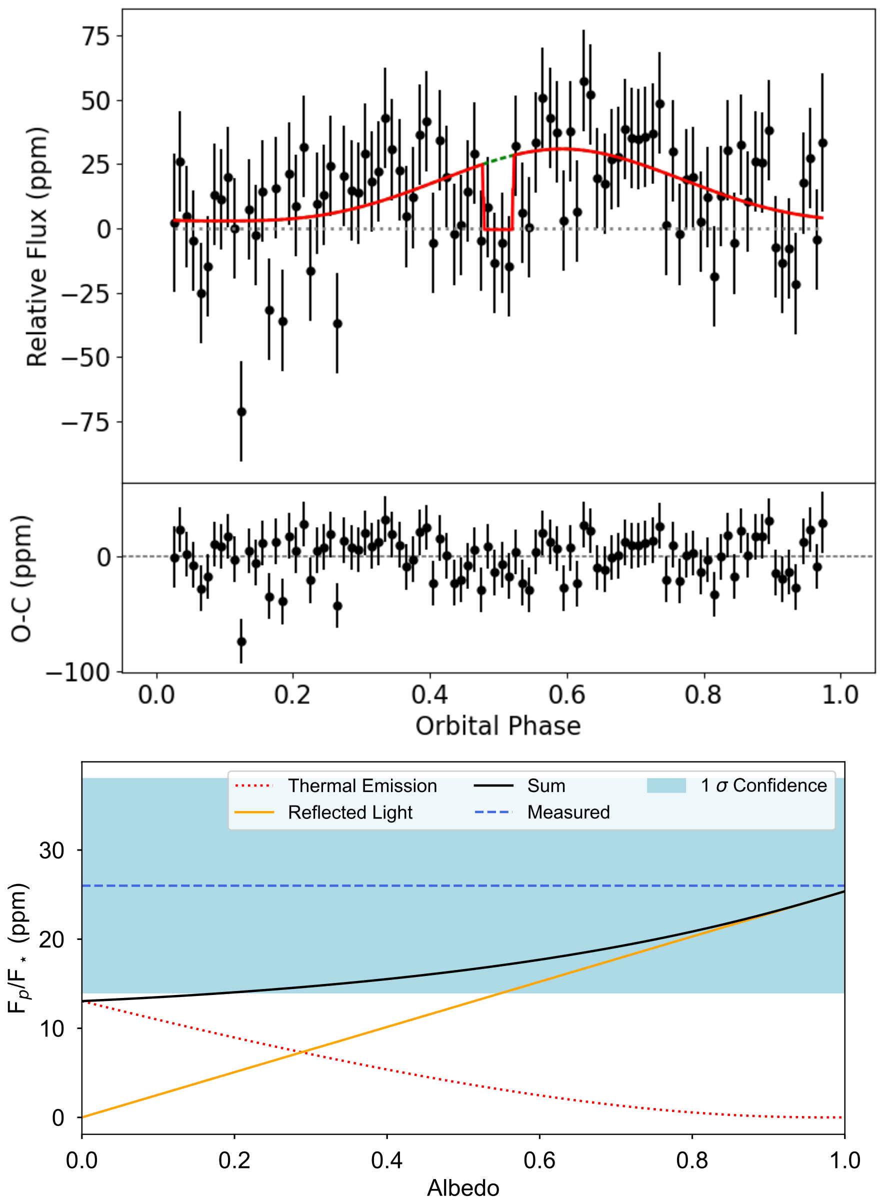

Figure 2.6: **Upper**: The phase curve and secondary eclipse of TOI-1347 b as observed by *TESS*. The best-fit model is shown by the red curve. The green dotted line gives the model with no eclipse. The phase curve is detected at the 2σ level. It is likely a combination of thermal emission and reflected light in the *TESS* band (600–1000 nm). **Lower**: The thermal emission (red dotted line) and reflected light (orange solid line) from TOI-1347 b as a function of the Bond albedo. The blue dashed line and shaded area are the measured secondary eclipse depth ($F_p/F_\star$) and its 1σ central interval.

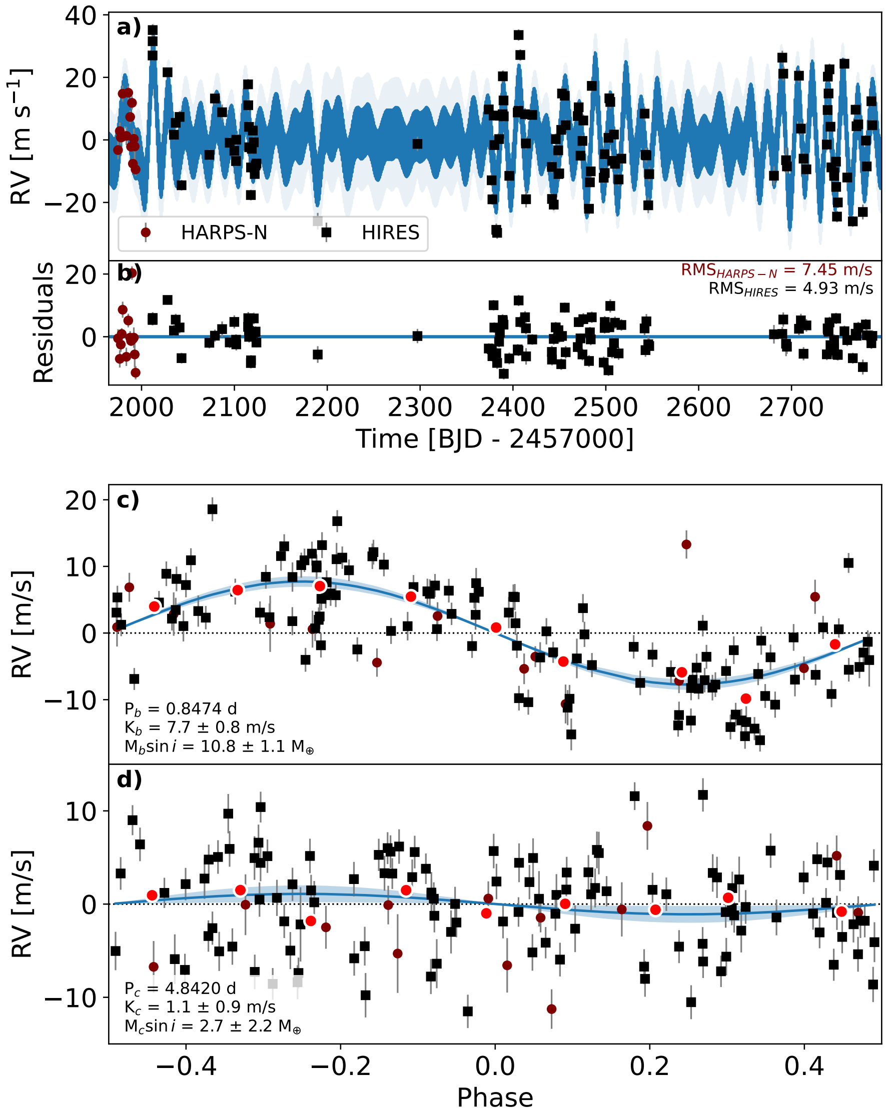

Figure 2.7: The adopted radial velocity model. Panel **a)** shows the HARPS-N and HIRES RV datasets, with the MAP RV model (Keplerian + GP and 1σ uncertainty) overplotted in blue. Panel **b)** shows the residuals between the data and the MAP RV model. Panels **c)** and **d)** show the data phase-folded to the orbital period of planets b and c, respectively, with contributions from the other planet and the GP removed. The red points are equal RV bins spanning 0.1 in phase. The median and central 68% CI of each Keplerian model is plotted in blue. The MCMC posteriors for the recovered semiamplitude and derived $M \sin i$ are also summarized in the lower-left annotations. Note that we do not include the MAP stellar jitter in the plotted errorbars; errorbars are drawn only as the measurement uncertainties to highlight the degree of unexplained scatter (i.e., jitter), given by the annotated residual RMS, to which the stellar jitter fits.

Table 2.3: TOI-1347 RVs and S-Indices

Time BJD-2457000	RV[a] m s^{-1}	RV Error m s^{-1}	S_{HK}	S_{HK} Error	Instrument
2458974.658616	-2.385	2.91	–	–	HARPS-N
2458976.56778	3.675	2.77	–	–	HARPS-N
2458977.647243	1.645	2.3	–	–	HARPS-N
2459011.871925	27.023	1.73	0.291	0.001	HIRES
2459011.945652	31.576	1.75	0.285	0.001	HIRES
2459011.999298	35.149	1.85	0.287	0.001	HIRES
2459028.000963	21.648	1.49	0.285	0.001	HIRES
2459034.871693	1.685	1.74	0.284	0.001	HIRES
⋮	⋮	⋮	⋮	⋮	⋮

[a]A median value of -13965.395 km s^{-1} has been subtracted from the HARPS-N RVs. Full table of RVs can be found in the published article (Rubenzahl et al., 2024b).

data. The S_{HK} index shows a weaker power excess around P_{rot} in a Lomb-Scargle periodogram than the RVs (Fig. 2.4) but are primarily dominated by a 1 day sampling alias. The S_{HK} indices are correlated with the RVs at the 3.5σ level with a Pearson correlation coefficient of 0.31 (p-value of 0.0005). This weak correlation is likely why our models in Section 2.5 that were trained on the S-Index time series did not improve the overall fit.

RV Model

We chose to adopt the same two-component SHO model for our RV model that we used to model stellar variability in photometry. We used the `exoplanet` (Foreman-Mackey et al., 2021) package to construct a Gaussian Process (GP) stellar activity model with a kernel defined by the built-in `RotationTerm` parameterization. This kernel is a mixture of two SHOs analogous to the first and second cosine terms in Eq. 2.1. We also tried a GP with the quasiperiodic kernel implemented in `radvel` (Fulton et al., 2018), both untrained and trained on the S-Indices. We found that the quasiperiodic kernel struggled to identify a single primary period, often jumping between 8 days and 16 days. In order for the MCMC to converge, a reasonably strong prior (± 0.5 d or less) had to be placed on one of these period solutions. We found this undesirable compared to the SHO kernel in `exoplanet`, which was able to lock onto the 16 day period even with wide priors of > 10 d. We also found the final fit to be statistically indistinguishable whether the GP was trained on the S-Indices or not, so for our final model we opted for an untrained SHO GP.

For the full mathematical definition of the SHO GP kernel, the interested reader is directed to Foreman-Mackey et al. (2017). In brief, the kernel is parameterized by the GP amplitude (A_{GP}), the primary period of variability (P_{GP}), the quality factor of the primary mode Q_0, the difference in quality factors between the period and half-period modes (ΔQ_0), and lastly the fractional amplitude between the two modes (f). We followed the guidance of the `exoplanet` tutorials to choose the appropriate priors on these parameters, which are tabulated in Table 2.2.

In practice, the Keplerian models are only parameterized by the RV semi-amplitude K, which we place a wide uninformative Gaussian prior on. We do not restrict K to positive values only, as such a prior can bias mass estimates to higher values, especially in the case of non-detections (Weiss and Marcy, 2014). We imposed Gaussian priors on the periods and times of conjunction using the best-fit mean and standard deviation derived from our transit fits (Table 2.2), effectively fixing them to the tight transit constraints. Like the transit model, we fixed the eccentricity (e) and argument of periastron (ω) to zero. We included separate jitter terms for HIRES (σ_{HIRES}) and HARPS-N (σ_{HARPS}), and likewise separate RV offsets (γ_{HIRES}) and HARPS-N (γ_{HARPS}).

We initialized our model at the best-fit values from photometry, where applicable, and determined initial guesses for the RV semiamplitudes using `exoplanet.estimate_semi_amplitude`. We then solved for the MAP solution using `scipy.optimize.minimize`. The MAP parameters were then used as a seed for a MCMC exploration of the posterior. We employed a Hamiltonian Monte Carlo HMC; Duane et al., 1987; Neal, 2012 implemented in `PyMC3` (Salvatier, Wiecki, and Fonnesbeck, 2016), specifically the No-U-Turn Sampler (NUTS; Hoffman and Gelman, 2014). HMC and NUTS are generally more efficient than the traditional Metropolis-Hatings algorithm (Metropolis et al., 1953; Hastings, 1970), resulting in well-mixed MCMC chains in far fewer samples. We sampled with NUTS in four parallel chains for 5000 "tuning" steps, which are discarded. The number of tuning steps was chosen to obtain an acceptance fraction near the target of 0.9 which balances number of retained samples and efficient exploration of the posterior space. Each chain then collects 5000 samples for a total of 20000 posterior samples. We ensured adequate statistical independence amongst these samples by requiring that the per-parameter $\hat{R}$ statistic (Vehtari et al., 2021) be < 1.001.

Our best-fitting RV model is shown in Figure 2.7. The GP robustly recovers a primary period of 16.2 ± 0.3 days, even with a wide prior, independently verifying our assessment of the stellar rotation period from photometry. The USP TOI-1347 b is also robustly detected at consistent semiamplitudes, regardless of the activity model used (trained/untrained, quasi-periodic/SHO). The resulting mass of TOI-1347 b is 11.1 ± 1.2 $M_{\oplus}$. The second planet, TOI-1347 c, is not detected in the RVs. We adopt an upper limit of < 6.4 $M_{\oplus}$ at 95% confidence. The residual RMS to the combined Keplerian + GP model is 4.9 m s^{-1} for HIRES and 7.5 m s^{-1} for HARPS-N, which is (expectedly) similar to the fitted stellar jitter values (4.0 ± 0.7 m s^{-1} and $8.2^{+2.7}_{-2.0}$ m s^{-1} respectively), but larger than the per-measurement uncertainty of each instrument (2.5 and 1.9 m s^{-1}).

Of note is the large jitter for the HARPS-N RVs. We suspect this is due to the GP being primarily conditioned on the HIRES RVs, resulting in poor predictive accuracy for activity during the timespan of the HARPS-N data, which occur about 1–2 rotation cycles before the HIRES data. As a result, the jitter term for HARPS-N is inflated to compensate. We tried separate GPs for both datasets, sharing all hyperparameters except for the GP amplitude (A_{GP}). We found a nearly identical result (in fact, the best-fit HARPS-N jitter was higher) with statistically indistinguishable planet parameters, likely due to the relatively few HARPS-N data points. As a result, we adopt the single GP model, but encourage further investigation into the nature of stellar activity on TOI-1347. As it stands, there are too few HARPS-N data points to condition independent GPs, but the single GP model is potentially overfitted to the HIRES points, reducing its out-of-sample predictive accuracy (Blunt et al., 2023).

2.6 Discussion

A Heavy Core Pushing the Limit of Photoevaporation

TOI-1347 b is the largest (in both mass and radius) of the super-Earth USPs to date. It seems to be rocky in composition and similar in iron core mass fraction to the Earth. Figure 2.8 shows the two planets in the context of known exoplanets on the mass-radius diagram[2]. We modeled the core composition of TOI-1347 b assuming a simple two-layer model with an iron core

[2] Data from the NASA Exoplanet Archive, accessed on 2023-10-04 at 11:55, returning 35086 rows.

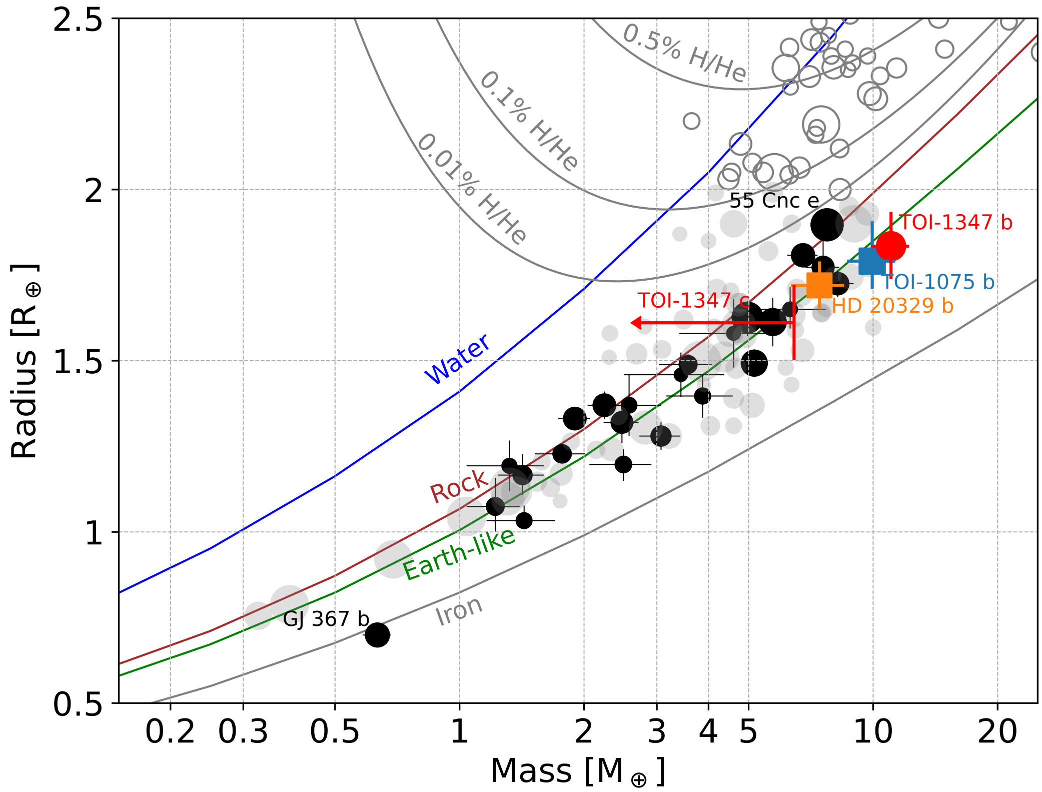

Figure 2.8: Mass-radius diagram of known super-Earths ($R_p < 2$ R$_\oplus$, filled circles) and sub-Neptunes (4 R$_\oplus > R_p \geq 2$ R$_\oplus$, empty circles) with 5σ or better mass measurements, obtained from the NASA Exoplanet Archive (NASA Exoplanet Archive, 2019). Bold fill denotes USPs. Contours from Zeng, Sasselov, and Jacobsen (2016) are drawn for pure-iron, Earth-like (30% iron, 70% rock), pure-rock, and pure-water compositions. Contours from Chen and Rogers (2016) are also drawn for 0.5%, 0.1%, and 0.01% H/He envelopes surrounding rocky-composition cores, at an age of 1.4-Gyr-old and at the maximum insolation flux of 400 S$_\oplus$ for their model grids; it is worth noting that TOI 1347 b (1400 K, $A = 0.7$) receives an insolation flux of around 3000 S$_\oplus$. Our mass-radius constraints for TOI-1347 b and c (95% upper limit in mass) are plotted and labelled in red. The size of each point is proportional to M/σ_M. TOI-1347 b is the most massive super-Earth USP to date, while TOI-1347 c is smaller but likely also rocky.

and a silicate ("rock") mantle (Zeng, Sasselov, and Jacobsen, 2016). Our mass and radius measurements suggest an iron core mass fraction of 41± 27%, not far from Earth's 33% core mass fraction. TOI-1347 b joins a group of well-characterized USP planets (Dai et al., 2019) that are consistent with an Earth-like composition.

With a core mass larger than 10 $M_\oplus$, TOI-1347 b, along with the USPs TOI-1075 b (Essack et al., 2023), and HD 20329 b (Murgas et al., 2022), are close to the theoretical limit for runaway accretion (see, e.g., Rafikov, 2006). How did these planets evade runaway accretion and not become gas giants? Lee (2019) and Chachan, Lee, and Knutson (2021) both noted that the local hydrodynamic conditions, the envelope opacity, and the timescale of core assembly relative to disk dissipation could all contribute to quenching runaway accretion. As more of these systems are discovered, population-level analyses may shed light on which planets are able to evade runaway and which grow into gas giants.

TOI-1347 b also pushes the efficacy of photoevaporation to its limit. At > 10 $M_\oplus$, the outflowing atmosphere has to overcome a deep gravitational potential well. On the other hand, the temperature of atmospheric outflows is likely capped below 10^4 K due to strong radiative cooling at higher temperatures (see, e.g., Murray-Clay, Chiang, and Murray, 2009). An order of magnitude comparison reveals that the thermal sound speed ($\sim$10 km s^{-1} at 10^4 K) may not overcome the escape velocity of the planet ($\sim$25 km s^{-1} at 10 $M_\oplus$ and 1.9 $R_\oplus$), preventing bulk hydrodynamic outflow (i.e. photoevaporation). Previous models showed that photoevaporation is significantly quenched on planets with heavier cores ($\gtrsim 6$ $M_\oplus$, see e.g. Owen and Wu, 2017; Wang and Dai, 2018). Planets like TOI-1347 b are therefore important test cases to understand the limit of both photoevaporation and core-powered mass loss (Ginzburg, Schlichting, and Sari, 2018; Gupta and Schlichting, 2019). Our mass and radius measurements disfavor the presence of a thick H/He envelope (Fig. 2.8). Did TOI-1347 b have, and then lose, a primordial H/He envelope? Or, could TOI-1347 b have formed near to its present-day scorching orbit without ever acquiring a substantial atmosphere? We encourage further investigation on this question.

A Heavy-Mean-Molecular-Weight Atmosphere?

Even though TOI-1347 b has a mass and radius that suggest an Earth-like bulk composition, we cannot rule out the presence of a heavy-mean-molecular-weight atmosphere. Lopez (2017) showed that the largest of the non-giant USPs (such as 55 Cnc e) can hold onto high-metallicity atmospheres even in the presence of strong stellar radiation. Such an atmosphere would only marginally inflate the planet's radius (the scale height of a CO_2 based atmosphere is about 11 km, while planetary radii are $\sim$10,000 km).

In fact, our tentative phase curve (3σ) and secondary eclipse (2σ) detections of TOI-1347 b point to a nonzero albedo and a possible phase offset to the west. These features could indicate the presence of an atmosphere at least partially covered by reflective silicate clouds. It may be the case that the deep gravitational wells of the most massive super-Earth USPs are sufficient to cling to such an atmosphere and resist atmospheric loss mechanisms. Hu et al. (in prep.) show that their JWST NIRCam and MIRI observations of 55 Cnc e, a similar massive USP (0.73-day orbit; $9M_\oplus$), can only be explained if the planet still has a CO or CO_2 based atmosphere. Future observations with JWST might uncover a similar story for TOI-1347 b (TSM= 19, ESM= 5.6, using the equations of Kempton et al. 2018).

Alternatively, the high-amplitude *TESS* phase curve of TOI-1347 b may be a consequence of outgassed Na emission on the hot dayside of the planet. Zieba et al. (2022) showed that this emission can explain the phase curve of the lava world K2-141 b, which has been observed in both the *Kepler* passband and *Spitzer*-4.5 μm passband (Malavolta et al., 2018). In their analysis, they found that the two phase curves are inconsistent with a blackbody model, with the visible-light phase curve having a higher amplitude than expected. Similarly high visible-light phase curve amplitudes have been reported for the lava worlds 55 Cnc e (Kipping and Jansen, 2020) and Kepler-10 b (Batalha et al., 2011; Rouan et al., 2011), although the latter has not yet been observed in the infrared, which would test blackbody emission. If Na emission is responsible for the observations of TOI-1347 b reported here, it may more easily explain the tentative phase curve offset than reflective clouds, which would need to be nonuniformly distributed across the planet.

2.7 Summary

We have characterized two transiting planets in the TOI-1347 system, TOI-1347 b, a USP (0.85 d), and its outer small companion TOI-1347 c (4.84 d). Using *TESS* photometry and an independent transit fitting pipeline, we measured a radius of 1.8 ± 0.1 $R_\oplus$ for the USP, and 1.6 ± 0.1 $R_\oplus$ for its companion. We conducted a RV campaign of the TOI-1347 system with HIRES (as part of TKS) and with HARPS-N. We measured a mass of 11.1 ± 1.2 $M_\oplus$ for the

USP, consistent with a bulk Earth-like composition and inconsistent with a H/He envelope (see Fig 2.8). This composition is perhaps unsurprising given the system age of 1.4 ± 0.4 Gyr, the short timescale on which intensive photoevaporation operates (few 100 Myr), and the high insolation flux at TOI 1347 b's orbit; any primordial H/He envelope should have been destroyed by now. We were unable to detect the companion TOI-1347 c with RVs. We placed a 95% upper limit of < 6.4 $M_\oplus$. Of note is the minimum mutual inclination between planets b and c implied by our measured orbital inclinations: $\sim 7°$. This is unusually large compared to typical *Kepler* multis (Fabrycky et al., 2014), which may be another indicator of the migration dynamics that produce USPs.

TOI-1347 b is the most massive of the < 2 $R_\oplus$ (i.e., primarily solid by volume) USPs to date. Its mass sets an upper limit on runaway accretion processes and places TOI-1347 b in a region of the mass-radius diagram in which the pressures and temperatures reached inside the planet have not been well characterized either by experiments or theoretical modeling.

Intriguingly, we measured a tentative (3σ) phase-curve variability, as well as a secondary eclipse (2σ) for the USP TOI-1347 b. The phase curve asymmetry strongly suggests an optically thick atmosphere. However, our mass and radius measurements of TOI-1347 b are highly inconsistent with any significant H/He envelope. As a result, any such atmosphere must have a high mean molecular weight. It could be comprised of reflective silicate clouds, or may be the result of the outgassing of Na from the molten surface. Future observations (e.g. with JWST) would help confirm such an atmosphere and reveal its composition.

Acknowledgements

Some of the data presented herein were obtained at the W. M. Keck Observatory, which is operated as a scientific partnership among the California Institute of Technology, the University of California, and the National Aeronautics and Space Administration. The Observatory was made possible by the generous financial support of the W. M. Keck Foundation. Keck Observatory occupies the summit of Maunakea, a place of significant ecological, cultural, and spiritual importance within the indigenous Hawaiian community. We understand and embrace our accountability to Maunakea and the indigenous Hawaiian community, and commit to our role in long-term mutual stewardship. We are most fortunate to have the opportunity to conduct observations from Maunakea.

This paper made use of data collected by the *TESS* mission and are publicly available from the Mikulski Archive for Space Telescopes (MAST) operated by the Space Telescope Science Institute (STScI). All the *TIC* data used in this paper can be found in MAST (STScI, 2018). All the *TESS* data used in this paper can be found in MAST (MAST, 2021). Funding for the *TESS* mission is provided by NASA's Science Mission Directorate. We acknowledge the use of public *TESS* data from pipelines at the *TESS* Science Office and at the *TESS* Science Processing Operations Center. This work is based also on observations made with the Italian Telescopio Nazionale Galileo (TNG) operated on the island of La Palma by the Fundación Galileo Galilei of the INAF (Istituto Nazionale di Astrofisica) at the Spanish Observatorio del Roque de los Muchachos of the Instituto de Astrofisica de Canarias. Some of the observations in this paper made use of the High-Resolution Imaging instrument ʻAlopeke. ʻAlopeke was funded by the NASA Exoplanet Exploration Program and built at the NASA Ames Research Center by Steve B. Howell, Nic Scott, Elliott P. Horch, and Emmett Quigley. ʻAlopeke was mounted on the Gemini North telescope of the international Gemini Observatory, a program of NSF's NOIRLab, which is managed by the Association of Universities for Research in Astronomy (AURA) under a cooperative agreement with the National Science Foundation.

We thank the time assignment committees of the University of California, the California Institute of Technology, NASA, and the University of Hawaii for supporting the TESS-Keck Survey with observing time at Keck Observatory and on the Automated Planet Finder. We thank NASA for funding associated with our Key Strategic Mission Support project. We gratefully acknowledge the efforts and dedication of the Keck Observatory staff for support of HIRES and remote observing.

R.A.R. acknowledges support from the National Science Foundation through the Graduate Research Fellowship Program (DGE 1745301). M.R. acknowledges support from Heising-Simons grant #2023-4478. D.H. acknowledges support from the Alfred P. Sloan Foundation, the National Aeronautics and Space Administration (80NSSC21K0652) and the Australian Research Council (FT200100871).

2.8 Appendix A

Here we present the posterior distributions for the full RV model (Figure 2.9).

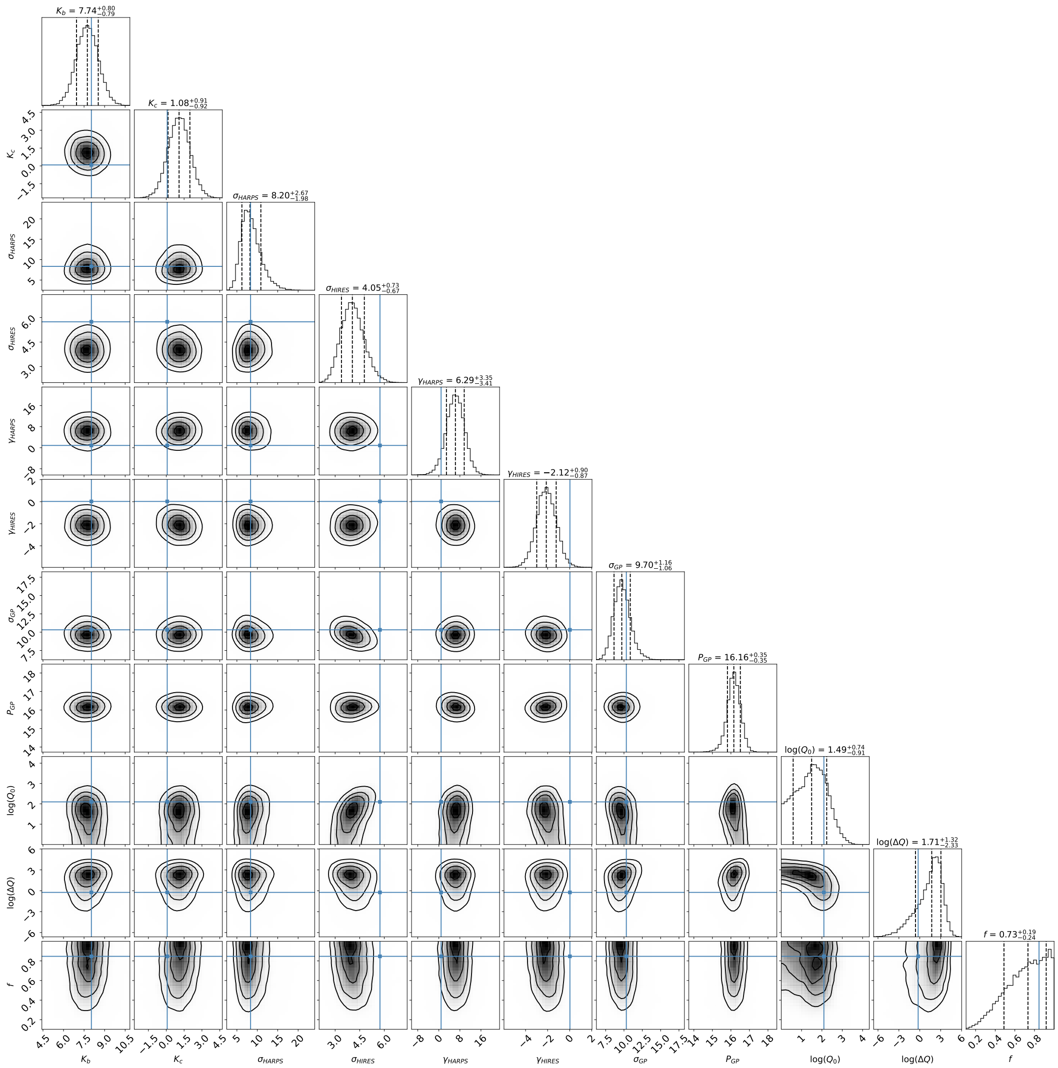

Figure 2.9: Full posterior distributions for the RV model described in Section 2.5. The blue lines denote the MAP values.

Chapter 3

THE KPF SOLAR CALIBRATOR

Rubenzahl, R. A. et al. (Dec. 2023). "Staring at the Sun with the Keck Planet Finder: An Autonomous Solar Calibrator for High Signal-to-noise Sun-as-a-star Spectra." In: *Publications of the Astronomical Society of the Pacific* 135.1054, 125002, p. 125002. DOI: `10.1088/1538-3873/ad0b30`. arXiv: `2311.05129 [astro-ph.IM]`.

3.1 Introduction

Since the first detection of an exoplanet with radial velocities (RVs), 51 Pegasi b (50 m s^{-1} semiamplitude; Mayor and Queloz, 1995), RV instruments can now detect RV signals as small as 50 cm s^{-1} (e.g. Zhao et al., 2023a). This leap of two orders of magnitude in sensitivity has been enabled by cycles of instrumentation development, rigorous testing, and a systematic understanding of the myriad instrumental systematics in modern and next-generation Extreme Precision Radial Velocity (EPRV) spectrographs (Halverson et al., 2016). There are now a number of such instruments with sub-m s^{-1} capability, including the Keck Planet Finder (KPF; Gibson et al., 2016; Gibson et al., 2018; Gibson et al., 2020), the High-Accuracy Radial-velocity Planet Searcher (HARPS; Pepe, F. et al., 2004) and its northern twin (HARPS-N; Cosentino et al., 2012), the Echelle SPectrograph for Rocky Exoplanets and Stable Spectroscopic Observations (ESPRESSO; Pepe et al., 2013; Pepe, F. et al., 2021), the EXtreme PREcision Spectrometer (EXPRES; Jurgenson et al., 2016), the NN-explore Exoplanet Investigations with Doppler spectroscopy instrument (NEID; Schwab et al., 2016), and the M dwarf Advanced Radial velocity Observer Of Neighboring eXoplanets (MAROON-X; Seifahrt et al., 2018). The task remains to reduce this *internal* noise floor to below 10 cm s^{-1}; this is the level needed to measure the masses of Earth-like planets in 1 AU orbits around Sun-like stars (9 cm s^{-1} RV semiamplitude). In fact, the EPRV measurement technique remains the only viable method to make such a measurement (Crass et al., 2021), and is perhaps the most promising method for discovering exo-Earths for follow-up characterization by the future Habitable Worlds Observatory (National Academies of Sciences, Engineering, and Medicine, 2021).

To complicate the precision goal of the EPRV community, surface phenomena on stars can induce apparent RV variability of up to many m s^{-1} (Haywood, 2016). This *external* noise is present across all timescales. Acoustic oscillations occur on timescales of minutes (Kjeldsen et al., 2005; Arentoft et al., 2008; Dumusque, X. et al., 2011a; Chaplin et al., 2019; Gupta et al., 2022), while convective granulation (Del Moro, 2004; Meunier, N. et al., 2015; Dumusque, X. et al., 2011a; Cegla et al., 2018) and supergranulation (Rincon and Rieutord, 2018; Meunier, N. and Lagrange, A.-M., 2019) occur on hours–days timescales. Surface inhomogeneities (e.g. starspots, faculae, plage) which break the symmetry of the star's rotational velocity profile (Saar and Donahue, 1997; Meunier, Desort, and Lagrange, 2010; Boisse, I. et al., 2011; Dumusque, X. et al., 2011b) as well as suppress the convective blueshift (dominant source in the Sun; Meunier, N., Lagrange, A.-M., and Desort, M., 2010b; Meunier, N. and Lagrange, A.-M., 2013; Haywood et al., 2016; Milbourne et al., 2019) are modulated by the star's rotation period on weeks–months timescales. Long-term magnetic activity cycles can produce RV variations on decades timescales (Meunier, N., Lagrange, A.-M., and Desort, M., 2010b; Lovis et al., 2011; Luhn et al., 2022). This so-called "stellar activity" can complicate the measurement of precise planetary properties (Blunt et al., 2023), mimic the signal of an exoplanet (Lubin et al., 2021), or otherwise prevent real planets from being detected, even with thousands of observations of a single star over decades (Langellier et al., 2021; Luhn et al., 2023; Gupta and Bedell, 2023). While activity-induced RVs can be partially mitigated by intentional observing strategies (Dumusque, X. et al., 2011a), algorithmic models (Haywood et al., 2014; Rajpaul et al., 2015; Aigrain and Foreman-Mackey, 2023), more robust RV extraction methods (Dumusque, X., 2018), or by detrending with "activity indicators" (Queloz, D. et al., 2009; Isaacson and Fischer, 2010a; Aigrain, Pont, and Zucker, 2012; Siegel et al., 2022), it remains an active area of research to derive activity-*invariant* RVs.

While stars as are observed as unresolved point sources, the surface of the Sun is under constant monitoring at multiple wavelengths in photometry, spectroscopy, polarimetry, and spectropolarimetry at high angular resolution from the ground (e.g. The Daniel K. Inouye Solar Telescope Rimmele et al., 2020) and space (e.g. NASA's Solar Dynamics Observatory Schou et al., 2012). There is no other star for which observed spectra and RVs can be studied in connection to directly observed active processes (e.g. Haywood et al., 2016;

Thompson et al., 2020; Milbourne et al., 2021; Ervin et al., 2022) with full confidence that the observed RV variability is due to *only* stellar and instrumental noise (i.e., all Solar System planets are known and their signals removed). This makes the Sun the ideal laboratory for studying how activity manifests in spectra, especially in solar-type stars, the primary target for discovering exo-Earths.

As such, solar feeds are becoming a crucial component of EPRV facilities. The first solar feed was the Low Cost Solar Telescope (LCST; Phillips et al., 2016) for HARPS-N at the Telescopio Nazionale Galileo (TNG), which has been observing the Sun-as-a-star since 2015. The HARPS Experiment for Light Integrated Over the Sun (HELIOS) was later added to HARPS in 2018, and the NEID Solar Feed (Lin et al., 2022) and Lowell Observatory Solar Telescope (LOST; Llama in prep) both began operations in 2020. Also at TNG, the LOw Cost NIR Extended teleScope (LOCNES; Claudi et al., 2018b) was installed to feed GIANO-B (Claudi et al., 2018a). The Potsdam Echelle Polarimetric and Spectroscopic Instrument (PEPSI; Strassmeier et al., 2015) also has a solar feed installed. Solar feeds are currently being installed for MAROON-X and Near Infra Red Planet Searcher (NIRPS; Bouchy et al., 2017). The Paranal solar Espresso Telescope (PoET; Leite et al., 2022) and A dual-Beam pOlarimetric Robotic Aperture for the Sun (ABORAS; Jentink et al., 2022) are planned for ESPRESSO and HARPS-3 respectively.

Solar feeds can also be used to independently monitor the instrumental "drift" (Lin et al., 2022), diagnose instrumental problems, and perform commissioning tests without using (precious) telescope time at night. These tests are often superior to tests with calibration sources because the stellar spectra are processed by the instrument's data reduction pipeline (DRP) in the same way as stellar spectra. Cross-comparisons between the various solar datasets are also uniquely advantageous. Zhao et al. (2023b) compared one month of solar data between HARPS, HARPS-N, EXPRES, and NEID and found an astounding agreement of 15–30 cm s^{-1} between instruments on intra-day timescales. Longer timescales showed a larger 50–60 cm s^{-1} variability, but are more affected by unshared observing conditions (e.g. different differential extinction due to different airmasses and solar disk positions at each site at a given time). Importantly, common variability in such multi-instrument contemporaneous datasets can be uniquely attributed to astrophysical processes on the Sun, while variability seen in only one instrument can be diagnosed as intrinsic systematic noise. Of course, this requires multiple instruments to be on-Sun at the same time, which is complicated by the geographic location of each facility.

For all of these reasons, we designed and built the Solar Calibrator (SoCal) to feed disk-integrated sunlight to the Keck Planet Finder, a newly commissioned EPRV spectrograph at W. M. Keck Observatory. In Section 3.2 we describe the design and hardware of SoCal. Section 3.3 details the daily operations procedure and autonomous control loop. We discuss the data reduction and quality control of the solar datastream in Section 3.4. Lastly in Section 3.5 we report on commissioning progress, present first results on the Sun, and validate KPF's performance as an EPRV facility.

3.2 Instrument Design

The Keck Planet Finder (KPF; Gibson et al., 2016; Gibson et al., 2018; Gibson et al., 2020) is a fiber-fed, ultra-stabilized EPRV system for the W. M. Keck Observatory (WMKO) that was recently commissioned in 2022. KPF is designed to achieve an instrumental measurement precision of $\sim$30 cm s^{-1} or better. The KPF main spectrometer spans 445–870 nm in two separate channels with a median resolving power of 98,000, enabled by an image slicer assembly that slices the science fiber image into three separate channels. KPF is wavelength-calibrated by several sources including a commercial laser frequency comb from Menlo Systems, a broadband Fabry-Pérot etalon, and hollow cathode lamps (ThAr and UNe). A simultaneous calibration fiber is used to track instantaneous instrumental drift, and a dedicated sky fiber is used to monitor background sky contamination. The core KPF spectrometer is designed around a novel all-Zerodur optical bench, which has a near-zero coefficient of thermal expansion to suppress instrumental systematics related to thermomechanical motions. KPF also includes a dedicated near-UV spectrometer to monitor the chromospheric Ca H&K lines for stellar activity tracking. The combination of CCD pixels with deep wells and optical slicing of the science spectrum onto three traces spread out in cross-dispersion allows KPF to achieve per-spectrum signal-to-noise ratios (SNR) more than twice that of other EPRV facilities.

SoCal utilizes the same principles as existing, proven solar feeds at other EPRV facilities. Like these instruments, SoCal focuses sunlight through a small (75 mm) lens into an integrating sphere, a hollow sphere internally coated with highly reflective material (Polytetrafluoroethylene, PTFE, aka Teflon). After $\sim$1000 reflections within the integrating sphere, a fraction of light rays will eventually land on the tip of a 200 μm optical fiber that is connected to a port on the side of the sphere. This process spatially scrambles the light from the resolved solar disk and produces a highly homogenized “point-source-like” output. The disk-integrated sunlight travels through $\sim$90 m of fiber from SoCal on the WMKO roof to the KPF calibration bench in the WMKO basement, where a shutter and beamsplitter allow solar light to be injected into the KPF science (SCI), sky (SKY), and calibration (CAL) fibers, or combinations of them. Figure 3.1 illustrates the full optical path for KPF-SoCal.

The main driving design principles for SoCal were 1. enable EPRV-quality stellar activity studies, 2. provide long-term instrumental calibration/tracking, and 3. be robust to the extreme weather environment on the summit of Maunakea. We selected a location on the observatory roof between the Keck I and Keck II domes that would maximize the amount of time during the year when the Sun is observable above airmass < 2 and is not shadowed by either of the Keck domes. Because nearly all of the WMKO roof is tiled with solar panels, SoCal is positioned near Keck II (see Figure 3.2). This location does place SoCal just inside the 30 ft boundary from the Keck II dome where there is a risk of ice sheets sliding off the Keck II dome and falling. Since there were no other locations on the roof with year-round unobstructed access to the Sun, we accepted this small risk.

Tracker and Optical System

The optical system of SoCal inherits many design aspects from proven, existing solar feeds at other EPRV facilities, particularly the NEID Solar Feed at the WIYN 3.5 m Telescope at Kitt Peak National Observatory, which largely made use of commercial off-the-shelf (COTS) parts for most components (Lin et al., 2022). This was especially desirable as we could quickly obtain a working system to test with KPF during the Assembly, Integration, and Testing (AIT) phase of the development of KPF at the Space Sciences Lab (SSL) at UC Berkeley. See Table 2 in Lin et al., 2022 for a list of all of the major components in the sun tracker, pyrheliometer, lens & lens tube housing, integrating sphere,

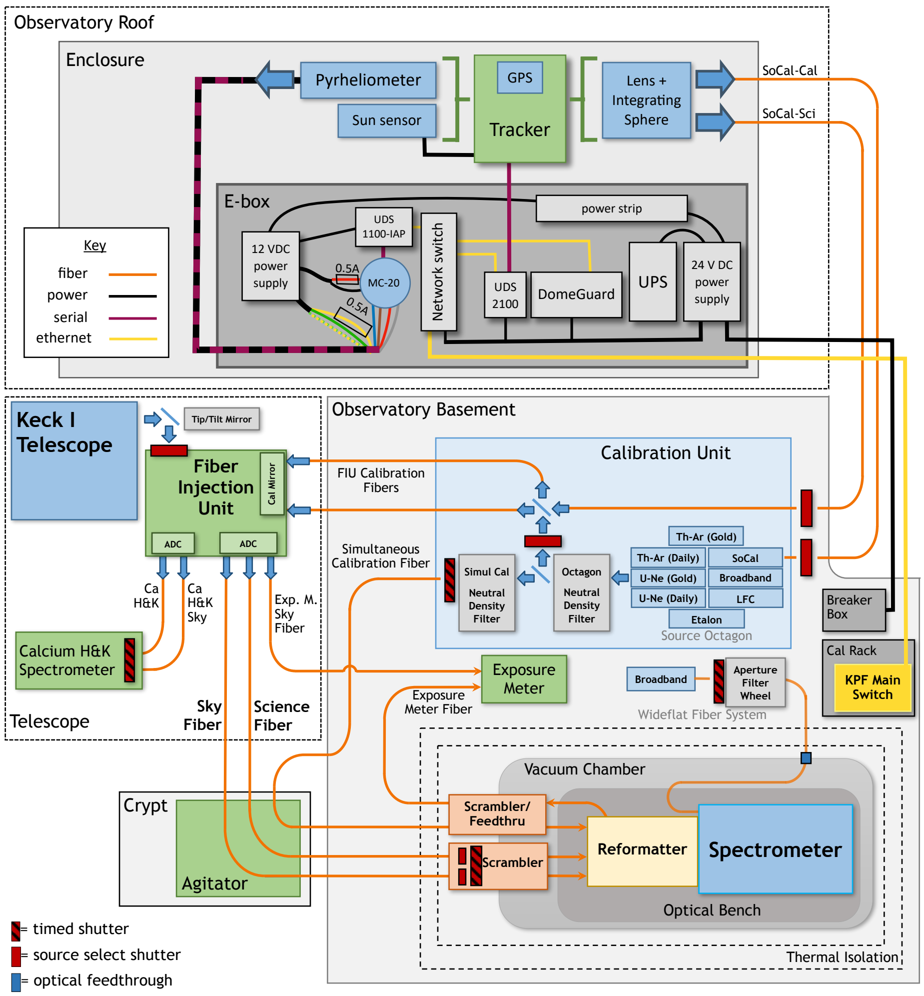

Figure 3.1: Block diagram illustrating how SoCal interfaces with the rest of the KPF system. SoCal is contained in the top dashed-line box labeled "Observatory Roof." A pair of optical fibers carry sunlight to KPF's Calibration Unit in the observatory basement, where the "SoCal-Cal" fiber connects to the calibration source selector assembly and the "SoCal-Sci" fiber feeds dedicated calibration fibers that connect directly to the FIU. The latter path sends solar light through the same path as starlight from the Keck I telescope. In this mode, a calibration source (e.g., the etalon) can be used for simultaneous calibration. The pyrheliometer irradiance is directly recorded by a computer which polls every second. Also shown are the electronics in the SoCal electronics box ("e-box"'), and the power and network connections to the observatory.

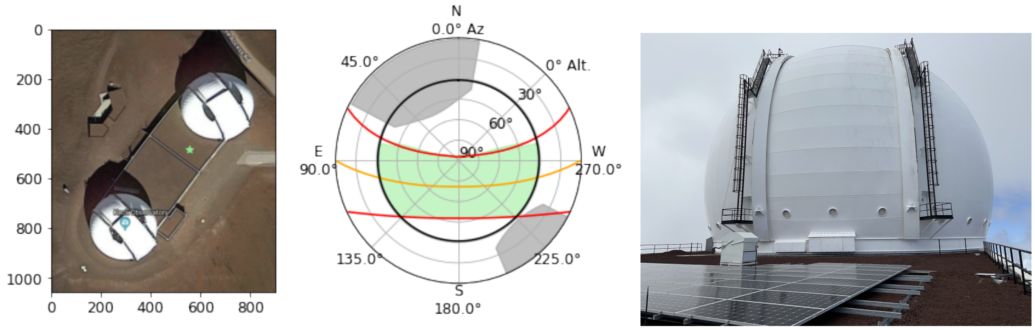

Figure 3.2: Top: SoCal's location on the WMKO roof (green star in the satellite image on the left), and the shadows of the Keck I and Keck II domes projected on the sky from this location. The path of the Sun is shown for the summer and winter solstices in red and equinoxes in orange. The parts of the sky that the Sun traverses above airmass < 2 (black circle) during a full year are highlighted in green. Bottom: Image showing the SoCal enclosure adjacent to the solar panels, with Keck II in the background.

and shutter mechanism, which are identical for SoCal. The SoCal tracker and optics are shown inside the enclosure in Figure 3.3. Here we summarize each briefly.

We purchased the same commercial sun-tracking mount as the NEID Solar Feed, the EKO STR-22G, which has been successfully operated in extreme environments for decades-long experiments (a number of such trackers currently operate at Mauna Loa Observatory). The tracker is an alt-az mount and comes with a built-in quad-pixel "sun sensor," which has provided exceptional active guiding performance for the NEID Solar Feed (see Section 2.4.1 in Lin et al. 2022) and also produces helpful telemetry for assessing guiding stability. The tracker is bolted to the upper level of an enclosure with the "North" leg of the tripod aligned with geographic north (see Figure 3.3). Normally this alignment does not need to be very precise as the sun sensor has a 15° field-of-view and will find and guide on the Sun using an onboard control loop. However, because SoCal is in the tropics, the Sun will often reach elevations of 87°–90° (see the top panel in Figure 3.2) where the active guiding capability is not possible with this tracker. When the Sun passes near zenith, the azimuth angle rotates a full 180°. Because of this, the tracker operates using a predictive calculation above 87° by which an onboard GPS sensor uses the device's latitude, longitude, elevation, and current time to adjust the azimuth to the Sun's expected azimuth, while the elevation angle is still adjusted using the sun sensor. As such, precise horizontal leveling and true north alignment

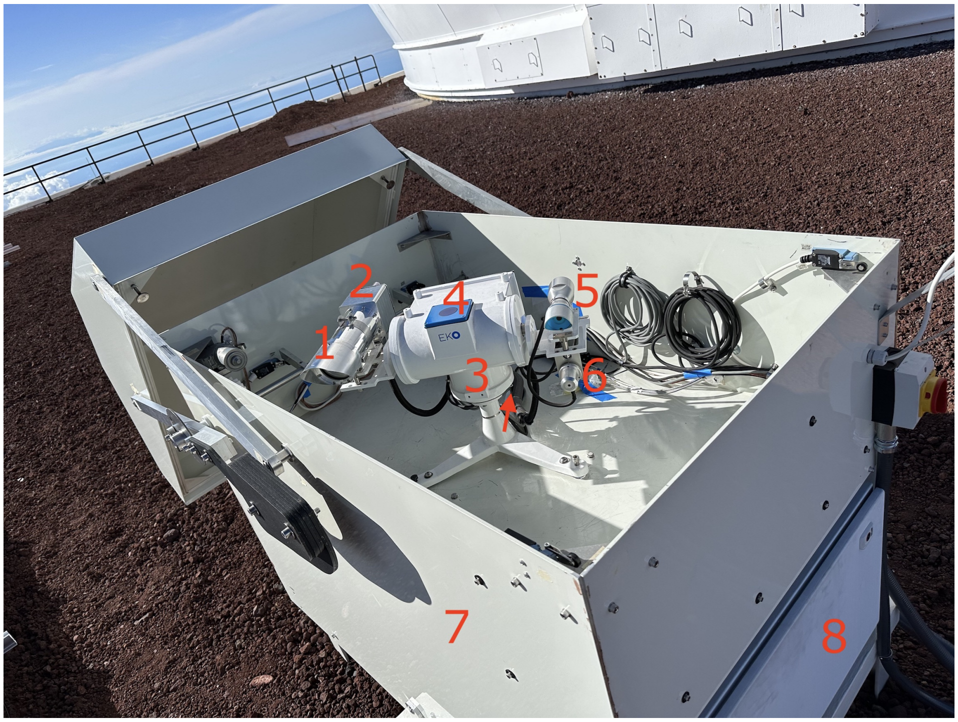

Figure 3.3: The SoCal tracker with mounted optics, inside its enclosure with the lid open. The numbered components are 1. Lens and lens tube, 2. Integrating sphere, 3. EKO Sun Tracker, 4. GPS sensor, 5. Pyrheliometer, 6. Sun-sensor, 7. Enclosure, and 8. E-box. The arrow indicates geographic north; i.e., the tracker is pointed south in this image.

are critical for tracking through solar noon. We aligned the tracker to true north by iteratively rotating the tripod by hand, enabling active-guide mode, noting how far the tracker adjusts compared to the predicted position, and then realigning the tripod to minimize the difference between the predicted position and the active-guided position. While the tracker faces south to follow the Sun through the sky during most of the year, for several weeks around the summer solstice the tracker instead must face north. As such, a careful treatment of the cable wrap behind the tracker was needed to accommodate a near 360° rotation without snagging.

We also adopted the achromatic lens (3-inch Edmund Optics 88–596-INK), custom aluminum housing, and Thorlabs integrating sphere used in the NEID solar feed (Lin et al., 2022), as these have also been demonstrated to perform well in exposed outdoor environments. Lin et al. (2022) also performed a trade study for several different lens choices and found that this model lens best preserved the size of the Sun in the focal plane across the wide wavelength range of the NEID spectrometer while maintaining sufficient transmission and aperture size. The integrating sphere used is a COTS Thorlabs 2P3 2-inch integrating sphere. The entrance port of the sphere is placed in the approximate focal plane of the lens, centered on the position of the Sun. It is essential to have the image of the Sun formed in free space to avoid overheating the optical components and minimize the risk of vignetting the solar disk.

Like the NEID Solar Feed, SoCal uses the EKO MS-57 pyrheliometer mounted to the secondary arm of the sun tracker to monitor cloud coverage directly in front of the Sun. A pyrheliometer measures the direct normal irradiance (DNI) from the Sun by focusing photons (200–4000 nm) within a narrow range of incident angles (5° field-of-view) onto a blackbody which then radiates to a thermopile. The thermopile converts heat to an output voltage that is proportional to the incident flux, allowing for a simple conversion to W m^{-2} by multiplying by the factory-calibrated sensitivity (7.717 μV/W m^{-2} in our case, as listed on the pyrheliometer spec sheet and the device itself). The voltage is automatically converted to irradiance by an EKO MC-20 signal converter, which outputs the resulting data packet in Modbus format. A Lantronix UDS1100-IAP provides a TCP/IP interface for a computer to regularly poll this data once per second.

The shutter assembly on the KPF calibration bench is also a similar design to the NEID Solar Feed shutter assembly. Light from the SoCal delivery fiber is reimaged onto a downstream fiber using a pair of achromats. In the collimated space between the lenses, a Uniblitz shutter provides source selection to the KPF calibration fibers. As SoCal contains two separate optical fibers (one for feeding the KPF science fiber, the other for feeding the dedicated calibration fiber), an identical shutter assembly is used for the second fiber.

Optical Fibers & Path to KPF

The light path and interface between SoCal and the rest of KPF and WMKO are shown in Figure 3.1. Four separate fiber runs connect SoCal on the roof to the WMKO basement: “SoCal-SCI,” “SoCal-CAL,” and a spare fiber terminate at the KPF calibration bench, while a separate fiber run for the upcoming HISPEC instrument (Mawet et al., 2019) is terminated in the basement near the future location of HISPEC. All four fiber runs exit the enclosure, enter a

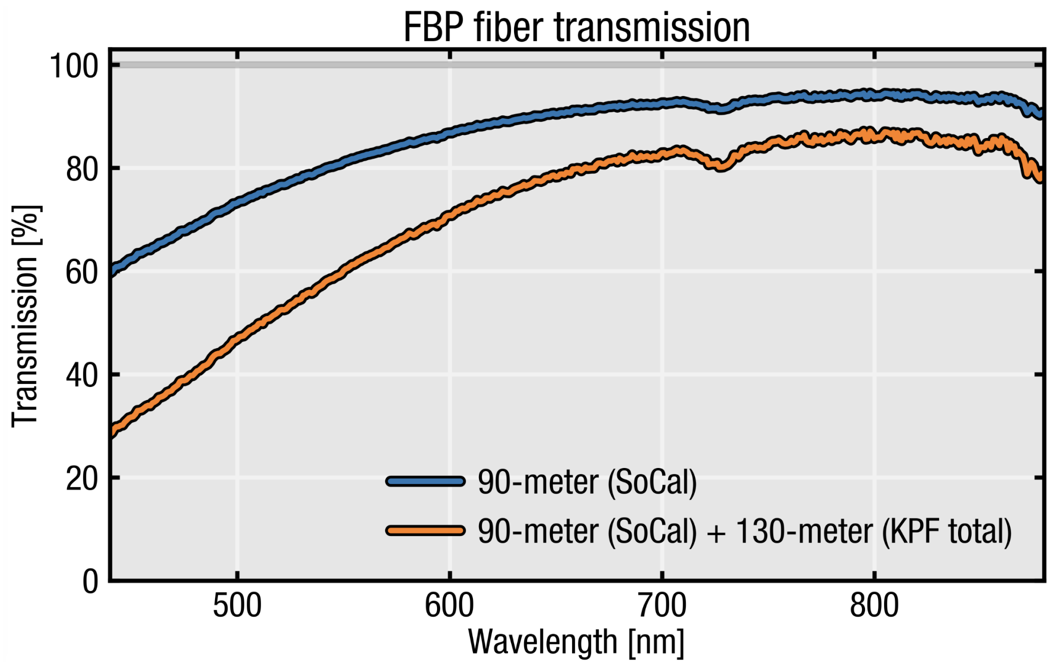

Figure 3.4: Transmission of the 90 meter SoCal fiber run from the Keck Observatory roof to the KPF Calibration Bench in the basement (blue), and the additional fiber run (orange, 130 meters) which includes the KPF calibration fiber (from the Calibration Bench to KPF's Fiber Injection Unit mounted on the Keck I telescope) and science fiber cable (back from the telescope to KPF spectrometer in the observatory basement).

long conduit run along the roof, then enter the building and travel down into the observatory basement for a total length of 90 m.

In the enclosure, a 1-meter COTS Thorlabs 2×1 fiber ($2{\times}200$ μm) fan-out cable plugs into the integrating sphere and splits the collected light into two output fibers, each of which terminates at an FC/PC patch panel at the base of the enclosure. Connected on the other side of the patch panel are the two stainless steel jacketed 90 m fiber runs for SoCal-SCI and SoCal-CAL. The HISPEC fiber is currently capped at both ends, with the output end coiled up near the installation location for HISPEC (also in the WMKO basement). The spare fiber is similarly capped at both ends and serves as a drop-in replacement for any of the other three fibers.

After traveling 90 m from the roof to the basement, sunlight reaches the KPF calibration bench. Here, the SoCal-SCI fiber injects sunlight into a shutter system. A patch fiber then directs the sunlight into a beam-splitter, where a pair of fibers transport the sunlight from the basement to the Fiber Injection

Unit (FIU) on the Nasmyth platform of the Keck I telescope. Once at the FIU, sunlight follows the same path as starlight collected by the Keck I telescope. That is, solar photons are injected into the main SCI and SKY fibers in the FIU and transported to KPF via the same optical path as is used for nighttime observations. The non-common path between sunlight and starlight is thus everything before the FIU; the Keck I telescope is used to bring starlight to the FIU while the SoCal optics and roof–to–FIU fiber run does the same for sunlight. In this mode, KPF sees the Sun as a point source just like it would any other star, hence we call this "Sun-as-a-star" mode. Likewise it is possible to observe the Sun and a simultaneous calibration source, such as the etalon. The main spectrometer receives four copies of the solar spectrum (the Sky fiber plus the three "slices" of the Science fiber) and the Ca H&K spectrometer can be simultaneously illuminated.

The SoCal-CAL fiber connects directly to the SoCal port on the KPF calibration source selector, allowing sunlight to be injected into the Cal fiber just like any other calibration source. Hence, this mode is called "Sun-as-a-calibrant" mode.

The on-sky performance of SoCal matches predictions made during the planning phase based on estimates of the throughput of the KPF and SoCal systems and the KPF Exposure Time Calculator[1]. The system throughput up to the entrance to the fibers in the integrating sphere is 5.6×10^{-6}; that is, the atmosphere, lens, and integrating sphere reduce the amount of sunlight injected into the SoCal fibers by a factor of $\sim 1.8 \times 10^5$ (the integrating sphere has a reflectivity of $\sim$0.99 and a photon has of order 1000 internal reflections before entering a fiber). The roof–basement–FIU fiber run and numerous optical interfaces along the way introduce another factor of $\sim$40 in flux loss (see Figure 3.4 for the throughput contribution from the fibers themselves). Overall, as seen by KPF, the flux of the Sun through SoCal is comparable to the flux from a $V = 1$ magnitude star using the Keck I telescope.

Enclosure

To maximize the science productivity (e.g., tracking solar activity over the 11-year solar cycle) and provide long-term instrumental characterization, SoCal needs to operate on a nearly daily basis for many years. To do so, it must

[1]https://github.com/california-Planet-Search/KPF-ETC

survive the extreme weather conditions on Maunakea. Winds in excess of 100 mph (gusts exceeding 150 mph) and significant ice/snow storms are common in the winter months. Weather is generally stable in the summer, although the chance of a tropical storm or (more rarely) a hurricane is ever-present. In November 2022, the eruption of Mauna Loa deposited volcanic ash particulates and "Pele's hair" at WMKO, which can damage sensitive optics and equipment. With the additional (though unlikely) risk of ice falling off the Keck II dome onto SoCal, it was necessary to design and build a protective enclosure for SoCal to weather these natural phenomena.

Other EPRV solar feeds have approached this problem differently. The HARPS-N/LCST and HARPS/HELIOS solar telescopes are each completely enclosed beneath an acrylic dome (Phillips et al., 2016). This has the benefit of no moving parts but requires heat management and introduces the potential for aberrations, as scratches or imperfections on the dome could distort the solar image and produce spurious (possibly chromatic) RV shifts. In fact, accumulated dust on the HELIOS dome is likely responsible for observed oscillations in some of the HARPS solar RVs (Zhao et al., 2023b). Meanwhile, the GIARPS/LOCNES solar telescope lives inside a small aluminum box with a motorized lid (Claudi et al., 2018b). In contrast, the NEID solar feed does not use an enclosure of any kind; Lin et al. (2022) instead opted for highly ruggedized components for the entire system, which is mounted in the open on the roof of the WIYN control room building.

As the sun tracker, pyrheliometer, lens, lens tube assembly, and associated cables are all similar to those in to the NEID solar feed, which itself has weathered monsoons and survived being fully encased in ice, we have confidence that SoCal can likewise withstand significant weather events. In fact, a number of EKO STR-22G Sun Trackers operate enclosure-less at nearby Mauna Loa Observatory, which experiences similar weather. However, due to the high frequency of hurricane-force winds, which could uplift cinder and impact SoCal, and the chance of ice fall, we opted for a rugged, highly-weatherproofed motorized enclosure to protect the sun tracker and optics. Additionally, keeping SoCal covered when not in use reduces UV degradation, extending the lifespan of various components.

We opted for a proven solution to shield SoCal from the elements when necessary; the clamshell-style design of our enclosure is the same as that for the

Hungarian-made Automated Telescope Network (HATNet), also on Maunakea (Bakos et al., 2002; Bakos et al., 2004), and was custom-built for our purposes by the same manufacturer, Fornax Mounts[2]. The SoCal enclosure is visible in Figures 3.2, 3.3, and 3.5. The enclosure control electronics, called "Dome Guard," are controlled by a Raspberry Pi single-board computer. A sensor monitors the current sent to the dome motor and cuts off the power if the measured current exceeds a user-specified threshold. This prevents the lid from opening into an obstruction (e.g., a snowbank) and straining the worm gear/cogwheel.

The SoCal enclosure is kept in place by burying attached steel plates under the layer of 0.5 m thick volcanic cinder that covers the roof of the building connecting Keck I and II. This approach was adopted so that it wouldn't be necessary to puncture the water-tight membrane on the roof. The enclosure frame is welded to six legs which were bolted to the steel plates. The frame and foundation were designed by M3 Engineering & Technology, who designed an analogous ballasted mounting scheme for WMKO's solar panel array[3]. The weight and area of the steel plates were determined by considering the wind-loading of the enclosure to ensure that the combined weight of the enclosure ($\sim$700 lbs), steel frame and foundation ($\sim$700 lbs), and backfilled cinder would be sufficient to withstand winds up to 200 mph (3 sec gust). Mechanical latches were also installed to securely hold the lid in its closed position in anticipation of strong winds.

The enclosure was installed on December 16, 2022, with a partially assembled sun tracker inside. Two days later the summit experienced an extreme winter storm with sustained winds in excess of 100 mph and severe snow/ice (see Figure 3.5). The severe winter weather continued for roughly four months before we were able to return and complete the installation. The enclosure successfully protected the sun tracker inside; only a slight dusting of volcanic cinder was found in the interior, which was wiped away with a cloth.

Electronics

The control electronics for SoCal are stored in a dedicated weatherproof box (the "e-box") stowed in the lower level of the enclosure (visible in the lower-right corner of Figure 3.3). Most cabling is internal; the only external electrical

[2]https://fornaxmounts.com/
[3]https://m3eng.com/

Figure 3.5: Webcam image of the SoCal enclosure frozen in a block of ice after a winter storm in December 2022.

cables are a 120 V/15 A AC power cable and a pair of cat-6 ethernet cables (main and spare). Power is grounded in the same manner as other rooftop devices and the cat-6 cables have surge suppressors in series to protect against lightning strikes. Two power supplies (24 V DC and 12 V DC) inside the e-box supply power to all electronics devices. The 24 V devices (including the tracker and enclosure) have backup power from an uninterruptible power supply (UPS). In the event of a power failure, the enclosure control logic detects the switch to the UPS and automatically commands the lid to close using backup power.

Our primary selection criterion for the various electronics devices was the ability to operate in a wide operating temperature range. While the ambient temperature on the summit is generally stable (T $\approx 0 \pm 10^\circ$ C), we set a conservative requirement of -30° C to 60° C operating temperature as temperatures can be more extreme inside the sealed e-box in shaded or direct sunlight conditions. The temperature inside the e-box, inside the enclosure, and outside the enclosure are each monitored using a dedicated temperature probe.

We also required TCP/IP interfaces for each device to integrate with the KPF and WMKO facility networks. The sun tracker communicates using RS232, so a Lantronix UDS2100 provides direct control over TCP/IP. The output voltage from the pyrheliometer is converted into Modbus protocol using an EKO MC-20 signal converter, and a Lantronix UDS1100-IAP provides the

TCP/IP interface. The enclosure is fully operable over WebSocket so it is directly controlled without an additional device server. Since the enclosure has its own computer, it monitors connections to its IP address and automatically triggers the lid to close should it lose connection to the KPF server.

Control Software

The SoCal system consists of three main devices: the sun tracker, the pyrheliometer, and the enclosure. We communicate with each device using Python functions. We use the `socket` module to send RS232 commands to the sun tracker, `pymodbus` to poll data from the pyrheliometer, and `websockets` to communicate with the Dome Guard Raspberry Pi single-board computer.

For operations at WMKO, these Python functions are wrapped into the Keck Task Library (KTL; Conrad and Lupton, 1993; Lupton and Conrad, 1993; Deich, 2014) keyword framework using `KTLPython`. This allows users to interface with SoCal using the same syntax as is used for other Keck instruments. Telemetry is stored using a set of KTL keywords. The history of these keywords (e.g. tracker altitude, sun sensor offset, enclosure open/close state, temperatures) is stored in a database on WMKO servers which can be queried to determine the current or past state of SoCal. One way to visualize this information is through a Grafana web page (Figure 3.6).

3.3 Operations

Daily Schedule

The daily calibration schedule for KPF consists of a set of morning and evening calibrations with the fiber illuminated by Thorium-Argon (ThAr) and Uranium-Neon (UNe) hollow cathode lamps, a broadband laser frequency comb (LFC), a stabilized Fabry-Perot etalon, and a quartz flat lamp, plus dark and bias frames. These automated calibration sequences are scheduled at fixed times, with morning calibrations ending around 08:42 HST (Sun at 30–40° elevation, or airmass 2–1.6) and evening calibrations beginning at 3:00 HST (Sun at 30–55°, or airmass 2–1.2). This leaves roughly $\sim$6 hours of available daytime for SoCal, year-round. Currently, the time from noon HST to 3:00 HST is used to collect continuous stacks of flat-field frames, so thus far SoCal has operated in the morning hours from 08:45 – noon HST. We preferred morning over evening as the former overlaps with solar observations in Arizona by both NEID and EXPRES. Long term, we are exploring scheduling flat-field calibra-

Figure 3.6: Screenshot of the Grafana web page displaying the SoCal telemetry for an example day. Grafana is a web-based interactive visualization software for displaying and plotting values from a database. In this example near the summer solstice, the tracker performed a large slew in azimuth through solar noon at near 90° elevations. The sun sensor guiding offset is plotted in the upper right-hand corner (box titled "EKO Sun-Sensor Guiding Offset"). Near solar noon the sun tracker switches to predictive guiding mode, hence the gap in recorded guider offsets. The elevation offset is stable at $\sim 0.5° \pm 0.05°$ all day. While the azimuth offset increases near zenith, the actual angular separation between the predicted Sun location and the sun tracker's position is never more than $\sim 0.5°$. Other panels display weather information and the status of subsystems.

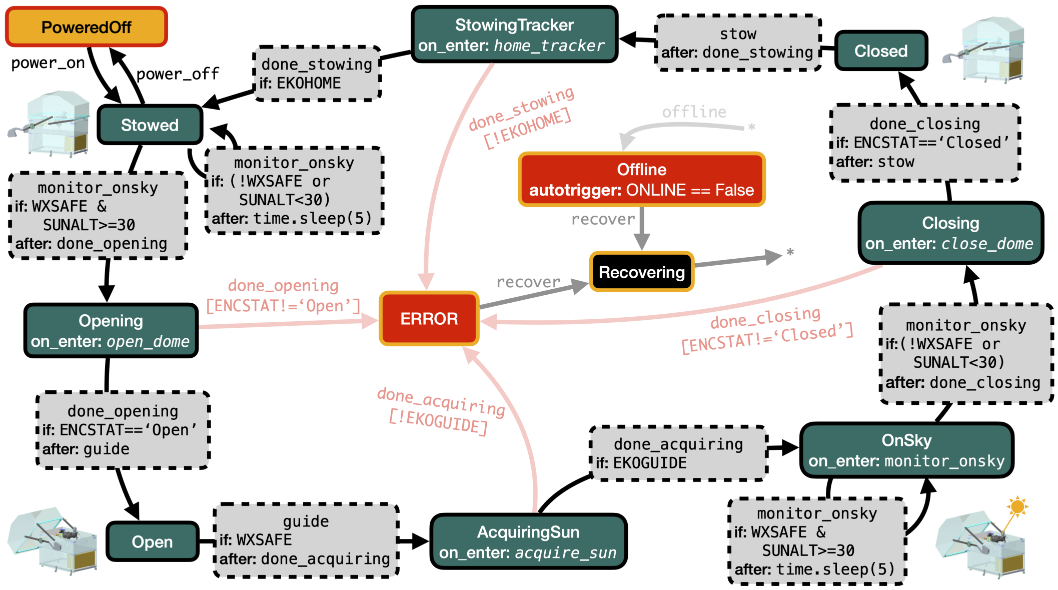

Figure 3.7: State machine logic flowchart defining the automation loop for SoCal operations. Nominal operations begin in the upper left and flow counter-clockwise. First, the enclosure opens and the tracker acquires the Sun. As the tracker guides on the Sun, the KPF spectrometer records solar spectra. At the end of the day, the dome closes, and the tracker is stowed (see Section 3.3 for more details). Green boxes with solid borders represent the states of the system, while grey boxes with dashed borders represent transitions between states. The special states "Offline" and "ERROR" are visualized with red boxes, while "Recovering" is colored black. The state to which a named transition moves to may depend on a conditional, which is printed as an `if` statement. While most states execute a function upon entering (`on_enter`), the `Open` and `Closed` states generally immediately transition to the ensuing state due to the `after` function of the transition used to enter those states.

tions during off-sky nighttime hours to free up the full daytime for SoCal. An additional ∼2 hours of daytime in the summer months may be obtained by dynamically scheduling calibrations according to sunrise/sunset times. However, this would result in the morning/evening calibration sequences occurring at different relative times to the fixed liquid nitrogen fill schedule (∼11:00 HST) throughout the year.

Following the morning calibration sequence, the SoCal observing script initiates operations. This script first checks that SoCal is in the `OnSky` state (i.e., the sun tracker is guiding on the Sun above 30° elevation, see Section 3.3 for more details). If so, the script configures the FIU to select the SCI and SKY calibration fibers, configures KPF to use the green and red CCDs as well as the Ca H&K spectrometer, configures and activates the exposure meter, runs the agitator, configures the shutters, and finally turns and directs etalon light into the simultaneous calibration fiber. Then, as long as SoCal remains in the `OnSky` state, repeated exposures are taken. The autonomous loop regularly monitors (every 5 seconds) weather keywords from the observatory's meteorological system (sustained wind speed, wind gust speed, dew point, and precipitation) and if any become "unsafe," or if the Sun sets, SoCal exits `OnSky` and exposures terminate. The observing script is re-executed if SoCal re-enters `OnSky` (e.g., if the weather becomes "safe" again) up until the evening calibration sequence is scheduled to begin. We adopted the same "safe/unsafe" conditions used for general operations at WMKO, which correspond to a dewpoint temperature within 0.2 C of ambient temperature, wind gusts over 45 mph, and/or sustained wind speeds over 30 mph. We have also noticed that at wind speeds near 30 mph, the enclosure lid visibly bounces up and down as its concave shape in the open position acts as a sail. Thus, keeping the enclosure closed in strong winds reduces strain on the mechanical components.

KPF exposures with SoCal are taken with a fixed exposure time of 5 sec (see discussion in Section 3.5). KPF has two readout modes, "standard" and "fast readout." The fast readout mode is primarily used for high-cadence asteroseismology during nighttime operations. Initial SoCal operations during commissioning were primarily in standard mode, which originally had a 55 sec readout time but has since been reduced to 49 sec. For comparison, the cadence of the NEID solar feed is 83 sec (55 s exposures + 28 sec readout), which is similar to SoCal's cadence in standard read mode. During most mornings with the current operating scheme, KPF records around 200 solar spectra in standard readout mode. Long-term post-commissioning SoCal operations are expected to utilize the fast readout mode (15 sec) to produce daily time series of solar spectra with < 30 sec cadence. In this mode, SoCal will accumulate $\sim$1000 spectra per 6 hr day. KPF has been tested with SoCal in fast readout mode on a few days, including a single full 6 hr day during which 1041 spectra were acquired.

Autonomous Loop

SoCal is autonomously controlled using state-machine logic that transitions the system between defined states. A state machine works by defining a number of known "states" which correspond to different configurations of the various devices in the system. "Transitions" define how one state moves to another. Pre-condition and post-condition functions can be attached to each state and transition so that they are executed before or after a transition, or upon entering or exiting a defined state.

The autonomous loop, which we implement using `pytransitions` (Neumann et al., 2022), is shown graphically in Figure 3.7 and is as follows. Beginning in the `Stowed` state, with the enclosure closed and the sun tracker pointed at "home" (due south at zero elevation), the `monitor_onsky` transition is called. This transition checks if the Sun is above the horizon and if all weather keywords report "safe." If false, the transition returns to the `Stowed` state, waits five seconds, and attempts to transition again. If true, the state machine transitions to `Opening`, and the enclosure is commanded to open. After opening, the sun tracker is set to active guiding mode. Upon acquiring the Sun (defined by the sun sensor guiding offset falling below $1°$), SoCal enters the `OnSky` state. Five seconds later the software checks if the weather keywords are all "safe" and that the sun altitude is still $> 30°$. If both are true, the state machine transitions to `OnSky`; in this case, there is no state change, and thus this check every 5 seconds continues. If one of the two conditions fails, then the state machine transitions to `Closing`, triggering the enclosure to close. Once closed, the sun tracker is commanded to move to its home position. SoCal then reenters the `Stowed` state, and the whole process starts over.

Three special states exist for gracefully catching errors and recovering without human intervention. The `Offline` state, which the state machine can transition to from any other state, occurs automatically if a regular ping to any of the SoCal devices fails. The state machine will hold in this state until all devices become ping-able again, at which point the state machine transitions to the `Recovery` state. The `ERROR` state is automatically transitioned to if an exception is caught during any of the `before`/`after`/`on_enter`/`on_exit` functions. Similarly, upon entering `ERROR`, the state machine will attempt a transition to `Recovery`.

Upon entering `Recovery`, the code evaluates the status of each SoCal device by requesting the relevant telemetry. If the telemetry is consistent with the last known state, then the state machine transitions back without executing any of the associated `before`/`after`/`on_enter`/`on_exit` functions. Otherwise, the code executes the relevant device commands to put the devices back in the correct configurations to be consistent with the last known state and then transitions to that state. If this too fails, then the state machine remains stuck in the `ERROR` state. After a timeout the enclosure is commanded to close and an email and Slack message are sent to relevant personnel. The enclosure also has its own hard-wired fail-safes that automatically close the enclosure in the event of a power outage (the UPS provides backup power) or if the enclosure becomes unreachable (flagged by regular pings between the enclosure and KPF computers).

3.4 Data Reduction

KPF Data Reduction Pipeline

SoCal spectra follow essentially the same data reduction steps as stellar spectra gathered using the Keck I telescope. Each of the three primary KPF science slices is independently extracted and reduced using the standard KPF DRP[4]. RVs are computed using the cross-correlation (CCF) technique, using a weighted numerical stellar mask based on spectral type (Pepe et al., 2002; Baranne et al., 1996, e.g.), for each SCI slice and for each CCD (green and red) independently. The KPF DRP currently uses the public release of the ESPRESSO cross-correlation masks; the G2 mask is used for the solar spectra. The KPF DRP produces three main data products in the form of .fits files: "Level 0" (L0) files contain the raw 2D images from the green and red CCDs, "Level 1" (L1) files contain the extracted 1D spectra for each fiber trace (three slices for SCI, one for SKY, one for CAL), and "Level 2" (L2) files contain the RVs in the green and red channels (averaging over the three slices). We further combine the green and red RVs into a single RV using an unweighted mean.

The main step that requires special treatment for solar data is the barycentric correction (Wright and Eastman, 2014). Using `barycorrpy` (Kanodia and Wright, 2018), the doppler shift due to the barycentric motion of the Sun due to the Solar System planets as well as the motion of the observatory along the line of sight is removed (Wright and Kanodia, 2020). This is accomplished by multiplying the wavelength solution of the CCF mask by $1/(1 + v_b/c)$, where v_b is the output of `barycorrpy.get_BC_vel` using `SolSystemTarget='Sun'` and `predictive=True`. We also compute and report heliocentric Julian dates ($\mathrm{HJD_{TDB}}$) using `barycorrpy.utc_tdb`, as opposed to barycentric Julian dates

[4]https://github.com/Keck-DataReductionPipelines/KPF-Pipeline/

(BJD_{TDB}) computed for stars. Consequently, the final KPF solar RVs are in the rest frame of the Sun. Thus, any observed variability must be due to solar activity, instrumental noise, or atmospheric/resolved-disk effects.

The current KPF DRP implementation does not correct for differential extinction (as described in Davies et al. 2014 and Collier Cameron et al. 2019). The L2 files provide information about instrument drift by reporting the RV of the simultaneous calibration (etalon) spectra; these RVs can be subtracted from the solar RVs to correct for the drift. However, during the first few months of SoCal operations, the etalon has not been consistently available with high enough flux to enable such an RV drift correction due to the etalon illumination source (an NKT supercontinuum laser) degrading over time. For observations since July 31, 2023, the extracted green etalon RVs are too noisy to be useful for a simultaneous drift correction. However, this limitation is expected to be short-lived as a replacement supercontinuum source will be installed in the very near future. With anticipated developments of the KPF DRP, a global drift model for the instrument will be constructed each day based on standalone and simultaneous calibrations taken throughout the day. This model could then be subtracted from the measured RVs for higher-precision measurements.

The L0–L2 solar data are publicly available on the Keck Observatory Archive[5] (KOA) by querying KPF data for `TARGNAME == 'Sun'`, or by using the `PyKOA` API[6]. SoCal data are categorized as calibration data and are therefore available for public use within a day of being collected. We expect to add a queryable, downloadable table of SoCal RVs with telemetry and quality control metrics using the pyrheliometer (see Section 3.4), as well as the raw irradiance time series for each day that SoCal was active. The irradiance measured during each exposure is also saved as an extension in the L0 file.

Quality Control

The largest variability in the solar RVs is caused by uneven throughput across the resolved stellar disk. While the integrating sphere spatially averages over the stellar disk to sufficient homogeneity, external factors such as clouds or objects on the horizon can obscure some or all of the solar disk, which breaks the symmetry of the solar rotational velocity profile and creates large time-variable RV shifts up to $v \sin i_\odot \sim 3$ km s^{-1}. Rather than create a quality

[5]http://koa.ipac.caltech.edu/cgi-bin/KOA/nph-KOAlogin
[6]https://koa.ipac.caltech.edu/UserGuide/PyKOA/PyKOA.html

flag based on the observed solar spectrum or RV, we used the pyrheliometer irradiance time series to identify observations that are contaminated by clouds or other obscurations. If the Sun is partially or completely obscured, the measured irradiance time series from the pyrheliometer shows a drop in flux. As a cloud moves across the solar disk, the irradiance time series can also show erratic variability. Conversely, clear-sky conditions produce a stable, slowly varying irradiance curve that peaks at solar noon.

We devised an algorithm to assess cloud coverage using the irradiance time series. For each day SoCal operates, the irradiance time series is divided into 5 min duration windows. This window size is adjustable, but 5 min was found to be both long enough to include enough data points for a reliable calculation as well as short enough to capture the fast timescale nature of cloud coverage. For each window, the algorithm fits a second-degree polynomial. The "clearness index" is the square of the residuals, dividing by the polynomial model, summed over the 5 min window. Essentially, this is a χ^2 test. With clear skies, the polynomial model is a good fit to the stable, slowly varying irradiance, and so the clearness index is low. If clouds are present, the large changes in irradiance produce a high clearness index. We found that setting a threshold of < 2 for the clearness index in 5 min windows effectively selects only the clearest portions of the day. Adding a secondary criterion that the observed irradiance be > 100 W m^{-2} eliminates cases where an obstruction causes a decrease in the measured irradiance to near 0 W m^{-2}, which would pass the χ^2 test should the zero flux be maintained for the duration of the window. For finer time resolution and increased robustness at the bin edges, we repeat this calculation five times, each time shifting the windows by one minute. The clearness index at a given timestamp is then the minimum of the values computed from the shifted windows which include that timestamp. Figure 3.8 shows example clear and cloudy days with times that pass this clearness threshold highlighted in green. Conveniently, the clearness index does not depend on a theoretical model for the irradiance, only the measured time series, and is fast to compute. Figure 3.8 also shows the corresponding RVs, which are masked (faded points) if the clearness threshold fails or if there is not at least three minutes of clear-sky time. An additional buffer of one minute is masked at any clear/not clear boundary.

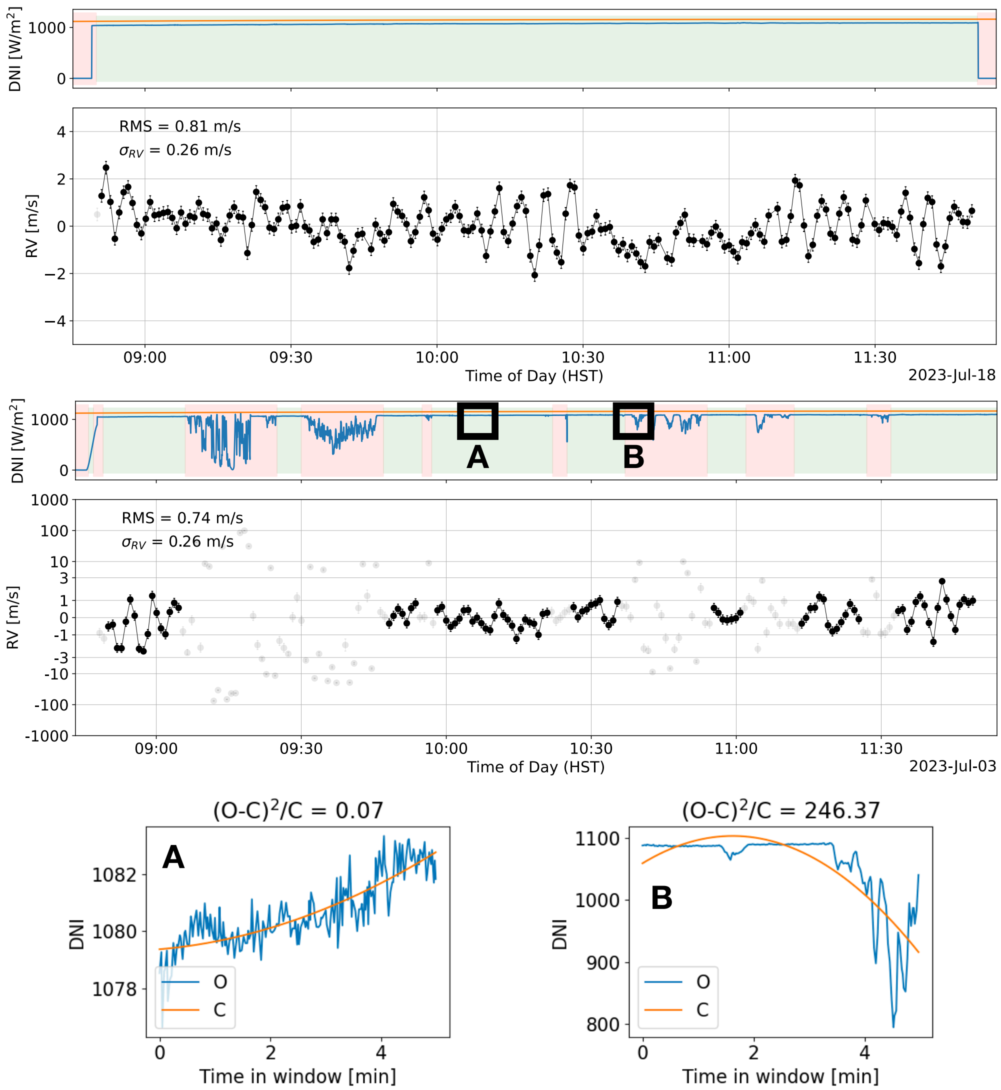

Figure 3.8: Example of a clear-sky day (top) and a day with sporadic clouds (bottom). The upper subplot shows the irradiance time series (blue) relative to the theoretical model (orange) computed using `pvlib` (Holmgren, Hansen, and Mikofski, 2018), with clear times highlighted in green and non-clear times in red as identified by the clearness index defined in Section 3.4. The lower subplot plots the RVs during the same time frame. Note the vertical axis scale for the RVs on the cloudy day; RVs observed through clouds show a wide range of sporadic variations from a few to hundreds of m s^{-1}. The ~ 5.5 minute p-mode oscillations are clearly seen in the clear-sky RVs; connecting lines are drawn to help guide the eye. Faded points are RVs masked according to the clearness criteria described in Section 3.4. The zoom-ins at A and B in the cloudy example show the polynomial fit and resulting clearness index for a reference clear and cloudy window.

Applying this filter to the full set of SoCal observations discards ∼16% of all RVs. We visually inspected the corresponding plot in Figure 3.8 for each day to ensure that data affected by clouds were being correctly identified.

3.5 First Results

We completed the installation of SoCal at WMKO and achieved "first light" on April 25, 2023. Initial data were collected on a few clear days in May under manual control while the control software was being finalized and hardware issues that disabled remote operation of the enclosure were resolved. Beginning on June 5, 2023, SoCal and KPF have observed the Sun nearly every "safe weather" day (which may or may not be cloudy) as described in Section 3.3, with occasional shutdowns for testing of other KPF subsystems. SoCal was intended to both assist with KPF commissioning tasks and collect useful data for studying stellar activity. Here we discuss the first results from these activities.

Doppler Performance

During commissioning, SoCal data were used to validate the Doppler performance of KPF, identify instrumental problems, and provide an additional calibration source and benchmark for the DRP. To validate Doppler performance we have accumulated over 19,000 solar spectra using the standard and fast readout modes over a few to six hours per day during 111 calendar days spanning 4.5 months. The solar spectra were reduced using the KPF DRP as described in Section 3.4. Observations taken in cloudy conditions were removed using the "clearness index" presented in Section 3.4. The KPF DRP is being actively refined and currently works best over short time periods, hence in this work we only scrutinize KPF's performance on intra-day timescales. Future work will probe KPF's Doppler performance on timescales of weeks to months.

In a 5 sec exposure, the extracted 1-D KPF spectra have a peak signal-to-noise (SNR) of ∼450 in the green channel (∼550 nm) and ∼800 in the red channel (∼750 nm), per SCI trace (the large differences come from the significantly worse throughput at bluer wavelengths from the long fiber run, see Figure 3.4). Combining the three SCI traces yields SNR ∼800 in green and ∼1400 in red. For reference, nonlinearity in the response of the KPF CCDs is expected to set in for SNR $\gtrsim$1500 in a single trace, or ∼2600 combined (true saturation at 1900 and 3300 respectively). Combining the measured green and red RVs yields a

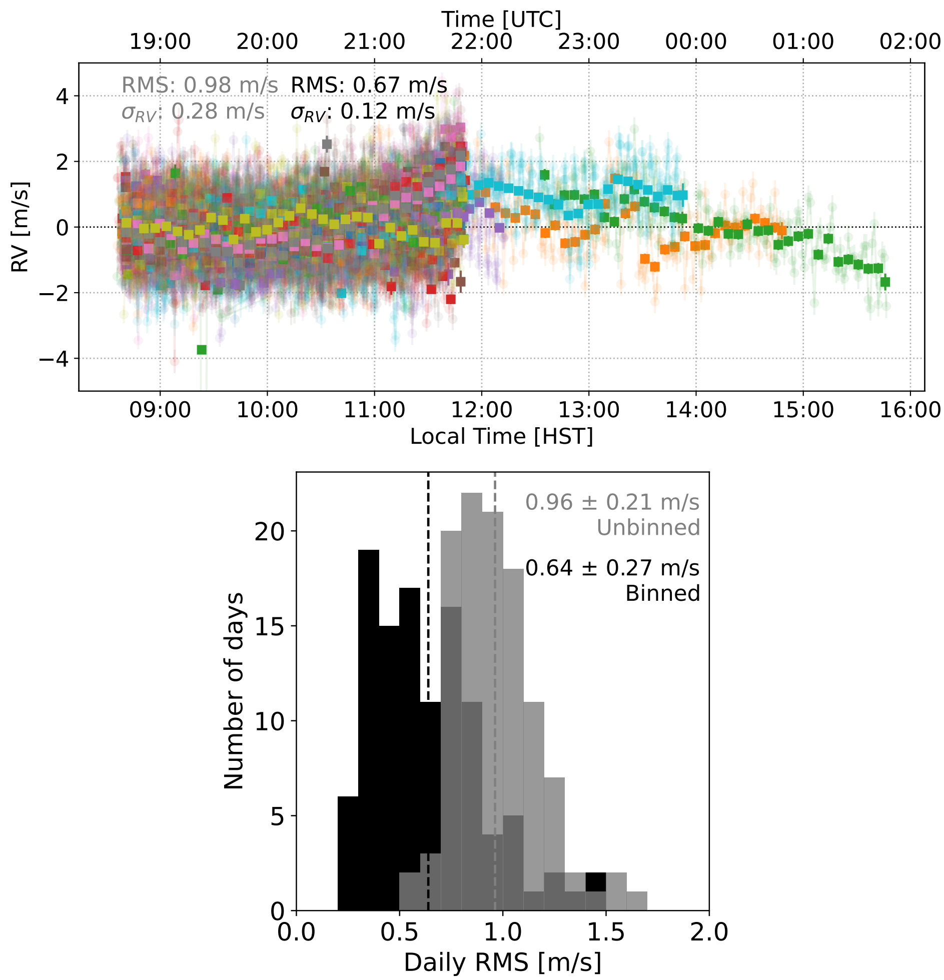

Figure 3.9: All clear-sky SoCal RVs to date, phased to the time-of-day local time. A daily median value has been subtracted. The raw measured RVs (no drift correction) are shown as faded points, color-coded by day. The bolded points show the same data binned over 5.5 min. The histogram below shows the distribution of daily RMS for both the binned and unbinned RVs.

photon-limited precision of around 28 cm s^{-1}for a given 5 *sec* exposure. Since we also expose the SKY fiber to sunlight, in theory we can gain an additional $\sim\sqrt{4/3}$ increase in SNR by combining SKY with the three SCI traces; however, this is currently untested.

The daily root-mean-squared (RMS) of the RVs after binning over the 5.5 min solar oscillations, without correcting for instrumental drift, is typically around 0.64 ± 0.27 m s^{-1} (Figure 3.9). Instrument drift over a daily SoCal sequence (3–6 hrs) is typically below the 1 m s^{-1} level, although some days show stronger deviations.

Charge Transfer Inefficiency Issue

Another KPF commissioning activity was to measure the impact of charge transfer inefficiency (CTI) in the CCDs on stellar RVs. CTI can produce a SNR-dependent RV shifts since spectral lines will become skewed by the leftover charge smearing across the detector (Bouchy et al., 2009; Halverson et al., 2016; Blake, Halverson, and Roy, 2017). To directly probe the effects of CTI on the KPF RVs, we gathered sequences of 20 exposures at exposure times of 10 sec, 8 sec, 5 sec, 3 sec, 2 sec, 1 sec, and 0.5 sec (see Figure 3.10). We noticed significant systematic jumps in RV between each sequence. We isolated this effect to one of the four amplifiers on the green CCD by observing that this effect was only present in RVs computed using that quadrant of the 2D spectrum. We measured that this amplifier has roughly 100 times worse CTI than what was measured during laboratory CCD tests performed at Caltech (prior to shipping KPF to Hawaiʻi in the summer of 2022).

To work around the CTI problem affecting one amplifier on the Green CCD, we developed a new read mode of KPF that utilizes two low-CTI amplifiers operating at 200 kHz in place of the original 4-amplifier, 100 kHz mode. This is the new "standard" readout mode of KPF as of June 24, 2023. Note that the fast readout mode still requires all four amplifiers operating at 400 kHz. As a result, all fast readout data as well as all standard readout data prior to June 24, 2023 must have the affected quadrant of the green CCD masked when computing RVs. This masking is now automatically applied to all previously-collected data in the standard KPF DRP and does successfully resolve the CTI issue (see bottom panel of Figure 3.10), at the cost of slightly degraded RV precision since over a quarter[7] of the spectrum is being ignored. We are considering raising the exposure time to 10–12 s when using fast readout mode to compensate for this. This would result in a 26 s cadence, slightly better duty cycle (38%), and $\sim$800 spectra per 6 hr day, but would reach 25 cm s^{-1} photon-limited precision vs. 36 cm s^{-1} in a 5 sec exposure. For comparison, in standard read mode we can reach $\sim$ 20 cm s^{-1} in 10 sec or 28 cm s^{-1} in 5 sec. Longer exposure times would also fully utilize KPF's unique ability to obtain high SNR spectra; SNR $\sim$1400 *per trace* is reached in the red channel for a 12 sec exposure, and nonlinear CCD response only begins to set in above SNR $\sim$1500 per trace.

[7]The CTI-affected quadrant is the bluest end of the green detector, where the inter-order spacing is smallest.

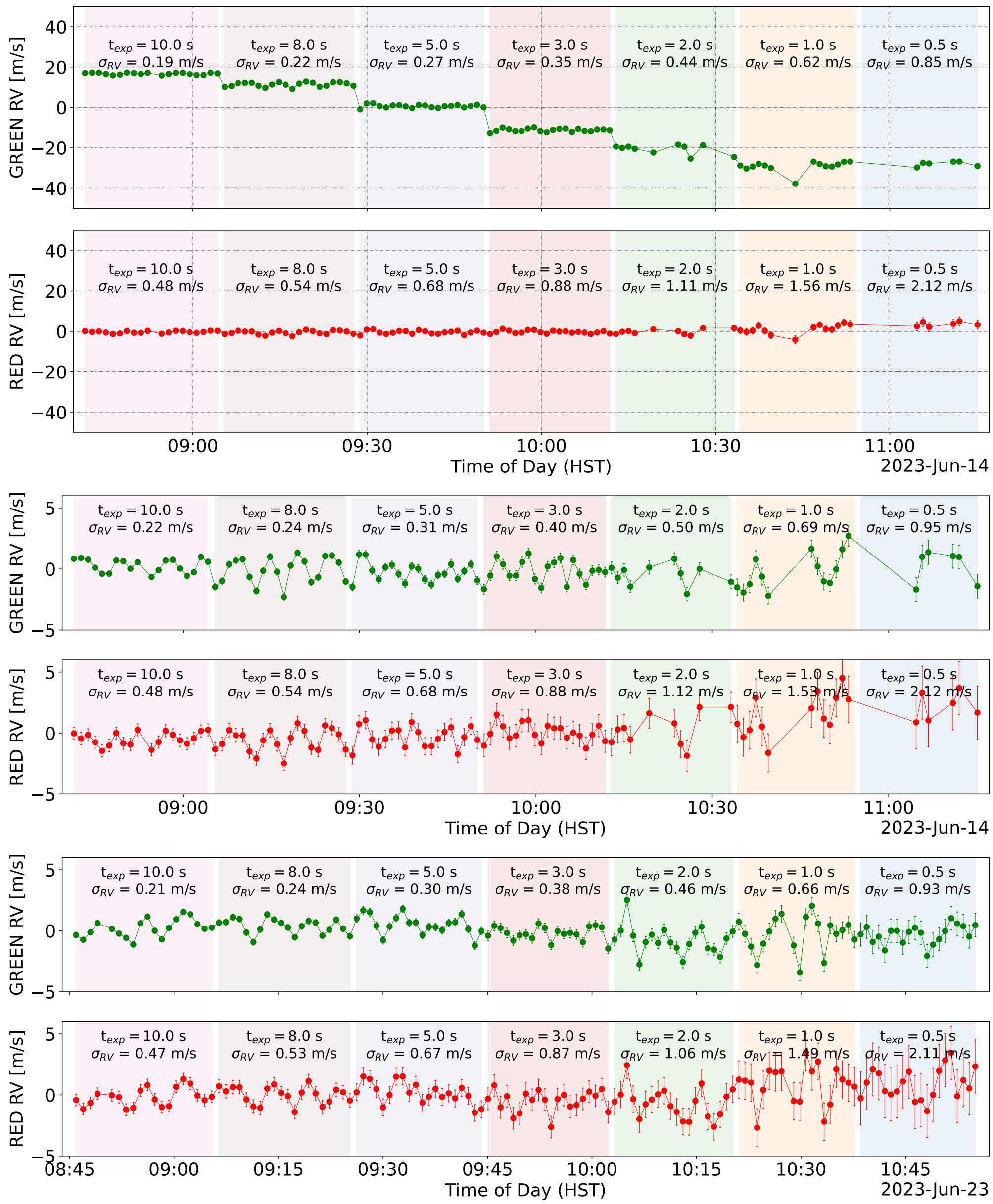

Figure 3.10: **Top:** SoCal RVs (green and red) during our CTI test stepping across a range of exposure times. The large offsets between each sequence in the green RVs are caused by CTI effects in one of the four amplifiers. Some gaps exist due to intermittent clouds. **Middle:** The same data but recomputed by masking the quadrant of the green CCD that is read by the affected amplifier. The offsets disappear below the instrumental noise, at the expense of slightly worse RV precision since over 1/4 of the spectrum in the green channel is not used. **Bottom:** The same sequence of exposure times taken on a different day using a 2-amplifier readout scheme. By not using the affected amplifier, the CTI effects disappear and full RV precision is maintained.

Comparison to Other EPRV Solar Feeds

While most active EPRV solar feeds have opted to publish their data in large data releases (e.g., Collier Cameron et al., 2019; Dumusque et al., 2021), the NEID Solar Feed makes its data available to the public immediately after it is acquired and reduced[8]. We prioritized morning observations with SoCal (08:45 – 12:00 HST) as this window fully overlaps with the early afternoon NEID solar observations in Arizona. This way we could immediately compare RVs between instruments.

Figure 3.11 shows the measured SoCal (orange) and NEID (blue) RVs for ten days with fully clear skies at both sites. We observed the majority of these days with KPF in the standard readout mode (5 sec exposure, 55 sec cadence), with tests of the fast readout mode (5 sec exposure, 21 sec cadence) on June 28, 2023 and July 6, 2023. Since the fast readout data are taken in 4-amplifier mode, the RVs are computed using an order mask on the green CCD to avoid contamination by CTI effects (see Section 3.5), hence the larger than usual per-measurement uncertainty. The NEID solar RVs have a longer exposure time (55 sec) but an intermediate readout time (28 sec), resulting in a similar cadence (83 sec cadence) as our standard read mode data. Both instruments clearly resolve the 5.5 minute solar p-mode oscillations, which dominate the common RV variability on these $\sim$hours intra-day timescales (see Kjeldsen et al., 2008). The bottom panel of each daily plot shows the residuals between the NEID RVs and a spline fit of the KPF RVs interpolated to the NEID timestamps. The RMS of these residuals is typically around 30–40 cm s^{-1}, which is slightly lower than the quadrature-sum of the KPF and NEID single-measurement errorbars (40–46 cm s^{-1}). As the KPF RVs are corrected for instrumental drift using the simultaneous etalon RVs, this means that there are no other sources of unaccounted instrumental noise in these data. For any observations that show large disagreements (e.g. June 8 near 21:30 UTC), a deeper investigation is warranted to isolate which instrument the source of disagreement is coming from. As the KPF DRP, wavelength solutions, calibration source RVs, and drift models are still converging on a long-term stable solution, we leave this investigation for future work when the KPF RVs reach the same level of maturity as the NEID RVs.

[8]Available at https://neid.ipac.caltech.edu/search_solar.php

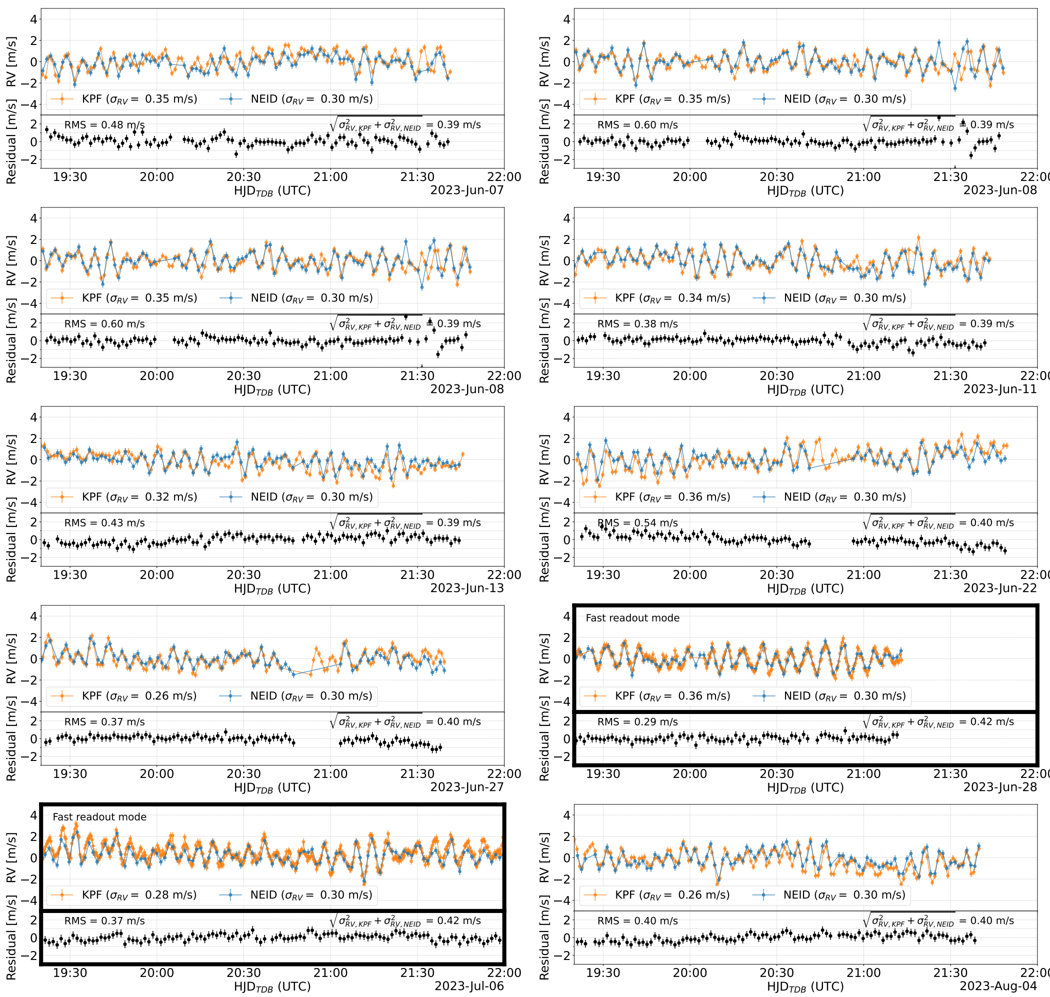

Figure 3.11: Solar RVs measured by KPF (corrected for drift) and NEID for a selection of days where both sites had clear weather conditions and a drift correction was possible for KPF using the simultaneous calibration. KPF data (orange points) on two of the days, June 28 and July 6, were taken in the fast readout mode (bolded frames), with the rest of the days taken in standard readout mode. The NEID RVs are shown in blue. The 5.5 minute solar p-mode oscillations are clearly observed by both instruments at the same amplitude and phase. The lower panel of each plot shows the residuals between a spline-interpolation of the KPF RVs, sampled at the NEID timestamps, and the NEID RVs. The residual RMS is comparable to the combined instrumental noise floor for most days; some days show a smaller RMS than the combined noise floor. On some days, such as June 22, the RVs disagree near UT 21:30. This is likely caused by additional instrumental drift in the KPF RVs due to liquid nitrogen fills around HST 11:00 (UT 21:00) not being fully removed by the simple drift model.

The fact that the "out-of-the-box" KPF RVs line up so well with the NEID RVs over daily timescales is extremely encouraging. Drift on these timescales for KPF is < 0.5 m s^{-1} hr^{-1}, so we expect similar levels of agreement on longer timescales once the day-to-day offsets between KPF wavelength solutions become sub-m s^{-1}. Future work expanding on the investigation conducted by Zhao et al. (2023b), who studied one month of overlap between solar RVs from HARPS, HARPS-N, EXPRES, and NEID, will be especially fruitful. Additionally, SoCal will observe the Sun for an additional 2–3 hours after the Sun has set in Arizona for EXPRES and NEID, meaning these five instruments will collect nearly 20 hours of continuous solar RVs in the summer months and $\sim$17 hours in the winter months. By cross-calibrating instruments using the overlapping windows of solar observations, longer-term variability like granulation will be better resolved. However, each instrument adopts a unique observing strategy. HARPS-N takes $\sim$5 min exposures to average over p-modes, EXPRES uses an adaptive exposure time to reach a fixed SNR threshold (typical exposures are around 3 min), and HARPS and NEID both use short fixed exposure times of 30 sec and 55 sec respectively. To compare RVs on longer timescales, these RVs must be binned to shared "exposure times" and timestamps, which introduces some uncertainty. The faster cadence of KPF (5 sec exposure and 15 sec readout) directly traces the p-mode oscillations, thus the KPF RVs can be binned to these shared exposure times and timestamps with less inherent error (Zhao et al., 2023b). Long term, the publicly available SoCal and NEID RVs will provide crucial benchmarks for understanding instrument performance and for isolating solar activity signals.

3.6 Conclusions and Future Work

We have developed, built, and installed the Solar Calibrator for KPF at W. M. Keck Observatory. SoCal makes use of proven, off-the-shelf components and is protected from extreme weather by a rugged motorized enclosure. Daily operations are performed autonomously with little-to-no human intervention required. We achieved first light on April 25, 2023 and have been observing the Sun almost daily since June 2023, accumulating over 19,000 solar spectra at the time of submitting this manuscript (October 18, 2023). SoCal obtains SNR $\sim$ 1200 solar spectra in a 5 sec exposure. When paired with KPF's fast readout mode we are able to record solar RV time series at 21 sec cadence with < 30 cm s^{-1} photon-limited precision. Long-term operations can further utilize KPF's high SNR capabilities to acquire spectra with SNR as high as ∼2400.

On short timescales, SoCal is demonstrating the EPRV capabilities of KPF extremely well. With no drift correction, binning over the p-mode oscillations reduces the RMS of observed solar RVs to just 20–30 cm s^{-1} on days with minimal instrumental drift and 67 cm s^{-1} across all days. We compared solar RVs from SoCal to those taken simultaneously with NEID and found excellent agreement within individual days; the residual RV between KPF and NEID was comparable to their combined photon-limited precision (∼40 cm s^{-1}).

Long-term performance validation still requires improvements to the KPF DRP, particularly the stability of daily wavelength solutions, but preliminary results are encouraging. SoCal has also enabled independent monitoring of instrumental drift and will become even more so once comparisons with NEID on longer timescales become possible. This has been especially valuable during times when the LFC was not working and the etalon lamp was degrading. SoCal data was also instrumental in discovering and diagnosing the CTI issue in the KPF detectors as well as exercising and improving the DRP throughout commissioning.

Continued monitoring of the Sun by EPRV facilities across the globe will not only allow for multi-instrument comparisons and calibrations (such as in Zhao et al. 2023b), but will also provide near-continuous solar monitoring which may help constrain granulation effects. Additionally, the Sun is currently increasing in activity towards solar maximum (Upton and Hathaway 2023 estimate the peak in fall 2024), making forthcoming cross-instrument studies especially opportune for probing the effects of active features such as spots/faculae/-plages on EPRV data. The fast cadence and high SNR of SoCal data allow for more precise binning over short-term oscillations enabling more effective comparisons to other instruments. Soon, the solar feed for MAROON-X will come online. As Gemini-N and WMKO share the same observing conditions (and the same Sun), comparisons between SoCal and MAROON-X solar data will be uniquely advantageous as the only variable is the instrument. Lastly, SoCal's geographic location fills a large gap in reaching continuous 24-hour coverage using the global network of solar feeds.

It will also be interesting to compare EPRV solar data with solar RVs obtained by dedicated asteroseismology observatories. There are two ground-based global networks of solar observatories performing 24/7 helioseismology, the Global Oscillation Network Group (GONG; Harvey et al., 1996) and the Birmingham Solar Oscillations Network (BiSON; Davies et al., 2014; Hale et al., 2016). These facilities use a single spectral line to measure solar RVs and have set the standard for measuring the oscillation frequencies of the Sun (Broomhall et al., 2009). The Stellar Oscillations Network Group (SONG; Grundahl et al., 2006) is a global network of 1 m telescopes with iodine-cell calibrated spectrographs designed to do asteroseismology with RVs on the nearest and brightest stars. A sun tracker was installed at the Hertzsprung SONG telescope at the Teide Observatory in 2017, which collected m s^{-1} quality RVs of the Sun at a blazing 4 sec cadence (0.5 sec exposure, 3.5 sec readout) for three months in 2018 (Fredslund Andersen, M. et al., 2019). Our interpretations of our solar EPRV datasets would benefit greatly from collaborations with the heliophysics community and detailed comparisons between our rich datasets.

SoCal data is publicly available on the Keck Observatory Archive. Future studies to develop new spectral activity indicators or activity-invariant RV extraction algorithms will be most fruitful on the high SNR, high cadence, and long-baseline solar time series that SoCal and other similar facilities are producing. Solar EPRV datasets are becoming ever more important not just for understanding, calibrating, and optimizing individual spectrograph performance, but also for paving the way to the data analysis tools needed to uncover exo-Earths in stellar EPRV time series.

Acknowledgements

We gratefully acknowledge the efforts and dedication of the Keck Observatory staff, particularly Maylyn Carvalho, Rick Johnston, Matt Barnett, Derek Park, Jerry Pascua, Steve Baca, Bobby Harrington III, Danny Baldwin, Randy Ching, Hamza Elwir, Ed Wetherell, Justin Ballard, Todd Von Boeckmann, Chris Martins, Daniel Orr, Max Brodheim, and Kyle Lanclos. We thank Gábor Kovács for designing the enclosure electronics and providing troubleshooting guidance, and Gaspar Bakos for helpful design discussions and for facilitating the acquisition of the enclosure. We thank Kodi Rider for helping to coordinate SoCal operations at SSL in Berkeley. We thank Bradford Holden and William Deich for designing the KPF data structures and helping with FITS/KTL keywords. We thank Andy Monson and Andrea Lin for useful discussions about the tracker assembly, and for providing detailed solid models of key components of the NEID Solar tracker assembly.

We extend our deepest gratitude to the Kahu Kū Mauna (Guardians of the Mountain), the Center for Maunakea Stewardship's Environmental Committee, and the Maunakea Management Board for their thoughtful review and approval of the SoCal project permit. The summit of Maunakea is a place of significant ecological, cultural, and spiritual importance within the indigenous Hawaiian community. We understand and embrace our accountability to Maunakea and the indigenous Hawaiian community, and commit to our role in long-term mutual stewardship.

R.A.R. acknowledges support from the National Science Foundation through the Graduate Research Fellowship Program (DGE 1745301). The Solar Calibrator was supported in part by the Heising-Simons Foundation through grant 2022-3931, the Simons Foundation grant "Planetary Context of Habitability and Exobiology," and the Suzanne & Walter Scott Foundation.

Some of the data presented herein were obtained at the W. M. Keck Observatory, which is operated as a scientific partnership among the California Institute of Technology, the University of California, and the National Aeronautics and Space Administration. The Observatory was made possible by the generous financial support of the W. M. Keck Foundation. This research has made use of the Keck Observatory Archive (KOA), which is operated by the W. M. Keck Observatory and the NASA Exoplanet Science Institute (NExScI), under contract with the National Aeronautics and Space Administration. The research was carried out, in part, at the Jet Propulsion Laboratory, California Institute of Technology, under a contract with the National Aeronautics and Space Administration (80NM0018D0004).

Chapter 4

A RETROGRADE, POLAR ORBIT FOR THE ULTRA-LOW-DENSITY, HOT SUPER-NEPTUNE WASP-107 B

Rubenzahl, R. A. et al. (Mar. 2021). "The TESS-Keck Survey. IV. A Retrograde, Polar Orbit for the Ultra-low-density, Hot Super-Neptune WASP-107b." In: *The Astronomical Journal* 161.3, 119, p. 119. DOI: 10.3847/1538-3881/abd177. arXiv: 2101.09371 [astro-ph.EP].

4.1 Introduction

WASP-107 b is a close-in (P = 5.72 days) super-Neptune orbiting the cool K-dwarf WASP-107. Originally discovered via the transit method by WASP-South, WASP-107 b was later observed by K2 in Campaign 10 (Howell et al., 2014). These transits revealed a radius close to that of Jupiter, $R_b = 10.8 \pm 0.34\ \mathrm{R}_\oplus = 0.96 \pm 0.03\ \mathrm{R}_{\mathrm{Jup}}$ (Dai and Winn, 2017; Močnik et al., 2017; Piaulet et al., 2021). However, follow-up radial velocity (RV) measurements with the CORALIE spectrograph demonstrated a mass of just $38 \pm 3\ \mathrm{M}_\oplus$ (Anderson et al., 2017), meaning this Jupiter-sized planet has just one-tenth its density. Higher-precision RVs from Keck/High Resolution Echelle Spectrometer (HIRES) suggested an even lower mass of $30.5 \pm 1.7\ \mathrm{M}_\oplus$ (Piaulet et al., 2021). This low density challenges the standard core-accretion model of planet formation. If runaway accretion brought WASP-107 b to a gas-to-core mass ratio of ~ 3 but was stopped prematurely before growing to gas giant size, orbital dynamics and/or migration may have played a significant role in this system (Piaulet et al., 2021). Alternatively WASP-107 b's radius may be inflated from tidal heating, which would allow a lower gas-to-core ratio consistent with core accretion (Millholland, Petigura, and Batygin, 2020).

With a low density, large radius, and hot equilibrium temperature, WASP-107 b's large atmospheric scale height makes it a prime target for atmospheric studies. Indeed analyses of transmission spectra obtained with the Hubble Space Telescope (HST)/WFC3 have detected water amongst a methane-depleted atmosphere (Kreidberg et al., 2018). WASP-107 b was the first exoplanet to be observed transiting with excess absorption at 10830 Å, an absorption line of a metastable state of neutral helium indicative of an escaping atmosphere (Oklopčić and Hirata, 2018). These observations suggest that WASP-107 b's atmosphere is photoevaporating at a rate of a few percent in mass per billion years (Spake et al., 2018; Allart et al., 2019; Kirk et al., 2020).

The orbit of WASP-107 b is suspected to be misaligned with the rotation axis of its host star. The angle between the star's rotation axis and the normal to the planet's orbital plane, called the stellar obliquity ψ (or just obliquity), was previously constrained by observations of WASP-107 b passing over starspots as it transited (Dai and Winn, 2017). As starspots are regions of reduced intensity on the stellar photosphere that rotate with the star, this is seen as a bump of increased brightness in the transit light curve. By measuring the time between spot-crossing events across successive transits, combined with the absence of repeated spot crossings, Dai and Winn (2017) were able to constrain the sky-projected obliquity, λ, of WASP-107 b to $\lambda \in$[40–140] deg. Intriguingly, long-baseline RV monitoring of the system with Keck/HIRES has revealed a distant ($P_c \sim 1100$ days) massive ($M \sin i_{\mathrm{orb,c}} = 115 \pm 13$ $\mathrm{M}_{\oplus}$) planetary companion, which may be responsible for this present day misaligned orbit through its gravitational influence on WASP-107 b (Piaulet et al., 2021).

The sky-projected obliquity can also be measured spectroscopically. The Rossiter–McLaughlin (RM) effect refers to the anomalous Doppler-shift caused by a transiting planet blocking the projected rotational velocities across the stellar disk (McLaughlin, 1924; Rossiter, 1924). If the planet's orbit is aligned with the rotation of the star (prograde), its transit will cause an anomalous redshift followed by an anomalous blueshift. A anti-aligned (retrograde) orbit will cause the opposite to occur.

Following the first obliquity measurement by Queloz et al. (2000), the field saw measurements of 10 exoplanet obliquities over the next 8 years that were all consistent with aligned, prograde orbits. After a few misaligned systems had been discovered (e.g., Hébrard et al., 2008), a pattern emerged with hot Jupiters on highly misaligned orbits around stars hotter than about 6250 K (Winn et al., 2010a). This pattern elicited several hypotheses such as damping of inclination by the convective envelope of cooler stars (Winn et al., 2010a) or magnetic realignment of orbits during the T Tauri phase (Spalding and Batygin, 2015).

More recently a number of exoplanets have been found on misaligned orbits around cooler stars, such as the hot Jupiter WASP-8b (Queloz et al., 2010; Bourrier et al., 2017), as well as lower-mass hot Neptunes like HAT-P-11b (Winn et al., 2010b), Kepler-63b (Sanchis-Ojeda et al., 2013a), HAT-P-18b (Esposito, M. et al., 2014), GJ 436b (Bourrier et al., 2018), and HD 3167 c (Dalal et al., 2019). Strikingly, all of these exoplanets are on or near polar orbits. Some of these systems have recently had distant, giant companions detected (e.g. HAT-P-11c; Yee et al., 2018), hinting that these obliquities arise from multibody planet-planet dynamics.

In this paper we present a determination of the obliquity of WASP-107 b from observations of the RM effect (Section 4.2). These observations were acquired under the TESS–Keck Survey (TKS), a collaboration between scientists at the University of California, the California Institute of Technology, the University of Hawai‘i, and NASA. TKS is organized through the California Planet Search with the goal of acquiring substantial RV follow-up observations of planetary systems discovered by TESS (Dalba et al., 2020). TESS observed four transits of WASP-107 b (TOI 1905) in Sector 10. An additional science goal of TKS is to measure the obliquities of interesting TESS systems. WASP-107 b, which is already expected to have a significant obliquity (Dai and Winn, 2017), is an excellent target for an RM measurement with HIRES.

In Section 4.3 we confirm a misaligned orientation; in fact, we found a polar/retrograde orbit. This adds WASP-107 b to the growing population of hot Neptunes in polar orbits around cool stars. We explored possible mechanisms that could be responsible for this misalignment in Section 4.4. Lastly in Section 4.5 we summarized our findings and discussed the future work needed to better understand the obliquity distribution for small planets around cool stars.

4.2 Observations

We observed the RM effect for WASP-107 b during a transit on 2020 February 26 (UTC) with HIRES (Vogt et al., 1994) on the Keck I Telescope on Maunakea. Our HIRES observations covered the full transit duration ($\sim$ 2.7 hr) with a $\sim$ 1 hour baseline on either side. We used the “C2” decker ($14'' \times 0.''861$, $R = 45,000$) and integrated until the exposure meter reached 60,000 counts (signal-to-noise ratio (S/N) $\sim$ 100 per reduced pixel, $\lesssim$ 15 minutes) or readout

Table 4.1: Radial Velocities of WASP-107

Time $\mathrm{BJD_{TDB}}$	RV m $\mathrm{s^{-1}}$	σ_{RV} m $\mathrm{s^{-1}}$	Exposure time sec
2458905.90111	5.05	1.50	900
2458905.91189	6.43	1.42	883
2458905.92247	0.14	1.49	862
2458905.93288	-1.35	1.65	844
2458905.94266	-0.25	1.45	783
⋮	⋮	⋮	⋮

A machine readable version of the full table is available on the online published version (Rubenzahl et al., 2021).

Table 4.2: Adopted parameters of the WASP-107 System

Parameter	Value	Unit	Source
P_b	5.7214742	days	1
t_c	7584.329897 ± 0.000032	JD[a]	1
b	0.07 ± 0.07		1
$i_{\mathrm{orb},b}$	$89.887^{+0.074}_{-0.097}$	degrees	1
$R_p/R_\star$	0.14434 ± 0.00018		1
$a/R_\star$	18.164 ± 0.037		1
e_b	0.06 ± 0.04		2
ω_b	40^{+40}_{-60}	degrees	2
M_b	30.5 ± 1.7	$\mathrm{M_\oplus}$	2
P_c	1088^{+15}_{-16}	days	2
e_c	0.28 ± 0.07		2
ω_c	-120^{+30}_{-20}	degrees	2
$M_c \sin i_{\mathrm{orb},c}$	0.36 ± 0.04	M_J	2
T_{eff}	4245 ± 70	K	2
M_*	$0.683^{+0.017}_{-0.016}$	$\mathrm{M_\odot}$	2
R_*	0.67 ± 0.02	$\mathrm{R_\odot}$	2
u_1	0.6666 ± 0.0062		1
u_2	0.0150 ± 0.0110		1

[a]Days since JD 2,450,000. Sources: (1) Dai and Winn (2017); (2) Piaulet et al. (2021).

after 15 minutes. The spectra were reduced using the standard procedures of the California Planet Search (Howard et al., 2010a), with the iodine cell serving as the wavelength reference (Butler et al., 1996). In total we obtained 22 RVs, 12 of which were in transit (Table 4.1).

Visually inspecting the observations (Fig. 4.1) shows an anomalous blueshift following the transit ingress, followed by an anomalous redshift after the transit midpoint,[1], indicating a retrograde orbit. The asymmetry and low-amplitude of the signal constrain the orientation to a near-polar alignment, but whether the orbit is polar or anti-aligned is somewhat degenerate with the value of $v \sin i_\star$. The expected RM amplitude is $v \sin i_\star (R_p/R_\star)^2 \sim 40$ m s^{-1}, using previous estimates of $R_p/R_\star = 0.144$ (Dai and Winn, 2017) and $v \sin i_\star \sim 2$ km s^{-1} (e.g., Anderson et al., 2017). The signal we detected with HIRES is only ~ 5.5 m s^{-1} in amplitude. Dai and Winn (2017) found the transit impact parameter to be nearly zero, therefore the small RM amplitude suggests either a much lower $v \sin i_\star$ than was spectroscopically inferred (see Section 4.3), a near-polar orbit, or both.

4.3 Analysis

Rossiter–McLaughlin Model

We used a Gaussian likelihood for the RV time series ($\boldsymbol{t}$, $\boldsymbol{v}_r$) given the model parameters $\boldsymbol{\Theta}$, and included a RV jitter term (σ_j) to account for additional astrophysical or instrumental noise,

$$p(\boldsymbol{v}_r,\, \boldsymbol{t}|\boldsymbol{\Theta}) = \prod_{i=1}^{N} \frac{1}{\sqrt{2\pi\sigma^2}} \exp\left[-\frac{(v_{r,i} - f(t_i,\, \boldsymbol{\Theta}))^2}{2\sigma_i^2}\right], \tag{4.1}$$

where $\sigma_i^2 = \sigma_{\mathrm{RV,i}}^2 + \sigma_j^2$. The model $f(t_i,\, \boldsymbol{\Theta})$ is given by

$$f(t_i,\, \boldsymbol{\Theta}) = \mathrm{RM}(t_i,\, \boldsymbol{\theta}) + \gamma + \dot{\gamma}(t_i - t_0), \tag{4.2}$$

where $\boldsymbol{\Theta} = (\boldsymbol{\theta},\, \gamma,\, \dot{\gamma})$ is the RM model parameters ($\boldsymbol{\theta}$) as well as an offset (γ) and slope ($\dot{\gamma}$) term which we added to approximate the reflex motion of the star and model any other systematic shift in RV throughout the transit (e.g., from noncrossed spots). The reference time t_0 is the time of the first observation (BJD).

$\mathrm{RM}(t_i,\, \boldsymbol{\theta})$ is the RM model described in Hirano et al. (2011). We assumed zero stellar differential rotation and adopted the transit parameters determined by Dai and Winn, 2017, which came from a detailed analysis of K2 short-cadence photometry. We performed a simultaneous fit to the photometric and spectroscopic transit data using the same photometric data from K2 as in Dai and Winn (2017) to check for consistency. We obtained identical results for the transit parameters as they did, hence we opted to simply adopt their values,

[1]Propagating the uncertainty in t_c in Table 4.2 the transit midpoint on the night of observation is uncertain to about 9 s.

including their quadratic limb-darkening model. These transit parameters are all listed in Table 4.2. Our best-fit RV jitter is $\sigma_j = 2.61^{+0.64}_{-0.51}$ m s^{-1}, smaller than the jitter from the Keplerian fit to the full RV sample of $3.9^{+0.5}_{-0.4}$ m s^{-1} (Piaulet et al., 2021). This is expected as the RM sequence covers a much shorter time baseline as compared to the full RV baseline, and as a result is only contaminated by short-term stellar noise sources such as granulation and convection.

The free parameters in the RM model are the sky-projected obliquity (λ), stellar inclination angle ($i_\star$), and projected rotational velocity ($v \sin i_\star$). To first order, the impact parameter b and sky-projected obliquity λ determine the shape of the RM signal, while $v \sin i_\star$ and $R_p/R_\star$ set the amplitude. We adopted the parameterization ($\sqrt{v \sin i_\star} \cos\lambda$, $\sqrt{v \sin i_\star} \sin\lambda$) to improve the sampling efficiency and convergence of the Markov Chain Monte Carlo (MCMC). A higher order effect that becomes important when the RM amplitude is small is the convective blueshift, which we denote v_{cb} (see Section 4.3 for more details). There are thus seven free parameters in our model: $\sqrt{v \sin i_\star} \cos\lambda$, $\sqrt{v \sin i_\star} \sin\lambda$, $\cos i_\star$, $\log(|v_{cb}|)$, γ, $\dot{\gamma}$, and σ_j. We placed a uniform hard-bounded prior on $v \sin i_\star \in [0, 5]$ km s^{-1} and on $\cos i_\star \in [0, 1]$, and used a Jeffrey's prior for σ_j. All other parameters were assigned uniform priors.

Micro/Macroturbulence Parameters

The shape of the RM curve is also affected by processes on the surface of the star that broaden spectral lines, which affect the inferred RVs. In the Hirano et al. (2011) model, these processes are parameterized by $\gamma_{\rm lw}$, the intrinsic line width, ζ, the line width due to macroturbulence, given by the Valenti and Fischer (2005) scaling relation

$$\zeta = \left(3.98 + \frac{T_{\rm eff} - 5770\ {\rm K}}{650\ {\rm K}}\right)\ {\rm km\ s^{-1}}, \tag{4.3}$$

and β, given by

$$\beta = \sqrt{\frac{2k_B T_{\rm eff}}{\mu} + \xi^2 + \beta_{\rm IP}}, \tag{4.4}$$

where ξ is the dispersion due to microturbulence and $\beta_{\rm IP}$ is the Gaussian dispersion due to the instrument profile, which we set to the HIRES line-spread function (LSF) (2.2 km s^{-1}). We tested having $\gamma_{\rm lw}$, ξ, and ζ as free parameters in the model (with uniform priors) but only recovered the prior distributions for these parameters. Moreover we saw no change in the resulting posterior distribution for λ or $v \sin i_\star$. Because of this, we opted to instead adopt fixed nominal values of $\xi = 0.7$ km s^{-1}, $\gamma_{\mathrm{lw}} = 1$ km s^{-1}, and $\zeta = 1.63$ km s^{-1} (from Eq. 4.3 using T_{eff} from Table 4.2).

Convective blueshift

Convection in the stellar photosphere, caused by hotter bubbles of gas rising to the stellar surface and cooler gas sinking, results in a net blueshift across the stellar disk. This is because the rising (blueshifted) gas is hotter, and therefore brighter, than the cooler sinking (redshifted) gas. Since this net-blueshifted signal is directed at an angle normal to the stellar surface, the radial component seen by the observer is different in amplitude near the limb of the star compared to the center of the stellar disk, according to the stellar limb-darkening profile. Thus the magnitude of the convective blueshift blocked by the planet varies over the duration of the transit. The amplitude of this effect is ~ 2 m s^{-1}, which is significant given the small amplitude of the RM signal we observe for WASP-107 b (~ 5.5 m s^{-1}).

For this reason we included the prescription of Shporer and Brown, 2011 in the RM model, which is parameterized by the magnitude of the convective blueshift integrated over the stellar disk (v_{cb}). This quantity is negative by convention. Since the possible value of v_{cb} could cover several orders of magnitude, we fit for $\log(|v_{cb}|)$ and set a uniform prior between -1 and 3. While we found that including v_{cb} has no effect on the recovered λ and $v \sin i_\star$ posteriors, we are able to rule out $|v_{cb}| > 450$ m s^{-1} at 99% confidence, and > 250 m s^{-1} at 95% confidence.

Evidence for a Retrograde/Polar Orbit

We first found the maximum a posteriori (MAP) solution by minimizing the negative log-posterior using Powell's method (Powell, 1964) as implemented in `scipy.optimize.minimize` (Virtanen et al., 2020). The MAP solution was then used to initialize an MCMC. We ran 8 parallel ensembles each consisting of 32 walkers for 10,000 steps using the python package `emcee` (Foreman-Mackey et al., 2013). We checked for convergence by requiring that both the Gelman–Rubin statistic (G–R; Gelman et al., 2003) was < 1.001 across the ensembles (Ford, 2006) and the autocorrelation time was < 50 times the length of the chains (Foreman-Mackey et al., 2013).

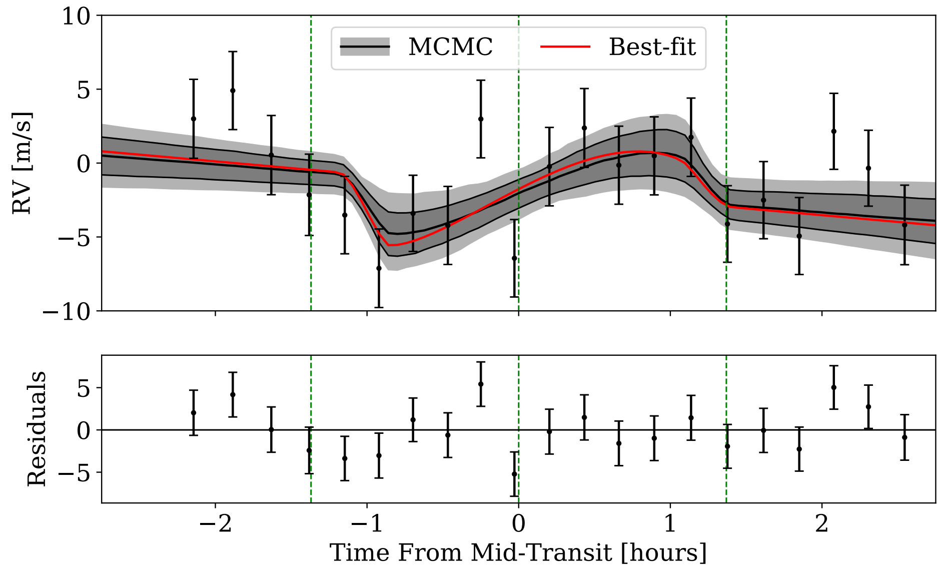

Figure 4.1: The RM effect for WASP-107 b. The dark shaded bands show the 16th–84th (black) and 5th–95th (gray) percentiles from the posterior distribution of the modeled RV. The red best-fit line is the maximum a-posteriori (MAP) model. The three vertical dashed lines denote, in chronological order, the times of transit ingress, midpoint, and egress. The residuals show the data minus the best-fit model. Data points are drawn with the measurement errors and the best-fit jitter added in quadrature.

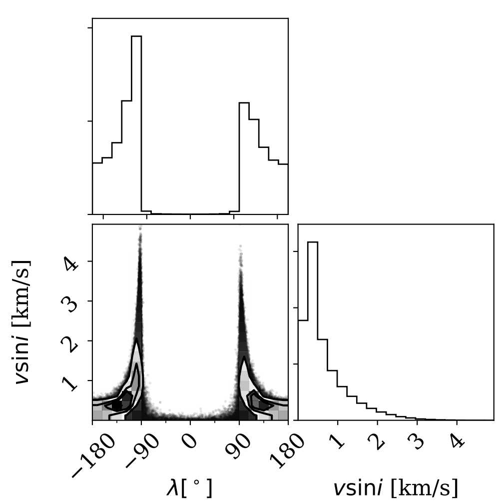

Figure 4.2: Posterior distribution for λ and $v \sin i_\star$. Although a more anti-aligned configuration is consistent with the data if $v \sin i_\star$ is small, the most likely orientations are close to polar. A prograde orbit ($|\lambda| < 90°$) is strongly ruled out.

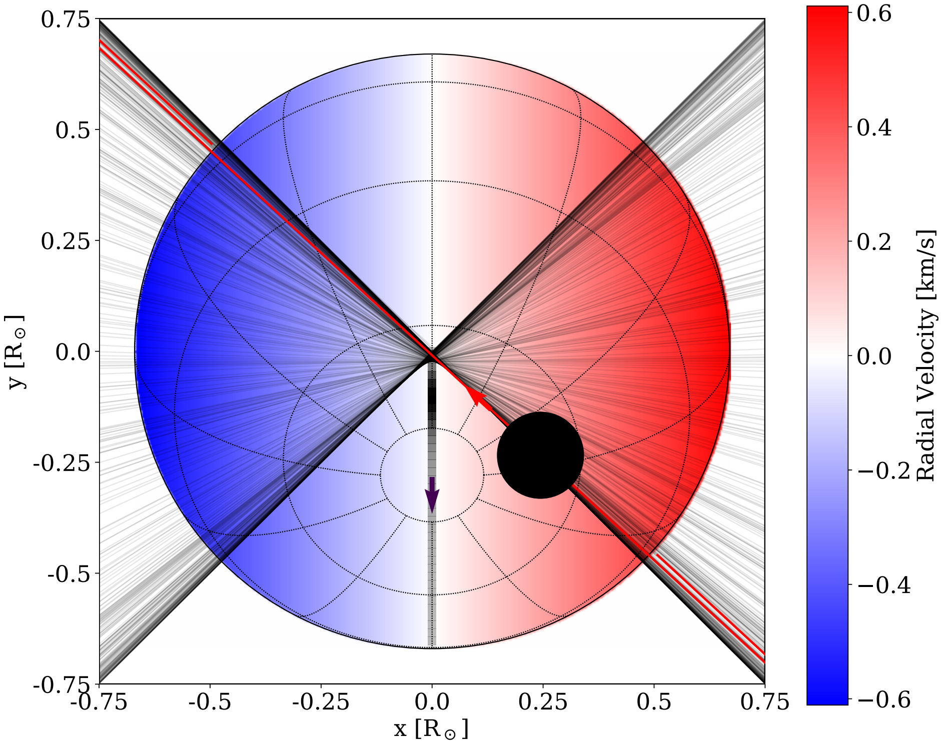

Figure 4.3: Sky-projected orbital configuration of WASP-107 b's orbit relative to the stellar rotation axis. The black lines correspond to posterior draws while the red line is the MAP orbit from Fig. 4.1. The direction of WASP-107 b's orbit is denoted by the red arrow. The stellar rotation axis (black arrow) and lines of stellar latitude and longitude are drawn for an inclination of $i_\star = 25°$. The posterior for $i_\star$ is illustrated by the shaded gray strip with a transparency proportional to the probability.

The MAP values and central 68% confidence intervals (CI) computed from the MCMC chains are tabulated in Table 4.3, and the full posteriors for λ and $v \sin i_\star$ are shown in Fig. 4.2. A prograde ($|\lambda| < 90°$) orbit is ruled out at $> 99\%$ confidence. An anti-aligned ($135° < \lambda < 225°$) orbit is allowed if $v \sin i_\star$ is small (0.26 ± 0.10 km s^{-1}), although a more polar aligned (but still retrograde) orbit with $90° < |\lambda| < 135°$ is more likely (if $v \sin i_\star \in [0.22, 2.09]$ km s^{-1}, 90% CI). The true obliquity ψ will always be closer to a polar orientation than λ, since λ represents the minimum obliquity in the case where the star is viewed edge-on ($i_\star = 90°$). While an equatorial orbit that transits requires $i_\star \sim 90°$, a polar orbit may be seen to transit for any stellar inclination.

To confirm that the signal we detected was not driven by correlated noise structures in the data, we performed a test using the cyclical residual permutation technique. We first calculated the residuals from the MAP fit to the

Table 4.3: WASP-107 b Rossiter–McLaughlin Parameters

Parameter	MCMC CI	MAP value	Unit
Model Parameters			
$\sqrt{v \sin i_\star} \cos\lambda$	$-0.309^{+0.150}_{-0.154}$	-0.30	[a]
$\sqrt{v \sin i_\star} \sin\lambda$	$-0.126^{+0.808}_{-0.771}$	-0.72	[a]
$\cos i_s$	$-0.003^{+0.682}_{-0.681}$	-0.56	
γ	$0.80^{+1.36}_{-1.38}$	0.97	m s^{-1}
$\dot{\gamma}$	$-20.83^{+11.05}_{-10.94}$	-21.85	m s^{-2}
$\sigma_{\rm jit}$	$2.61^{+0.64}_{-0.51}$	2.20	m s^{-1}
$\log(\lvert v_{cb}\rvert)$	$0.89^{+1.18}_{-1.27}$	2.17	[a]
Derived Parameters			
$\lvert\lambda\rvert$	$118.1^{+37.8}_{-19.1}$	112.63	degrees
$v \sin i_\star$	$0.45^{+0.72}_{-0.23}$	0.61	km s^{-1}
v_{cb}	$-7.74^{+7.33}_{-109.71}$	-149.41	m s^{-1}
$i_\star$	$28.17^{+40.38}_{-20.04}$	7.06	degrees
$\lvert\psi\rvert$	$109.81^{+28.17}_{-13.64}$	92.60	degrees

[a] $v \sin i_\star$ is in km s^{-1} and v_{cb} is in m s^{-1}.

original RV time series. We then shifted these residuals forward in time by one data point, wrapping at the boundaries, and added these new residuals back to the MAP model. This new "fake" dataset was then fit again and the process was repeated N times where $N = 22$ is the number of data points in our RV time series. This technique preserves the red noise component, and permuting multiple times generates datasets that have the same temporal correlation but different realizations of the data. If we assume that the signal we detected is caused by a correlated noise structure, then we would expect to see the detected signal vanish or otherwise become significantly weaker across each permutation as that noise structure becomes asynchronous with the transit ephemeris. We found that the signal is robustly detected at all permutations, with and without including the convective blueshift (fixed to the original MAP value). The MAP estimate for λ tended to be closer to polar across the permutations compared as to the original fit, which is consistent with the posterior distribution estimated from the MCMC, but did not vary significantly. While this method is not appropriate for estimating parameter uncertainties (Cubillos et al., 2017), we conclude that our results are not qualitatively affected by correlated noise in our RV time series.

Spot-crossing events can also affect the RM curve since the planet would block a different amount of red/blueshifted light. Out of the nine transits observed by Dai and Winn (2017), a single spot-crossing event was seen in only three of the transits. Hence there is roughly a one in three chance that the transit we observed contained a spot-crossing event. As we did not obtain simultaneous high-cadence photometry, we do not know if or when such an event occurred. Judging from the durations (~ 30 min) of the spot crossings observed by Dai and Winn (2017), this would only affect one or maybe two of our 15-minute exposures. While we don't see any significant outliers in our dataset, these spots were only $\sim 10\%$ changes on a $\sim 2\%$ transit depth, amounting to an overall spot depth of $\sim 0.2\%$. Given our estimate of $v \sin i_\star \sim 0.5$ km s^{-1} this suggests a spot-crossing event would produce a ~ 1 m s^{-1} RV anomaly, small compared to our measurement uncertainties (~ 1.5 m s^{-1}) and the estimated stellar jitter (~ 2.6 m s^{-1}). In other words, there is a roughly 33% chance that a spot-crossing event introduced an additional 0.5σ error on a single data point. If there were multiple spot-crossing events this anomaly would vary across the transit similar to other stellar-activity processes. In practice this introduces a correlated noise structure in the RV time series which our cyclical residual permutation test demonstrated is not significantly influencing our measurement of the obliquity or other model parameters. From this semi-analytic analysis we conclude that spot crossings are not a leading source of uncertainty in our model.

Constraints on the Stellar Inclination

Given a constraint on $v \sin i_\star$ and v, we can constrain the stellar inclination $i_\star$. Previous studies have found a range of estimates for the $v \sin i_\star$ of WASP-107. Anderson et al., 2017 found a value of 2.5 ± 0.8 km s^{-1}, whereas John Brewer (private communication) obtained a value of 1.5 ± 0.5 km s^{-1} using the automated spectral synthesis modeling procedure described in Brewer et al. (2016). We note that the Specmatch-Emp (Yee, Petigura, and von Braun, 2017) result for our HIRES spectrum only yields an upper bound for $v \sin i_\star$ of < 2 km s^{-1}, as this technique is limited by the HIRES PSF. All three of these methods derive $v \sin i_\star$ by modeling the amount of line broadening present in the stellar spectrum, which in part comes from the stellar rotation. However these estimates may be biased from other sources of broadening which are not as well constrained in these models. Our RM analysis on the other hand incorporates a direct measurement of $v \sin i_\star$ by observing how much of the projected stellar rotational velocity is blocked by the transiting planet's

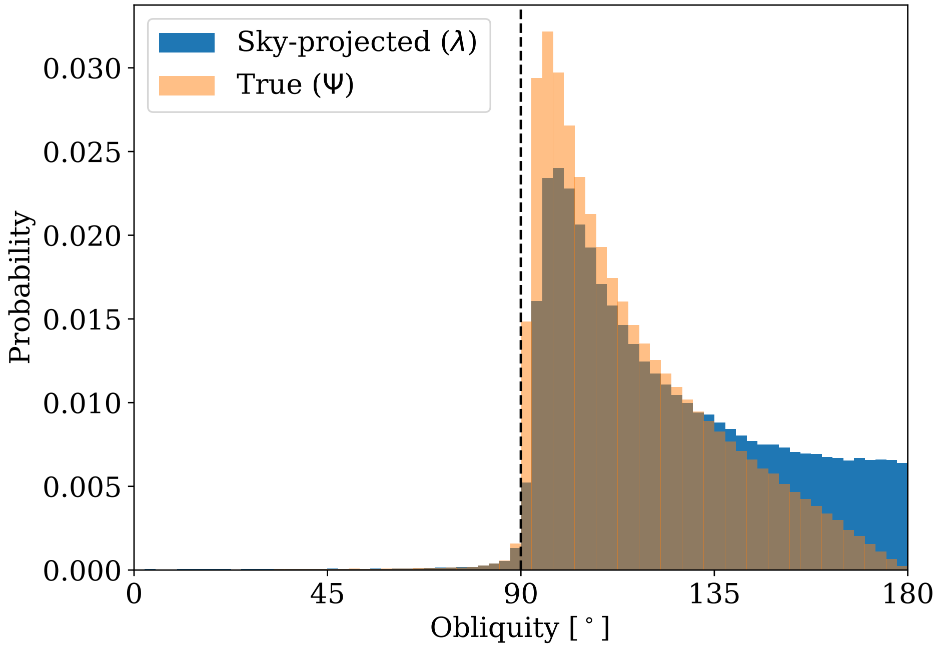

Figure 4.4: Obliquity of WASP-107 b. The true obliquity ψ is calculated using the constraints on the stellar inclination as inferred from the $v \sin i_\star$ posterior (Section 4.3).

shadow. Our RM analysis found $v \sin i_\star = 0.45^{+0.72}_{-0.23}$ km s^{-1}, lower than the spectroscopic estimates. We adopted this posterior for $v \sin i_\star$ to keep internal consistency.

The rotation period of WASP-107 has been estimated to be 17 ± 1 days from photometric modulations due to starspots rotating in and out of view (Anderson et al., 2017; Dai and Winn, 2017; Močnik et al., 2017). We combined this rotation period with the stellar radius of 0.67 ± 0.02 $R_\odot$ inferred from the HIRES spectrum (Piaulet et al., 2021) using Specmatch-Emp (Yee, Petigura, and von Braun, 2017) to constrain the tangential rotational velocity $v = 2\pi R_\star / P_{\rm rot}$. We then used the statistically correct procedure described by Masuda and Winn, 2020 and performed an MCMC sampling of v and $\cos i_\star$, using uniform priors for each, and using the posterior distribution for $v \sin i_\star$ obtained in the RM analysis as a constraint. Sampling both variables simultaneously correctly incorporates the nonindependence of v and $\cos i_\star$, since $v \leq v \sin i_\star$. We found that $i_\star = 25.8^{+22.5}_{-15.4}$ degrees (MAP value 7.1°), implying a viewing geometry of close to pole-on for the star. Thus any transiting configuration will necessarily imply a near-polar orbit, even for orbital solutions with λ near 180° (see Fig. 4.3). It is worth mentioning that one of the three spot-crossing events observed by Dai and Winn (2017) occurred near the transit midpoint. This small stellar inclination implies that this spot must be at a relatively high latitude ($90° - i_\star$) compared to that of our Sun, which has nearly all of its sunspots contained within $\pm 30°$ latitude.

Knowledge of the stellar inclination $i_\star$, the orbital inclination $i_{\rm orb}$, and the sky-projected obliquity λ allows one to compute the true obliquity ψ, as these four angles are related by

$$\cos\psi = \cos i_{\rm orb}\cos i_\star + \sin i_{\rm orb}\sin i_\star \cos\lambda. \tag{4.5}$$

The resulting posterior distribution for the true obliquity ψ is shown in Fig. 4.4. As expected, the true orbit is constrained to a more polar orientation than is implied by the wide posteriors on λ, due to the nearly pole-on viewing geometry of the star itself.

4.4 Dynamical History

How did WASP-107 b end up in a slightly retrograde, nearly polar orbit? To explore this question, we examined the orbital dynamics of the WASP-107 system considering the new discovery of a distant, giant companion WASP-107c (Piaulet et al., 2021). As in Mardling, 2010, Yee et al., 2018, and Xuan and Wyatt, 2020, we can understand the evolution of the WASP-107 system by examining the secular three-body Hamiltonian. Assuming the inner planet is a test particle (i.e., $M_b\sqrt{a_b} \ll M_c\sqrt{a_c}$), and since $a_b/a_c \ll 1$, we can approximate the Hamiltonian by expanding to quadrupole order in semimajor axis ratio

$$\begin{aligned}\mathcal{H} \;=\; & \frac{1}{16} n_b \frac{M_c}{M_\star}\left(\frac{a_b}{a_c\sqrt{1-e_c^2}}\right)^3 \left[\frac{(5-3G_b^2)(3H_b^2-G_b^2)}{G_b^2}\right. \\ & \left. + \frac{15(1-G_b^2)(G_b^2-H_b^2)\cos(2g_b)}{G_b^2}\right] + \frac{GM_\star}{a_b c^2}\frac{3n_b}{G_b},\end{aligned} \tag{4.6}$$

where the last term is the addition from general relativity (GR) and $n_b = 2\pi/P_b$. The quantities G and H are the canonical Delaunay variables

$$\begin{aligned} G_b &= \sqrt{1-e_b^2} && \leftrightarrow\; g_b = \omega_b, \\ H_b &= G\cos i_b && \leftrightarrow\; h_b = \Omega_b, \end{aligned} \tag{4.7}$$

where the double-arrow ($\leftrightarrow$) symbolizes conjugate variables, ω_b is the argument of perihelion of the inner planet, Ω_b is the longitude of ascending node of

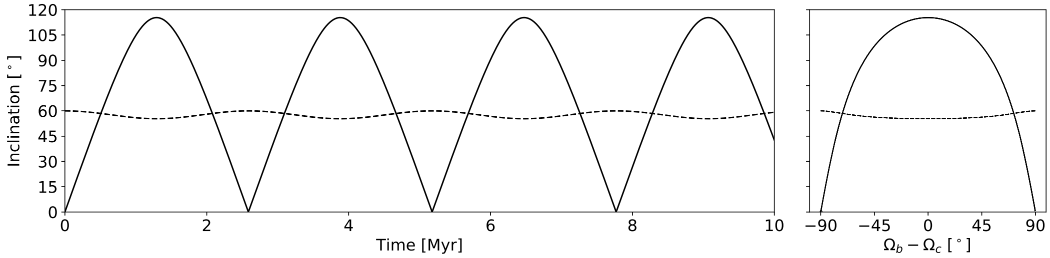

Figure 4.5: Evolution of WASP-107 b's true obliquity (ψ_b, solid line) throughout the the N-body simulation using the system parameters given in Table 4.2. The outer planet has $M_c = M \sin i_{\mathrm{orb},c}$ and was initialized with an obliquity of $\psi_c = 60°$ (dashed line). The obliquity of planet b oscillates between $\psi_c \pm \psi_c$ every $\sim$ 2.5 Myr due to nodal precession. If $\sin i_{\mathrm{orb},c} < 1$ then the larger M_c simply produces a shorter nodal precession timescale. The right panel shows the evolution of the inclinations with the difference in the longitudes of ascending node.

the inner planet, and i_b is the inclination of the inner planet with respect to the invariant plane. The invariant plane is the plane normal to the total angular momentum bmtor, which to good approximation is simply the orbital plane of the outer planet (since angular momentum is $\propto Ma^{1/2}$). With this approximation, i_b is the relative inclination between the two planets.

Kozai–Lidov oscillations

Since the Hamiltonian $\mathcal{H}$ does not depend on h_b, the quantity $H_b = \sqrt{1-e_b^2}\cos i_b$ is conserved. This leads to a periodic exchange of e_b and i_b, so long as the outer planet has an inclination greater than a critical value of $\sim 39.2°$ (Kozai, 1962; Lidov, 1962). These Kozai–Lidov cycles also require a slowly changing argument of perihelion, which may precess due to GR as is famously seen in the orbit of Mercury. This precession can suppress Kozai–Lidov cycles if fast enough, as is the case for HAT-P-11 and π Men (Xuan and Wyatt, 2020; Yee et al., 2018). The precession rate from GR is given by

$$\dot{\omega}_{GR} = \frac{GM_\star}{a_b c^2}\frac{3n_b}{G_b^2}, \tag{4.8}$$

which has an associated timescale of $\tau_{GR} = 2\pi/\dot{\omega} \approx 42,500$ years for WASP-107 b. The Kozai timescale (Kiseleva, Eggleton, and Mikkola, 1998) is

$$\tau_{\mathrm{Kozai}} = \frac{2P_c^2}{3\pi P_b^2}\frac{M_\star}{M_c}(1-e_c^2)^{3/2} \approx 210,000 \text{ yr}, \tag{4.9}$$

five times longer. The condition for Kozai–Lidov cycles to be suppressed by relativistic precession is $\tau_{\mathrm{Kozai}}\dot{\omega}_{\mathrm{GR}} > 3$ (Fabrycky and Tremaine, 2007), which the MAP minimum mass and orbital parameters WASP-107c satisfy. This is nicely visualized in Figure 6 of Piaulet et al. (submitted), which shows the full posterior distributions of $\tau_{\rm Kozai}$ and $\tau_{\rm GR}$. While the true mass of WASP-107c is likely to be larger than the derived $M \sin i_{\rm orb,c}$, it would need to be ~ 10 times larger for Kozai–Lidov oscillations to occur. This would imply a near face-on orbit of at most $i_{\rm orb,c} < 5.5°$. Such a face-on orbit is unlikely but is still plausible if it is aligned with the rotation axis of the star, given our constraints on the stellar inclination angle in Section 4.3.

Nodal precession

An alternative explanation for the high obliquity of WASP-107 b is nodal precession, as was proposed for HAT-P-11b (Yee et al., 2018) and for π Men c (Xuan and Wyatt, 2020). In this scenario the outer planet must have an obliquity greater than half that of the inner planet, which in this case would require $\psi_{\rm c} \sim 55°$. Then the longitude of ascending node Ω_b evolves in a secular manner according to Yee et al. (2018),

$$\frac{d\Omega_b}{dt} = \frac{\partial \mathcal{H}}{\partial H_b} = \frac{n_b}{8}\frac{M_c}{M_\star}\left(\frac{a_b}{a_c\sqrt{1-e_c^2}}\right)^3 \left(\frac{15-9G_b^2}{G_b^2}\right) H_b. \tag{4.10}$$

The associated timescale $\tau_{\Omega_b} = 2\pi/\dot{\Omega}_b$ is only about 2 Myr, much shorter than the age of the system. Yee et al. (2018) pointed out that such a precession will cause the relative inclination of the two planets to oscillate between $\approx \psi_c \pm \psi_c$. Thus at certain times the observer may see a highly misaligned orbit ($\psi_b \sim 2\psi_c$) for the inner planet, while at other times the observer may see an aligned orbit ($\psi_b = 0$).

We examined this effect by running a 3D N-body simulation in `REBOUND` (Rein and Liu, 2012). We initialized planet c with an obliquity of 60° (which sets the maximum obliquity planet b can obtain, $\sim 2\psi_c = 120°$) and planet b with an obliquity of 0° (aligned, prograde orbit). We included the effects of GR and tides using the `gr` and `modify_orbits_forces` features of `REBOUNDx` (Kostov et al., 2016; Tamayo et al., 2019) and used the the WHFast integrator (Rein and Tamayo, 2015) to evolve the system forward in time for 10 Myr.

Fig. 4.5 shows that over these 10 Myr ψ_b oscillates in the range 0°–120° due to the precession of Ω_b. Thus nodal precession can easily produce high relative inclinations, despite Kozai–Lidov oscillations being suppressed by GR. A configuration like what is observed today in which the inner planet is misaligned on a polar, yet slightly retrograde orbit is attainable at times during this cycle where the mutual inclination is at or near its maximum. The obliquity is $\gtrsim 80\%$ the amplitude from nodal precession ($\sim 2\psi_c$) approximately one-third of the time (bottom panel in Fig. 4.6). Therefore, even though the observed obliquity depends on when during the nodal precession cycle the system is observed, there is a decent chance of observing ψ_b near its maximum.

In the simulation we ran, WASP-107 b is only seen by an observer to be in a transiting geometry about 2.8% of the time. Xuan and Wyatt (2020) did a more detailed calculating accounting for the measured mutual inclination and found that the dynamical transit probability for π Men c and HAT-P-11b is of order 10-20%. However, as Xuan and Wyatt (2020) point out, this does not affect the population-level transit likelihood since the overall orientations of extrasolar systems can still be treated as isotropic. It merely suggests that a system with a transiting distant giant planet may be harboring a nodally precessing inner planet that just currently happens to be nontransiting.

Both Kozai–Lidov and nodal precession require a large mutual inclination in order for the inner planet to reach polar orientations. The origin of this large mutual inclination may be hidden in the planet's formation history, or perhaps was caused by a planet-planet scattering event with an additional companion that was ejected from the system. This could also explain the moderately eccentric orbit of WASP-107c (Piaulet et al., 2021). Indeed a significant mutual inclination is observed for the inner and outer planets of the HAT-P-11 and π Men systems (Xuan and Wyatt, 2020), although the inner planet in π Men is only slightly misaligned with $\lambda = 24 \pm 4.1$ degrees (Kunovac Hodžić et al., 2021), while HAT-P-11b has $\lambda = 103^{+26}_{-10}$ degrees (Winn et al., 2010b).

As more close-in Neptunes with distant giant companions are discovered, the distribution of observed obliquities for the inner planet will help determine if we are indeed simply seeing many systems undergoing nodal precession but at different times during the precession cycle. If so, we might observe a sky-projected obliquity distribution that resembles the bottom panel of Fig. 4.6. However, we may instead be observing two classes of close-in Neptunes: ones aligned with their host stars and ones in polar or near-polar orbits (see the top panel of Fig. 4.6). This suggests an alternative mechanism that favors either polar orbits or aligned orbits depending on the system architecture.

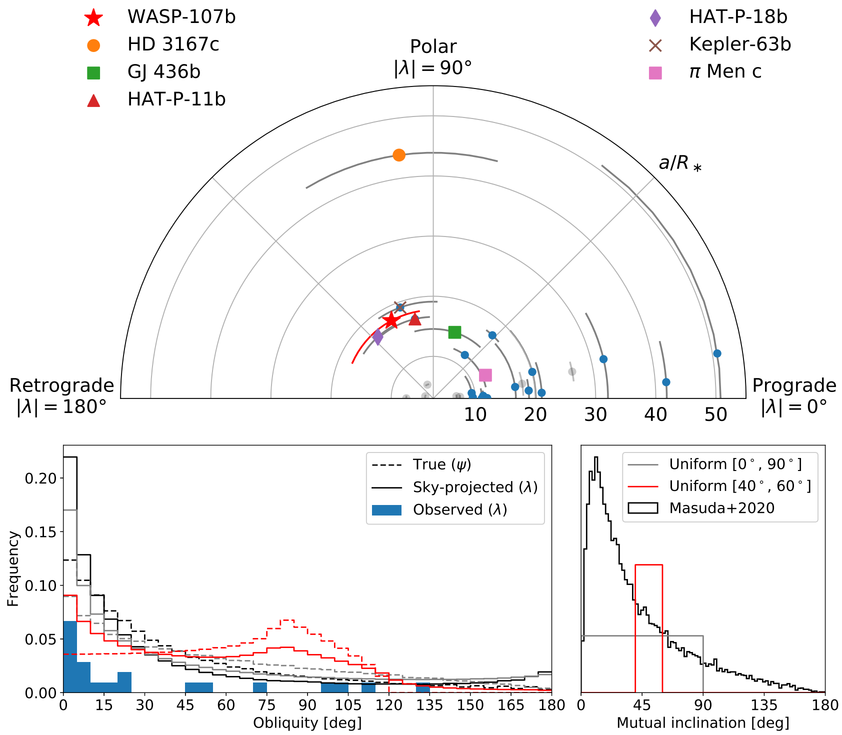

Figure 4.6: Top: polar plot showing the absolute sky-projected obliquity as the azimuthal coordinate and normalized orbital distance as the radial coordinate, for <100 $M_\oplus$ planets around stars with $T_{\rm eff} < 6250$ K (similar mass planets around hotter stars are shown as faded gray points). The red point is WASP-107 b. Other noteworthy systems are shown with various colors and markers (see Section 4.1 for references). Data compiled from TEPCat as of 2020 October (Southworth, 2011). Only WASP-107, HAT-P-11, and π Men have distant giant companions detected. Kepler-56 (Huber et al., 2013) is another similar system but is not included in this plot as it is an evolved massive star. Bottom: the fraction of a nodal precession cycle spent in a given obliquity bin (left). The true obliquity ψ is assumed to vary as $\cos[(\pi/2)\psi(t)/\psi_{\rm max}] = \sin^2(\pi t/\tau)$, where $t \in [0, \tau = 1]$. This recreates the shape of the oscillating inclination in Fig. 4.5. The amplitude $\psi_{\rm max}$ is twice the outer planet's inclination which is plotted for three different distributions (shown on the right): uniform between [0°, 90°] (gray), uniform between [40°, 60°] (red), and using the von-Mises Fisher distribution from Masuda, Winn, and Kawahara (2020) calculated in a hierarchical manner incorporating their posterior distribution for the shape parameter σ for all. In all three cases the true obliquity is shown as a dashed histogram. The sky-projected obliquity is computed given a transiting geometry ($i_{{\rm orb},b} = 90°$) and is marginalized over stellar inclination angle (solid histogram). $M_p < 100$ $M_\oplus$ planets with observed sky-projected obliquities are shown as a filled histogram for comparison. Note that while the gray and black predictions are relatively similar, an excess of polar orbits can be observed if the mutual inclination distribution is clustered around $\sim$ 40–60°.

Disk dispersal-driven tilting

Recently, Petrovich et al. (2020) showed that, even for $\psi_c \sim 0°$, a resonance encountered as the young protoplanetary disk dissipates can excite an inner planet to high obliquities, even favoring a polar orbit given appropriate initial conditions. To summarize the model, consider a system with a close-in planet and a distant (few astronomical units) giant planet, like WASP-107, after the disk interior to the outer planet has been cleared but the disk exterior remains. The external gaseous disk induces a nodal precession of the outer planet at a rate proportional to the disk mass (Eq. 4.10 with $b \mapsto c$ and $c \mapsto$ disk). The outer planet still induces a nodal precession on the inner planet according to Eq. 4.10. If at first the rate $d\Omega_c/dt > d\Omega_b/dt$, then as the disk dissipates (and $M_{\rm disk}$ decreases) the precession rate for planet c will decrease until it matches the precession rate of the inner planet. At this point the system will pass through a secular resonance, driving an instability which tilts the inner planet to a high obliquity; a small initial obliquity of a few degrees can quickly reach 90°. Additionally, depending on the relative strength of the stellar quadrupole moment and GR effects, the inner planet may obtain a high eccentricity (if GR is unimportant), a modest eccentricity (if GR is important), or a circular orbit (if GR dominates). Tidal forces can circularize the orbit, although the planet may retain a detectable eccentricity even after several gigayears. This process well explains the polar, close-in, and eccentric orbits of small planets like HAT-P-11b. Nodal precession alone is unable to explain the eccentricity of such planets.

Given the planet and stellar properties of the WASP-107 system, we calculated the instability criteria developed in Petrovich et al. (2020). The steady-state evolution of the system can be inferred by comparing the relative strength of GR ($\eta_{\rm GR}$) with the stellar quadrupole moment ($\eta_\star$). We found that $\eta_{\rm GR} > \eta_\star + 6$ at 99.76% confidence, $\eta_\star + 6 > \eta_{\rm GR} > 4$ at 0.155% confidence, and $\eta_{\rm GR} < 4$ at 0.084% confidence (i.e., $\eta_{\rm GR} \sim 30 - 80$ and $\eta_\star \sim 1$). Thus WASP-107 b is stable against eccentricity instabilities and lives in the polar, circular region of parameter space in Fig. 4 of Petrovich et al. (2020).

We calculated the final obliquity of WASP-107 b using the procedure outlined in Petrovich et al. (2020), incorporating the uncertainties in $M \sin i_{\rm orb,c}$ and P_c and integrating over all possible initial obliquities for the outer planet. Evaluating their Eq. (3), we found that the resonance that drives the inner planet to high obliquities is always crossed. We calculated the adiabatic parameter $x_{\rm ad} \equiv \tau_{\rm disk}/\tau_{\rm adia}$ from the disk dispersal timescale and the adiabatic time (their Eq. 7), taking $\tau_{\rm disk}$ to be 1 Myr. In the orbital configurations where $x_{\rm ad} > 1$ (adiabatic crossing) we computed the final obliquity from their Eq. (12) ($I_{\rm crit}$). Otherwise, the final obliquity was set to $I_{\text{non-ad}}$ from their Eq. (15).

The resulting probability of the final obliquity of WASP-107 b is 7.6% for a nonpolar (but oblique) orbit and 92.4% for a polar orbit. A polar orbit is likely if the outer planet's orbit is inclined at least $\sim 8°$, and is guaranteed for $\psi_{\rm init,c} \gtrsim 25°$. In an equivalent parameterization, Petrovich et al. (2020) explicitly predict a polar orbit for WASP-107 b if the mass and semiminor axis of WASP-107c satisfy $(b_c/2\ \mathrm{AU})^3 > (M_c/0.5\ \mathrm{M_{Jup}})$. Since we only have a constraint on $M \sin i_{{\rm orb},c}$, this condition is satisfied if $i_{\rm orb,c} \in [60° - 90°]$. Such a viewing geometry, in conjunction with an obliquity of $\psi_c > 25°$, is plausible given the likely stellar orientation (Section 4.3).

A key deviation from this model is that while the orbit of WASP-107 b is indeed close to polar, it is quite definitively retrograde. In the disk dispersal-driven tilting scenario, the inner planet approaches a $\psi = 90°$ polar orbit from below and stops at $\psi_b = 90°$. In order to reach a super-polar/retrograde orbit, WASP-107c must have a significant obliquity, either primordial from formation or through a scattering event (Petrovich et al., 2020). As we alluded to in Section 4.4, a scattering event could also explain the moderate eccentricities of the outer giants WASP-107c and HAT-P-11c, and could easily give WASP-107c a high enough obliquity to guarantee a polar/super-polar configuration for WASP-107 b (Huang, Petrovich, and Deibert, 2017). In fact a scattering event is more likley to produce the modest obliquity for planet c needed to produce a super-polar orbit under the disk dispersal framework than it is to produce the large ($\psi_c \gtrsim 40-50°$) obliquity needed to excite either Kozai–Lidov or nodal precession cycles.

4.5 Discussion and Conclusion

We observed the RM effect during a transit of WASP-107 b on 2020 February 26, from which we derived a near-polar and retrograde orbit as well as a low stellar $v \sin i_\star$. This low $v \sin i_\star$ implies that we are viewing the star close to one of its poles, reinforcing the near-polar orbital configuration of WASP-107 b. However, we are unable to conclusively say how WASP-107 b acquired such an orbit. Nodal precession or disk dispersal-driven tilting are both plausible mechanisms for producing a polar orbit, while Kozai–Lidov oscillations may be possible but only for a very narrow range of face-on orbital geometries for WASP-107c. RV observations (Piaulet et al., 2021) as well as constraints on the velocity of the escaping atmosphere of WASP-107 b (e.g., Allart et al. 2019, Kirk et al. 2020, Spake, J. J. et al. 2020, in preparation) are consistent with a circular orbit. The eccentricity damping timescale due to tidal forces is only ~ 60 Myr (Piaulet et al., 2021), so this is not unexpected. While a circular orbit does not rule out any of these pathways, only disk dispersal-driven tilting can explain both the eccentric and polar orbit of WASP-107 b's doppelganger HAT-P-11 b.

Since all three scenarios depend on the obliquity of the outer giant planet, measuring the mutual inclination of planet b and c is essential to understand the dynamics of this system. This has been done for similar system architectures such as HAT-P-11 (Xuan and Wyatt, 2020) and π Men (Xuan and Wyatt, 2020; De Rosa, Dawson, and Nielsen, 2020) by observing perturbations in the astrometric motion of the star due to the gravitational tugging of the distant giant planet, using data from Hipparcos and Gaia. Unfortunately WASP-107 is significantly fainter ($V = 11.5$; Anderson et al., 2017) and barely made the cutoff in the Tycho-2 catalog of Hipparcos (90% complete at V=11.5; Høg et al., 2000). The poor Hipparcos astrometric precision, combined with the small angular scale of the orbit of WASP-107 on the sky (10 - 30 μas), prevents a detection of the outer planet using astrometry. Assuming future Gaia data releases have the same astrometric precision as in DR2 (44 μas for WASP-107), WASP-107c will be at the threshold of detectability using the full five-year astrometric time series.

On the population level, the disk dispersal-driven model favors low-mass and slowly rotating stars due to its dependence on the stellar quadrupole moment, and also can explain eccentric polar orbits. Since nodal precession has no stellar type preference nor a means of exciting eccentric orbits, measuring the obliquities and eccentricities for a population of close-in Neptunes will be essential for distinguishing which process is the dominant pathway to polar orbits. Additionally a large population is needed to determine if the overall distribution of planet obliquities is consistent with catching systems at different stages of nodal precession, or if there are indeed two distinct populations of aligned or polar close-in Neptunes. As these models all depend on the presence of an outer giant planet, long-baseline RV surveys will be instrumental for discovering the nature of any perturbing companions (e.g. Rosenthal et al. submitted). Moreover RV monitoring of systems with small planets that already have measured obliquities, but do not have mass constraints or detected outer companions, will further expand this population. Recent examples of such systems include Kepler-408b (Kamiaka et al., 2019), AU Mic b (Palle et al., 2020b), HD 63433 (b, Mann et al. 2020; and c, Dai et al. 2020), K2-25b (Stefánsson et al., 2020), and DS Tuc b (Montet et al., 2020; Zhou et al., 2020). Comparing the proportions of systems with and without companions which have inner aligned or misaligned planets will further illuminate the likelihood of these different dynamical scenarios.

Acknowledgements

We thank Konstantin Batygin, Cristobol Petrovich, and Jerry Xuan for helpful comments and productive discussions on orbital dynamics, and Josh Winn for constructive feedback that improved this manuscript. R.A.R. and A.C. acknowledge support from the National Science Foundation through the Graduate Research Fellowship Program (DGE 1745301, DGE 1842402). C.D.D. acknowledges the support of the Hellman Family Faculty Fund, the Alfred P. Sloan Foundation, the David & Lucile Packard Foundation, and the National Aeronautics and Space Administration via the TESS Guest Investigator Program (80NSSC18K1583). I.J.M.C. acknowledges support from the NSF through grant AST-1824644. D.H. acknowledges support from the Alfred P. Sloan Foundation, the National Aeronautics and Space Administration (80NSSC18K1585, 80NSSC19K0379), and the National Science Foundation (AST-1717000). E.A.P. acknowledges the support of the Alfred P. Sloan Foundation.

We thank the time assignment committees of the University of California, the California Institute of Technology, NASA, and the University of Hawai‘i for supporting the TESS–Keck Survey with observing time at the W. M. Keck Observatory. We gratefully acknowledge the efforts and dedication of the Keck Observatory staff for support of HIRES and remote observing. We recognize and acknowledge the cultural role and reverence that the summit of Maunakea has within the indigenous Hawaiian community. We are deeply grateful to have the opportunity to conduct observations from this mountain.

Chapter 5

KPF CONFIRMS A POLAR ORBIT FOR KELT-18 B

Rubenzahl, R. A. et al. (2024). "KPF Confirms a Polar Orbit for KELT-18 b" *Submitted to the Astronomical Journal*

5.1 Introduction

KELT-18 b is an ultra-hot Jupiter discovered by the KELT transit survey (McLeod et al., 2017). The 1.57 R_{Jup} planet orbits its F5 type (6670 K) host star every 2.87 days. Hot stars ($\gtrsim$ 6250 K) with hot Jupiters (HJs) have been observed to have a broad range of obliquities, where the obliquity is defined as the angle between the host star's rotation axis and the planet's orbital plane. Conversely, HJs orbiting cooler stars ($\lesssim$ 6250 K) tend to be aligned with their host star's rotation axis (Winn et al., 2010a; Schlaufman, 2010; Albrecht, Dawson, and Winn, 2022). The transition temperature is near the Kraft Break (Kraft, 1967), suggesting realignment mechanisms that are effective for cooler stars–which have convective envelopes and strong magnetic fields–but are ineffective for hotter stars–which have radiative envelopes and weak magnetic fields (Albrecht et al., 2012; Dawson, 2014).

While it is still an unsolved problem, the origins of HJs are likely a combination of multiple formation channels (see Dawson and Johnson 2018 for a review), namely in-situ formation, disk migration, and high eccentricity migration (HEM). HEM likely plays a significant role in shaping the overall HJ population (Rice, Wang, and Laughlin, 2022) but must be triggered by an additional body in the system. This could be another planet, in the case of planet-planet scattering (Rasio and Ford, 1996) or von-Zeipel-Kozai-Lidov[1] oscillations (ZKL; von Zeipel, 1910; Kozai, 1962; Lidov, 1962) induced by an outer planetary (Naoz et al., 2011; Teyssandier et al., 2013) or stellar companion (Fabrycky and Tremaine, 2007). In the HEM scenario, the HJ originally formed beyond the water ice-line (~2 AU) where giant planet formation is efficient (Pollack et al., 1996). The orbital eccentricity was increased through interactions with a perturbing companion until the planet's periastron distance became small enough for tides to dissipate energy and transfer orbital angular

[1]See Ito and Ohtsuka (2019) for a historical monograph.

momentum to the star, causing the orbit to shrink and circularize. Either this HEM process, or perhaps a primordial misalignment of the protoplanetary disk (Batygin, 2012), leaves the HJ on an orbit that may be tilted by a large angle relative to the stellar equatorial plane. Only the HJs around stars cooler than the Kraft Break were then able to realign their host star's rotation axis.

The spin-orbit angle is usually measured as projected on the plane of the sky (λ), but for systems in which the inclination of the host star's rotation axis ($i_\star$) can be inferred, the true 3D obliquity can be derived (ψ). Recently, Albrecht et al. (2022) noted that hot Jupiters around hot stars do not span the full range of ψ, but instead show a preference for near polar orbits (80°–120°). However, there are still too few systems to be sure that the obliquity distribution has a peak near 90° (Siegel, Winn, and Albrecht, 2023; Dong and Foreman-Mackey, 2023). If there is a "polar peak" it would have important theoretical implications on plausible HJ formation mechanisms, which predict different obliquity distributions (see Albrecht, Dawson, and Winn, 2022). For small planets with massive outer companions, secular resonance crossing in the disk dispersal stage may produce polar orbits (Petrovich et al., 2020). For giant planets, an initially inclined orbit inherited from a torqued protoplanetary disk in the presence of a binary companion can give the necessary starting point for subsequent ZKL-driven migration to create a polar HJ (Vick, Su, and Lai, 2023).

The most commonly employed method for measuring the projected obliquity of a star with a transiting planet is to obtain high-resolution spectra throughout a transit and model the Rossiter-McLaughlin effect (Rossiter, 1924; McLaughlin, 1924), which results from the planet's obscuration of part of the rotating stellar photosphere. This effect is often modeled as an anomalous radial velocity (RV) signal, but measuring precise RVs for hot stars can often be challenging due to their fast rotation rates. The projected equatorial rotation velocity, $v \sin i_\star$, broadens (and blends) spectral lines, diminishing the Doppler information content (Bouchy, Pepe, and Queloz, 2001). As a result, stars with $v \sin i_\star \gtrsim 10$ km s^{-1} are usually not amenable to anomalous-RV modeling. However, these fast rotating stars lend themselves to more detailed and direct methods of measuring the stellar obliquity. The Reloaded RM (RRM) method, developed by Cegla et al. (2016b), directly models the distortion of the line profile by the transiting planet. By subtracting an out-of-transit reference

CCF (representing the star alone) from each in-transit CCF (corresponding to the stellar line profile integrated over the full disk, minus the integrated line profile from within the patch of the star beneath the planet's shadow), the resulting signal represents the "local" CCF, i.e., the spectrum originating from the portion of the star obscured by the transiting exoplanet ($\mathrm{CCF}_{\mathrm{loc}}$). The RRM method is also sensitive to stellar differential rotation, should the planet be highly misaligned so that it transits a wide range of stellar latitudes (Roguet-Kern, Cegla, and Bourrier, 2022).

In this paper we report our derivation of the obliquity of the host star in the KELT-18 system based on a time series of spectra taken during a transit of KELT-18 b with the Keck Planet Finder (KPF). By modeling the spectra according to the RRM method, we found the orbit of KELT-18 b to be nearly perpendicular to the star's equatorial plane. In Section 5.2 we derive stellar properties, reexamine the rotation period with *TESS* photometry, and identify the nearby star KELT-18 B as a bound companion. We describe the Keck Planet Finder and our observations in Section 5.3, the RRM modeling procedure in Section 5.4, and dynamical implications for the KELT-18 system in Section 5.5.

5.2 KELT-18 System

KELT-18 is a rapidly rotating F4 V star with one known transiting exoplanet, discovered by McLeod et al. (2017) (hereafter M17), and a stellar neighbor. M17 derived robust stellar properties using high resolution spectra, SED fitting, photometry, and evolutionary modeling in a global fit with their transit model. We adopted their best-fit stellar and transit parameters for our analyses herein, with two distinctions noted below. Table 5.1 lists the full set of adopted parameters.

For the transit midpoint and orbital period of KELT-18 b, we adopted the improved ephemeris of Ivshina and Winn (2022) which implies an uncertainty of only 20 sec in the predicted transit midpoint on the night of our spectroscopic observations (Section 5.3).

For the projected stellar rotation velocity $v \sin i_\star$, M17 noted that their value of 12.3 ± 0.3 km s^{-1} obtained from a TRES (Szentgyorgyi and Furész, 2007) spectrum is likely an overestimate as the method they used conflates macroturbulence and rotation. M17 also measured a value of 10 ± 1 km s^{-1} using

Table 5.1: Parameters of the KELT-18 System

Parameter	Value	Unit	Source
KELT-18			
$T_{\rm eff}$	6670 ± 120	K	M17
M_*	$1.524^{+0.069}_{-0.068}$	$M_\odot$	M17
R_*	$1.908^{+0.042}_{-0.035}$	$R_\odot$	M17
u_1	$0.337^{+0.011}_{-0.010}$		M17
u_2	$0.3229^{+0.0066}_{-0.0059}$		M17
$\mathrm{RV_{sys}}$	-11.7 ± 0.1	km s^{-1}	This work
KELT-18 b			
$P_{\rm orb}$	$2.87169867 \pm 0.00000085$	days	I22
t_c	$2458714.17773 \pm 0.00011$	JD	I22
b	$0.10^{+0.10}_{-0.07}$		M17
$i_{\rm orb}$	$88.86^{+0.79}_{-1.20}$	degrees	M17
$R_p/R_\star$	0.08462 ± 0.00091		M17
$a/R_\star$	$5.138^{+0.038}_{-0.078}$		M17
e	0		M17
M_p	1.18 ± 0.11	M_J	M17
KELT-18 B			
$T_{\rm eff}$	3900	K	M17
M_*	$0.575^{+0.025}_{-0.026}$	$M_\odot$	B22
sep	1082	AU	B22
$\Delta\mu_{\rm RA}$	0.21 ± 0.05	mas yr^{-1}	B22
$\Delta\mu_{\rm Decl.}$	0.41 ± 0.05	mas yr^{-1}	B22
Δparallax	0.07 ± 0.04	mas	B22
ΔG	-5.4	mag	B22
$\ln(\mathcal{L}_1/\mathcal{L}_2)$	4.83	—	B22

(M17) McLeod et al. (2017); (I22) Ivshina and Winn (2022); (B22) Behmard, Dai, and Howard (2022).

a HIRES (Vogt et al., 1994) spectrum and the `SpecMatch-Synthetic` (Petigura, 2015) framework, but did not adopt this value because the best-fit $T_{\rm eff}$ was outside the range 4800–6500 K over which the code had been calibrated. Since then, the `SpecMatch-Emperical` (Yee, Petigura, and von Braun, 2017) tool was developed to derive stellar properties for a wider range of effective temperatures (3000–7000 K) by interpolating a grid of library spectra obtained with Keck/HIRES. We ran the same HIRES spectrum obtained by M17 through `SpecMatch-Emperical` to obtain new estimates of $T_{\rm eff}$, Fe/H, and $R_\star$. The resulting $T_{\rm eff} = 6330 \pm 110$ K is cooler than the 6670 ± 120 K value of M17 and is within the `SpecMatch-Synthetic` regime. We therefore ran `SpecMatch-Synthetic` on the same HIRES spectrum and found $T_{\rm eff}$ = 6530 ± 100 K and $v \sin i_\star = 10.4 \pm 1.0$ km s^{-1}. Thus, the true value of $v \sin i_\star$ is likely in the 9–12 km s^{-1} range. All this together informs our adoption of an informed prior on $v \sin i_\star$ of 10.4 ± 1 km s^{-1} for our spectroscopic transit analysis in Section 5.4.

Stellar rotation period

A significant peak at 0.707 days was observed in the Lomb-Scargle periodogram of the KELT photometry, which M17 interpreted as the rotation period of KELT-18. Given the measured stellar radius, this implied an equatorial rotational velocity of $v_{eq} = 134$ km s^{-1}. While large, it is not atypical for stars of KELT-18's $T_{\rm eff}$ and $\log g$ to have rotation speeds on the order of 100 km s^{-1}. Combining this with their measured $v \sin i_\star$ of 12.3 km s^{-1}, McLeod et al. 2017 noted that the star must have an inclination of $\sim$5°. In other words, we are observing KELT-18 nearly pole-on. Since the planet's orbit is viewed at high inclination, the implication was that the planet's orbit is nearly polar.

Since the rotation signal in the KELT photometry appeared small compared to the measurement noise, we downloaded the available TESS photometry for KELT-18 to search for variability. KELT-18 was observed by TESS as TIC 293687315 (TOI-1300) in sectors 15, 16, 22, 23, 48, 50, and 75. We downloaded the 1800 s cadence data for sectors 48 and 50, 120 s data for sector 75, and the 600 s data for the other sectors. We selected data processed by the TESS Science Processing Operations Center pipeline (Caldwell et al., 2020), removed flagged values, stitched the six sectors together, and binned to a common 1 hour cadence using `lightkurve` (Lightkurve Collaboration et al., 2018). The resulting light curve is shown in Figure 5.1 along with its Lomb-Scargle periodogram.

The TESS periodogram does not contain any significant peaks below $\sim$3 days. There is a clustering of peaks around $\sim$5 days with a maximum power at 4.76 d, and variability on this timescale is visible by eye in the TESS photometry. If this is the true rotation period of KELT-18, the equatorial rotational velocity would be $v_{eq} \sim 20$ km s^{-1}. This is still a factor of two larger than the measured $v \sin i_\star$, so it remains likely that KELT-18 is viewed at low inclination ($i_\star \lesssim 30°$). Stars with KELT-18's $T_{\rm eff}$ tend to have rotation rates < 8 d at $> 3\sigma$ (Bouma, Palumbo, and Hillenbrand, 2023b), so a $\sim$5 day rotation period is

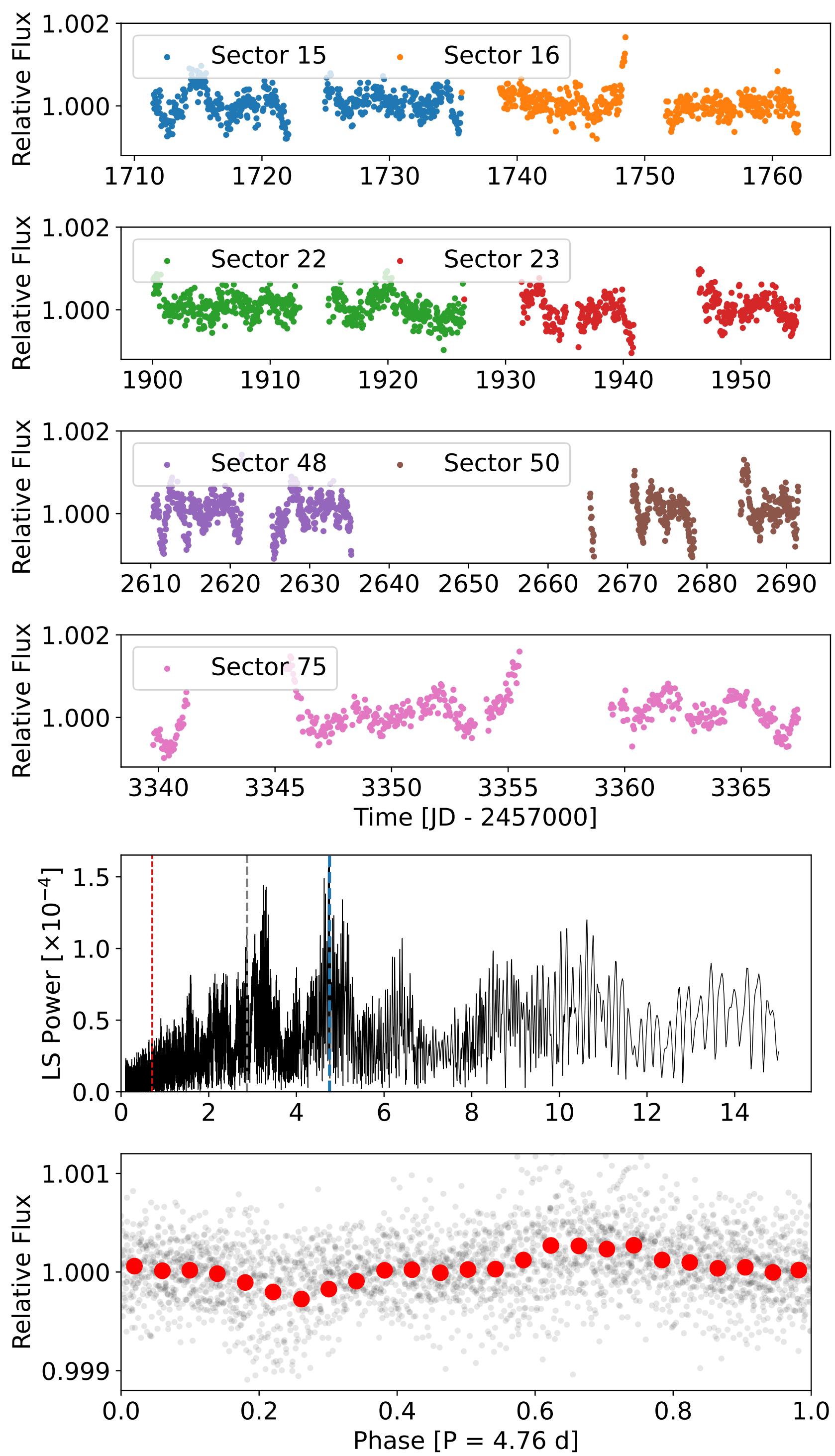

Figure 5.1: Analysis of the rotation period using TESS photometry. The top three panels show the 1 hour binned TESS photometry described in Section 5.2. The fourth panel displays a Lomb-Scargle periodogram. We marked the 0.707 d period from M17 with a red dashed line, KELT-18's orbital period with a grey dashed line, and the maximum peak with a blue dashed line. The bottom panel shows all TESS data points (grey) phase-folded to that period with the maximum power. Red points show the data evenly binned in phase with bin size 0.05.

reasonable. Additional photometry will further constrain the true rotation period. KELT-18 will be revisited by TESS in sector 77 (April 2024).

KELT-18 B: Neighbor or Companion?

M17 noted a stellar neighbor at 3".43 separation from KELT-18 B. The neighbor is fainter at $K = 12.9 \pm 0.2$. Under the assumption that the neighbor is at the same distance as KELT-18, M17 obtained $T_{\mathrm{eff}B} \sim 3900$ K. The available astrometry were not precise enough to identify the neighbor as comoving based on its proper motion, though the relatively small sky density of stars in the field around KELT-18 (at high galactic latitude) makes a chance alignment at such a small angular separation unlikely ($>3\sigma$).

KELT-18 and KELT-18 B appear in the catalog of stellar companions to TESS Objects of Interest of Behmard, Dai, and Howard (2022) (B22). B22 applied the methodology of Oh et al. (2017) to the *Gaia* DR3 astrometry (Gaia Collaboration et al., 2023) to determine the likelihood the two stars are comoving. The method propagates the astrometric uncertainties from *Gaia* into a likelihood ratio comparing the comoving hypothesis ($\mathcal{L}_1$) to the null (not comoving) hypothesis ($\mathcal{L}_2$). B22 added a jitter term to account for any unknown systematic effects to improve the reliability of this hypothesis testing. B22 computed $\ln(\mathcal{L}_1/\mathcal{L}_2) = 4.83$ for KELT-18 and KELT-18 B, giving strong evidence for the comoving hypothesis. They computed a stellar mass for KELT-18 B of $0.575^{+0.025}_{-0.026}$ $M_\odot$ using `isoclassify` (Huber et al., 2017b) and the *Gaia* magnitudes, in agreement with the $T_{\mathrm{eff}B}$ estimate from M17. Given the consistent parallaxes (3.16 ± 0.01 mas for the primary and 3.23 ± 0.04 mas for the secondary), B22 computed a binary separation from the *Gaia* astrometry of 1082 AU. The relative velocity vector in the sky plane is thus 0.695 ± 0.075 km s^{-1}. For reference, if both stars were orbiting in the sky-plane on circular orbits, their relative velocity would be 1.8 km s^{-1}. So, unless the two stars have a significant relative radial velocity (which *Gaia* did not measure), they are likely bound.

5.3 Observations

We observed a transit of KELT-18 b on UT May 22, 2023 with the Keck Planet Finder (KPF; Gibson et al., 2016; Gibson et al., 2018; Gibson et al., 2020). KPF is a newly commissioned, optical (445–870 nm), high-resolution ($R \sim 98,000$), fiber-fed, ultra-stabilized radial velocity system on the Keck I

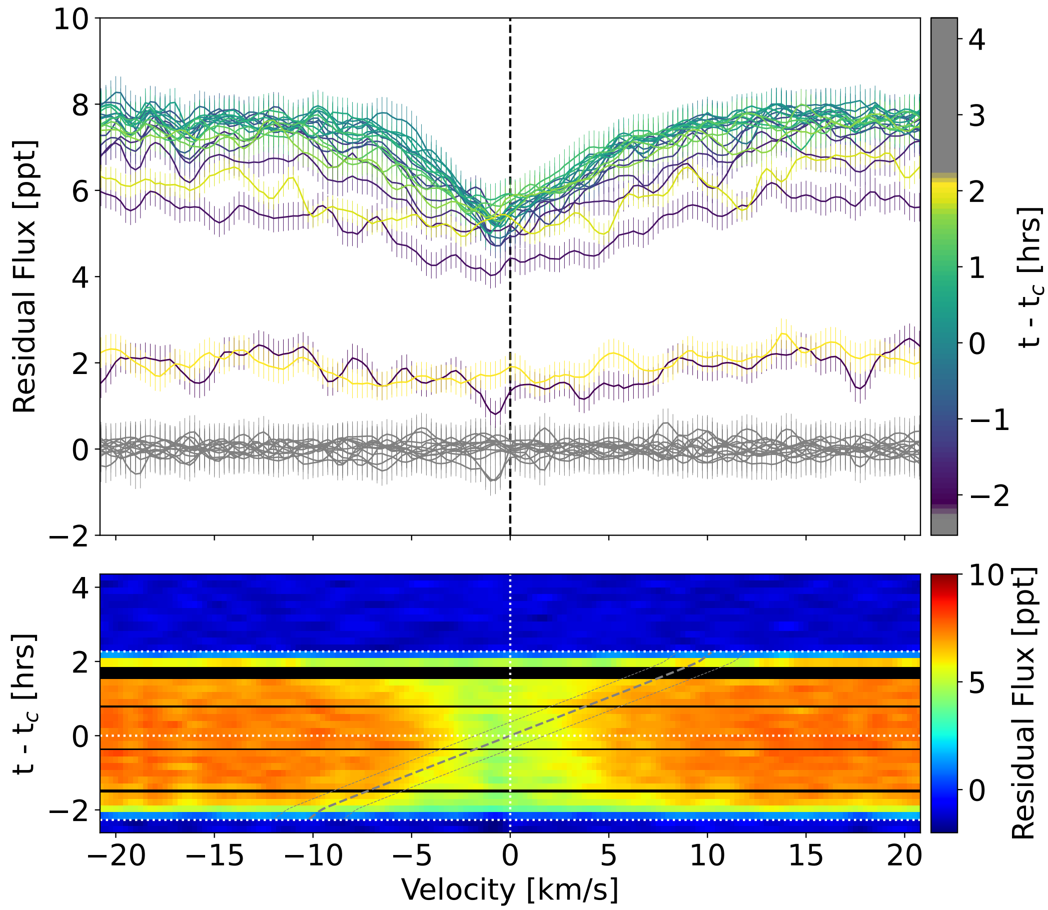

Figure 5.2: The timeseries of CCF_{loc} measured with KPF. The top panel shows each 1D CCF_{loc}, with out-of-transit observations in grey and in-transit observations colored according to the timestamp. The bottom panel displays the same data as a 2D heatmap with time relative to mid-transit on the y-axis and colored by flux. The shadow of KELT-18 b if it were aligned is traced by the grey dashed lines. Black rows correspond to gaps in the time series; the narrow hourly bands correspond to etalon calibration images and the large band near +1.8 hrs is when the tip/tilt guiding system failed.

telescope at W. M. Keck Observatory. Our observations began 25 min before transit ingress and continued until 2 hours after transit egress, only being interrupted by hourly calibration exposures (described below) and a ∼20 min window near transit egress during which issues with the tip/tilt system prevented precise fiber positioning on the stellar PSF.

We chose a fixed 600 sec exposure time to balance averaging over p-mode oscillations (14 min from the scaling relations of Brown et al. 1991; Kjeldsen and Bedding 1995) with temporal resolution of the transit, while reaching a spectral signal-to-noise ratio (S/N) of at least 100 (typical values were 130 ± 11 in the green channel and 140 ± 13 in the red). The KPF "SKY" fiber collected background sky contamination from a position offset several arcsec from KELT-18. We simultaneously acquired broadband Fabry-Pérot etalon spectra in the "CAL" fiber to track instrumental drift, and periodically (once per ∼hour) took a single internal frame with etalon light in the "SKY", "CAL", and science fibers as an additional sanity check on drift. We observed a stable linear drift as traced by the simultaneous etalon spectra of -0.92 ± 0.01 m s^{-1} per hour in the green channel and -0.36 ± 0.02 m s^{-1} per hour in the red channel. This was well-matched by the hourly all-etalon RVs across each fiber. As a result, we drift-corrected our stellar spectra by Doppler-shifting the derived CCFs by estimated drift using our linear fit to the simultaneous etalon RVs.

We independently extracted 1D stellar spectra from each of the three science "slices" using the public KPF data reduction pipeline (DRP)[2]. Wavelength calibration was performed for each spectral order using a state-of-the-art laser frequency comb (for $\gtrsim 490$ nm) and a ThAr lamp (for $\lesssim 490$ nm) using calibration frames taken during the standard KPF calibration sequences performed that day. We used the F9 ESPRESSO mask (e.g. Pepe et al., 2002) to derive cross-correlation functions (CCF; Baranne et al., 1996) for each spectral order. This dataset was obtained before a significant charge transfer inefficiency (CTI) in one of the green CCD amplifiers was diagnosed using solar data (Rubenzahl et al., 2023). Because of this, the green CCD readout utilized the original four-amplifier scheme and was thus affected by significant CTI. We masked the flux corresponding to the quadrant of the raw 2D image read by the affected amplifier when deriving CCFs. This affects half of the bluest 20 orders (roughly 445–530 nm). Fortunately, about 78% of the affected wave-

[2]https://github.com/Keck-DataReductionPipelines/KPF-Pipeline/

lengths also appear in the "good" amplifier of the subsequent order, so much of the spectral information is still contained in the final 1D spectrum. The CCFs from each slice were combined in a weighted sum, taking the weights to be proportional to the total flux in each slice from a representative high S/N spectrum. We repeated the same process across all orders, and then again across the green and red CCDs to obtain the final CCF for each observation. We also calculated the unweighted summed CCF to derive photon-noise uncertainties, which we scaled by the relative total flux in the weighted vs. unweighted CCF to yield appropriate uncertainties in each CCF.

We independently verified the systemic velocity reported by M17. We measured this by fitting the CCF of each of the three science traces, for each out-of-transit spectrum. The result was -11.7 ± 0.1 km s^{-1}, in agreement with -11.6 ± 0.1 km s^{-1} from M17. We found a slightly smaller value of -11.3 ± 0.1 km s^{-1} by comparing the HIRES spectra used in Section 5.2 to a telluric model (Kolbl et al., 2015). *Gaia* (Gaia Collaboration et al., 2023) reports a smaller but less certain -10.83 ± 0.46 km s^{-1} for KELT-18. We adopt the -11.7 ± 0.1 km s^{-1} value from our KPF spectra for our analysis.

5.4 Obliquity of KELT-18 b

Reloaded Rossiter-McLaughlin Modeling

To measure the obliquity of KELT-18 b, we applied the Reloaded Rossiter-McLaughlin technique (Cegla et al., 2016b) to our KPF spectra. We breifly summarize the process here.

First, we transformed into the stellar rest frame by Doppler shifting the CCFs by our measured systemic velocity and by the expected Keplerian RV induced by KELT-18 b's orbital motion (using the planet's mass M_p from M17). The aligned CCFs were then normalized to a continuum value of 1. We then created a stellar template, $\mathrm{CCF_{out}}$, by averaging the out-of-transit normalized CCFs. $\mathrm{CCF_{out}}$ describes the unperturbed average stellar line profile of KELT-18. To isolate the shadow of KELT-18 b, we subtracted each in-transit observation ($\mathrm{CCF_{in}}$) from the template to obtain the local line profile within the planet's shadow, $\mathrm{CCF_{loc}} = \mathrm{CCF_{out}} - \mathrm{CCF_{in}}$. Since we normalized the CCFs, we multiplied each $\mathrm{CCF_{loc}}$ by the calculated flux at that time according to a white-light synthetic transit light curve model, integrated over the exposure time of each observation. This placed each $\mathrm{CCF}_{\mathrm{loc}}$ on the appropriate flux scale.

The resulting $\mathrm{CCF}_{\mathrm{loc}}$ time series is shown in Figure 5.2. Each $\mathrm{CCF}_{\mathrm{loc}}$ is fit with a Gaussian profile using `curve_fit` from `scipy` (Virtanen et al., 2020), where the continuum, amplitude (i.e., depth), width, and centroid are free parameters. The centroid corresponds to the flux-weighted integrated stellar velocity profile within the shadow of the transiting planet; i.e., the local RV. The local RV is modelled by Eq. 9 in (Cegla et al., 2016b),

$$\mathrm{RV}_{\mathrm{loc}} = \frac{\int I(x,y) v_{\mathrm{stel}}(x,y) dA}{\int I(x,y) dA}, \tag{5.1}$$

where I is the limb-darkened intensity, the integral is over the patch of star within the planet shadow, and v_{stel} is the stellar velocity field

$$v_{\mathrm{stel}} = x_{\perp} v_{eq} \sin i_{\star} (1 - \alpha y_{\perp}^{\prime 2}), \tag{5.2}$$

where α is the relative differential rotation rate (the difference in rotation rates at the poles compared to the equator, divided by the equatorial rotation rate). For the Sun, $\alpha = 0.27$. We used the same coordinate definitions for $(x_{\perp}, y'_{\perp})$ as in Cegla et al. (2016b), but we adapted the implementation of the integral for improved resolution. Instead of defining a Cartesian grid of points (x_k, y_k) centered on the planet's shadow spanning $-R_p/R_*$ to $+R_p/R_*$ and only keeping the points in the grid which satisfied $x^2 + y^2 < (R_p/R_*)^2$, we generated a "grid" of N points (x_k, y_k) according to the sunflower pattern,

$$\begin{gathered} r_k = \sqrt{\frac{k - 1/2}{N - 1/2}},\ \theta_k = k(2\pi\phi), \\ x_k = r_k \cos\theta_k,\ y_k = r_k \sin\theta_k, \end{gathered} \tag{5.3}$$

where $\phi = (1 + \sqrt{5})/2$ is the golden ratio. The result is a set of points $(x_k,\ y_k)$ uniformly spaced over a circle of radius unity. The points can then be scaled to R_p/R_* and centered at the position of the planet to quickly obtain a densely packed grid of points for which each point represents the same projected area dA of the stellar photosphere. The improved resolution of this grid at the shadow and disk limbs helped to reduce artifacts during ingress/egress, and greatly boosted performance when simulating full line profiles for stars with surface inhomogeneities (Rubenzahl, R. et al., in prep).

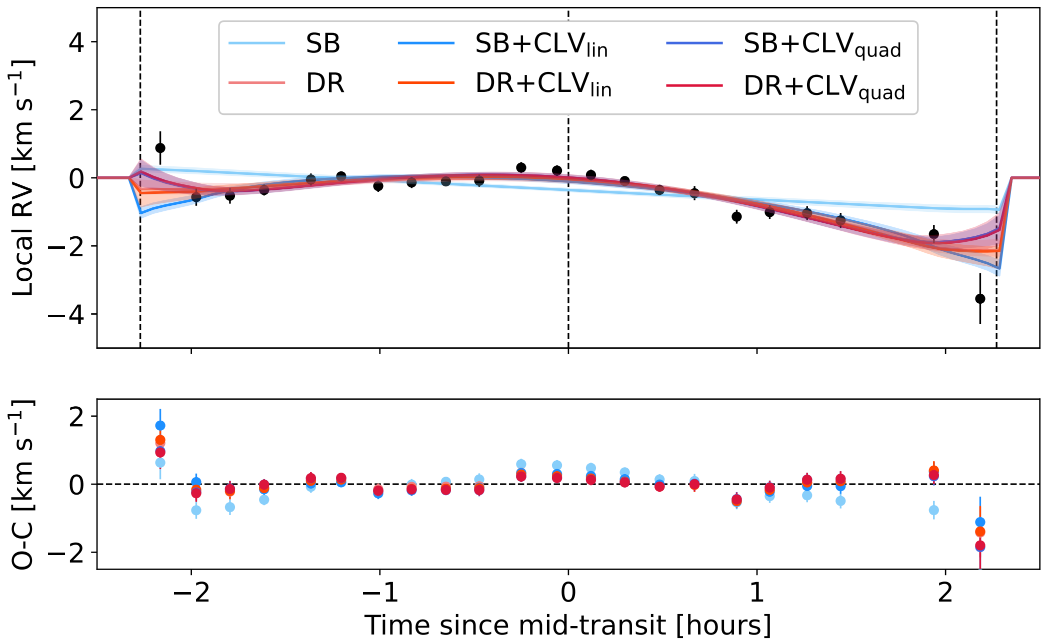

Figure 5.3: The extracted local RVs and the best-fit RRM models (SB=solid body, DR=differential rotation, CLV=center-to-limb variations as a linear (lin) or quadratic (quad) effect in $\langle\mu\rangle$). The solid lines are the MAP model while the shaded regions cover the 16th–84th percentile of posterior distribution of models. Thee bottom panel compares the residuals between the data and the MAP fit for each model.

To fit the local RVs, we modified the `radvel` package (Fulton et al., 2018) to accept a new function that computes Eq. 5.1 for each observation. The `radvel` framework automatically enabled us to perform maximum a-posteriori (MAP) fitting, MCMC sampling using `emcee` (Foreman-Mackey et al., 2013), and model comparison with the BIC and AIC. We tested several different models: solid body (SB) rotation vs. differential rotation (DR), and with/without center-to-limb variations (CLVs); see Doyle et al. (2023) for more details. The former is a matter of fixing α to zero (SB) or letting it float (DR), while the latter requires adding an additional term to Eq. 5.1 of the form

$$v_{\rm conv} = \sum_{i=0}^{n} c_i \langle\mu\rangle^i. \quad (5.4)$$

This polynomial in the intensity-weighted center-to-limb position $\langle\mu\rangle$ is a good model for the velocity field introduced by granulation, which is azimuthally symmetric around the disk and varies with center-to-limb position as the line-of-sight intersects the tops of granules at disk-center and the sides of granules at the limb (Cegla et al., 2016b). Since $\mathrm{CCF}_{\rm loc}$ has the out-of-transit template subtracted, the net convective blueshift integrated across the full stellar disk has also been removed from the data. Consequently, c_0 must be constrained according to Eq. 13 in Cegla et al. (2016b). The additional model parameters are thus c_1 for a linear ($n = 1$) CLV and (c_1, c_2) for a quadratic ($n = 2$) CLV.

MCMC Sampling

We tested a suite of models within the RRM framework corresponding to each combination of SB or DR, and no CLV, linear CLV ($\mathrm{CLV_{lin}}$), and quadratic CLV ($\mathrm{CLV_{quad}}$). The free parameters in all models were the sky-projected obliquity λ, the projected rotational velocity $v \sin i_\star$, the sine of the stellar inclination $\sin i_\star$, and the impact parameter b. Models with DR include the degree of differential rotation α, and models with CLVs include either c_1 (linear) or c_1 and c_2 (quadratic). We allowed for anti-solar differential rotation by permitting α to be negative, with a uniform prior over $(-1, 1)$.

To improve the sampling efficiency, we make the change of coordinates for our fitting basis into a polar coordinate system with λ as the azimuthal angle and $\sqrt{v \sin i_\star}$ as the radial dimension. The parameters for the fit are thus $\sqrt{v \sin i_\star} \cos \lambda$, $\sqrt{v \sin i_\star} \sin \lambda$, $\sin i_\star$, b, α, and the CLV coefficients.

Because of the suspected polar orientation of the transit chord, we placed an informed Gaussian prior on $v \sin i_\star$ of 10.4 ± 1 km s^{-1} based on our analysis of the spectroscopic $v \sin i_\star$ (Section 5.2). We also found that this prior, in conjunction with a prior on i_{orb} based on previous transit fits (Table 5.1), was necessary to discourage the sampler from wandering to solutions of extremely low $v \sin i_\star$ ($\sim$1 km s^{-1}) with (unrealistic) grazing transits. The final distributions for λ were unaffected by the exact boundaries chosen for these priors. We note that Maciejewski (2020) found values of i_{orb} ($82.90^{+0.62\circ}_{-0.54}$) and a/R_* ($4.36^{+0.11}_{-0.09}$) that were significantly discrepant with those measured by M17. We tried setting a prior on i_{orb} to this value and found the MCMC to both not converge and produce a bimodal $v \sin i_\star$ posterior around 2 km s^{-1}, which is highly inconsistent with the observed width of lines in the KPF spectra and the HIRES, TRES, and APF spectra of M17.

We first found the MAP solution for each model using `scipy.optimize.minimize` (Virtanen et al., 2020). This best-fit solution was used as the initial location (plus a small Gaussian perturbation) for a MCMC exploration of the posterior. We ran `emcee` (Foreman-Mackey et al., 2013) as implemented in `radvel`

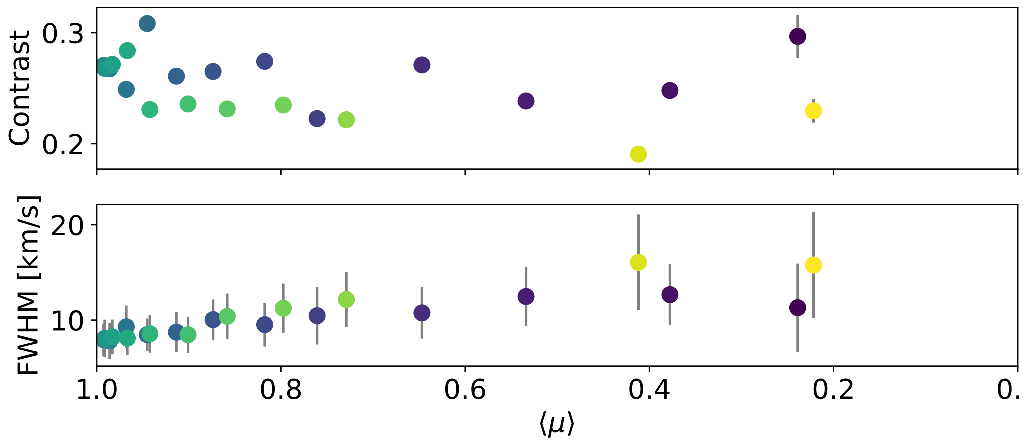

Figure 5.4: The contrast (top) and FWHM (bottom) of CCF_{loc} as a function of the flux-weighted center-to-limb position $\langle\mu\rangle$. The color scale is the same used in Figure 5.2 based on the observation timestamps (purple=ingress, green=mid transit, yellow=egress).

(Fulton et al., 2018) with 8 ensembles of 32 walkers each for a maximum of 10,000 steps, or until the Gelman–Rubin statistic (G–R; Gelman et al., 2003) was < 1.001 across the ensembles (Ford, 2006). In all cases, the G-R condition for convergence was satisfied and the sampler was terminated with a typical total number of posterior samples around 100,000. A second and final MAP fit was then performed using the median parameter values from the MCMC samples. The MAP fit for each model is plotted over the RV_{loc} time series in Figure 5.3, and Table 5.2 lists our derived best-estimates for each parameter.

Center-to-Limb Variations

Fig. 5.4 plots the depth and full-width-at-half-maximum (FWHM) of the CCF_{loc} as a function of $\langle\mu\rangle$. A strong trend in both can be seen from center to limb, with the local line profiles deepest and narrowest at disk center and becoming shallower and wider towards disk limb. The RV_{loc} time series likewise has significant curvature with a maximum (minimum blueshift) at disk center (mid-transit) and minimum (maximum blueshift) at disk limb (ingress/egress).

Only CLVs can explain all of these observed effects. While differential rotation alone can reproduce the observed curvature in the local RV time series, it cannot explain the large (factor of two) increase in FWHM from disk center to limb. Beeck et al. (2013b) showed using spectral line synthesis in 3D radiative magnetohydrodynamical (MHD) simulations that surface-layer granula-

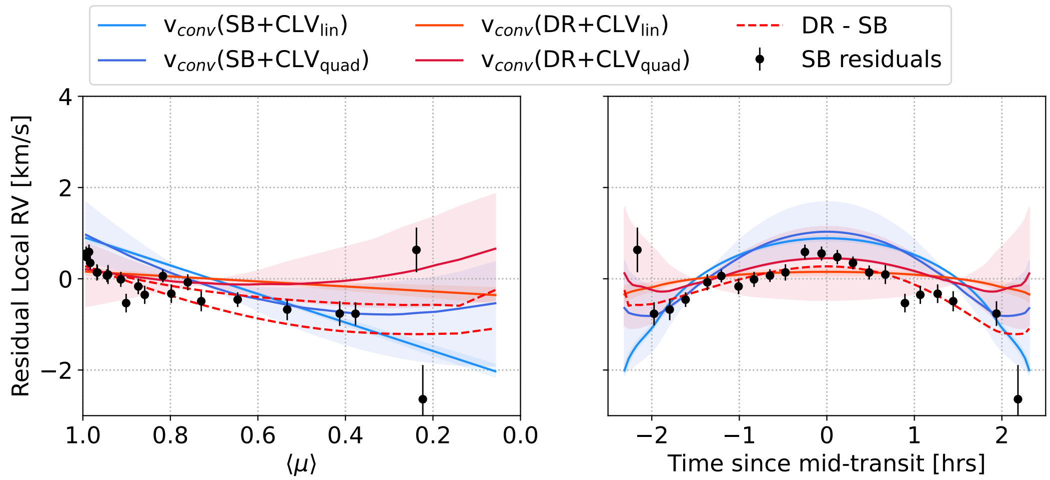

Figure 5.5: The best-fit convective velocity profiles within the patches of star occulted by KELT-18 b as a function of center-to-limb position (left) and time (right). The $v_{\rm conv}$ for models with DR are consistent with zero, i.e. the DR models are primarily fit by extreme DR. The velocity contribution from DR alone is shown by the dashed red line, which plots the difference between the DR-only and SB-only models. Residuals (data minus model) to the SB-only model are plotted in black; these points represent the amount of local RV that must be coming from either DR or CLVs.

tion causes the width of spectral lines to increase towards disk limb, an effect that is relatively muted for GKM stars but is significant for F-type stars. The F3 V star in their simulation showed increases to the FWHM of iron lines by a factor of 1.5–2 from disk center to $\mu = 0.2$. This effect is caused by the horizontal flows, which dominate the line-of-sight velocity at disk limb, having roughly three times as high a velocity dispersion compared to the vertical velocity (Beeck et al., 2013a). They also found line cores to have a net convective blueshift about 500 m s^{-1} less (i.e., larger RV) at disk limb than at disk center. We see the opposite in the modelled CLV vs. μ (Fig. 5.5) for the SB scenario, whereas in the DR scenario we find negligible convective velocities.

Model Comparison

We computed the Bayesian information criterion (BIC) and Akaike information criterion (AIC) for each model. Their relative values to the minimum are listed in Table 5.2. The only model that is confidently ruled out is SB rotation with no CLV, at ΔBIC=74 and ΔAIC=73. The slightly preferred model is SB rotation with CLVs quadratic in $\langle\mu\rangle$. The models with DR all have ΔBIC and ΔAIC < 5, and thus are statistically similar descriptions of the model.

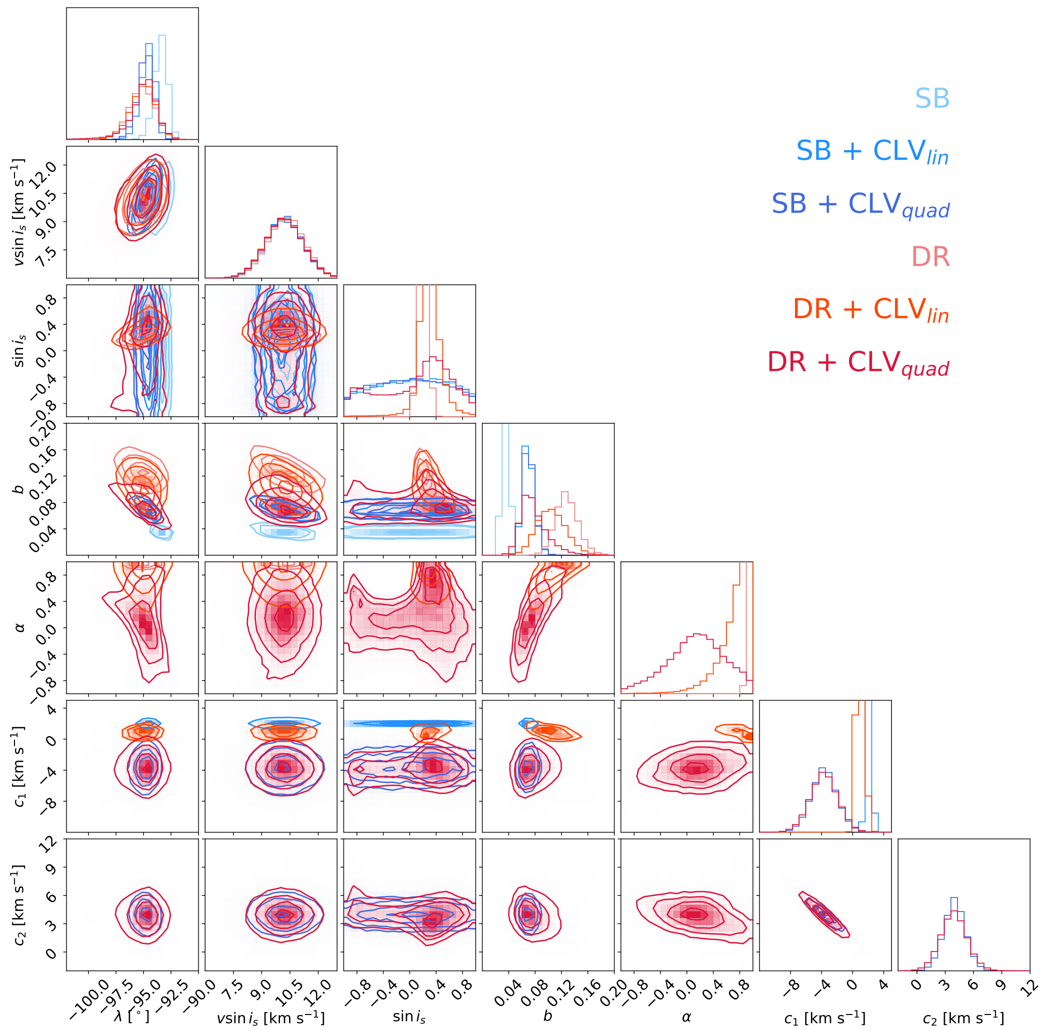

Figure 5.6: The posterior distributions for all RRM parameters. The models with DR are colored red while SB models are colored blue, and models with no, linear, or quadratic CLVs are given progressively darker colors. All models generally agree on the value of λ, while models with DR tend towards extreme values of α at near-polar $i_\star$. This degeneracy arises because of the tight prior on $v \sin i_\star$ (2nd column), which all models are confined to.

Table 5.2: Best-fit Parameters and Model Comparison

Parameter	SB	SB+CLV$_{\rm lin}$	SB+CLV$_{\rm quad}$	DR	DR+CLV$_{\rm lin}$	DR+CLV$_{\rm quad}$
Best-Fit						
λ (°)	$-93.4^{+0.6}_{-0.6}$	$-94.6^{+0.6}_{-0.7}$	$-94.8^{+0.7}_{-0.7}$	$-95.2^{+1.2}_{-1.2}$	$-95.0^{+1.0}_{-1.2}$	$-94.9^{+1.0}_{-1.3}$
$v \sin i_\star$ (km s^{-1})	$10.2^{+1.0}_{-1.0}$	$10.2^{+1.0}_{-1.0}$	$10.2^{+1.0}_{-1.0}$	$10.3^{+1.0}_{-1.0}$	$10.2^{+1.0}_{-1.0}$	$10.2^{+1.0}_{-1.0}$
$\sin i_\star$	$0.03^{+0.6}_{-0.63}$	$0.06^{+0.59}_{-0.64}$	$0.0^{+0.6}_{-0.61}$	$0.2^{+0.06}_{-0.05}$	$0.29^{+0.15}_{-0.12}$	$0.22^{+0.38}_{-0.81}$
b	$0.035^{+0.006}_{-0.005}$	$0.069^{+0.01}_{-0.008}$	$0.07^{+0.009}_{-0.009}$	$0.127^{+0.018}_{-0.016}$	$0.104^{+0.023}_{-0.021}$	$0.075^{+0.023}_{-0.015}$
α	—	—	—	$0.98^{+0.01}_{-0.03}$	$0.8^{+0.14}_{-0.27}$	$0.15^{+0.42}_{-0.45}$
c_0 (km s^{-1})	—	$2.1^{+0.2}_{-0.3}$	$-3.7^{+1.7}_{-1.6}$	—	$0.9^{+0.6}_{-0.4}$	$-3.7^{+1.8}_{-1.8}$
c_1 (km s^{-1})	—	—	$4.0^{+1.1}_{-1.1}$	—	—	$3.9^{+1.4}_{-1.4}$
ΔBIC	74.0	9.2	0.0	1.5	3.4	3.0
ΔAIC	73.0	8.5	0.0	0.7	3.4	4.3
Derived						
ψ (°)	$89.7^{+2.1}_{-2.0}$	$89.5^{+2.8}_{-2.7}$	$89.2^{+3.0}_{-2.8}$	$89.6^{+0.4}_{-0.3}$	$90.2^{+0.9}_{-0.6}$	$90.1^{+2.1}_{-3.5}$

Values and their uncertainties represent 68% credible intervals as defined by the 16th, 50th, and 84th percentiles of the sampled posterior. Models with SB rotation do not constrain $\sin i_\star$, whereas models with DR prefer large α and small $\sin i_\star$ (Fig. 5.6). Posteriors in ψ are derived self-consistently using only the posterior samples in $\sin i_\star$. That is, they do not incorporate any information about the rotation period.

The model with DR alone requires an extremely high values of α, in the 0.9–1 range. While it is not impossible for the stellar poles to rotate at just 10% the rate of the equator, it seems extremely unlikely for a star to have a rotational shear of this magnitude. Slowly rotating ($v \sin i_\star \lesssim 50$ km s^{-1}) F-type stars do commonly show signs of differential rotation ($\alpha \geq 0.1$), whereas rapid rotators do not (Reiners and Schmitt, 2003). Our analysis of the TESS photometry in Section 5.2 more likely places KELT-18 in the former category of slow rotators. Interestingly, the DR model with linear CLVs finds a smaller $\alpha = 0.8^{+0.14}_{-0.27}$, and the flexibility of the quadratic CLV model results in an unconstrained α, as the two effects are degenerate. In contrast, the SB models rely on strong CLVs to generate the measured curvature (Fig. 5.5). It is therefore ambiguous from the RV$_{\rm loc}$ time series alone whether the curvature is coming from a significant differential rotation, CLVs, or a mixture of the two. The difference between these two cases is greatest at low $\langle\mu\rangle$, i.e. near the disk limb. This is where CLV effects are strongest whereas DR is only affected by the subplanet stellar latitude. However, the data near disk limb (i.e. near ingress/egress) are the lowest S/N observations, weakening their utility as a discriminatory lever-arm.

If the star is differentially rotating, the varying line-of-sight rotational velocities as a function of stellar latitude break the $\sin i_\star$ degeneracy, allowing an independent constraint on the stellar inclination. In the DR-only model, the resulting stellar inclination is $i_\star = 11.8^{+3.3}_{-3.2}$. This value is in agreement with the 5–30° range expected from the estimated rotation period and known R_* (Section 5.2). Consequently, the true 3D obliquity can be determined via the equation

$$\cos\psi = \cos i_\star \cos i_{\rm orb} + \sin i_\star \sin i_{\rm orb} \cos\lambda. \tag{5.5}$$

The corresponding values of ψ for each of fitted models are listed in Table 5.2. For the SB models, the posterior in $\sin i_\star$ is unconstrained (uniform in 0 to 1) so this represents the maximally uncertain value of ψ. For instance, if we adopt $\lambda = -94.8 \pm 0.7^\circ$ from the best-fitting SB+CLV$_{\rm quad}$ model, and take $i_\star$ to be isotropic (uniform in $\cos i_\star$), then $\psi = 93.8^{+1.6\circ}_{-1.8}$. If instead we take $i_\star$ to be isotropic within 5–30° as suggested from photometric analyses, we get $\psi = 91.0^{+0.6\circ}_{-0.7}$. Our estimated obliquity measurements are consistent within 1σ across all models, thus we adopt the SB+CLV$_{\rm quad}$ model as our preferred fit as it is both the best-fitting model by the ΔBIC and ΔAIC tests, is more physically justified than the $\alpha \sim 0.9$ models, and utilizes photometric constraints on the stellar inclination rather than the values from the RRM posteriors.

5.5 Orbital Dynamics

KELT-18 b joins the population of close-in planets orbiting hot stars in polar orbits (Albrecht, Dawson, and Winn, 2022). There are no other known transiting planets in the system (Maciejewski, 2020), though there is a stellar companion, KELT-18 B (Section 5.2). It is likely that KELT-18 B influenced the orbital evolution of KELT-18 b. In this section we examine possible mechanisms.

Hierarchical triple systems such as KELT-18, KELT-18 b, and KELT-18 B will experience von-Zeipel-Kozai-Lidov (ZKL) oscillations if the mutual inclination between the two orbiting bodies is larger than 39.2° (Naoz, 2016). ZKL oscillations are usually suppressed for planets on HJ-like orbits because of the general relativistic precession of the argument of periapsis. However ZKL oscillations may have taken place early in the system's history if KELT-18 b formed at a further orbital distance. Fabrycky and Tremaine (2007) showed that such a scenario can lead to HEM, producing the HJ we see today in a close-in, highly misaligned orbit.

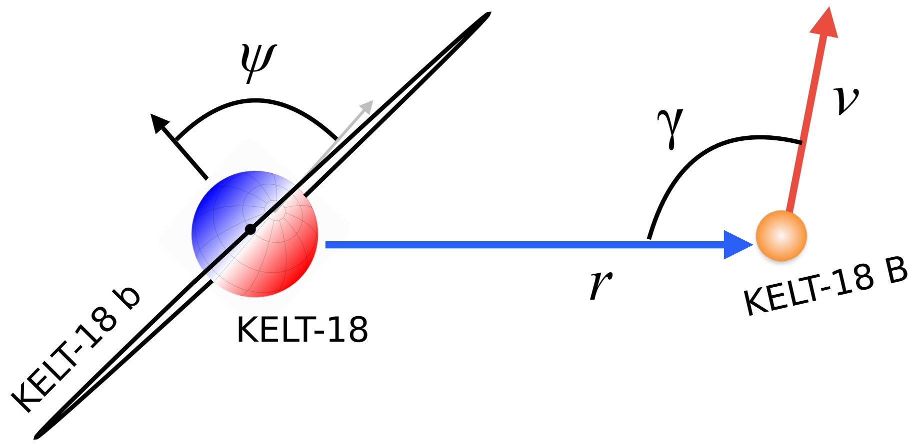

Figure 5.7: On-sky geometry of the KELT-18 system. KELT-18 and KELT-18 b (and its orbit) are drawn to scale in size and relative orientation. The black arrow denotes the normal to KELT-18 b's orbital plane and the grey arrow denotes the rotation axis of KELT-18; the angle between these in 3D space is the stellar obliquity, ψ, while λ is the sky-projection of this angle and is independent of the stellar inclination. The separation between KELT-18 and KELT-18 B is not to scale and is drawn at an arbitrary orientation on-sky. KELT-18 is colored according to its rotational velocity profile (with no differential rotation) and lines of latitude/longitude are drawn to illustrate the orientation of the pole ($i_\star = 30°$). The angle between the binary star position vector ($\vec{r}$, blue arrow) and relative proper motion ($\vec{v}$, red arrow), γ, is labelled.

The *Gaia* astrometry enables a constraint on the inclination of KELT-18 B's orbit. The angle between the vector connecting the astrometric positions of the two stars ($\vec{r}$) and the difference in velocity vectors ($\vec{v}$), called γ (e.g., Tokovinin and Kiyaeva, 2015; Hwang, Ting, and Zakamska, 2022, see Fig. 5.7), encodes information about the companion's orbital inclination (though is degenerate with eccentricity). If $\gamma \sim 0°$ or $180°$, then the companion's orbit is viewed edge-on. Otherwise, the companion's orbit may be viewed face-on or at some intermediate inclination. Since KELT-18 b transits, we know it has $i_{\mathrm{orb}} \sim 90°$, so γ can test for mutual (mis)alignment. We calculated $\gamma = 95.2 \pm 6.4°$, which is most consistent with a low orbital inclination for a circular KELT-18 B and thus a large mutual inclination (Fig. 5.7).

For ZKL to excite KELT-18 b's orbit, it must have formed far away from its host star. By equating the timescales for GR precession and ZKL oscillations, one can solve for the minimum orbital separation at which ZKL oscillations are not quenched by GR (Eq. 4 of Dong, Katz, and Socrates, 2014). We computed this value for the KELT-18 system and obtained $\gtrsim 6.6 \pm 0.25$ AU. In other words, if KELT-18 b was born beyond 6.6±0.25 AU, for instance via traditional core accretion beyond the ice-line, then it could have plausibly migrated to its current orbit via ZKL-induced HEM. B22 calculated typical minimum formation distances of 0.5–10 AU across the broader population of HJs for binary star induced ZKL HEM migration, which conspicuously aligns with the peak in cold Jupiter occurrence around 1–10 AU (Fulton et al., 2021). Future studies of KELT-18 b's atmosphere via transmission spectroscopy (Householder, A., Dai, F., et al. in prep) will seek additional evidence for KELT-18 b's birth conditions by measuring its inventory of refractory and volatile elements, the fingerprints of the original planetary building blocks (Lothringer et al., 2021).

It may also be the case that KELT-18 b formed in a protoplanetary that was primordially misaligned, as can be the case when an outer stellar companion is involved (Batygin, 2012). Alternatively, the stellar companion may have torqued the outer regions of the protoplanetary disk into a misalignment, producing a broken protoplanetary disk which itself can play the role of an outer perturber in exciting large stellar obliquities (Epstein-Martin, Becker, and Batygin, 2022). Vick, Su, and Lai (2023) showed that such an initial configuration, in which the star has a disk-induced nonzero obliquity relative to the proto-HJ before ZKL oscillations induced by the stellar companion initiate HEM, the final obliquity distribution of the HJ is broadly retrograde with a peak near polar orbits. This is in contrast with the classical picture of ZKL starting with initially aligned planetary orbits, which produce HJs with a bimodal obliquity distribution near 40° and 140° (Anderson, Storch, and Lai, 2016). Thus it may be that the orbit of KELT-18 b was already misaligned with the star's rotation before undergoing HEM into its present day HJ orbit, the result of which is an orbit with $\psi \sim 90°$ rather than 40° or 140°.

5.6 Conclusion

We have presented the first science results from KPF on the Keck-I telescope: a transit of the inflated ultra-hot Jupiter KELT-18 b. We found the orbit to be nearly perpendicular to the stellar equatorial plane: $\psi = 91.0^{+0.6}_{-0.7}{}^{\circ}$. This result is robust to model choice and is largely constrained by the tight posterior on $\lambda = -94.8 \pm 0.7°$ and the relatively low value of $v \sin i_\star$. Taken in context with the binary stellar companion, which we find to be on a likely bound orbit that could be orthogonal to KELT-18 b's orbit, a history of ZKL-induced HEM is plausible if KELT-18 b formed beyond about 6 AU from its host star. Our main observational takeaways are as follows:

- We searched the available TESS photometry for clues as to the rotation period of the host star and found evidence for modulation around $\sim$5 days. We did not see variability at 0.707 days as previously reported by M17 using KELT photometry. Both values are consistent with the tendency for F-type stars to have < 8 day rotation periods, and when combined with the measured $v \sin i_\star$ imply a near pole-on viewing geometry ($i_\star \lesssim 30°$).

- The stellar neighbor KELT-18 B is highly likely to be a bound companion, based on *Gaia* DR3 astrometry. Its orbit is also likely orthogonal to KELT-18 b's orbit, based on the angle between the on-sky position vector and proper motion vectors.

- We observed evidence of CLVs, as traced by the FWHM of the local line profile beneath the planet's shadow. The FWHM increased towards the disk limb by nearly a factor of two, in agreement with previous 3D MHD simulations of velocity flows in the near-surface layers of F-type stellar atmospheres.

- We modelled the centroid of the local line profile using the RRM technique and found that either strong differential rotation ($\alpha = 0.9$) or CLVs are needed to explain the curvature in the local RV time series. However, all of the models produce consistent, well-constrained posteriors for the sky-projected obliquity. Ambiguity between DR and CLVs is a common challenge of the RRM technique (see e.g. Roguet-Kern, Cegla, and Bourrier, 2022; Doyle et al., 2023) and is complicated by the uncertainty in the stellar inclination (and thus the stellar latitudes occulted). A firm detection of a stellar rotation period from additional photometry would enable a better constraint of the degree of DR needed to explain the data. As it stands, the polar transiting geometry requires a low (near pole-on) stellar inclination in order to generate the observed curvature in the local RV timeseries, with maximum blueshift occulted at ingress/egress and near-zero velocity occulted at mid-transit. An edge on stellar inclination would produce the opposite effect, since the lowest velocity latitudes at the poles would instead be occulted at ingress/egress, while the maximum velocity latitude (the equator) would be occulted at mid-transit. If KELT-18 does have an edge-on stellar inclination, then DR would be inconsistent with the data and CLVs would be strongly favored.

- The 3D orbital geometry of the KELT-18 system is explainable by a history of ZKL-induced migration, providing support for the HEM formation pathway for HJs. Future work will further test this by inventorying the elemental abundances in KELT-18's atmosphere, connecting the planet to the disk in which it formed.

5.7 Acknowledgements

We are grateful to Heather Cegla and Michael Palumbo for illuminating discussions on center-to-limb variations. Some of the data presented herein were obtained at Keck Observatory, which is a private 501(c)3 non-profit organization operated as a scientific partnership among the California Institute of Technology, the University of California, and the National Aeronautics and Space Administration. The Observatory was made possible by the generous financial support of the W. M. Keck Foundation. Keck Observatory occupies the summit of Maunakea, a place of significant ecological, cultural, and spiritual importance within the indigenous Hawaiian community. We understand and embrace our accountability to Maunakea and the indigenous Hawaiian community, and commit to our role in long-term mutual stewardship. We are most fortunate to have the opportunity to conduct observations from Maunakea.

R.A.R. acknowledges support from the National Science Foundation through the Graduate Research Fellowship Program (DGE 1745301). This paper made use of data collected by the TESS mission and are publicly available from the Mikulski Archive for Space Telescopes (MAST) operated by the Space Telescope Science Institute (STScI). All the *TESS* data used in this paper can be found in MAST (MAST, 2021). This research was carried out, in part, at the Jet Propulsion Laboratory and the California Institute of Technology under a contract with the National Aeronautics and Space Administration and funded through the President's and Director's Research & Development Fund Program.

Chapter 6

KPF CONSTRAINS THE OBLIQUITY OF THE EXTREMELY ECCENTRIC SUB-SATURN KEPLER-1656 B

Rubenzahl, R. A. et al. (2024). "KPF Constrains the Obliquity of the Extremely Eccentric Sub-Saturn Kepler-1656 b" *Submitted to The Astrophysical Journal Letters*

6.1 Introduction

High-eccentricity migration (HEM) is a leading explanation for the formation of close-in giant exoplanets, such as hot Jupiters (HJs), with orbital periods less than 10 days (Dawson and Johnson, 2018; Rice, Wang, and Laughlin, 2022). In the HEM scenario, the giant planet forms beyond a few AU and is excited to extremely high eccentricity ($e > 0.9$) either through planet-planet scattering (Rasio and Ford, 1996, e.g.,) or secular interactions with an outer planetary or stellar companion (Fabrycky and Tremaine, 2007; Naoz et al., 2011; Teyssandier et al., 2013). To excite large enough eccentricities, the companion must either possess a large mutual inclination to the inner planet, in which case von-Zeipel Kozai-Lidov (ZKL; Kozai, 1962; Lidov, 1962; Ito and Ohtsuka, 2019) oscillations can occur, or the companion must have an eccentric orbit, in which case higher-order eccentric Kozai-Lidov (EKL; Naoz et al., 2013b; Naoz et al., 2013a; Naoz, 2016) oscillations can yield the same result. Subsequently, tidal interactions with the star at periastron passage (e.g., Rasio and Ford, 1996; Wu, 2018) circularize the orbit, causing the planet to migrate. The HEM process can also increase the stellar obliquity, the angle between the host star's rotation axis and the normal to the exoplanet's orbital plane. Obliquity damping mechanisms may then come into play, as we observe HJs to be aligned around cool stars (below the Kraft Break, $\lesssim 6250$ K; Kraft, 1967) and misaligned around hot stars (Winn et al., 2010a; Schlaufman, 2010; Albrecht, Dawson, and Winn, 2022). Cool stars are able to damp HJ obliquities faster than the age of the system either through tidal effects in their convective envelopes (Albrecht et al., 2012; Lai, 2012; Dawson, 2014) or resonance locking in their radiative cores (Zanazzi, Dewberry, and Chiang, 2024).

There is no reason, however, that HEM should be limited to giant planets. Many small (< 100 M$_\oplus$) close-in exoplanets likely migrated from further out in their protoplanetary disks, as evidenced by their large envelope mass fraction (e.g., WASP-107 b, Piaulet et al. 2021) and/or highly inclined orbit (Albrecht, Dawson, and Winn, 2022; Attia et al., 2023). Misaligned orbits could arise from the HEM process or be excited post-formation through interactions such as resonance crossing during the disk-dispersal stage (Petrovich et al., 2020) or nodal precession cycles (Yee et al., 2018; Rubenzahl et al., 2021), in either case with the same outer companion that triggered HEM. Though, the census of outer companions to close-in small planets with measured obliquities is relatively incomplete. Only HAT-P-11 (Yee et al., 2018) and WASP-107 (Piaulet et al., 2021) have fully-resolved outer companions. While these mechanisms require a large mutual inclination between the inner and outer planet, only HAT-P-11 has a mutual inclination measurement (near polar; Xuan and Wyatt, 2020).

If exoplanets do experience HEM, then we should expect to observe of order a few systems in the act of migration (Socrates et al., 2012). Approximately half a dozen known exoplanets have an eccentricity and semimajor axis such that the tidal circularization timescale is less than the age of the system (so the planet's orbit should still be circularizing), and such that the planet is not expected to be engulfed by its host star; see Figure 6.1. Several of these have obliquity measurements. Most recently, the proto-HJ TOI-3362 b (Dong et al., 2021) was found to be aligned to within 3° (Espinoza-Retamal et al., 2023). This striking result indicates that perhaps some planets are able to migrate without obtaining a large obliquity. Petrovich (2015a) found that coplanar HEM (CHEM) can occur as a result of EKL oscillations between an outer planetary perturber ("c") and the inner proto-HJ ("b"), provided the outer planet be relatively eccentric ($e_c > 0.67$ if $e_b = 0$ or both e_b, $e_c > 0.5$) and the planets maintain a low mutual inclination ($< 20°$). However, any outer planetary companions in the TOI-3362 system remain undetected.

Kepler-1656 b is another such highly eccentric exoplanet ($e_b = 0.84 \pm 0.01$, 48 M$_\oplus$, 31 day; Brady et al., 2018), and is the only known member of this class less massive than 100 M$_\oplus$. Kepler-1656 b is also the only highly eccentric exoplanet with a known outer planetary companion. Angelo et al. (2022) discovered Kepler-1656 c ($M_c \sin i_{\mathrm{orb},c} = 0.4 \pm 0.1$ M$_{\mathrm{Jup}}$), a giant planet in a

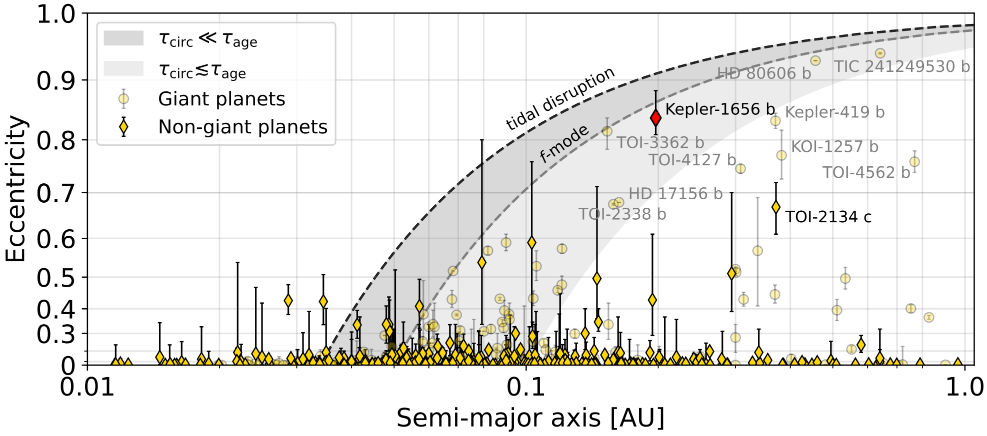

Figure 6.1: Eccentricity-semimajor axis diagram for transiting exoplanets. Giant planets, defined as >100 $M_\oplus$ or >8 $R_\oplus$ if there is no mass measurement, are plotted as faded points. Following Dong et al. (2021), the y-axis is scaled uniformly in e^2, and the high-eccentricity migration track is shaded in light grey. The dashed grey line traces $a = 0.05/(1 - e^2)$, corresponding to the minimum semimajor axis to excite f-mode oscillations and produce rapid orbital decay (Wu, 2018). Planets above this line would therefore be extremely rare. The black dashed upper boundary $(0.034/(1-e^2))$ represents the line of constant angular momentum where a 1 M_J, 1.3 R_J exoplanet would become tidally disrupted at its closest approach to a solar mass star (Dong et al., 2021); no giant planets can persist above this boundary. The lower boundary $(0.1/(1 - e^2)$ corresponds to a final semimajor axis of 0.1 AU, beyond which circularization timescales become much longer than typical system ages. The boundaries are not exact as they depend on the strength and efficiency of tides in the system. Exoplanets with $e > 0.6$ are labelled; Kepler-1656 b is the only sub-Saturn firmly in the HEM track. Data are from the NASA Exoplanet Archive, accessed on 2024-04-01 (NASA Exoplanet Archive, 2019).

wide (~2000 day) and eccentric ($e_c = 0.53 \pm 0.05$) orbit. These authors ran a suite of dynamical integrations using the EKL formalism (Naoz, 2016) and found that those which matched the observed system properties either rapidly ($\lesssim$ 1 Gyr) circularized into a HJ-like orbit (or in a few cases crashed into the star), or achieved high eccentricity through EKL oscillations which could persist much longer than the age of the system (6.3 Gyr) without inducing tidal migration. These solutions tended to occur at high (60°–130°) mutual inclinations and would often ($\gtrsim$ 75%) excite planet b to large stellar obliquities ($> 40°$).

In this letter, we report our measurement of the stellar obliquity of Kepler-1656 b. We present our observations of a single transit of Kepler-1656 b with the Keck Planet Finder in Section 6.2. In Section 6.2 we modeled the Rossiter-McLaughlin (RM; Rossiter, 1924; McLaughlin, 1924) effect in our transit radial velocity time series and derived a projected stellar obliquity of $|\lambda| = 35.0^{+14.9}_{-21.6}{}^{\circ}$, though the data are fully consistent with an aligned orbit. We discuss the implications of this result on the dynamical history of the system and place Kepler-1656 b in the context of the broader exoplanet population in Section 6.3, and conclude in Section 6.4.

6.2 Obliquity Measurement

Observations

We observed a single transit of Kepler-1656 b on UT June 30, 2023 with the Keck Planet Finder (KPF; Gibson et al., 2016; Gibson et al., 2018; Gibson et al., 2020). We used a fixed exposure time of 480 sec to average over solar-type oscillations (Brown et al., 1991; Chaplin et al., 2019) and reach a typical signal-to-noise ratio (S/N) of 100. We used the public KPF data reduction pipeline (DRP)[1] to derive cross-correlation functions (CCFs; Baranne et al., 1996) using the G2 ESPRESSO mask (Pepe et al., 2002) and obtained the radial velocity (RV) as the centroid of a fitted Gaussian. We separately extracted an RV from the green and red channels of KPF and combined the two in a weighted average, taking the weight to be proportional to the relative flux in each channel and constant in time. The resulting RV time series (shown in Figure 6.2) spans a baseline from 1 hr before to 1 hr after the transit.

Rossiter-McLaughlin Modeling

We fit the RV time series using `rmfit` (Stefànsson et al., 2022), a Python-based model for the anomalous RV produced by the RM effect based on the equations of Hirano et al. (2011). We adopted the ephemeris from Brady et al. (2018) based on their fits to the *Kepler* transit light curves and adopted their fitted values as Gaussian priors for the time of conjunction (t_c), orbital period ($P_{\rm orb}$), transit depth (R_p/R_*), scaled semimajor axis (a/R_*), orbital inclination ($i_{\rm orb}$), orbital eccentricity (e), and argument of periastron (ω). Limb darkening coefficients for the KPF bandpass (V) were computed with `EXOFAST` (Eastman, Gaudi, and Agol, 2013), incorporating the spectroscopic $T_{\rm eff}$ (5731 ± 60 K), [Fe/H] (0.19 ± 0.04), and $\log(g)$ (4.37 ± 0.10) from Brady et al. (2018).

[1]https://github.com/Keck-DataReductionPipelines/KPF-Pipeline/

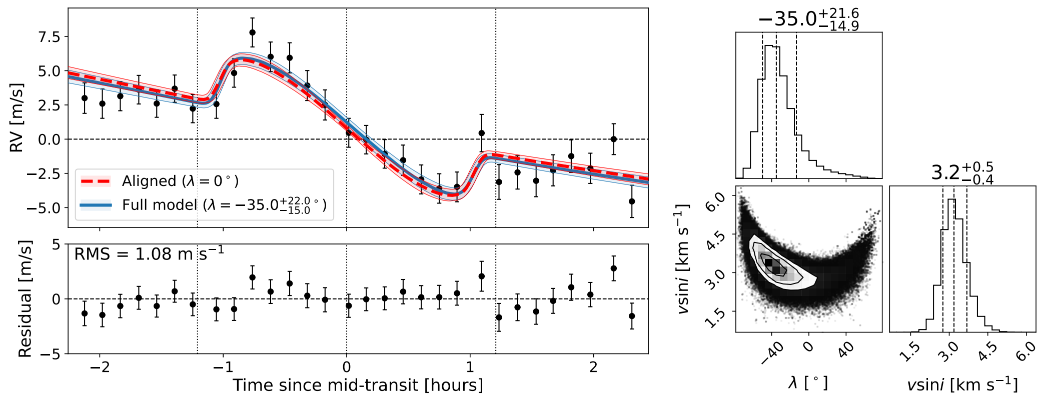

Figure 6.2: **Left:** The KPF RV time series, in black, during the transit of Kepler-1656 b. The blue curve shows the median RV from the posterior distribution of the full model, with the shaded band denoting the 16th–84th percentiles. The red curve shows the same for the aligned model where λ is fixed to 0°. The bottom panel shows the residuals to the median full model. **Right:** The posterior distribution for λ and $v \sin i_\star$ for the full model. Misaligned λ requires $v \sin i_\star > 3$ km s^{-1}.

There are two existing literature measurements of $v \sin i_\star$ for Kepler-1656. The California-*Kepler* Survey (Petigura et al., 2017) reported a value of 2.8 ± 1.0 km s^{-1} from a `SpecMatch-Synthetic` (Petigura, 2015) analysis of a Keck-HIRES spectrum. We reanalyzed the same HIRES spectrum with `SpecMatch-Synthetic` and instead obtained an upper bound of < 2 km s^{-1}, which `SpecMatch-Synthetic` reports if the spectrum is dominated by instrument broadening. However, Masuda, Petigura, and Hall (2022) found while analyzing > 100 Keck/HIRES FG-type spectra that the population-level distributions obtained by applying `SpecMatch-Synthetic` to their sample were more consistent if upper-limits were instead interpreted as < 3 km s^{-1}. Kepler-1656 also appeared in the catalog of Brewer et al. (2016), who found a smaller $v \sin i_\star$ of 1.1 km s^{-1} with 3.2 km s^{-1} macroturbulence, though this is also likely limited by instrumental broadening. As a result, we opted to place a Gaussian prior on $v \sin i_\star$ of 2.8 ± 1.0 km s^{-1} from the CKS result and not restrict $v \sin i_\star$ to any upper-bound.

The main free parameter in our model is the sky-projected obliquity, λ. The parameter quantifying the non-rotational line broadening, v_β, was unconstrained by the RM data, so we fixed this value to 3 km s^{-1} based on a 2.6 km s^{-1} (FWHM) instrumental broadening from KPF and the intrinsic line dispersion for $T_{\rm eff} = 5731$ K from Eq. (20) in (Hirano et al., 2011). Our model is a combination of a Keplerian RV signal and the RM effect, with an arbitrary offset term (γ). For the Keplerian term, we adopted the best-fit K_b from Angelo et al. (2022) as a prior. Because of the low amplitude of the RM signal ($\sim$4.5 m s^{-1}), we also included the convective blueshift effect parameterized by v_{CB} using the prescription of Shporer and Brown (2011), which can contribute at the m s^{-1} level. We set a wide prior of $\pm$10 km s^{-1} on v_{CB}. Lastly, we include a RV jitter term ($\sigma_{\rm jit}$) to account for any underestimated white noise.

We first found the maximum a-posteriori (MAP) solution using the `PyDE` differential evolution optimizer (Parviainen, 2016). This solution was used as a starting point for a Markov-Chain Monte Carlo (MCMC) exploration of the posterior. We ran an `EnsembleSampler` with 100 walkers using the package `emcee` (Foreman-Mackey et al., 2013), each of which obtained 30,000 samples. We discarded the first 10% as "burn-in" and checked for convergence by requiring the Gelman–Rubin statistic (Gelman et al., 2003) be $\ll$ 1% of unity for all parameters and ensuring that the autocorrelation time was $<$ 2% the length of the independent chains per walker (Hogg and Foreman-Mackey, 2018). The posteriors in λ and $v \sin i_\star$ were unaffected by the inclusion of v_{CB}, which itself is orthogonal to the RM effect and was not detected ($v_{CB} = -560 \pm 930$ km s^{-1}). As a result, we fixed $v_{CB} = 0$ km s^{-1} in our final fit.

Our best-fitting RM model, shown in Figure 6.2, has $|\lambda| = 35.0^{+14.9\circ}_{-21.6}$. The negative λ solutions, which the MCMC exploration finds, correspond to $i_{\rm orb} <$ 90°. However, a symmetric positive solution for λ exists for $i_{\rm orb} > 90°$. There is also a degeneracy between λ and $v \sin i_\star$ due to the central (low impact parameter) transit. The RM fit found $v \sin i_\star = 3.2^{+0.5}_{-0.4}$ km s^{-1}, which is consistent with the results from spectral broadening but is also degenerate with varying λ (see Figure 6.2, right panel). The spectral fitting results downweight RM solutions with $v \sin i_\star$ significantly greater than 3 km s^{-1}, i.e., larger values of λ. The full set of fitted parameters is tabulated in Table 6.1.

For comparison, we also fit a model with λ fixed to 0°. This aligned model, also shown in Figure 6.2, produces a fit with statistically indistinguishable goodness-of-fit metrics (χ^2, BIC), though with a slightly larger $\sigma_{\rm jit}$ term (see Table 6.1). The aligned model yielded a lower $v \sin i_\star = 2.7 \pm 0.3$ km s^{-1}, which is slightly more consistent with the spectroscopic constraints. To summarize, neither an aligned model nor one with modest misalignment is ruled out by

Table 6.1: Best-fit RM Parameters

Parameter	Full model	Aligned model	Unit
$\lvert\lambda\rvert$	$35.0^{+14.9}_{-21.6}$	0	$^\circ$
$v \sin i_\star$	$3.2^{+0.5}_{-0.4}$	$2.7^{+0.3}_{-0.3}$	m s^{-1}
$i_{\rm orb}$	$88.9^{+0.5}_{-0.5}$	$89.2^{+0.6}_{-0.6}$	$^\circ$
e	$0.824^{+0.013}_{-0.014}$	$0.824^{+0.013}_{-0.014}$	
ω	$54.5^{+4.7}_{-4.7}$	$54.7^{+4.8}_{-4.7}$	$^\circ$
K	$13.3^{+1.6}_{-1.5}$	$13.4^{+1.7}_{-1.6}$	m s^{-1}
γ	$-5.8^{+1.1}_{-1.1}$	$-5.5^{+1.1}_{-1.2}$	m s^{-1}
$\sigma_{\rm jit}$	$0.51^{+0.37}_{-0.33}$	$0.7^{+0.34}_{-0.36}$	m s^{-1}
ΔBIC	0.0	5.0	
χ^2	0.92	0.95	

Posterior values display the 50^{th} percentile with the upper and lower errorbars giving the difference relative to the 84^{th} and 16^{th} percentiles, respectively. The reduced χ^2 includes the median $\sigma_{\rm jit}$ added in quadrature to the measurement uncertainties.

the data. Without any further information on $v \sin i_\star$, our RM measurement can only constrain $|\lambda| < 57^\circ$ at 95% confidence.

6.3 Discussion

Dynamics in the Kepler-1656 system

As a consequence of Kepler-1656 b's central transit and the uncertainty in $v \sin i_\star$, our RM dataset is consistent with an aligned orbit but cannot rule out a misaligned λ as high as 57° at 2σ confidence. Of the other known exoplanets in the HEM track, only TOI-3362 b and HD 80606 b have obliquity measurements. The former is aligned, with $\lambda = 1.2 \pm 2.8^\circ$ (Espinoza-Retamal et al., 2023). Like Kepler-1656 b, TOI-3362 b orbits a single star, though it is not known if an outer giant planet exists in that system. HD 80606 b, on the other hand, is in a binary-star system and is misaligned, with $\lambda = 42 \pm 8^\circ$ (Pont et al., 2009; Hébrard, G. et al., 2010). Here we revisit plausible dynamics between Kepler-1656 b and c and their implications on b's obliquity.

The simulations conducted by Angelo et al. (2022) that were most consistent with Kepler-1656 b and c's orbital eccentricities and semimajor axes tended towards large mutual inclinations (60°–130°). The highly inclined companion excited e_b either to the point of tidal migration or maintained long-lasting ($>$ the age of the system) eccentricity oscillations. In either case, the inner planet's obliquity tended towards misalignment; only $\sim$10% of simulations yielded $\psi_b < 20^\circ$. In the long-lasting eccentricity oscillation scenario, $\sim$75%

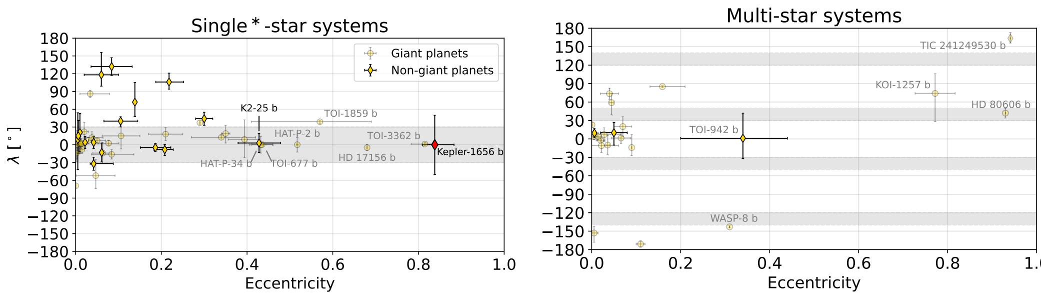

Figure 6.3: Projected obliquity λ for measured systems as a function of eccentricity, for single-star systems (left) and multi-star systems. The shaded bar on the left plot covers $\pm 20°$, the range of obliquities for which CHEM could operate given an appropriate companion with zero stellar obliquity. The shaded bands on the multi-star plot highlight $\pm 10°$ around the angles $\pm 40°$ and $\pm 130°$ corresponding to the bimodal peaks of the expected true obliquity distribution from star-planet Kozai (Anderson, Storch, and Lai, 2016). Note that these angles refer to the true orbital inclinations, while the data points are for λ, the sky projection. The true obliquity ψ is between λ and sign(λ)90°. The data are the same from Figure 6.1, supplemented with updates for HD 80606 b ($42 \pm 8°$; Hébrard, G. et al., 2010) and 55 Cnc e (11^{+17}_{-20}° Zhao et al., 2023a), and the addition of TIC 241249530 b ($163.5^{+9.4}_{-7.7}$°; Gupta, A. et al. in review), TOI-3362 b ($1.2 \pm 2.8°$; Espinoza-Retamal et al., 2023), TOI 677 b ($0.3 \pm 1.3°$; Sedaghati et al., 2023; Hu et al., 2024), and of course Kepler-1656 b, where we have drawn the 1σ upper-limit of 50° (this work).

of simulations produced $\psi_b > 60°$. Simulations that migrated planet b into a tidally locked orbit were more consistent with alignment, though only $\sim$1/3rd had $\psi_b < 60°$.

In the low-mutual-inclination regime, an eccentric ($e_c > 0.2$–0.5) outer companion can still excite the inner planet's eccentricity to large values ($\gtrsim 0.9$), in some cases causing the inner planet's orbit to flip 180° from prograde to retrograde (Naoz et al., 2013b; Li et al., 2014). If the eccentricity grows sufficiently large such that the periastron distance is small enough for strong tidal dissipation, the planet's orbit will shrink and circularize. Petrovich (2015a) showed that throughout this coplanar HEM (CHEM), the migrating inner planet maintains a low stellar obliquity ($\psi < 30°$) so long as the mutual inclination between the two planets is low ($\lesssim 20°$).

Petrovich (2015a) derived the initial criteria for CHEM to operate: either (i) the inner planet begins in a circular orbit, in which case the outer planet must have $e_c \gtrsim 0.67$ and $M_b/M_c(a_b/a_c)^{1/2} \lesssim 0.3$, or (ii) both planets begin eccentric ($e \gtrsim 0.5$) and $M_b/M_c(a_b/a_c)^{1/2} \lesssim 0.16$. Given the posterior distributions in

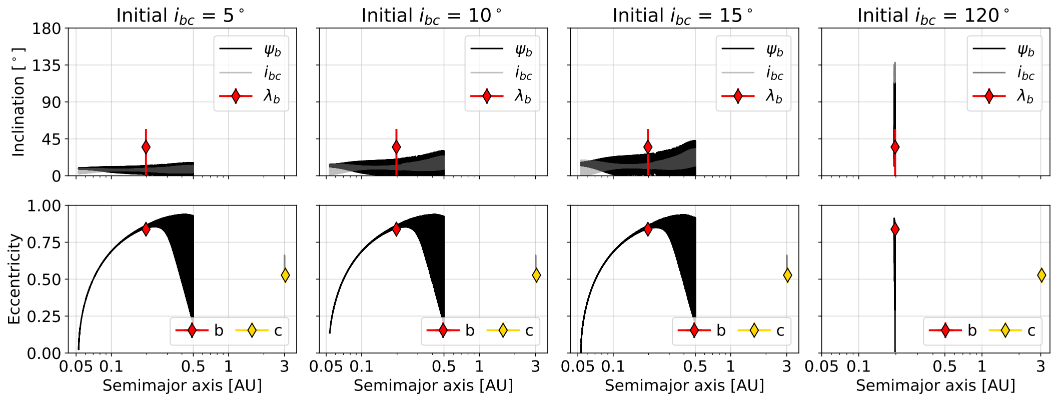

Figure 6.4: Three-body simulations of the orbits of Kepler-1656 b (black) and c (grey), for variable initial mutual inclinations i_{bc}, (5°, 10°, 15°, and 120° from left to right). The top row shows the evolution of the mutual inclination (grey) and the inner planet's obliquity (black), as a function of semimajor axis. The lower panel shows the eccentricity evolution of planet b (black) and c (grey). The first three ($i_{bc} \leq 15°$) are initialized as described in Section 6.3. The fourth ($i_{bc} = 120°$) is an example of a simulation from Angelo et al. (2022) initalized *in-situ* with a circular planet b. All four scenarios can reproduce the observed Kepler-1656 system (red and yellow data points). Though, $i_{bc} \leq 15°$ requires starting planet b at a more distant orbit that subsequently migrates through its present-day location, before circularizing in ~100 Myr; larger mutual inclinations excite large eccentricities without triggering migration, with brief excursions to low obliquity over many ~Gyr. The measured projected obliquity is plotted for the positive-λ scenario (to match $\psi_b > 0$) in the top panel at 35° with errorbars covering 0°–50°.

mass and semimajor axis for both planets (Angelo et al., 2022), this ratio for Kepler-1656 is $M_b/M_c(a_b/a_c)^{1/2} = 0.11 \pm 0.02$, and is less than 0.16 at 99.2% confidence. This calculation assumed $M_c \sin i_{\mathrm{orb},c}$ in place of M_c, i.e., the planets are coplanar. The true mass of Kepler-1656 c may be larger, in which case this ratio would be smaller, still satisfying the CHEM criterion. Thus, given Kepler-1656 c's presently measured eccentricity (0.53 ± 0.05; Angelo et al., 2022), CHEM is a plausible explanation if either Kepler-1656 b formed with–or was able to gain–an eccentricity > 0.5, or if Kepler-1656 c used to be moderately more eccentric ($\gtrsim 0.67$). Such eccentricities are naturally produced by planet-planet scattering events (e.g., Chatterjee et al. 2008).

We integrated the three-body equations of motion expanded to octupole order (Ford, Kozinsky, and Rasio, 2000) as described in the appendix of Petrovich (2015b), given the measured planet masses of Angelo et al. (2022). We initialized planet b with an eccentricity of 0.2 at semimajor axis 0.5 AU and planet c with an eccentricity of 0.67 at its present-day semimajor axis of 3 AU. We included tidal dissipation in planet b parameterized with a 0.01 yr viscous timescale[2] and Love number 0.25. We ran three simulations with the inner planet aligned at 0° obliquity but with the outer planet at 5°, 10°, and 15° mutual inclination. We found in all three cases the inner planet's eccentricity became excited up to 0.94 and underwent oscillations for ∼100 Myr before tidal effects quenched oscillations and triggered planet b's migration into a HJ-like orbit. We stress that while the migration phase of the simulation agrees with the data, it is relatively short-lived ($<$ 100 Myr) and thus has a low probability of being observed. We conclude that CHEM could be operating in the Kepler-1656 system, but the data remain consistent with a non-migrating in-situ formed planet b being observed at a snapshot of high-eccentricity oscillations, as suggested by Angelo et al. (2022). The key to distinguishing these scenarios is the planet-perturber mutual inclination. Unfortunately, at 186 ± 0.5 pc (Gaia Collaboration et al., 2023) Kepler-1656 (V=11.6) is too far for such a measurement with Gaia astrometry. The expected astrometric signal from Kepler-1656 c is just 5.2 μas, but at $G = 11$ we can expect a single-epoch precision of 34.2 μas with Gaia (Perryman et al., 2014).

Kepler-1656 in context

Espinoza-Retamal et al. (2023) noted a dichotomy in eccentric ($e \gtrsim 0.3$) planet obliquities; those in single-star[3] systems tend to be aligned, while those in multi-star systems tend to be misaligned. We plot the updated λ–e diagram in Figure 6.3. For single-star systems, the next most eccentric sub-Saturn ($<$ 100 $M_\oplus$) with a measured obliquity is K2-25 b ($e = 0.43 \pm 0.05$, $\lambda = 3.0 \pm 16.0°$; Stefansson et al., 2020). Kepler-1656 b and HAT-P-2 b (Beurs et al., 2023), a HJ, are the only highly eccentric ($e > 0.3$) exoplanets with fully measured outer planetary companions.

If close-in exoplanets, large and small alike, form primarily from HEM, Figure 6.3 suggests that the identity of the perturber plays the key role in determining the obliquity. In multi-star systems, exoplanets with large obliquities

[2]For simplicity, we have adopted a much lower viscous timescale than Angelo et al. (2022) of 1.5 yr, allowing significant migration within $\sim 10^8$ yr. For reference, a viscous timescale of 0.01 yr (1.5 yr) is equivalent to setting a tidal quality factor of $Q_b \sim 10^4$ ($Q_b \sim 10^6$) at the planet's current location.

[3]*The presence of stellar companions is not homogenously constrained. For simplicity, here we define "single star" to be those in the Exoplanet Archive with `sy_snum==1`.

span a wide range of mutual inclinations with their outer stellar companions (Behmard, Dai, and Howard, 2022; Rice, Gerbig, and Vanderburg, 2024). Though, there is an overabundance of edge-on binary orbits for systems hosting transiting exoplanets compared to field binaries, suggestive of a tendency towards mutual alignment (Dupuy et al., 2022; Rice, Gerbig, and Vanderburg, 2024). It is still a small sample size, but the four oblique and eccentric exoplanets in multi-star systems (see Figure 6.3) have obliquities near those expected from star-planet Kozai (e.g. Anderson, Storch, and Lai, 2016), which requires mutual inclinations $> 39.2°$ (Kozai, 1962; Lidov, 1962; Naoz, 2016). Rice, Gerbig, and Vanderburg (2024) calculated the "linear motion parameter" (γ; Tokovinin and Kiyaeva, 2015), for WASP-8 B ($4.0 \pm 0.5°$) and HD 80606 B ($174.3 \pm 0.3°$). Both are consistent with edge-on orbits and perhaps mutual alignment, which in addition to the wide separation for HD 80606 B would make Kozai less likely. KOI-1257 is unresolved by *Gaia*, preventing an astrometric detection. However, computing γ for TIC 241249530 from its *Gaia* DR3 astrometry (Gaia Collaboration et al., 2023) yields $85.9 \pm 36.0°$, which could indicate a near face-on orbit and thus a significant mutual misalignment. Interpreting inclinations from the γ parameter alone is still poorly constrained and degenerate with eccentricity. Longer baseline multi-epoch astrometry is needed to constrain individual systems.

Exoplanets in single-star systems, by definition, must instead be perturbed by outer planetary companions. Cold Jupiter companions in systems with inner small exoplanets show a tendency towards coplanarity (Masuda, Winn, and Kawahara, 2020). This would preclude classical Kozai oscillations, though eccentric coplanar outer companions could still excite large eccentricities via the EKL mechanism (Naoz, 2016). In such systems, CHEM could produce close-in but aligned planets. On the other hand, large mutual inclinations have been observed in the π Men and HAT-P-11 systems. Both have large (polar) mutual inclinations between inner and outer planet (as evidenced by *Gaia* astrometry; Xuan and Wyatt, 2020). In such systems, ongoing nodal precession will make it more likely than not to observe the planet in a misaligned orbit (Becker et al., 2017). Accordingly, π Men is slightly misaligned ($\lambda = 24 \pm 4.1$; Kunovac Hodžić et al., 2021) and HAT-P-11 b is near-polar ($\lambda = 106^{+15}_{-12}°$; Winn et al., 2010c; Sanchis-Ojeda and Winn, 2011). So while there may not be a mutual inclination requirement for exciting eccentricities, and consequently triggering migration, the obliquity of the inner planet is likely still dependent.

For the closest systems ($<$ 60–100 pc), the full astrometric timeseries in the upcoming Gaia DR4 will enable constraints on the outer planet's inclination (Espinoza-Retamal, Zhu, and Petrovich, 2023).

6.4 Conclusions

We measured the stellar obliquity of Kepler-1656 b from the Rossiter-McLaughlin anomaly observed with the Keck Planet Finder. We found the orbit to be consistent with alignment, but could not rule out misalignments up to 57° at 2σ confidence. Kepler-1656 b is one of four exoplanets to have an obliquity measurement that lives in the HEM track of the $e - a$ diagram. Two of these are in multi-star systems and are misaligned, while TOI-3362 b orbits a single star and is aligned. The mutual inclination of the perturber likely plays a leading role in determining the migration process and subsequently the obliquity of the migrating/migrated planet.

Since obliquity damping is less efficient for small planets ($\tau_\psi \propto (M_p/M_*)^{-2}$; Hut, 1981), the obliquity distribution of small planets offers a more pristine view of post-migration obliquities, analogous to HJs around hot stars. There is a growing population within the < 100 $M_\oplus$ regime of polar orbits (Attia et al., 2023) which has been noted for the HJs (Albrecht et al., 2022) but is not yet statistically robust in that sample (Dong and Foreman-Mackey, 2023; Siegel, Winn, and Albrecht, 2023). Kepler-1656 b represents a rare example of such a proto-hot-Neptune/Saturn that could be in the act of migrating, kick-started by its outer planetary companion. If obliquities are not excited in conjunction with HEM, then post-migration dynamics must be important for exciting the broad obliquity distribution we observe today.

6.5 Acknowledgements

Some of the data presented herein were obtained at Keck Observatory, which is a private 501(c)3 non-profit organization operated as a scientific partnership among the California Institute of Technology, the University of California, and the National Aeronautics and Space Administration. The Observatory was made possible by the generous financial support of the W. M. Keck Foundation. Keck Observatory occupies the summit of Maunakea, a place of significant ecological, cultural, and spiritual importance within the indigenous Hawaiian community. We understand and embrace our accountability to Maunakea and the indigenous Hawaiian community, and commit to our role in long-term mutual stewardship. We are most fortunate to have the opportunity to conduct observations from Maunakea.

R.A.R. acknowledges support from the National Science Foundation through the Graduate Research Fellowship Program (DGE 1745301). A.W.H. acknowledges funding support from NASA award 80NSSC24K0161 and the JPL President's and Director's Research and Develop Fund. CP acknowledges support from ANID BASAL project FB210003, FONDECYT Regular grant 1210425, CASSACA grant CCJRF2105, and ANID+REC Convocatoria Nacional subvencion a la instalacion en la Academia convocatoria 2020 PAI77200076. D.H. acknowledges support from the Alfred P. Sloan Foundation, the National Aeronautics and Space Administration (80NSSC21K0652), and the Australian Research Council (FT200100871).

This research was carried out, in part, at the Jet Propulsion Laboratory and the California Institute of Technology under a contract with the National Aeronautics and Space Administration and funded through the President's and Director's Research & Development Fund Program.

Chapter 7

STARSPOT MAPPING AND OBLIQUITY CONSTRAINTS FOR THE SUBGIANT KEPLER-1658

This chapter presents work still in progress that spurred from an unexpected surprise in one of our KPF datasets–a gigantic starspot. The spot obscures the Doppler shadow of the planet, leading me, in collaboration with Adolfo Carvalho, to develop a custom modeling framework that could forward model a stellar CCF in the presence of spots so that we might remove the effect and reveal the planet signal.

7.1 Introduction

The obliquity distribution of hot Jupiters (HJs) is likely shaped by tidal dissipation. As discussed in Chapter 1.2, this is an observation-driven hypothesis based on the discovery of a transition from alignment to misalignment at the Kraft Break (Winn et al., 2010a). Dissipation of tidally excited inertial waves in the convective envelopes of cool stars can act as a sufficient angular momentum sink to damp obliquities into spin-orbit alignment (Lai, 2012). Additional effects such as resonance locking with g-modes in the radiative cores of cool stars (Zanazzi, Dewberry, and Chiang, 2024) as well as magnetic breaking (Li and Winn, 2016) can also boost the efficiency of obliquity damping. Overall, the star-planet tidal potential is complex[1], nonlinear, and inherently coupled to the evolution of the stellar spin, fluid dynamics in the differentially rotating stellar interior, the elasticity of the planet, and the orbit of the planet (see Ogilvie 2014 for a review). Dissipation in the planet or in the star can act as the energy sink, and the efficiencies at which tides operate can vary in both by orders of magnitude. It is therefore of particular utility to measure the tidal efficiencies by observing tide-driven evolution directly.

A change to one of the orbital elements (e.g., a, e, ψ) adds a small perturbation to the tidal potential, and vice-versa. The corresponding response on the system is different for each orbital element and depends on the corresponding Love number, which itself is a (dimensionless) function of frequency, associated with a particular component of the tidal potential, and depends on the tidal

[1] In both the literal and the mathematical sense.

amplitude as well as the size and elastic modulus of the body. This is generally not known *a priori*, and so tends to get summarized single dimensionless parameter called the tidal quality factor, Q (Goldreich and Soter, 1966), which can span many orders of magnitude. There are very few systems for which orbital evolution has been observed, owing to the incredibly slow timescale ($\gtrsim$Myr) relative to typical observation baselines ($\sim$10 yr).

To-date, orbital decay has only been observed in two systems: WASP-12 b, a 1.4 M_{Jup} HJ in a 1.1 day orbit around a 1.35 $M_{\odot}$ star (Hebb et al., 2009) whose orbit is decaying at a rate of $\dot{P}/P \sim 3$ Myr (Yee et al., 2020), and Kepler-1658 b, a 6 M_{Jup} HJ in a 3.8 day orbit around a 1.4 $M_{\odot}$ star (Chontos et al., 2019) whose orbit is decaying at a rate of $\dot{P}/P \sim 2.5$ Myr (Vissapragada et al., 2022). While both stars are more massive than the Kraft Break, Kepler-1658 is a subgiant that has evolved across the Kraft Break (was $\sim$7200 K, now 6200 K) and now possesses and convective envelope, confirmed by the detection of asteroseismic oscillations (Chontos et al., 2019). Kepler-1658 may have therefore just recently ($<$ 1 Gyr) acquired the ability to tidally damp any primordial obliquity. As a unique system with a tidal constraint from observed orbital decay and an upper limit on realignment timescales set by stellar evolution, an obliquity measurement for Kepler-1658 b would help constrain the efficiency of obliquity damping mechanisms.

One other stellar property of note is the rotation period and observed $v_{eq} \sin i_{\star}$. The *Kepler* lightcurve of Kepler-1658 exhibits strongly coherent variability at the 1 ppt level at a periodicity of 5.66 ± 0.31 days (Chontos et al., 2019). If this is due to photometric modulation by starspots, then the rotational velocity at the spot latitude is 25.82 ± 1.77 km s^{-1} based on their asteroseismic stellar radius. This is significantly smaller than the observed rotational broadening in the Keck/HIRES spectra of 33.95 ± 0.97 km s^{-1}. Chontos et al. (2019) calculated that this difference can be reconciled by a latitudinal differential rotation of 20-40% with the spot placed at a high latitude.

7.2 KPF Observations of Kepler-1658

We observed a transit of Kepler-1658 on UT July 15, 2023 with the Keck Planet Finder (Gibson et al., 2016; Gibson et al., 2018; Gibson et al., 2020). We exposed for 5 minutes to achieve a typical signal-to-noise (S/N) 90–110 in the green channel and $\sim$120 in the red channel. We collected 51 exposures

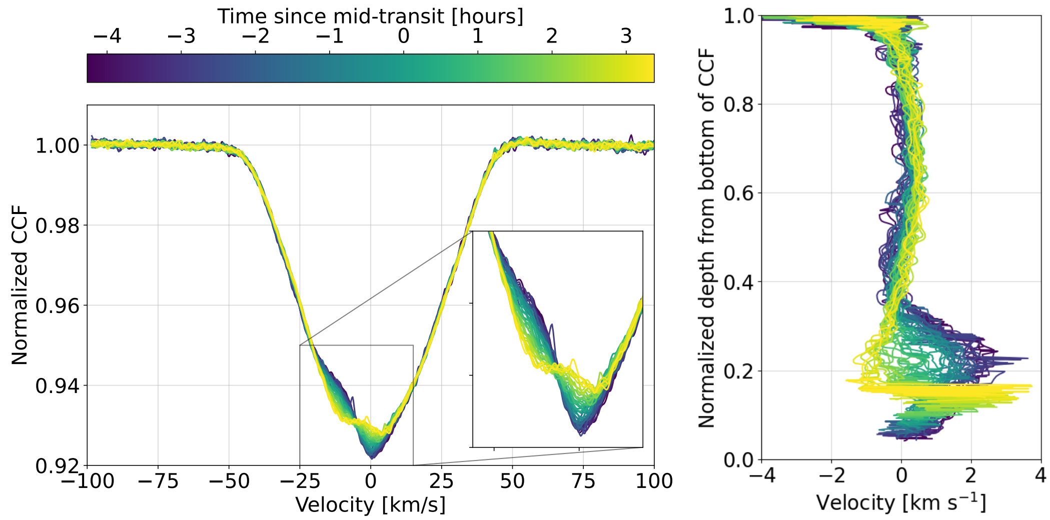

Figure 7.1: **Left:** KPF CCFs for Kepler-1658, shifted to the stellar rest frame. The colorbar denotes the time of the observation. The inset zooms-in on the region which contains the perturbation from the starspot. **Right:** Bisectors computed from the observed CCFs. The C-shape above 0.4 in depth is from a general asymmetry, which only translates as the spot progresses. The distortion below 0.4 is from the spot's effect on the rotational broadening profile.

starting about 3 hours before the predicted ingress time using the ephemeris of Vissapragada et al. (2022) until 2 hours after the predicted egress time, resulting in 16 in-transit exposures. Two exposures were affected by a known issue in the CCD controller failing to terminate the exposure, causing photons to expose the detector while reading out and smearing the image.

The remaining 49 images were processed using the public KPF data reduction pipeline (DRP)[2] which performs dark, bias, and flat-fielding corrections, and extracts 1D spectra using the optimal extraction algorithm (Horne, 1986; Piskunov and Valenti, 2002). The wavelength solution is derived from the evening calibration sets taken with a thorium argon (ThAr) lamp and a Menlo Systems laser frequency comb (LFC). Orders bluer than $\lesssim 490$ nm adopt the ThAr solution while the rest adopts the LFC solution. We derived cross-correlation functions (CCF) using the F9 ESPRESSO mask for each of the three traces per spectral order. The final CCF per observation was obtained by performing a weighted sum first across the three "SCI" traces and then across all orders, taking the weights to be proportional to the total flux at each step. Photon-noise uncertainties were computed using the unweighted

[2]https://github.com/Keck-DataReductionPipelines/KPF-Pipeline/

summed CCF. Lastly, we measured the systemic velocity by fitting a Gaussian to each out-of-transit CCF, masking the portion of the CCF < -50 km s^{-1} and > -10 km s^{-1} (see next paragraph). The result was -23.95 ± 0.06 km s^{-1}, which we shifted the CCFs by to bring into the stellar rest frame.

The resulting time series of CCFs are shown in Figure 7.1. A significant deformation in the blue side of the CCF can be seen to traverse redwards as the time series progresses. Critically, the distortion exists out-of-transit and proceeds at constant velocity in time. This is the signature of a large starspot, which is expected to exist on Kepler-1658 based on the significant photometric variability seen with *Kepler*. We performed the same Reloaded Rossiter-McLaughlin (RRM) analysis as described in Chapter 5 to search for the Doppler shadow of the planet. These steps involved constructing an out-of-transit template $\mathrm{CCF_{out}}$, which by construction will include the averaged distortion from the starspot. We then subtracted the in-transit observations, $\mathrm{CCF_{in}}$, to obtain the local average line profile $\mathrm{CCF_{loc}}$.

The $\mathrm{CCF_{loc}}$ time series is plotted in Figure 7.2. The residuals from the spot dominate the structured variability, with photon noise at around the 500 ppm level. The expected amplitude of the Doppler shadow from Eq. 1.6 is $\sim$1 ppt. This spurred us to model a synthetic $\mathrm{CCF_{out}}$ which includes the perturbations to the CCF in order to remove the structured noise.

7.3 Synthetic CCFs for planets transiting spotted stars

The effects of starspots are commonly observed in both photometry and spectroscopy across all spectral types (e.g., Giles, Collier Cameron, and Haywood, 2017), and present a challenge to extracting the Doppler shadow of a transiting planet (e.g., Zhou et al., 2020; Sicilia et al., 2024). As spots are both physically interesting probes of the stellar magnetic field and nuisances for planet searches, significant effort has been invested in modeling their impact to photometric and spectroscopic data. Some recent examples include `starry` (Luger et al., 2021), which uses spherical harmonics as a basis set for forward modeling surface brightness fluctuations to fit to observed photometric or spectroscopic variability. The Spot Oscillation And Planet (Boisse, Bonfils, and Santos, 2012; Dumusque, Boisse, and Santos, 2014; Zhao and Dumusque, 2023, SOAP,) tool simulates observations of CCFs, and even spectra, for stars with user-defined spot locations and temperatures. SOAP generates synthetic

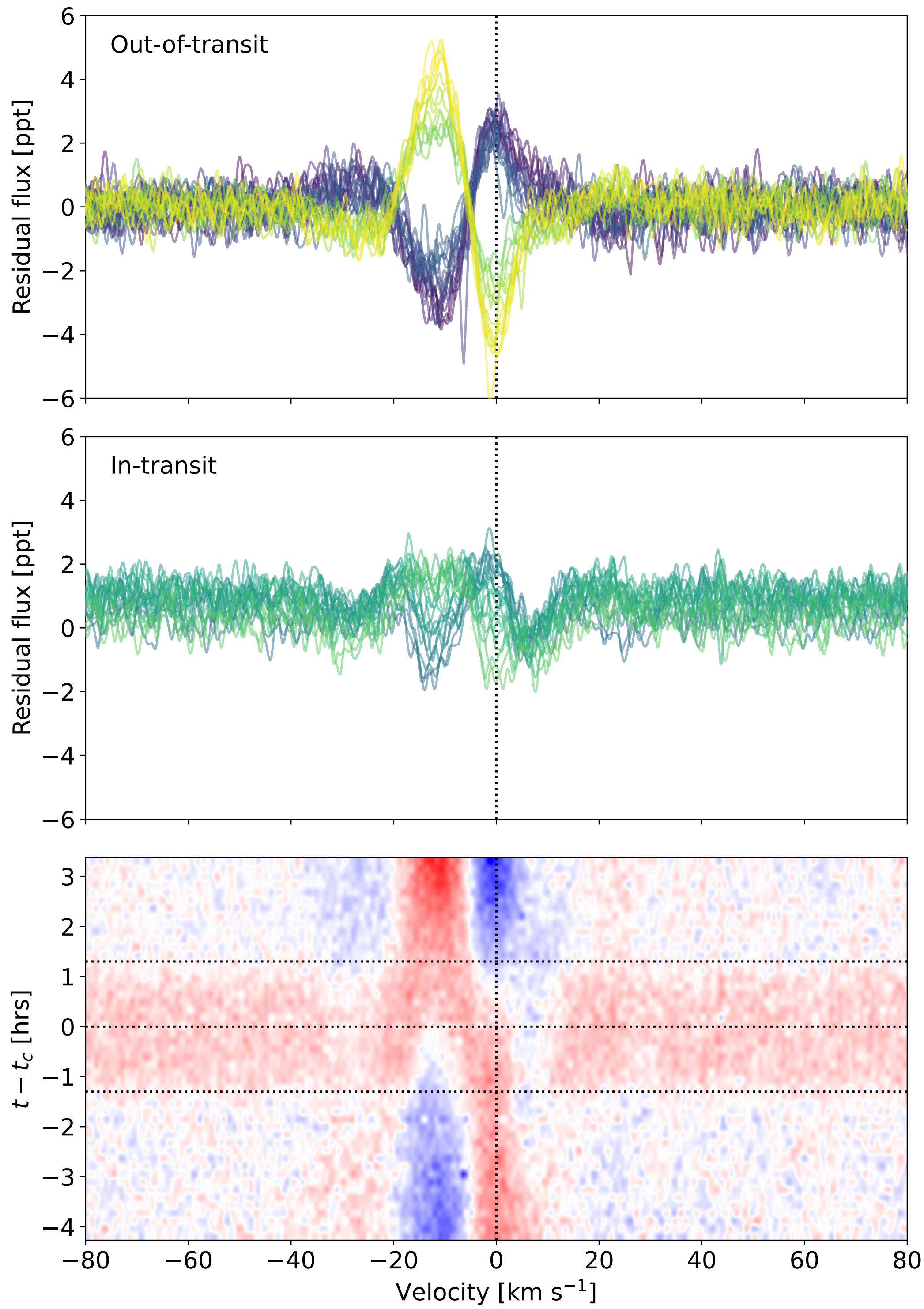

Figure 7.2: **Top:** $\mathrm{CCF_{loc}}$ for the out-of-transit observations. Since the average CCF is removed, these show a symmetric residual Doppler shift from pre to post-transit. **Middle:** $\mathrm{CCF_{loc}}$ for the in-transit observations. The bumps and wiggles are consistent with the self-subtraction of the average starspot; the planet shadow is not visible by eye. The colorscale in this and the top panel is the same as in Figure 7.1. **Bottom:** 2D heatmap of the above, with time on the vertical axis. The planet shadow is not visible.

observations by assigning each patch of the stellar surface its own CCF (or spectrum), and integrating across the rotating disk including the effects of convective blueshift suppression to produce synthetic observations. Solar intensity images from NASA SDO/HMI can even be used as input to define the pixel-level intensity map. More recently, Di Maio et al. 2024 developed the `SpotCCF` tool for the use-case of rapidly rotating stars by focusing just on the impact of a spot to the rotational broadening function.

To model the spot in the Kepler-1658 dataset, we will need to include differential rotation to match the discrepancy between the spot rotation period from photometry and the projected rotational velocity $v_{eq} \sin i_\star$. We also want to include the effects of a transiting planet to enable injection-recovery testing so that we may place limits on the projected obliquity in Section 7.5. As we will also see, we likely need to include convective blueshift suppression and center-to-limb effects to reproduce the observed asymmetries in the CCFs. For these reasons, we developed our own synthetic CCF modeling toolkit. Our model is designed in a user-friendly, object-oriented set of Python modules for ease of use and flexible experimentation. The following sections describe the three components of the model: a star, a set of starspots, and a transiting planet.

The Star

We start with an intrinsic stellar line profile in velocity space, $f(v)$. A non-rotating star will have Gaussian broadening from microturbulence and thermal broadening, as well as pressure broadening which produces a Lorentzian distribution (Gray, 2005). Thus, we take $f(v)$ to be a Voigt profile (convolution of a Gaussian and a Lorentzian) as implemented in `astropy` by the `Voigt1D` function,

$$f(v) = -\texttt{Voigt1D}(A_L, \mathrm{FWHM}_G, \mathrm{FWHM}_L), \tag{7.1}$$

where A_L is the amplitude of the Lorentizian, FWHM_L is its full-width-at-half-maximum (FWHM), and FWHM_G is the FWHM of the Gaussian. $f(v)$ is defined to be centered at zero and to be negative (absorption line). Values for the amplitude and FWHMs can be estimated from a PHEONIX spectrum[3] (Husser et al., 2013) at the given stellar $T_{\rm eff}$, $\log g$, and [Fe/H]. Alternatively, a PHOENIX spectrum could be used as $f(v)$ itself for full-spectrum modeling.

[3]https://phoenix.astro.physik.uni-goettingen.de/

We used the methodology of Carvalho and Johns-Krull (2023) to efficiently numerically integrate the rotational broadening, with a few modifications. First, we adopted the approach of Hirano et al. (2011) to simultaneously account for rotation and macroturbulence, as the two effects are coupled. The broadened CCF is obtained by convolving $f(v)$ with a broadening kernel,

$$F_*(v) = f(v) * M(v), \tag{7.2}$$

where $M(v)$ is

$$M(v) = \iint_{\text{disk}} I(x,\, y, \vec{u})\Theta(v - v_*(x,\, y))dxdy, \tag{7.3}$$

and $\Theta(v)$ is the radial-tangential model for macroturbulence (Gray, 2005),

$$\Theta(v) = \frac{1}{2\sqrt{\pi}}\left[\frac{1}{\zeta\cos\theta}e^{-\left(\frac{v}{\zeta\cos\theta}\right)^2} + \frac{1}{\zeta\sin\theta}e^{-\left(\frac{v}{\zeta\sin\theta}\right)^2}\right]. \tag{7.4}$$

The integral for $M(v)$ (Eq. 7.3) is numerically computed by assigning a grid of points $(x,\, y)$ in the 2D sky-plane across the stellar disk, each with area element $dA = dxdy$. Our coordinate system is a cartisian coordinate system in units of R_* with the x-y plane defining the sky-plane, the y-axis defining the stellar rotation axis, and the z-axis towards the observer (so $z > 0$ is the visible hemisphere). At each point, the macroturbulence kernel Θ (Eq. 7.4) is evaluated at the Doppler-shifted velocity at that position, $v - v_*(x,\, y)$, given the macroturbulent velocity ζ and the center-to-limb angle $\sin\theta = x^2 + y^2$. To compute the rotational velocity on the stellar surface at point $(x,\, y)$, we use Eq. 8 from Cegla et al. (2016b) to include a solar differential rotation law,

$$v_*(x,\, y) = xv_{eq}\sin i_\star(1 - \alpha y'^2), \tag{7.5}$$

with $\alpha = (\Omega_{\rm eq} - \Omega_{\rm pole})/\Omega_{\rm eq}$. The rotations to project the position $(x,\, y)$ onto stellar surface $(x',\, y',\, z')$ are Eq. 6 and 7 in Cegla et al. (2016b), which simply involve rotating by $\beta = 90^\circ - i_\star$ about the x-axis,

$$\begin{aligned} z &= \sqrt{1 - x^2 - y^2} \\ z' &= z\cos\beta - y\sin\beta \\ y' &= z\sin\beta + y\cos\beta \\ x' &= x. \end{aligned} \tag{7.6}$$

The last piece is the intensity across the stellar disk $I(x,\, y)$. We adopted a quadratic limb darkening law with coefficients $\vec{u} = (u_1,\, u_2)$,

$$I(x,\, y,\, \vec{u}) = \begin{cases} \frac{(1-u_1(1-\mu)-u_2(1-\mu)^2}{\pi(1-u_1/3-u_2/6)}, & \text{if } \mu \in [0, 1] \\ 0, & \text{otherwise} \end{cases} \tag{7.7}$$

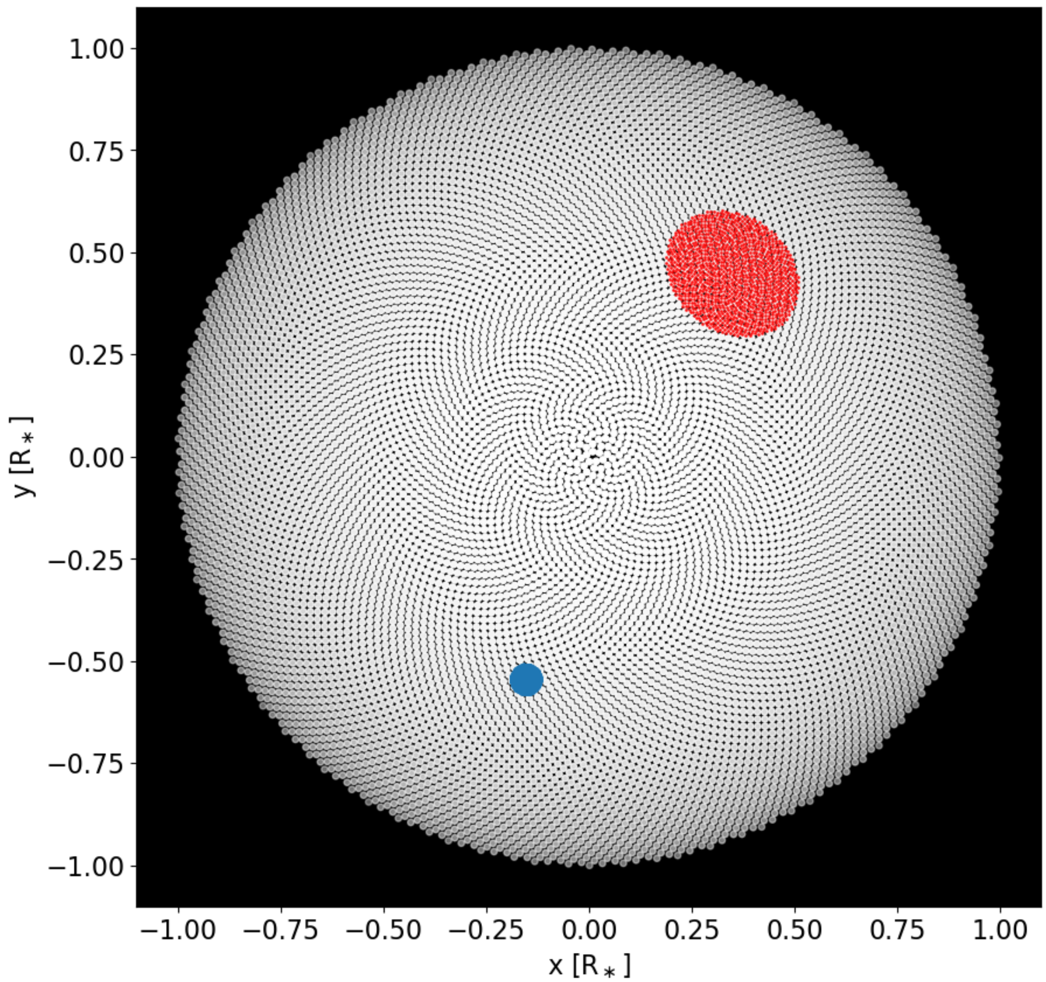

Figure 7.3: Example grid in the x-y sky-plane. The white points are an example $N = 10000$ grid across the stellar disk generated using the sunflower pattern (Eq. 7.8). The opacity of each point is given by $I(x, y)/I(0)$ for $u_1 = u_2 = 0.3$. The blue points are an identically generated grid of 2000 points scaled to R_p/R_* and centered at the position of a mock transiting planet at a random time. The red grid covers the boundary contained within a 10° radius starspot at 45° latitude and 30° longitude.

where $\mu \equiv \cos\theta$ is the center-to-limb position.

To compute the integral over the disk, we efficiently generate a set of N points in the (x, y) sky-plane according to the sunflower pattern

$$
\begin{aligned}
r_k &= \sqrt{\frac{k - 1/2}{N - 1/2}}, \quad \theta_k = k(2\pi\phi), \\
x_k &= r_k \cos\theta_k, \quad y_k = r_k \sin\theta_k,
\end{aligned}
\tag{7.8}
$$

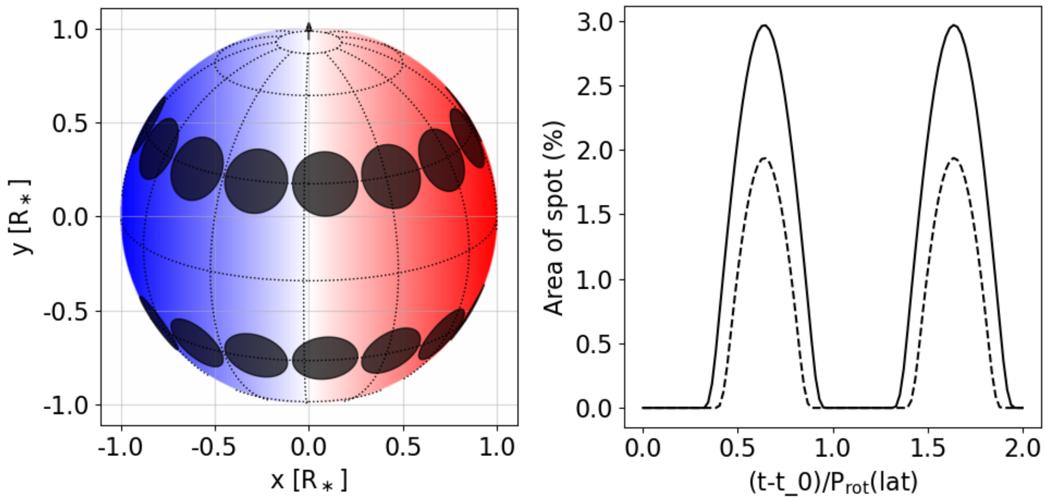

Figure 7.4: **Left:** Example starspots generated at lat $= \pm 30°$ at a series of longitudes. **Right:** The projected area of the spot on the visible hemisphere as it rotates in and out of view. The solid line is the spot at $+30°$. The dashed line is the spot at $-30°$ and is slightly less area as the star is slightly inclined ($i_\star = 70°$).

where $\phi = (1+\sqrt{5})/2$ is the golden ratio. The result is a set of points $(x_k,\, y_k)$ uniformly spaced across the unit circle. This gives the convenient property of constant $dA = dxdy = \pi/N$ in Eq. 7.3. An example grid is shown in Figure 7.3.

For the case of no macroturbulence ($\zeta = 0$ km s^{-1}), we simply integrate

$$F_*(v) = \iint_{\text{disk}} f(v - v_*(x,\, y)) I(x,\, y) dxdy. \tag{7.9}$$

The Spots

To produce the perturbation to the synthetic CCF due to the presence of a spot, we compute a separate line profile using the same formulation as for the full stellar disk

$$F_{\text{spot}}(v) = f(v) * M^{\text{spot}}(v), \tag{7.10}$$

where now $M^{\text{spot}}(v)$ is the rotational + macroturbulence broadening kernel given by Eq. 7.3 but integrated only over the portion of the stellar disk inside the boundary of the spot.

To generate a grid inside the spot to perform the integral, we first define the boundary of a spherical cap of arcradius s in spherical coordinates at polar angle $\theta = s$, and azimuthal angles $\phi \in [0, 2\pi]$. These are converted into cartesian coordinates to generate a ring of points circling the z-axis. This ring is rotated into the sky plane by successively multiplying by the rotation matrices $R_x(90 - \mathrm{lat})$, $R_y(\mathrm{lon} + \Delta\mathrm{lon})$, and $R_x(90 - i_\star)$ to place the spot at a given central latitude and longitude and inclined with the star. We can self-consistently account for the rotation of the star by comping the rotation period at the spot latitude (or at $90° - \cos^{-1}(z)$ to include the effects of spot-shearing), which is

$$P_{\mathrm{rot}}(\mathrm{lat}) = \frac{2\pi R_* \cos(\mathrm{lat})}{v_{eq}\sqrt{1 - \sin^2(\mathrm{lat})}(1 - \alpha \sin^2(\mathrm{lat}))}, \tag{7.11}$$

and computing $\Delta\mathrm{lon} = 2\pi(t - t_0)/P_{\mathrm{rot}}(\mathrm{lat})$ for a given time t relative to some reference time t_0.

The border of the spot is then examined for any $z <= 0$, i.e., portions of the spot which are rotated out of view. If a subset of the border satisfies this criteria, those values are replaced with the limb of the star, i.e., $\mathrm{sign}(x)\sqrt{1 - y^2}$ given the corresponding x and y (see Figure 7.4. To generate the grid, a sunflower grid of radius $2s$ is initialized at the spot center, and only points falling inside the spot boundary are kept . The boundary check is performed using `matplotlib` (Hunter, 2007) functions by defining a `matplotlib.path.Path` object and calling `Path.contains_points()`. The area of the spot can also be efficiently estimated by applying the Shoelace formula to the spot boundary. Then, each of the remaining N grid points has a uniform projected area $dA_{\mathrm{spot}} = A_{\mathrm{spot}}/N$, and Eq. 7.10 is readily computed to obtain $F_{\mathrm{spot}}(v)$. The only modification is

$$M^{\mathrm{spot}}(v) = \iint_{\mathrm{spot}} (1 - C) I(x, y, \vec{u}) \Theta(v - v_*(x, y)) dx dy, \tag{7.12}$$

where C is the spot contrast in intensity. C can also be converted to a temperature contrast by the ratio of two blackbody functions given the temperature of the photosphere (Boisse, Bonfils, and Santos, 2012).

We also include the effect of the suppression of the convective blueshift with center-to-limb variability by adding to Eq. 7.5 a term of the form

$$v_{\mathrm{conv}} = \sum_{i=0}^{n} c_i \langle\mu\rangle^i \tag{7.13}$$

within the spot, where $\langle\mu\rangle$ is the intensity-weighted center-to-limb position within the spot (Cegla et al., 2016b).

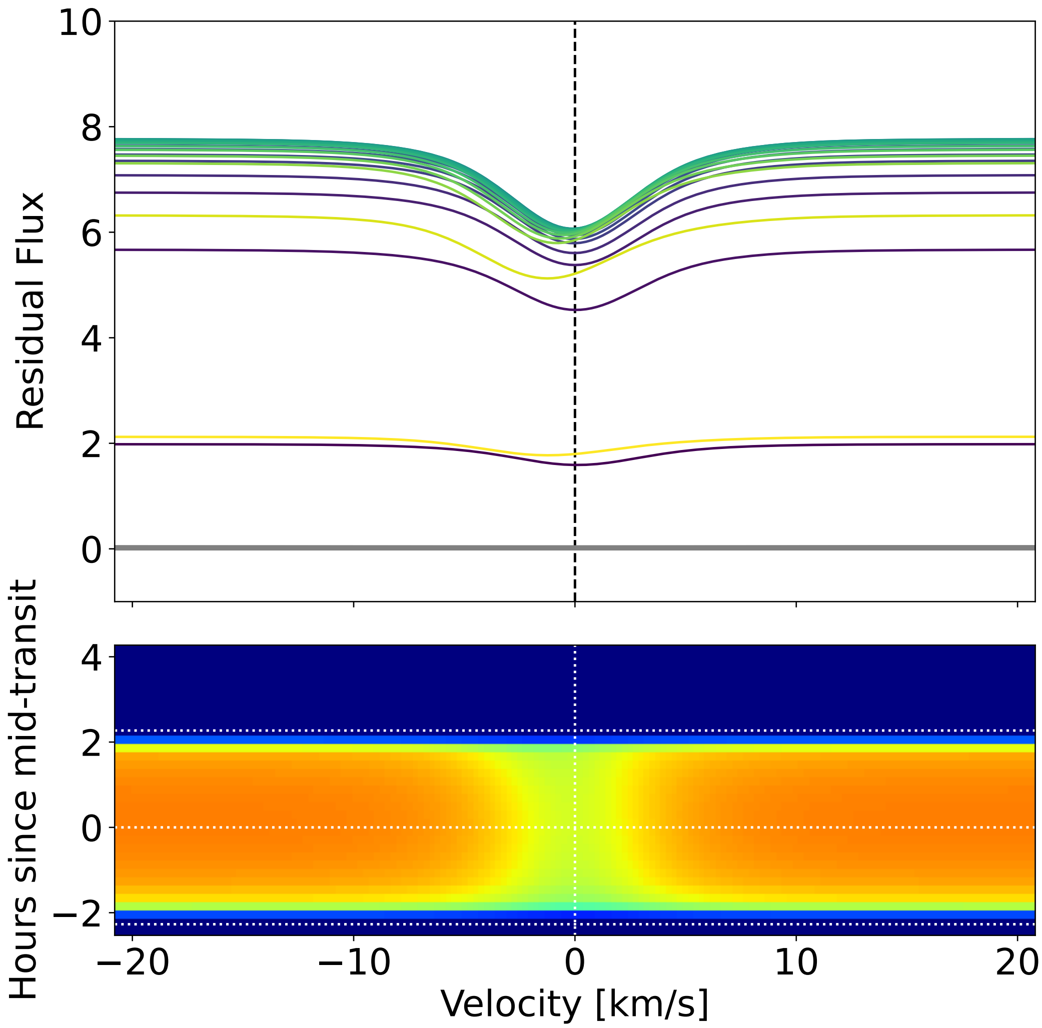

Figure 7.5: RRM analysis applied to our synthetic CCF model computed for KELT-18 b (with $\alpha = 0.9$), which reproduces a noiseless version of Figure 5.2.

The Planet

The line profile on the patch of star behind the planet is much more simple to work out, as the planet is simply a circle in the sky-plane. We can thus generate a grid from the sunflower pattern centered on the planet at time t and with radius R_p/R_*. Any points that fall off the star will automatically contribute zero flux by definition of $I(x, y)$. Since the planet occults all flux in its shadow, it is equivalent to integrate Eq. 7.3 just for the planet grid.

As a sanity check, we simulated a transit using the system parameters of KELT-18 (McLeod et al., 2017; Rubenzahl et al., 2024a). Figure 7.5 shows the result of performing the same Reloaded Rossiter-McLaughlin (RRM; Cegla et al., 2016b) analysis on this simulated data as was carried out in Chapter 5.

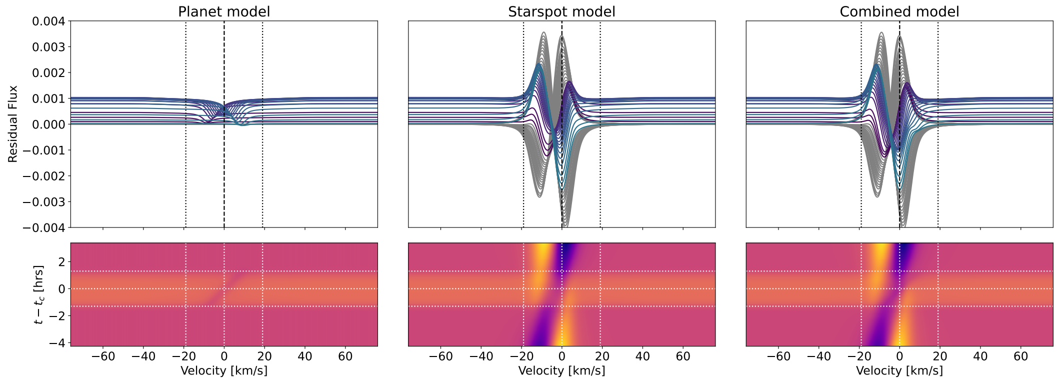

Figure 7.6: Simulated RRM residual maps for just the planet case (left), just the spot case (center), and the combined planet+spot case. The planet has an amplitude at the 1 ppt level, whereas the spot amplitude is ∼10 ppt.

Synthetic CCF

The synthetic CCF is finally obtained by convolving the overall line profile

$$F(v) = 1 + F_*(v) - \sum F_{\mathrm{spot}}(v) - F_{\mathrm{pl}}(v) \tag{7.14}$$

with an instrument broadening kernel,

$$\mathrm{CCF}_{\mathrm{star}} = F(v) * T(v). \tag{7.15}$$

For KPF, we take $T(v)$ to be a Gaussian with a FWHM of 3 km s^{-1}. For further accuracy, this could be replaced with a direct measurement of the CCF from a LFC spectrum, which shows the KPF line-spread-function is slightly non-Gaussian.

Figure 7.6 plots an example RRM residual map for the Kepler-1658 system parameters showing the planet shadow, a starspot bump matched by-eye to the data, and the combined effect. The planet signal is ten times smaller than the spot amplitude and only about twice the amplitude of the noise in the wings of the observed residuals (see Figure 7.2).

7.4 Directly measuring the spot

The latitude of the spot is already constrained from photometry to $> 30°$ based on the photometric rotation period being 76% slower than the projected equatorial rotational velocity $v_{eq} \sin i_\star$. Likewise its filling factor (% of flux removed) must be around 1–2 ppt, corresponding to a spot with size 5° at 100% contrast.

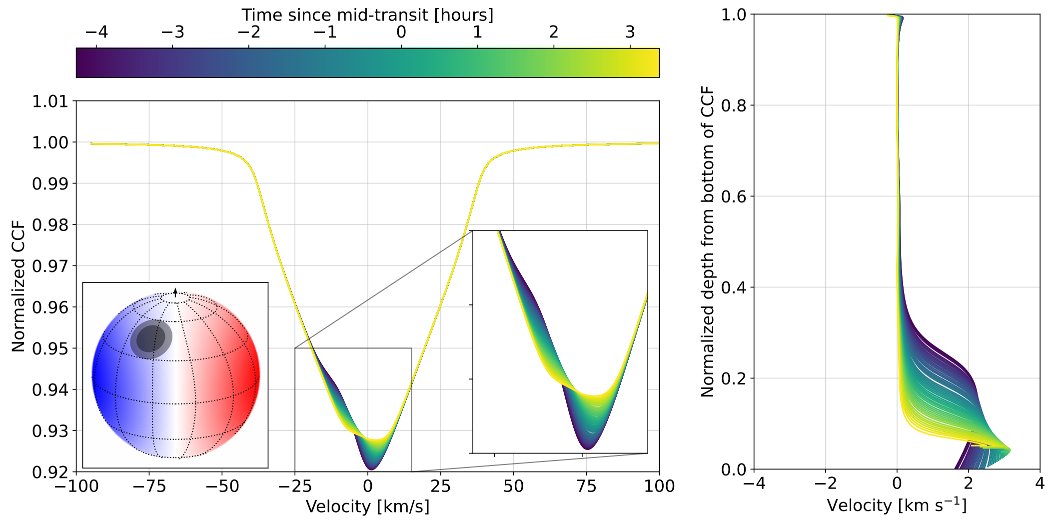

Figure 7.7: The same as Figure 7.1 but for synthetic KPF CCFs generated for a spot geometry tuned by-eye. The inset in the lower left shows the geometry of the spot, which has a radius of 10° (contrast 0.8) with an outer annulus at 15° (contrast 0.4). The lines of longitude on the star have been rotated according to the velocity at that latitude given the differential rotation law.

The observed CCFs (Figure 7.1) do not have the shape of a rotation profile, but are slightly V-shaped. We found that differential rotation with $\alpha = 0.55$ matched the steepness of the wings, while an intrinsic line profile with $\mathrm{FWHM}_L = 5$ km s^{-1}, $\mathrm{FWHM}_G = 1$ km s^{-1}, and $A_L = 0.165$ provided a good match to the wings with marginal additional macroturbulent broadening ($\zeta < 5$ km s^{-1}). We required $v_{eq} \sin i_\star$ in the 38–40 km s^{-1} range to match the width of the CCF, which is slightly larger than the value measured from HIRES spectra by Chontos et al. (2019) but is still somewhat degenerate with turbulent broadening. Finally, the star is inclined at $i_\star = 70°$.

We placed a pair of concentric starspots each with contrast 0.4 at a latitude of 45° (corresponding to $P_{\mathrm{rot}} = 5.66$ days given v_{eq}) and longitude at the final observation timestamp of $-2°$ (0° being along the y-axis). The central spot had a radius of 10° and represents the umbra. the outer spot has a radius of 15°; its outermost 5° annulus represents a penumbra. The choice to parameterize the spot in this manner as opposed to a single spot with contrast 0.8 was to obtain a larger width at the wings of the spot and a narrower width at the core, as is seen in the data. The starspot model and the resulting synthetic CCFs and their bisectors are shown in Figure 7.7. The distortion to the CCF qualitatively follows the pattern seen in the data purely by rotating the star

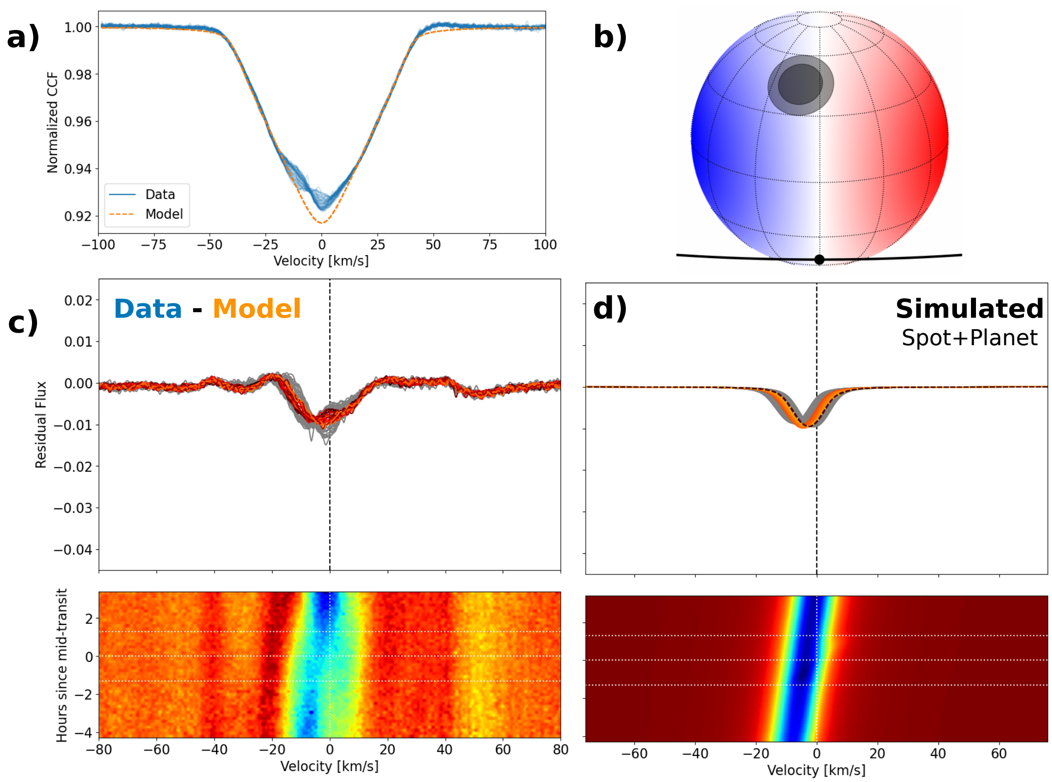

Figure 7.8: **a)** Observed CCFs (blue) and a model CCF (orange) of just the star with no spots. **b)** On-sky geometry of the spot+planet model. The spot is created by two concentric spots of different radii, which act as an umbra/penumbra to create a deep core with broader wings. **c)** The residual from panel (a) obtained by subtracting the model CCF from the data. Both the spot and planet signal are remaining. **d)** Simulated spot+planet residual, which qualitatively agrees with panel (c) but cannot reproduce the asymmetry or time-varying depth observed in the data.

at each timestamp of the observations. Though, fine-tuning the parameters to acquire a match at the 100 ppm level necessary to remove the spot effect and preserve the planet shadow has proven challenging.

As a result, we attempted to directly model the spot by taking the spotless version of the model as just described as our $\mathrm{CCF_{out}}$ and following the RRM procedure to isolate[4] $\mathrm{CCF_{spot}}$. Figure 7.8 shows this process. Modulo some residual bumps in the wings from not perfectly matching the symmetry of the CCF, the now-isolated CCF within the starspot shows significant asymmetry. This may be (at least in part) responsible for the observed C-shape in the data bisectors (Figure 7.1) which is not seen in our synthetic model (Fig-

[4]The planet shadow is also still in this residual CCF, but is a small perturbation.

ure 7.7). Visually, the observed $\mathrm{CCF}_{\mathrm{spot}}$ (panel c) can be seen to have a steeper blueshifted wing and more slanted redshifted wing. This could be due to the starspot suppressing the local convective blueshift, reducing the intensity of the blueshifted portion of $\mathrm{CCF}_{\mathrm{spot}}$ (Kunovac, V., Cegla, H., Chakraborty, H. et al. in prep). To complicate interpretations, the planet shadow is somewhere in the in-transit portion of the data (assuming an accurate ephemeris, which we propagated using the measured period decay of Vissapragada et al. 2022). However, the planet shadow will act as a perturbation to the now-isolated $\mathrm{CCF}_{\mathrm{spot}}$. Thus, by measuring the local RV of $\mathrm{CCF}_{\mathrm{spot}}$, we could potentially observe an anomaly analogous to the RM effect measured from the full CCF.

To obtain a local RV unbiased by the asymmetry of $\mathrm{CCF}_{\mathrm{spot}}$ itself, we fit each $\mathrm{CCF}_{\mathrm{spot}}$ with a Bi-Gaussian (Nardetto et al., 2006)

$$y(v) = \begin{cases} y_0 + D\exp\left(\frac{-(v-v_{\mathrm{loc}})^2}{2\sigma^2(1-A)^2)}\right), & v <= v_{\mathrm{loc}} \\ y_0 + D\exp\left(\frac{-(v-v_{\mathrm{loc}})^2}{2\sigma^2(1+A)^2)}\right), & v > v_{\mathrm{loc}} \end{cases} \tag{7.16}$$

where v_{loc} is the local RV of the spot, D is the line depth, y_0 is an arbitrary continuum level (should be zero if the $\mathrm{CCF}_{\mathrm{star}}$ model was perfect) A is the asymmetry, σ is the line width. We plot in Figure 7.9 the result of this fit to the observed time series of $\mathrm{CCF}_{\mathrm{spot}}$. We also computed equivalent widths by integrating the fitted Bi-Gaussian and computed the bisector inverse slope (BIS) of the $\mathrm{CCF}_{\mathrm{spot}}$.

Several curious features can be observed in the time series of the fitted spot properties, but interpretation is difficult. The local RV increases monotonically until around the expected transit egress, where it appears to flatten out. The line profile narrows (decreasing FWHM) and deepens (increasing depth) starting at the expected transit ingress time, but continues post-transit. The $\mathrm{CCF}_{\mathrm{spot}}$ also become more symmetric until the transit midpoint (seen in both BIS and A), at which point the $\mathrm{CCF}_{\mathrm{spot}}$ start becoming asymmetric again. There is likely some confluence of both the spot changing in morphology and viewing angle as well as the appearance and disappearance of the planet, though extracting anything more quantitative will require either expunging all remaining possible noise sources (e.g., there is a known fixed-pattern modal noise that produces correlated structure in the CCFs at about half the level of the variability in this dataset) or observing another transit of Kepler-1658 to get a fresh dataset at higher S/N with the star at a different activity state.

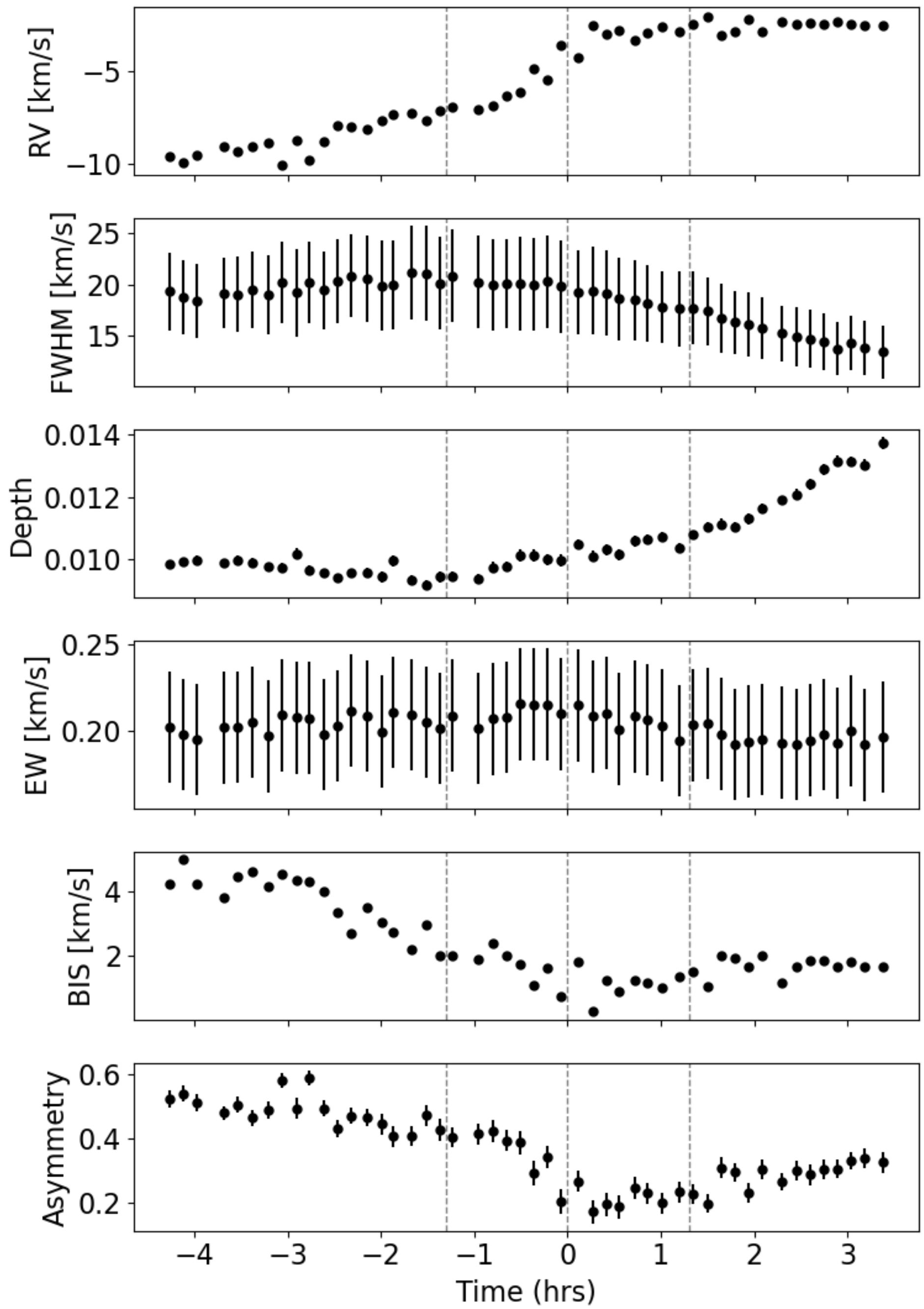

Figure 7.9: Properties derived from a Bi-Gaussian fit to the observed CCF_{spot} time series. From top to bottom, the local RV, FWHM, depth, equivalent width, bisector inverse slope, and asymmetry. The vertical dashed lines denote the predicted transit ingress, midpoint, and egress times.

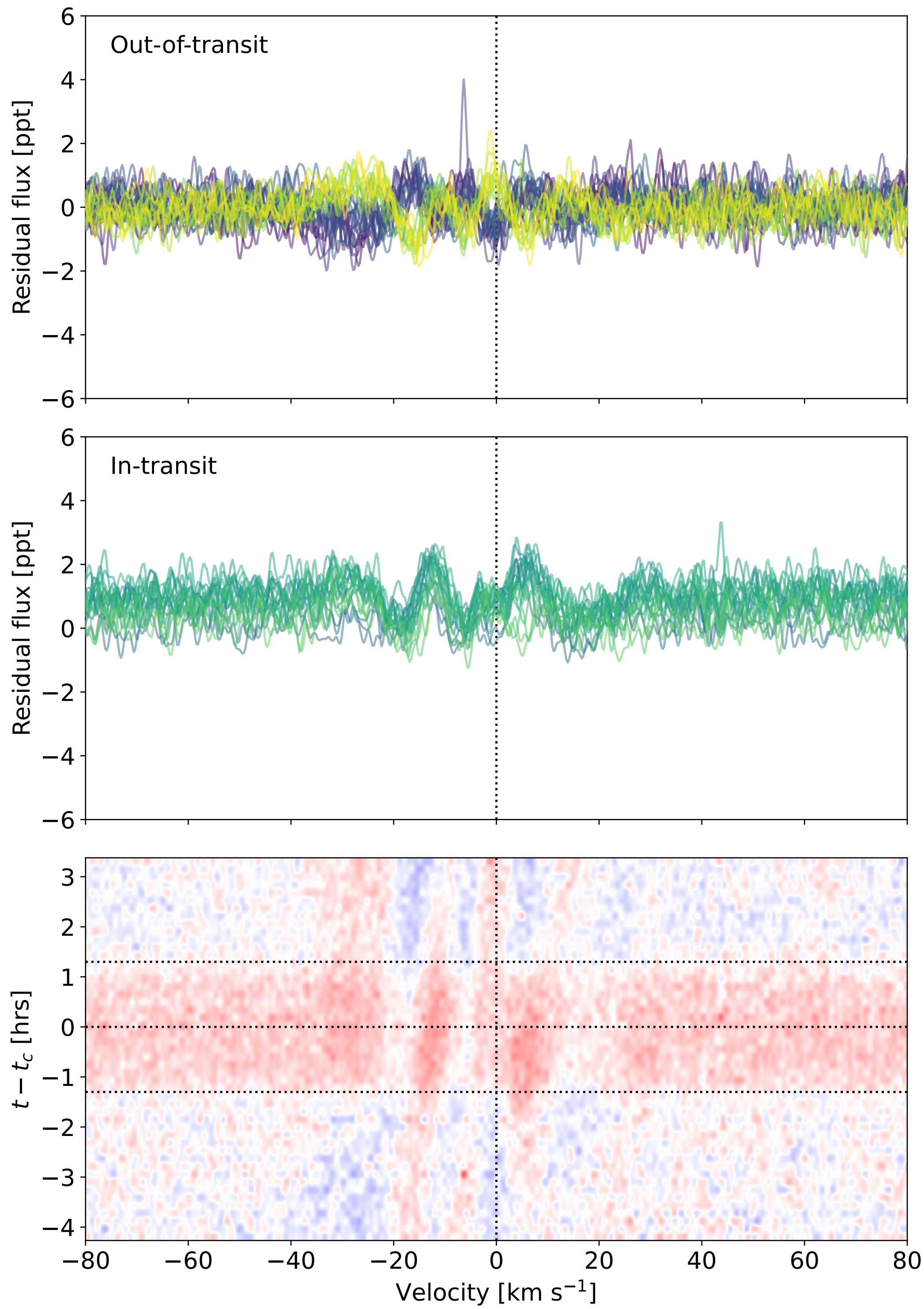

Figure 7.10: The residuals of $\mathrm{CCF}_{\mathrm{spot}}$ after subtracting their fitted Bi-Gaussian, for the out-of-transit (top) and in-transit (middle) observations. The colorscale is the same as Figure 7.10. **Bottom:** 2D heatmap of the above, with time on the vertical axis. The planet shadow is not visible.

Even so, we can subtract the Bi-Gaussian fit from the $\mathrm{CCF}_{\mathrm{spot}}$ to search the "residuals of the residuals" for the planet shadow. This is shown in Figure 7.10 in the same style as Figure 7.2. There are still structured residuals that persist out-of-transit at amplitudes comparable to and larger than the expected planet signal. Identifying any one residual "bump" as the planet shadow is indeterminate.

7.5 A Likely Aligned Orbit

Despite the non-detection of the planet shadow and unsuccessful removal of the spot effect, we can still place an upper-limit on Kepler-1658 b's obliquity. Since the planet transits at such a high impact parameter ($b = 0.95$; Chontos et al., 2019), the transit chord intersects only the stellar limb. Thus, as the projected obliquity increases, the transits chord sweeps along the limb of the star and crosses large projected rotational velocities (see panel b of Figure 7.8).

A full injection recovery analysis with accurate correlated noise is underway, but for visualization purposes, we plot in Figure 7.11 the range of velocities spanned by the planet shadow at each possible λ throughout the transit. The corresponding range of velocities spanned by the spot is over-plotted, with the wider band corresponding to ± 20 km s^{-1} as the average fitted FWHM of the $\mathrm{CCF}_{\mathrm{spot}}$. The only regions of this parameter space where the planet and spot do not overlap is $\lambda \in \pm[30^\circ, 150^\circ]$. Under the (to-be-verified) assumption that the simulated amplitude of the planet shadow ($\sim$1 ppt, Figure 7.6) being twice the noise level in the CCFs themselves (500 ppm) would lead to a detection, then we can rule these orbits out due to the absence of detecting the planet shadow in the CCF wings. The allowed solutions would be those which have the planet shadow overlap with the spot bump, $\lambda = \pm 30^\circ$ (aligned solutions) or $\lambda = 180^\circ \pm 30^\circ$ (anti-aligned solutions).

The degree of alignment would constrain tidal realignment theory. Using the obliquity damping timescale from Ogilvie (2014), their Eq. 9, in conjunction with the constraint on $k_{2,2,2}$ from the measurement of $\dot{P}/P$ by Vissapragada et al. (2022), we find that $(k_{2,1,0} - k_{2,1,2}) \gtrsim 3 \times 10^{-5}$ (or the associated $Q' \lesssim 5 \times 10^4$) to damp any primordial obliquity within 0.1–1 Gyr. Vissapragada et al. (2022) computed the tidal efficiency of period decay to be 2.5×10^4, thus if period and obliquity decay operate at similar efficiencies in Kepler-1658, then its evolution off the main sequence should have erased any primordial obliquity. Though,

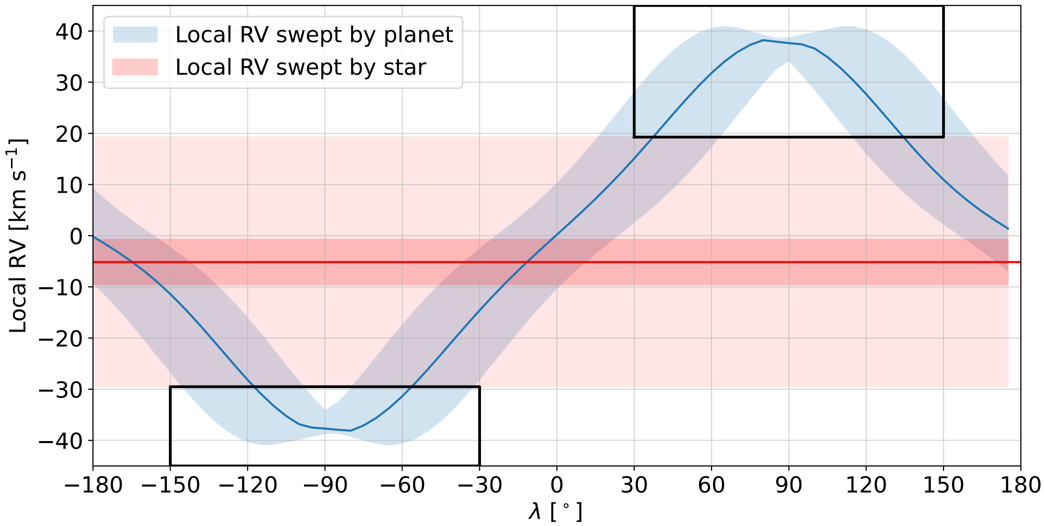

Figure 7.11: Local RV on the stellar surface spanned by the planet shadow (blue) and the spot (red) as a function of projected orbital misalignment λ. The central red band plots the span of local RVs at the spot center as it rotates across the stellar surface. The wider band expands this region by ± 20 km s^{-1}, the FWHM of the fitted $\mathrm{CCF}_{\mathrm{spot}}$. The boxed regions outline the part of parameter space where the planet shadow would be decoupled from that of the spot.

more detailed calculations (e.g., Spalding and Winn, 2022) will be needed to analyze the evolution of an oblique orbit across the Kraft Break in the highly coupled star–planet system.

Even if Kepler-1658 b were definitively aligned, its singular nature would not be an unambiguous signature of misaligned HJs around hot stars realigning over the course of stellar evolution; Kepler-1658 b could have formed aligned. More examples are needed to build a statistical sample to compare main-sequence hosts to evolved hosts at the population level. Saunders, N. et al. (in prep) observed the RM effect for three HJ systems around evolved stars more massive than the Kraft Break. All were aligned. This hints at the relative efficiency of obliquity damping to operate on short (< 1 Gyr) timescales. More examples of HJs experiencing orbital decay will allow direct comparisons between the tidal efficiencies governing both processes.

Chapter 8

CONCLUSION

This thesis has explored the cutting edge of extreme precision radial velocity (EPRV) astronomy and the mysterious origins of the shortest period planets. Can the most massive of rocky ultra-short-period planets retain gaseous envelopes (Chapter 2)? Can we learn more about stellar activity—perhaps the fundamental limit to the EPRV method itself—by building new instruments to study our Sun in unprecedented detail (Chapter 3)? Does the polar hot Neptune population share a common history of migration and orbit-tilting (Chapter 4)? Are extremely eccentric worlds with distant giant planetary companions their progenitors (Chapter 6)? How can we leverage the cutting-edge of EPRV to refine our understanding of hot-Jupiter formation, and at the same time study the surfaces of their host stars (Chapters 5 and 7)?

In this final chapter, I will summarize the key results of this thesis (8.1) and discuss the next steps in the field of EPRV and stellar obliquities (8.2).

8.1 Summary

The key findings of this thesis are as follows:

1. TOI-1347 b is the most massive rocky USP discovered to date. Like other super-Earth USPs, it has a nearby outer companion, TOI-1347 c.

    - We were able to measure the mass of the USP with two years of Keck/HIRES RVs as part of the TESS-Keck Survey. At 11.1 ± 1.2 $M_\oplus$ and 1.8 ± 0.1 $R_\oplus$, TOI-1347 b has a bulk density comparable to Earth while being an order of magnitude more massive. The outer planet's mass remained obscured by stellar activity (< 6.4 $M_\oplus$), but its size is similar at 1.6 ± 0.1 $R_\oplus$ as determined from transit photometry.
    - Of intrigue is the tentative (3σ) detection of phase-curve variability, as well as a secondary eclipse (2σ) for the USP. If confirmed (e.g., by JWST), the depth of the secondary eclipse requires a high-albedo atmosphere, which cannot be made of H/He due to the in-

tense irradiation at TOI-1347 b's 20 hr orbital period. Such a high mean-molecular weight atmosphere could be comprised of reflective silicate clouds, or may be the result of the outgassing of Na from the molten surface.

2. Sun-as-a-star EPRV spectroscopy is both an exquisite means of studying the impact of stellar activity, as well as a means of stress-testing, calibrating, and diagnosing issues throughout the instrument.

    - The Solar Calibrator (SoCal) is an autonomous solar tracker with a weatherized enclosure that feeds stable disc-integrated sunlight into the Keck Planet Finder (KPF).
    - With SoCal, KPF acquires R$\sim$98,000 optical (445–870 nm) solar spectra up to signal-to-noise (S/N) $\sim$ 2400 in 12 sec exposures. SoCal can leverage KPF's fast readout mode ($<$ 16 sec between exposures) to do helioseismology at $<$ 30 sec cadence.
    - SoCal RVs agree with the NEID Solar Feed at the photon-limit (30–40 cm s^{-1}) on intra-day timescales. SoCal data was significantly helpful in identifying and diagnosing a charge-transfer-inefficiency issue in the KPF green CCD.
    - SoCal data products are publicly available and will facilitate future studies of stellar activity at high S/N on our nearest solar-type star.

3. WASP-107 b, a hot super-Neptune with a distant outer companion, has a polar, slightly retrograde orbit.

    - The high obliquity of WASP-107 b is likely a remnant of its history of migration, which has been invoked to explain its ultra-low density and anomalously large envelope mass fraction ($>$ 85%).
    - We determined WASP-107 b's obliquity by observing the Rossiter-McLaughlin effect with Keck/HIRES.
    - If WASP-107 c's orbit is mutually inclined to WASP-107 b, ongoing nodal precession cycles would affect WASP-107 b's obliquity. A planet spends more time near its maximum obliquity during a nodal precession cycle than any other value, so if this mechanism is to explain the abundance of polar hot Neptunes, the mutual inclination distribution must be strongly peaked around 40–60°.

4. The ultra-hot Jupiter KELT-18 b has a polar orbit.

    - We observed a transit of KELT-18 b with KPF and modelled the distortion to the stellar line profile by the transiting planet using the Reloaded Rossiter-McLaughlin technique.
    - The star exhibits either significant differential rotation or center-to-limb variations. We found the latter is more likely based on spectral line shape changes that varied with center-to-limb position.
    - A binary stellar companion KELT-18 B exists in the system. Gaia astrometry revealed its orbit is face-on to our line-of-sight. As such, Kozai-Lidov oscillations and high-eccentricity migration are a plausible explanation for KELT-18 b's formation, provided it formed beyond about 6 AU in order for general relativistic precession effects to not quench eccentricity excitation.

5. The extremely eccentric ($e = 0.84$) sub-Saturn Kepler-1656 b has a low stellar obliquity.

    - The planet's extreme eccentricity places its periastron passage at just 0.03 AU, a distance close enough that tidal forces may be actively circularizing and shrinking the orbit.
    - The canonical framework of high-eccentricity migration should also tilt the planet's orbit, yet we observed Kepler-1656 b to be consistent with an aligned orbit.
    - Kepler-1656 b is the most eccentric exoplanet in a single star system to have its obliquity measured. Other eccentric exoplanets in single-star systems are also aligned, while eccentric exoplanets in multi-star systems are misaligned.
    - Kepler-1656 is the only eccentric exoplanet with a detected outer planetary companion. The system is consistent with either an ongoing coplanar high eccentricity migration, or could be a rare snapshot of a system actively undergoing large eccentricity and obliquity oscillations.
    - The mutual inclination of the outer companion would provide the key dynamical insight into the system, but is likely unmeasurable with future Gaia data releases.

6. Kepler-1658 b is a rare HJ experiencing tidal orbital decay that happens to orbit a host star which evolved across the Kraft Break.

    - Since Kepler-1658 was a hot star with a radiative envelope when on the main-sequence, it would have only just gained the ability to realign Kepler-1658 b since leaving the main sequence. A convective envelope was previously detected using asteroseismology.
    - The star is also heavily spotted and likely strongly differentially rotating (60% slower rotation at the poles relative to the equator).
    - We attempted to measure the obliquity of Kepler-1658 b using the Reloaded RM technique with KPF, but a significant starspot distorts the observed CCF. Extracting the planet shadow is difficult.
    - Even so, we tentatively place an upper limit of 30° on the projected obliquity thanks to the high impact parameter of the transit.
    - If Kepler-1658 b is aligned, it would be part of a growing trend towards post-main-sequence HJ realignment around massive stars.

8.2 Future Directions

Are the polar hot Netunes related to hot Jupiters?

While the vast majority of exoplanets to have their obliquities measured are HJs, EPRV instruments have opened a new frontier for measuring the orbits of smaller planets. Hot Neptunes (Stefânsson et al., 2022) and even rocky planets (e.g., Zhao et al., 2023a) are well within our capabilities. There are now more new planet candidates from the *TESS* mission as there are confirmed exoplanets from all previous missions (NASA Exoplanet Archive, 2019). Conveniently, the planets *TESS* is most sensitive to are precisely these close-in orbiting worlds like HJs and hot Neptunes. One recent example is TOI-1173 A b, an inflated super-Neptune (similar to WASP-107 b) which is the first of its type to be discovered in a wide binary star system (Galarza et al., 2024). An obliquity measurement for this world would help bridge the gap between HJs and the smaller worlds which also likely migrated in their past.

So far there has been one statistical survey of the hot Neptune population. The DREAM survey (Bourrier et al., 2023) included all known obliquities (dominated by HJs) but had a special focus on a sample of ∼30 sub-Saturns/hot-Neptunes (∼20 from literature, 12 from DREAM). Their sample yielded a larger fraction of polar orbits (2/3rds of the misaligned systems) than is observed in the HJ sample (Albrecht et al., 2022). Secular resonance crossings during the disk-dispersal stage (Petrovich et al., 2020) have been proposed to explain polar obliquities, but still require outer giant planets in appropriately distant orbits. Tidal sculpting of the hot Neptune obliquity distribution is likely important, as these small worlds are more feeble than their HJ relatives in dissipating tidal energy into their stars (Attia et al., 2023). Expanding this population may thus be a window into the same formation mechanisms that HJs experience, but without primordial misalignment erased by dissipative mechanisms. The outer architectures of extrasolar systems also need to be better understood. As this thesis demonstrated, the mass and orbital characteristics of outer bodies have significant implications on the evolution of the inner system. Targeted surveys like the Distant Giants Survey (Van Zandt et al., 2023) that are dedicated to mapping out the outer architectures of hot Neptune host stars will greatly narrow the range of plausible formation mechanisms. Complementing RV surveys will be the full Gaia astrometric timeseries in DR4 (2025), which will be more sensitive to massive (> 2 M_{Jup}) but more distant (> 2 AU) planets around the nearest < 100 pc stars (Espinoza-Retamal, Zhu, and Petrovich, 2023).

One final piece of evidence for a common history of migration is the trend for misaligned hot Neptunes to also be losing their atmospheres. WASP-107 b (Oklopčić and Hirata, 2018; Spake et al., 2018; Allart et al., 2019; Kirk et al., 2020) is well studied, but also HAT-P-11 b (Allart et al., 2018), GJ-436 b (Ehrenreich et al., 2015), GJ-3470 b (Palle et al., 2020a), and HAT-P-18 b (Paragas et al., 2021; Fu et al., 2022) all have polar orbits and escaping atmospheres. This trend has weakened with the helium survey of DREAM (Guilluy et al., 2023), though many of their targets had low atmospheric scale heights. A plethora of new targets from *TESS* have helium detections and await obliquity measurements, including TOI-1420 b (Yoshida et al., 2023; Vissapragada et al., 2024), TOI-1430 b (HD 235088; Orell-Miquel et al., 2023; Zhang et al., 2023), and TOI-560 b (Zhang et al., 2022). The last two, at 500–700 Myr, would also provide a closer look at post-formation architecture.

Remaining challenges for detecting terrestrial exoplanets with RVs

The search for exo-Earths has already begun. The HARPS-N Rocky Planet Search (Motalebi et al., 2015) and ESPRESSO RV blind search for Earth-class planets (Hojjatpanah et al., 2019) are ongoing, while the EXPRES 100 Earths (Brewer et al., 2020) and NEID Earth Twin Survey (Gupta et al., 2021) have recently begun their search. Upcoming instruments like HARPS-3 (Thompson et al., 2016) will conduct the Terra Hunting Experiment (Hall et al., 2018). These surveys will be spending hundreds to thousands of telesocpe hours over the next decades to monitor the nearest stars for Earth-like worlds. To ensure their success, the stellar activity barrier must be broken.

It is expected, but not yet directly measured, that specific forms of activity in the near infrared (NIR) should be weaker than in the optical, as the contrast between spots and the photosphere should be smaller (Marchwinski et al., 2015). Zeeman effects (Zeeman, 1897) in magnetically sensitive lines are also greater at redder wavelengths, as the Zeeman splitting factor goes as $\Delta\lambda \propto g_{\mathrm{eff}} B \lambda_0^2$ (Terrien et al., 2022). PARVI is a unique EPRV instrument in that it not only operates in the NIR, but its single mode fiber yields a static line spread function. This is ideal for resolving subtle line shape changes and Zeeman splitting, which may enable Zeeman Doppler-Imaging (ZDI; Donati, Semel, and Praderie, 1989; Kochukhov, 2016) techniques to be developed for EPRV use. A solar feed for PARVI is in active development. The combination of KPF+PARVI would be a powerful measure of magnetically driven modulations on the rotation period, and could assess the utility of moving to the NIR as a "silver bullet" for mitigating stellar activity.

Current solar feeds measure integrated intensity. Unsigned (unpolarized) magnetic flux, which can be derived from intensity spectra by measuring Zeeman broadening with multi-profile least-squares deconvolution (Kochukhov, Makaganiuk, and Piskunov, 2010; Mortier, 2016; Kochukhov et al., 2020; Lienhard et al., 2023), correlates strongly with activity (Haywood et al., 2022). Signed magnetic flux should in theory be more sensitive to active regions and is more readily measured with spectropolarimetry. HARPS-3 will be the first EPRV spectrograph built with polarimetric capabilities. Its solar feed, ABORAS (Jentink et al., 2022), will test the utility of this approach on the Sun.

Comparisons between solar EPRV feeds, such as that studied by Zhao et al. (2023b) over one month, should be extended to longer timescales to study activity over many solar rotation periods. With the longitudinal coverage now extended from HARPS-N in La Palma to KPF in Hawaiʻi, up to 20 hours of continuous solar RVs in the summer months ($\sim$17 hr in the winter months) is collectively achieved. By cross-calibrating instruments using the overlapping windows, intermediate-timescale variability like granulation—which may be more limiting than spots (Lakeland et al., 2024)—can be better resolved. These data also create an opportunity to assess the utility of the various design choices made by each EPRV instrument team. Optical (e.g., KPF, NEID, ESPRESSO, EXPRES) instruments use identically spec'd R4 echelle gratings, derive RVs by the CCF technique using the same line masks (G2 ESPRESSO), and wavelength calibrate using the same model of Laser Frequency Comb (LFC) developed by Menlo Systems. A common data reduction pipeline that derives RVs in a self-consistent way using a common wavelength range (or set of spectral lines) could further isolate instrumental systematics. Such a study was recommended by Crass et al. (2021), but has yet to be performed. Assessing the optimal spectrograph architectures and best performing subsystems would inform designs for the next generation of EPRV instruments.

For measuring masses, the standard approach of detrending against an activity indicator or applying Gaussian Process regression acts to remove activity after it has already been injected into the measured RV. To reach the cm s^{-1} level, we probably want to remove activity before deriving the RV. The approach of Collier Cameron et al. (2021) to separate line shape changes from translations using principle component analysis (PCA) on the CCF (Davis et al., 2017) gets us much closer to what we actually want–the uncontaminated bulk achromatic Doppler shift caused by an orbiting planet. Cretignier et al. (2023) applied PCA to line-by-line HARPS RVs to chromatically correct for instrumental effects and stellar activity and were able to detect a candidate super-Earth in a 600 day orbit around the G-dwarf HD 20794, with $K_{RV} = 60 \pm 6$ cm s^{-1}. We may also reconsider what quantity we are calling the RV: the position of the minimum of a fitted Gaussian? The center-of-flux of an absorption line? The Cepheid-variable astronomical community has made long use of the bi-Gaussian to handle asymmetric line profiles for deriving accurate RVs (Nardetto et al., 2006). Separately calculating RVs from segments of a line could further resolve activity, either as a function of depth (e.g., top/bottom RVs to separate rotation from convective effects, Siegel, J. et al. in prep) which traces formation temperature (Al Moulla, Dumusque, and Cretignier, 2024), or "part-by-part" in wavelength as another way to resolve line asymmetry effects. To make full use of the information contained in every pixel of an EPRV spectrum, machine learning methods (e.g., de Beurs et al., 2022; Liang, Winn, and Melchior, 2024) show promise for data-driven distinguishing of line shape changes from Doppler shifts.

As the Sun is now in solar maximum, the strength of active signals will be most detectable. Days in which the visible hemisphere of the Sun only has a single large isolated spot (or dense spot group), can be compared to past observations taken during solar minimum when the Sun had no active features. Better yet, an ultra-high S/N master spectrum could be constructed from all of the spectra taken with no sunspots and minimal granulation noise. If these spectra are selected from a single multi-hour sequence during a particularly quiet day, a GP model of the p-mode oscillations (e.g., Luhn et al., 2023) could be used to Doppler-shift each spectrum to a common rest frame before averaging into the master template, removing the "blurring" effect of averaging over p-modes. Then, an analysis analogous to the RRM technique (as in Chapter 7) can be employed to extract the contribution of the sunspot to the disc-integrated spectrum by subtracting the spotted spectrum ("in-transit") from the quiet template spectrum ("out-of-transit"). Comparing such a "sunspot spectrum" to disc-resolved solar spectroscopy would aid identification of active features. The Paranal solar Espresso Telescope (PoET; Leite et al., 2022), which will be connected to ESPRESSO (Pepe et al., 2013) in the coming years, is planned to have disc-resolved capability. Perhaps a library of sunspot spectra could be added to quiet-Sun spectra using perturbation theory to fit for any observed stellar spectrum.

Ultimately, the goal of the EPRV community is to detect and characterize Earth-like exoplanets. Investigations of these ultra-high S/N solar spectra will either yield the enabling technologies and methodologies needed to realize this goal, or they will reveal just how hard this problem truly is. Science is a process of iteration, reward, failure, learning, and overcoming. The discovery of an Earth-like exoplanet would fundamentally alter our collective perspective on life and our place in the universe. Such planets are almost surely out there; we just need to see beyond the stars which they orbit.

BIBLIOGRAPHY

National Academies of Sciences, Engineering, and Medicine (2021). *Pathways to Discovery in Astronomy and Astrophysics for the 2020s*. Washington, DC: The National Academies Press. ISBN: 978-0-309-46734-6. DOI: 10.17226/26141. URL: https://nap.nationalacademies.org/catalog/26141/pathways-to-discovery-in-astronomy-and-astrophysics-for-the-2020s.

Adams J. C., E. (Nov. 1846). "III. An Explanation of the observed Irregularities in the Motion of Uranus, on the Hypothesis of Disturbance caused by a more distant Planet; with a Determination of the Mass, Orbit, and Position of the disturbing Body." In: *Monthly Notices of the Royal Astronomical Society* 7.9, pp. 149–152. ISSN: 0035-8711. DOI: 10.1093/mnras/7.9.149. eprint: https://academic.oup.com/mnras/article-pdf/7/9/149/3063527/mnras7-0149.pdf. URL: https://doi.org/10.1093/mnras/7.9.149.

Aigrain, S., F. Pont, and S. Zucker (Jan. 2012). "A simple method to estimate radial velocity variations due to stellar activity using photometry*." In: *MNRAS* 419.4, pp. 3147–3158. ISSN: 0035-8711. DOI: 10.1111/j.1365-2966.2011.19960.x. eprint: https://academic.oup.com/mnras/article-pdf/419/4/3147/9506243/mnras0419-3147.pdf. URL: https://doi.org/10.1111/j.1365-2966.2011.19960.x.

Aigrain, S. and D. Foreman-Mackey (Aug. 2023). "Gaussian Process Regression for Astronomical Time Series." In: *ARA&A* 61, pp. 329–371. DOI: 10.1146/annurev-astro-052920-103508. arXiv: 2209.08940 [astro-ph.IM].

Al Moulla, K., X. Dumusque, and M. Cretignier (Mar. 2024). "Measuring precise radial velocities on individual spectral lines. IV. Stellar activity correlation with line formation temperature." In: *A&A* 683, A106, A106. DOI: 10.1051/0004-6361/202348150. arXiv: 2312.10836 [astro-ph.SR].

Albrecht, S. et al. (Sept. 2012). "Obliquities of Hot Jupiter Host Stars: Evidence for Tidal Interactions and Primordial Misalignments." In: *ApJ* 757.1, 18, p. 18. DOI: 10.1088/0004-637X/757/1/18. arXiv: 1206.6105 [astro-ph.SR].

Albrecht, S. H., R. I. Dawson, and J. N. Winn (Aug. 2022). "Stellar Obliquities in Exoplanetary Systems." In: *PASP* 134.1038, 082001, p. 082001. DOI: 10.1088/1538-3873/ac6c09. arXiv: 2203.05460 [astro-ph.EP].

Albrecht, S. H. et al. (June 2022). "A Preponderance of Perpendicular Planets." In: *Bulletin of the American Astronomical Society*. Vol. 54, 501.05, p. 501.05.

Allart, R. et al. (Dec. 2018). "Spectrally resolved helium absorption from the extended atmosphere of a warm Neptune-mass exoplanet." In: *Sci-*

ence 362.6421, pp. 1384–1387. DOI: 10.1126/science.aat5879. arXiv: 1812.02189 [astro-ph.EP].

Allart, R. et al. (2019). "High-resolution confirmation of an extended helium atmosphere around WASP-107b." In: *A&A* 623, A58. DOI: 10.1051/0004-6361/201834917.

Amard, L. et al. (Nov. 2019). "First grids of low-mass stellar models and isochrones with self-consistent treatment of rotation. From 0.2 to 1.5 $M_\odot$ at seven metallicities from PMS to TAMS." In: *A&A* 631, A77, A77. DOI: 10.1051/0004-6361/201935160. arXiv: 1905.08516 [astro-ph.SR].

Anderson, D. R. et al. (Aug. 2017). "The discoveries of WASP-91b, WASP-105b and WASP-107b: Two warm Jupiters and a planet in the transition region between ice giants and gas giants." In: *A&A* 604, A110, A110. DOI: 10.1051/0004-6361/201730439. arXiv: 1701.03776 [astro-ph.EP].

Anderson, K. R., N. I. Storch, and D. Lai (Mar. 2016). "Formation and stellar spin-orbit misalignment of hot Jupiters from Lidov-Kozai oscillations in stellar binaries." In: *MNRAS* 456.4, pp. 3671–3701. DOI: 10.1093/mnras/stv2906. arXiv: 1510.08918 [astro-ph.EP].

Angelo, I. et al. (May 2022). "Kepler-1656b's Extreme Eccentricity: Signature of a Gentle Giant." In: *AJ* 163.5, 227, p. 227. DOI: 10.3847/1538-3881/ac6094. arXiv: 2204.00019 [astro-ph.EP].

Arentoft, T. et al. (Nov. 2008). "A Multisite Campaign to Measure Solar-like Oscillations in Procyon. I. Observations, Data Reduction, and Slow Variations." In: *The Astrophysical Journal* 687.2, p. 1180. DOI: 10.1086/592040. URL: https://dx.doi.org/10.1086/592040.

Armstrong, D. J. et al. (July 2020). "A remnant planetary core in the hot-Neptune desert." In: *Nature* 583.7814, pp. 39–42. DOI: 10.1038/s41586-020-2421-7. arXiv: 2003.10314 [astro-ph.EP].

Astropy Collaboration et al. (Aug. 2022). "The Astropy Project: Sustaining and Growing a Community-oriented Open-source Project and the Latest Major Release (v5.0) of the Core Package." In: *ApJ* 935.2, 167, p. 167. DOI: 10.3847/1538-4357/ac7c74. arXiv: 2206.14220 [astro-ph.IM].

Attia, O. et al. (June 2023). "DREAM. II. The spin-orbit angle distribution of close-in exoplanets under the lens of tides." In: *A&A* 674, A120, A120. DOI: 10.1051/0004-6361/202245237. arXiv: 2305.00829 [astro-ph.EP].

Avila, G. and P. Singh (July 2008). "Optical fiber scrambling and light pipes for high accuracy radial velocities measurements." In: *Advanced Optical and Mechanical Technologies in Telescopes and Instrumentation*. Ed. by E. Atad-Ettedgui and D. Lemke. Vol. 7018. SPIE, 70184W, 70184W. DOI: 10.1117/12.789509.

Bailey, E., K. Batygin, and M. E. Brown (Nov. 2016). "Solar Obliquity Induced by Planet Nine." In: *AJ* 152.5, 126, p. 126. DOI: 10.3847/0004-6256/152/5/126. arXiv: 1607.03963 [astro-ph.EP].

Bakos, G. et al. (Mar. 2004). "Wide-Field Millimagnitude Photometry with the HAT: A Tool for Extrasolar Planet Detection." In: *PASP* 116.817, pp. 266–277. DOI: 10.1086/382735. arXiv: astro-ph/0401219 [astro-ph].

Bakos, G. Á. et al. (Sept. 2002). "System Description and First Light Curves of the Hungarian Automated Telescope, an Autonomous Observatory for Variability Search." In: *Publications of the Astronomical Society of the Pacific* 114.799, p. 974. DOI: 10.1086/342382. URL: https://dx.doi.org/10.1086/342382.

Baliunas, S. L. et al. (Jan. 1995). "Chromospheric Variations in Main-Sequence Stars. II." In: *ApJ* 438, p. 269. DOI: 10.1086/175072.

Baranne, A., M. Mayor, and J. L. Poncet (Jan. 1979). "Coravel— A new tool for radial velocity measurements." In: *Vistas in Astronomy* 23.4, pp. 279–316. DOI: 10.1016/0083-6656(79)90016-3.

Baranne, A. et al. (Oct. 1996). "ELODIE: A spectrograph for accurate radial velocity measurements." In: *A&AS* 119, pp. 373–390.

Barenfeld, S. A. et al. (Aug. 2016). "ALMA Observations of Circumstellar Disks in the Upper Scorpius OB Association." In: *ApJ* 827.2, 142, p. 142. DOI: 10.3847/0004-637X/827/2/142. arXiv: 1605.05772 [astro-ph.EP].

Barnes, J. W. (Nov. 2009). "Transit Lightcurves of Extrasolar Planets Orbiting Rapidly Rotating Stars." In: *ApJ* 705.1, pp. 683–692. DOI: 10.1088/0004-637X/705/1/683. arXiv: 0909.1752 [astro-ph.EP].

Baruteau, C. et al. (Jan. 2014). "Planet-Disk Interactions and Early Evolution of Planetary Systems." In: *Protostars and Planets VI*. Ed. by H. Beuther et al., pp. 667–689. DOI: 10.2458/azu_uapress_9780816531240-ch029. arXiv: 1312.4293 [astro-ph.EP].

Bastien, F. A. et al. (Feb. 2014). "Radial Velocity Variations of Photometrically Quiet, Chromospherically Inactive Kepler Stars: A Link between RV Jitter and Photometric Flicker." In: *AJ* 147.2, 29, p. 29. DOI: 10.1088/0004-6256/147/2/29. arXiv: 1310.7152 [astro-ph.SR].

Batalha, N. M. et al. (Mar. 2011). "Kepler's First Rocky Planet: Kepler-10b." In: *ApJ* 729.1, 27, p. 27. DOI: 10.1088/0004-637X/729/1/27. arXiv: 1102.0605 [astro-ph.EP].

Batygin, K. (Nov. 2012). "A primordial origin for misalignments between stellar spin axes and planetary orbits." In: *Nature* 491.7424, pp. 418–420. DOI: 10.1038/nature11560.

Batygin, K., F. C. Adams, and J. Becker (July 2023). "The Origin of Universality in the Inner Edges of Planetary Systems." In: *ApJL* 951.1, L19, p. L19. DOI: 10.3847/2041-8213/acdb5d. arXiv: 2306.08822 [astro-ph.EP].

Batygin, K., P. H. Bodenheimer, and G. P. Laughlin (Oct. 2016). "In Situ Formation and Dynamical Evolution of Hot Jupiter Systems." In: *ApJ* 829.2, 114, p. 114. DOI: 10.3847/0004-637X/829/2/114. arXiv: 1511.09157 [astro-ph.EP].

Batygin, K. and M. E. Brown (Feb. 2016). "Evidence for a Distant Giant Planet in the Solar System." In: *AJ* 151.2, 22, p. 22. DOI: 10.3847/0004-6256/151/2/22. arXiv: 1601.05438 [astro-ph.EP].

Batygin, K., A. Morbidelli, and M. J. Holman (Feb. 2015). "Chaotic Disintegration of the Inner Solar System." In: *ApJ* 799.2, 120, p. 120. DOI: 10.1088/0004-637X/799/2/120. arXiv: 1411.5066 [astro-ph.EP].

Batygin, K., D. J. Stevenson, and P. H. Bodenheimer (Sept. 2011). "Evolution of Ohmically Heated Hot Jupiters." In: *ApJ* 738.1, 1, p. 1. DOI: 10.1088/0004-637X/738/1/1. arXiv: 1101.3800 [astro-ph.EP].

Bauer, F. F., M. Zechmeister, and A. Reiners (Sept. 2015). "Calibrating echelle spectrographs with Fabry-Pérot etalons." In: *A&A* 581, A117, A117. DOI: 10.1051/0004-6361/201526462. arXiv: 1506.07887 [astro-ph.IM].

Beck, J. G. and P. Giles (Mar. 2005). "Helioseismic Determination of the Solar Rotation Axis." In: *ApJL* 621.2, pp. L153–L156. DOI: 10.1086/429224.

Becker, J. C. et al. (Oct. 2015). "WASP-47: A Hot Jupiter System with Two Additional Planets Discovered by K2." In: *ApJL* 812.2, L18, p. L18. DOI: 10.1088/2041-8205/812/2/L18. arXiv: 1508.02411 [astro-ph.EP].

Becker, J. C. et al. (Dec. 2017). "Exterior Companions to Hot Jupiters Orbiting Cool Stars Are Coplanar." In: *AJ* 154.6, 230, p. 230. DOI: 10.3847/1538-3881/aa9176. arXiv: 1710.01737 [astro-ph.EP].

Beckers, J. M. and G. D. Nelson (July 1978). "Some comments on the limb shift of solar lines. II: The effect of granular motions." In: *SoPh* 58.2, pp. 243–261. DOI: 10.1007/BF00157270.

Bedell, M. et al. (Oct. 2019). "WOBBLE: A Data-driven Analysis Technique for Time-series Stellar Spectra." In: *AJ* 158.4, 164, p. 164. DOI: 10.3847/1538-3881/ab40a7. arXiv: 1901.00503 [astro-ph.IM].

Beeck, B. et al. (2013a). "Three-dimensional simulations of near-surface convection in main-sequence stars - I. Overall structure." In: *A&A* 558, A48. DOI: 10.1051/0004-6361/201321343. URL: https://doi.org/10.1051/0004-6361/201321343.

Beeck, B. et al. (2013b). "Three-dimensional simulations of near-surface convection in main-sequence stars - II. Properties of granulation and spectral lines." In: *A&A* 558, A49. DOI: 10.1051/0004-6361/201321345. URL: https://doi.org/10.1051/0004-6361/201321345.

Behmard, A., F. Dai, and A. W. Howard (Mar. 2022). "Stellar Companions to TESS Objects of Interest: A Test of Planet–Companion Alignment." In: *The Astronomical Journal* 163.4, p. 160. DOI: 10.3847/1538-3881/ac53a7. URL: https://dx.doi.org/10.3847/1538-3881/ac53a7.

Berger, T. A., A. W. Howard, and A. M. Boesgaard (Mar. 2018). "Identifying Young Kepler Planet Host Stars from Keck-HIRES Spectra of Lithium." In: *ApJ* 855.2, 115, p. 115. DOI: 10.3847/1538-4357/aab154. arXiv: 1802.09529 [astro-ph.EP].

Berger, T. A. et al. (June 2020). "The Gaia-Kepler Stellar Properties Catalog. I. Homogeneous Fundamental Properties for 186,301 Kepler Stars." In: *AJ* 159.6, 280, p. 280. DOI: 10.3847/1538-3881/159/6/280. arXiv: 2001.07737 [astro-ph.SR].

Best, S. and C. Petrovich (Jan. 2022). "The Chaotic History of the Retrograde Multi-planet System in K2-290A Driven by Distant Stars." In: *ApJL* 925.1, L5, p. L5. DOI: 10.3847/2041-8213/ac49e9. arXiv: 2201.03586 [astro-ph.EP].

Beurs, Z. L. de et al. (Sept. 2023). "Revisiting Orbital Evolution in HAT-P-2 b and Confirmation of HAT-P-2 c." In: *The Astronomical Journal* 166.4, p. 136. DOI: 10.3847/1538-3881/acedf1. URL: https://dx.doi.org/10.3847/1538-3881/acedf1.

Blackman, R. T., J. M. J. Ong, and D. A. Fischer (July 2019). "The Measured Impact of Chromatic Atmospheric Effects on Barycentric Corrections: Results from the EXtreme PREcision Spectrograph." In: *AJ* 158.1, 40, p. 40. DOI: 10.3847/1538-3881/ab24c3. arXiv: 1906.01653 [astro-ph.EP].

Blackman, R. T. et al. (May 2020). "Performance Verification of the EXtreme PREcision Spectrograph." In: *AJ* 159.5, 238, p. 238. DOI: 10.3847/1538-3881/ab811d. arXiv: 2003.08852 [astro-ph.IM].

Blake, C. H., S. Halverson, and A. Roy (Apr. 2017). "The impact of charge transfer inefficiency on Extreme Precision Doppler measurements." In: *Journal of Instrumentation* 12.4, p. C04003. DOI: 10.1088/1748-0221/12/04/C04003.

Blunt, S. et al. (Aug. 2023). "Overfitting Affects the Reliability of Radial Velocity Mass Estimates of the V1298 Tau Planets." In: *AJ* 166.2, 62, p. 62. DOI: 10.3847/1538-3881/acde78. arXiv: 2306.08145 [astro-ph.EP].

Bodenheimer, P., O. Hubickyj, and J. J. Lissauer (Jan. 2000). "Models of the in Situ Formation of Detected Extrasolar Giant Planets." In: *Icarus* 143.1, pp. 2–14. DOI: 10.1006/icar.1999.6246. arXiv: 2111.08776 [astro-ph.EP].

Boisse, I., X. Bonfils, and N. C. Santos (Sept. 2012). "SOAP. A tool for the fast computation of photometry and radial velocity induced by stellar spots." In: *A&A* 545, A109, A109. DOI: 10.1051/0004-6361/201219115. arXiv: 1206.5493 [astro-ph.IM].

Boisse, I. et al. (2011). "Disentangling between stellar activity and planetary signals." In: *A&A* 528, A4. DOI: 10.1051/0004-6361/201014354. URL: https://doi.org/10.1051/0004-6361/201014354.

Boley, A. C., A. P. Granados Contreras, and B. Gladman (Feb. 2016). "The In Situ Formation of Giant Planets at Short Orbital Periods." In: *ApJL* 817.2, L17, p. L17. DOI: 10.3847/2041-8205/817/2/L17. arXiv: 1510.04276 [astro-ph.EP].

Borucki, W. J. et al. (Feb. 2010). "Kepler Planet-Detection Mission: Introduction and First Results." In: *Science* 327.5968, p. 977. DOI: 10.1126/science.1185402.

Bouchy, F., F. Pepe, and D. Queloz (2001). "Fundamental photon noise limit to radial velocity measurements." In: *Å* 374.2, pp. 733–739. DOI: 10.1051/0004-6361:20010730. URL: https://doi.org/10.1051/0004-6361:20010730.

Bouchy, F. et al. (Jan. 2009). "Charge Transfer Inefficiency effect for high-precision radial velocity measurements." In: *EAS Publications Series*. Ed. by P. Kern. Vol. 37. EAS Publications Series, pp. 247–253. DOI: 10.1051/eas/0937031.

Bouchy, F. et al. (Sept. 2017). "Near-InfraRed Planet Searcher to Join HARPS on the ESO 3.6-metre Telescope." In: *The Messenger* 169, pp. 21–27. DOI: 10.18727/0722-6691/5034.

Bouma, L. G., E. K. Palumbo, and L. A. Hillenbrand (Apr. 2023a). "The Empirical Limits of Gyrochronology." In: *ApJL* 947.1, L3, p. L3. DOI: 10.3847/2041-8213/acc589. arXiv: 2303.08830 [astro-ph.SR].

Bouma, L. G., E. K. Palumbo, and L. A. Hillenbrand (Apr. 2023b). "The Empirical Limits of Gyrochronology." In: *ApJL* 947.1, L3, p. L3. DOI: 10.3847/2041-8213/acc589. arXiv: 2303.08830 [astro-ph.SR].

Bourrier, V. et al. (2017). "Refined architecture of the WASP-8 system: A cautionary tale for traditional Rossiter-McLaughlin analysis." In: *A&A* 599, A33. DOI: 10.1051/0004-6361/201629973.

Bourrier, V. et al. (Jan. 2023). "DREAM. I. Orbital architecture orrery." In: *A&A* 669, A63, A63. DOI: 10.1051/0004-6361/202245004. arXiv: 2301.07727 [astro-ph.EP].

Bourrier, V. et al. (2018). "Orbital misalignment of the Neptune-mass exoplanet GJ 436b with the spin of its cool star." In: *Nature* 553.7689, pp. 477–480. DOI: 10.1038/nature24677.

Brady, M. T. et al. (Oct. 2018). "Kepler-1656b: A Dense Sub-Saturn with an Extreme Eccentricity." In: *AJ* 156.4, 147, p. 147. DOI: 10.3847/1538-3881/aad773. arXiv: 1809.08436 [astro-ph.EP].

Brewer, J. M. et al. (Aug. 2016). "Spectral Properties of Cool Stars: Extended Abundance Analysis of 1,617 Planet-search Stars." In: *ApJS* 225.2, 32, p. 32. DOI: 10.3847/0067-0049/225/2/32. arXiv: 1606.07929 [astro-ph.SR].

Brewer, J. M. et al. (Aug. 2020). "EXPRES. I. HD 3651 as an Ideal RV Benchmark." In: *AJ* 160.2, 67, p. 67. DOI: 10.3847/1538-3881/ab99c9. arXiv: 2006.02303 [astro-ph.EP].

Broomhall, A.-M. et al. (June 2009). "Definitive Sun-as-a-star p-mode frequencies: 23 years of BiSON observations." In: *Monthly Notices of the Royal Astronomical Society: Letters* 396.1, pp. L100–L104. ISSN: 1745-3925. DOI: 10.1111/j.1745-3933.2009.00672.x. eprint: https://academic.oup.com/mnrasl/article-pdf/396/1/L100/3024124/396-1-L100.pdf. URL: https://doi.org/10.1111/j.1745-3933.2009.00672.x.

Brown, T. M. (Jan. 1990). "High precision Doppler measurements via echelle spectroscopy." In: *CCDs in astronomy*. Ed. by G. H. Jacoby. Vol. 8. Astronomical Society of the Pacific Conference Series, pp. 335–344.

Brown, T. M. et al. (Feb. 1991). "Detection of Possible p-Mode Oscillations on Procyon." In: *ApJ* 368, p. 599. DOI: 10.1086/169725.

Bryan, M. L. and E. J. Lee (Mar. 2024). "Friends not Foes: Strong Correlation between Inner Super-Earths and Outer Gas Giants." In: *arXiv e-prints*, arXiv:2403.08873, arXiv:2403.08873. DOI: 10.48550/arXiv.2403.08873. arXiv: 2403.08873 [astro-ph.EP].

Bryan, M. L. et al. (Apr. 2016). "Statistics of Long Period Gas Giant Planets in Known Planetary Systems." In: *ApJ* 821.2, 89, p. 89. DOI: 10.3847/0004-637X/821/2/89. arXiv: 1601.07595 [astro-ph.EP].

Butler, R. P. et al. (June 1996). "Attaining Doppler Precision of 3 M s-1." In: *PASP* 108, p. 500. DOI: 10.1086/133755.

Butler, R. P. et al. (Jan. 1997). "Three New "51 Pegasi-Type" Planets." In: *ApJL* 474.2, pp. L115–L118. DOI: 10.1086/310444.

Butler, R. P. et al. (Dec. 1998). "A Planet with a 3.1 Day Period around a Solar Twin." In: *PASP* 110.754, pp. 1389–1393. DOI: 10.1086/316287.

Caldwell, D. A. et al. (Nov. 2020). "TESS Science Processing Operations Center FFI Target List Products." In: *Research Notes of the American Astronomical Society* 4.11, 201, p. 201. DOI: 10.3847/2515-5172/abc9b3. arXiv: 2011.05495 [astro-ph.EP].

Campbell, B. and G. A. H. Walker (Aug. 1979). "PRECISION RADIAL VELOCITIES WITH AN ABSORPTION CELL." In: *Publications of the Astronomical Society of the Pacific* 91.542, p. 540. DOI: 10.1086/130535. URL: https://dx.doi.org/10.1086/130535.

Campbell, B., G. A. H. Walker, and S. Yang (Aug. 1988). "A Search for Substellar Companions to Solar-type Stars." In: *ApJ* 331, p. 902. DOI: 10.1086/166608.

Carvalho, A. and C. M. Johns-Krull (May 2023). "A Simple Code for Rotational Broadening of Broad Wavelength Range High-Dispersion Spectra." In: *Research Notes of the American Astronomical Society* 7.5, 91, p. 91. DOI: 10.3847/2515-5172/acd37e. arXiv: 2305.09693 [astro-ph.IM].

Casanovas, J. (Jan. 1997). "Early Observations of Sunspots: Scheiner and Galileo." In: *1st Advances in Solar Physics Euroconference. Advances in Physics of Sunspots*. Ed. by B. Schmieder, J. C. del Toro Iniesta, and M. Vazquez. Vol. 118. Astronomical Society of the Pacific Conference Series, p. 3.

Cegla, H. M. et al. (Mar. 2016a). "Modeling the Rossiter-McLaughlin Effect: Impact of the Convective Center-to-limb Variations in the Stellar Photosphere." In: *ApJ* 819.1, 67, p. 67. DOI: 10.3847/0004-637X/819/1/67. arXiv: 1601.02054 [astro-ph.EP].

Cegla, H. M. et al. (Apr. 2016b). "The Rossiter-McLaughlin effect reloaded: Probing the 3D spin-orbit geometry, differential stellar rotation, and the spatially-resolved stellar spectrum of star-planet systems." In: *A&A* 588, A127, A127. DOI: 10.1051/0004-6361/201527794. arXiv: 1602.00322 [astro-ph.EP].

Cegla, H. M. et al. (Oct. 2018). "Stellar Surface Magneto-convection as a Source of Astrophysical Noise. II. Center-to-limb Parameterization of Absorption Line Profiles and Comparison to Observations." In: *ApJ* 866.1, p. 55. DOI: 10.3847/1538-4357/aaddfc. URL: https://dx.doi.org/10.3847/1538-4357/aaddfc.

Chachan, Y., E. J. Lee, and H. A. Knutson (Jan. 2021). "Radial Gradients in Dust Opacity Lead to Preferred Region for Giant Planet Formation." In: *arXiv e-prints*, arXiv:2101.10333, arXiv:2101.10333. arXiv: 2101.10333 [astro-ph.EP].

Chaplin, W. J. et al. (Apr. 2019). "Filtering Solar-Like Oscillations for Exoplanet Detection in Radial Velocity Observations." In: *AJ* 157.4, p. 163. DOI:

10.3847/1538-3881/ab0c01. URL: https://dx.doi.org/10.3847/1538-3881/ab0c01.

Charbonneau, D. et al. (Jan. 2000). "Detection of Planetary Transits Across a Sun-like Star." In: *ApJL* 529.1, pp. L45–L48. DOI: 10.1086/312457. arXiv: astro-ph/9911436 [astro-ph].

Chatterjee, S. et al. (Oct. 2008). "Dynamical Outcomes of Planet-Planet Scattering." In: *ApJ* 686.1, pp. 580–602. DOI: 10.1086/590227. arXiv: astro-ph/0703166 [astro-ph].

Chauvin, G. et al. (Oct. 2004). "A giant planet candidate near a young brown dwarf. Direct VLT/NACO observations using IR wavefront sensing." In: *A&A* 425, pp. L29–L32. DOI: 10.1051/0004-6361:200400056. arXiv: astro-ph/0409323 [astro-ph].

Chen, H. and L. A. Rogers (Nov. 2016). "Evolutionary Analysis of Gaseous Sub-Neptune-mass Planets with MESA." In: *ApJ* 831.2, 180, p. 180. DOI: 10.3847/0004-637X/831/2/180. arXiv: 1603.06596 [astro-ph.EP].

Chontos, A. et al. (May 2019). "The Curious Case of KOI 4: Confirming Kepler's First Exoplanet Detection." In: *AJ* 157.5, 192, p. 192. DOI: 10.3847/1538-3881/ab0e8e. arXiv: 1903.01591 [astro-ph.EP].

Chontos, A. et al. (June 2022). "The TESS-Keck Survey: Science Goals and Target Selection." In: *AJ* 163.6, 297, p. 297. DOI: 10.3847/1538-3881/ac6266. arXiv: 2106.06156 [astro-ph.EP].

Claudi, R. et al. (2018a). "GIARPS: commissioning and first scientific results." In: *Ground-based and Airborne Instrumentation for Astronomy VII*. Ed. by C. J. Evans, L. Simard, and H. Takami. Vol. 10702. International Society for Optics and Photonics. SPIE, 107020Z. DOI: 10.1117/12.2312555. URL: https://doi.org/10.1117/12.2312555.

Claudi, R. et al. (July 2018b). "LOCNES: low cost NIR extended solar telescope." In: *Ground-based and Airborne Telescopes VII*. Ed. by H. K. Marshall and J. Spyromilio. Vol. 10700. Society of Photo-Optical Instrumentation Engineers (SPIE) Conference Series, 107004N, 107004N. DOI: 10.1117/12.2312458. arXiv: 1808.03185 [astro-ph.IM].

Collier Cameron, A. et al. (May 2021). "Separating planetary reflex Doppler shifts from stellar variability in the wavelength domain." In: *MNRAS* 505.2, pp. 1699–1717. ISSN: 0035-8711. DOI: 10.1093/mnras/stab1323. eprint: https://academic.oup.com/mnras/article-pdf/505/2/1699/38488934/stab1323.pdf. URL: https://doi.org/10.1093/mnras/stab1323.

Collier Cameron, A. et al. (Mar. 2010). "Line-profile tomography of exoplanet transits - I. The Doppler shadow of HD 189733b." In: *MNRAS* 403.1, pp. 151–158. DOI: 10.1111/j.1365-2966.2009.16131.x. arXiv: 0911.5361 [astro-ph.SR].

Collier Cameron, A. et al. (July 2019). “Three years of Sun-as-a-star radial-velocity observations on the approach to solar minimum.” In: *MNRAS* 487.1, pp. 1082–1100. DOI: 10.1093/mnras/stz1215. arXiv: 1904.12186 [astro-ph.SR].

Conrad, A. R. and W. F. Lupton (Jan. 1993). “The Keck Keyword Layer.” In: *Astronomical Data Analysis Software and Systems II*. Ed. by R. J. Hanisch, R. J. V. Brissenden, and J. Barnes. Vol. 52. Astronomical Society of the Pacific Conference Series, p. 203.

Cosentino, R. et al. (2012). “Harps-N: the new planet hunter at TNG.” In: *Ground-based and Airborne Instrumentation for Astronomy IV*. Ed. by I. S. McLean, S. K. Ramsay, and H. Takami. Vol. 8446. International Society for Optics and Photonics. SPIE, p. 84461V. DOI: 10.1117/12.925738. URL: https://doi.org/10.1117/12.925738.

Coşkunoğlu, B. et al. (Apr. 2011). “Local stellar kinematics from RAVE data - I. Local standard of rest.” In: *MNRAS* 412.2, pp. 1237–1245. DOI: 10.1111/j.1365-2966.2010.17983.x. arXiv: 1011.1188 [astro-ph.GA].

Crass, J. et al. (July 2021). “Extreme Precision Radial Velocity Working Group Final Report.” In: *arXiv e-prints*, arXiv:2107.14291, arXiv:2107.14291. DOI: 10.48550/arXiv.2107.14291. arXiv: 2107.14291 [astro-ph.IM].

Cretignier, M. et al. (Jan. 2020). “Measuring precise radial velocities on individual spectral lines. II. Dependance of stellar activity signal on line depth.” In: *A&A* 633, A76, A76. DOI: 10.1051/0004-6361/201936548. arXiv: 1912.05192 [astro-ph.EP].

Cretignier, M. et al. (Sept. 2021). “YARARA: Significant improvement in RV precision through post-processing of spectral time series.” In: *A&A* 653, A43, A43. DOI: 10.1051/0004-6361/202140986. arXiv: 2106.07301 [astro-ph.EP].

Cretignier, M. et al. (Oct. 2023). “YARARA V2: Reaching sub-m s^{-1} precision over a decade using PCA on line-by-line radial velocities.” In: *A&A* 678, A2, A2. DOI: 10.1051/0004-6361/202347232. arXiv: 2308.11812 [astro-ph.EP].

Cubillos, P. et al. (Jan. 2017). “On Correlated-noise Analyses Applied to Exoplanet Light Curves.” In: *AJ* 153.1, 3, p. 3. DOI: 10.3847/1538-3881/153/1/3. arXiv: 1610.01336 [astro-ph.EP].

Cumming, A. et al. (May 2008). “The Keck Planet Search: Detectability and the Minimum Mass and Orbital Period Distribution of Extrasolar Planets.” In: *PASP* 120.867, p. 531. DOI: 10.1086/588487. arXiv: 0803.3357 [astro-ph].

Czesla, S. et al. (June 2019). *PyA: Python astronomy-related packages*. ascl: 1906.010.

Dai, F. and J. N. Winn (Apr. 2017). "The Oblique Orbit of WASP-107b fromK2Photometry." In: *AJ* 153.5, p. 205. DOI: 10.3847/1538-3881/aa65d1.

Dai, F. et al. (Sept. 2019). "Homogeneous Analysis of Hot Earths: Masses, Sizes, and Compositions." In: *ApJ* 883.1, 79, p. 79. DOI: 10.3847/1538-4357/ab3a3b. arXiv: 1908.06299 [astro-ph.EP].

Dai, F. et al. (Oct. 2020). "The TESS-Keck Survey. III. A Stellar Obliquity Measurement of TOI-1726 c." In: *AJ* 160.4, 193, p. 193. DOI: 10.3847/1538-3881/abb3bd. arXiv: 2008.12397 [astro-ph.EP].

Dai, F. et al. (Aug. 2021). "TKS X: Confirmation of TOI-1444b and a Comparative Analysis of the Ultra-short-period Planets with Hot Neptunes." In: *AJ* 162.2, 62, p. 62. DOI: 10.3847/1538-3881/ac02bd.

Dalal, S. et al. (2019). "Nearly polar orbit of the sub-Neptune HD 3167 c - Constraints on the dynamical history of a multi-planet system." In: *A&A* 631, A28. DOI: 10.1051/0004-6361/201935944.

Dalba, P. A. et al. (Apr. 2020). "The TESS–Keck Survey. I. A Warm Sub-Saturn-mass Planet and a Caution about Stray Light in TESS Cameras." In: *AJ* 159.5, p. 241. DOI: 10.3847/1538-3881/ab84e3.

Davies, G. R. et al. (May 2014). "BiSON data preparation: a correction for differential extinction and the weighted averaging of contemporaneous data." In: *Monthly Notices of the Royal Astronomical Society* 441.4, pp. 3009–3017. ISSN: 0035-8711. DOI: 10.1093/mnras/stu803. eprint: https://academic.oup.com/mnras/article-pdf/441/4/3009/4055353/stu803.pdf. URL: https://doi.org/10.1093/mnras/stu803.

Davis, A. B. et al. (Aug. 2017). "Insights on the Spectral Signatures of Stellar Activity and Planets from PCA." In: *The Astrophysical Journal* 846.1, p. 59. DOI: 10.3847/1538-4357/aa8303. URL: https://dx.doi.org/10.3847/1538-4357/aa8303.

Dawson, R. (Aug. 2014). "On the tidal origin of hot Jupiter stellar obliquity trends." English (US). In: *Astrophysical Journal Letters* 790.2. ISSN: 2041-8205. DOI: 10.1088/2041-8205/790/2/L31.

Dawson, R. I. and D. C. Fabrycky (Oct. 2010). "Radial Velocity Planets De-aliased: A New, Short Period for Super-Earth 55 Cnc e." In: *ApJ* 722.1, pp. 937–953. DOI: 10.1088/0004-637X/722/1/937. arXiv: 1005.4050 [astro-ph.EP].

Dawson, R. I. and J. A. Johnson (Sept. 2018). "Origins of Hot Jupiters." In: *ARA&A* 56, pp. 175–221. DOI: 10.1146/annurev-astro-081817-051853. arXiv: 1801.06117 [astro-ph.EP].

de Beurs, Z. L. et al. (Aug. 2022). "Identifying Exoplanets with Deep Learning. IV. Removing Stellar Activity Signals from Radial Velocity Measurements Using Neural Networks." In: *AJ* 164.2, 49, p. 49. DOI: 10.3847/1538-3881/ac738e. arXiv: 2011.00003 [astro-ph.EP].

De Rosa, R. J., R. Dawson, and E. L. Nielsen (2020). "A significant mutual inclination between the planets within the sae system." In: *A&A* 640, A73. DOI: 10.1051/0004-6361/202038496.

Deich, W. T. S. (2014). "EMIR: a configurable hierarchical system for event monitoring and incident response." In: *Software and Cyberinfrastructure for Astronomy III*. Ed. by G. Chiozzi and N. M. Radziwill. Vol. 9152. International Society for Optics and Photonics. SPIE, p. 91521I. DOI: 10.1117/12.2056730. URL: https://doi.org/10.1117/12.2056730.

Del Moro, D. (Dec. 2004). "Solar granulation properties derived from three different time series." In: *A&A* 428, pp. 1007–1015. DOI: 10.1051/0004-6361:20040466.

Demory, B.-O. et al. (Oct. 2013). "Inference of Inhomogeneous Clouds in an Exoplanet Atmosphere." In: *ApJL* 776.2, L25, p. L25. DOI: 10.1088/2041-8205/776/2/L25. arXiv: 1309.7894 [astro-ph.EP].

Demory, B.-O. et al. (Apr. 2016). "A map of the large day-night temperature gradient of a super-Earth exoplanet." In: *Nature* 532.7598, pp. 207–209. DOI: 10.1038/nature17169. arXiv: 1604.05725 [astro-ph.EP].

Di Maio, C. et al. (Mar. 2024). "The GAPS programme at TNG. LII. Spot modelling of V1298 Tau using the SpotCCF tool." In: *A&A* 683, A239, A239. DOI: 10.1051/0004-6361/202348223. arXiv: 2312.14269 [astro-ph.SR].

Donati, J. .-. et al. (Nov. 1997). "Spectropolarimetric observations of active stars." In: *MNRAS* 291.4, pp. 658–682. DOI: 10.1093/mnras/291.4.658.

Donati, J. .-., M. Semel, and F. Praderie (Nov. 1989). "Zeeman-Doppler imaging of active stars. II. Numerical simulation and first observational results." In: *A&A* 225, pp. 467–478.

Dong, J. and D. Foreman-Mackey (Sept. 2023). "A Hierarchical Bayesian Framework for Inferring the Stellar Obliquity Distribution." In: *AJ* 166.3, 112, p. 112. DOI: 10.3847/1538-3881/ace105. arXiv: 2305.14220 [astro-ph.EP].

Dong, J. et al. (Oct. 2021). "TOI-3362b: A Proto Hot Jupiter Undergoing High-eccentricity Tidal Migration." In: *The Astrophysical Journal Letters* 920.1, p. L16. DOI: 10.3847/2041-8213/ac2600. URL: https://dx.doi.org/10.3847/2041-8213/ac2600.

Dong, S., B. Katz, and A. Socrates (Jan. 2014). "Warm Jupiters Need Close "Friends" for High-eccentricity Migration—a Stringent Upper Limit on the Perturber's Separation." In: *ApJL* 781.1, L5, p. L5. DOI: 10.1088/2041-8205/781/1/L5. arXiv: 1309.0011 [astro-ph.EP].

Doyle, L. et al. (Apr. 2023). "WASP-131 b with ESPRESSO – I. A bloated sub-Saturn on a polar orbit around a differentially rotating solar-type star." In: *Monthly Notices of the Royal Astronomical Society* 522.3, pp. 4499–4514. ISSN: 0035-8711. DOI: 10.1093/mnras/stad1240. eprint: https://academic.oup.com/mnras/article-pdf/522/3/4499/50267967/stad1240.pdf. URL: https://doi.org/10.1093/mnras/stad1240.

Dravins, D., L. Lindegren, and A. Nordlund (Mar. 1981). "Solar granulation - Influence of convection on spectral line asymmetries and wavelength shifts." In: *A&A* 96.1-2, pp. 345–364.

Dravins, D. and H.-G. Ludwig (Apr. 2024). "Solar photospheric spectrum microvariability II. Observed relations to magnetic activity and radial-velocity modulation." In: *arXiv e-prints*, arXiv:2404.08035, arXiv:2404.08035. DOI: 10.48550/arXiv.2404.08035. arXiv: 2404.08035 [astro-ph.SR].

Duane, S. et al. (Sept. 1987). "Hybrid Monte Carlo." In: *Physics Letters B* 195.2, pp. 216–222. DOI: 10.1016/0370-2693(87)91197-X.

Dumusque, X., I. Boisse, and N. C. Santos (Dec. 2014). "SOAP 2.0: A Tool to Estimate the Photometric and Radial Velocity Variations Induced by Stellar Spots and Plages." In: *ApJ* 796.2, 132, p. 132. DOI: 10.1088/0004-637X/796/2/132. arXiv: 1409.3594 [astro-ph.SR].

Dumusque, X. et al. (Apr. 2021). "Three years of HARPS-N high-resolution spectroscopy and precise radial velocity data for the Sun." In: *A&A* 648, A103, A103. DOI: 10.1051/0004-6361/202039350. arXiv: 2009.01945 [astro-ph.SR].

Dumusque, X. (2018). "Measuring precise radial velocities on individual spectral lines - I. Validation of the method and application to mitigate stellar activity." In: *A&A* 620, A47. DOI: 10.1051/0004-6361/201833795. URL: https://doi.org/10.1051/0004-6361/201833795.

Dumusque, X. et al. (2011a). "Planetary detection limits taking into account stellar noise - I. Observational strategies to reduce stellar oscillation and granulation effects." In: *A&A* 525, A140. DOI: 10.1051/0004-6361/201014097. URL: https://doi.org/10.1051/0004-6361/201014097.

Dumusque, X. et al. (2011b). "Planetary detection limits taking into account stellar noise - II. Effect of stellar spot groups on radial-velocities." In: *A&A* 527, A82. DOI: 10.1051/0004-6361/201015877. URL: https://doi.org/10.1051/0004-6361/201015877.

Duncan, D. K. et al. (May 1991). "CA II H and K Measurements Made at Mount Wilson Observatory, 1966–1983." In: *ApJS* 76, p. 383. DOI: 10.1086/191572.

Dupuy, T. J. et al. (May 2022). "Orbital architectures of planet-hosting binaries - II. Low mutual inclinations between planetary and stellar orbits." In: *MNRAS* 512.1, pp. 648–660. DOI: 10.1093/mnras/stac306. arXiv: 2202.00013 [astro-ph.EP].

Eastman, J., B. S. Gaudi, and E. Agol (Jan. 2013). "EXOFAST: A Fast Exoplanetary Fitting Suite in IDL." In: *PASP* 125.923, p. 83. DOI: 10.1086/669497. arXiv: 1206.5798 [astro-ph.IM].

Eggleton, P. P., L. G. Kiseleva, and P. Hut (May 1998). "The Equilibrium Tide Model for Tidal Friction." In: *ApJ* 499.2, pp. 853–870. DOI: 10.1086/305670. arXiv: astro-ph/9801246 [astro-ph].

Ehrenreich, D. et al. (June 2015). "A giant comet-like cloud of hydrogen escaping the warm Neptune-mass exoplanet GJ 436b." In: *Nature* 522.7557, pp. 459–461. DOI: 10.1038/nature14501. arXiv: 1506.07541 [astro-ph.EP].

Epstein-Martin, M., J. Becker, and K. Batygin (May 2022). "Generating Stellar Obliquity in Systems with Broken Protoplanetary Disks." In: *The Astrophysical Journal* 931.1, p. 42. DOI: 10.3847/1538-4357/ac5b79. URL: https://dx.doi.org/10.3847/1538-4357/ac5b79.

Ervin, T. et al. (June 2022). "Leveraging Space-based Data from the Nearest Solar-type Star to Better Understand Stellar Activity Signatures in Radial Velocity Data." In: *AJ* 163.6, 272, p. 272. DOI: 10.3847/1538-3881/ac67e6. arXiv: 2204.09014 [astro-ph.SR].

Espinoza-Retamal, J. I., W. Zhu, and C. Petrovich (Nov. 2023). "Prospects from TESS and Gaia to Constrain the Flatness of Planetary Systems." In: *The Astronomical Journal* 166.6, p. 231. DOI: 10.3847/1538-3881/ad00b9. URL: https://dx.doi.org/10.3847/1538-3881/ad00b9.

Espinoza-Retamal, J. I. et al. (Dec. 2023). "The Aligned Orbit of the Eccentric Proto Hot Jupiter TOI-3362b." In: *ApJL* 958.2, L20, p. L20. DOI: 10.3847/2041-8213/ad096d. arXiv: 2309.03306 [astro-ph.EP].

Esposito, M. et al. (2014). "The GAPS Programme with HARPS-N at TNG - III: The retrograde orbit of HAT-P-18b." In: *A&A* 564, p. L13. DOI: 10.1051/0004-6361/201423735.

Essack, Z. et al. (Feb. 2023). "TOI-1075 b: A Dense, Massive, Ultra-short-period Hot Super-Earth Straddling the Radius Gap." In: *AJ* 165.2, 47, p. 47. DOI: 10.3847/1538-3881/ac9c5b. arXiv: 2210.14901 [astro-ph.EP].

Fabrycky, D. and S. Tremaine (Nov. 2007). "Shrinking Binary and Planetary Orbits by Kozai Cycles with Tidal Friction." In: *ApJ* 669.2, pp. 1298–1315. DOI: 10.1086/521702.

Fabrycky, D. C. et al. (Aug. 2014). "Architecture of Kepler's Multi-transiting Systems. II. New Investigations with Twice as Many Candidates." In: *ApJ* 790.2, 146, p. 146. DOI: 10.1088/0004-637X/790/2/146. arXiv: 1202.6328 [astro-ph.EP].

Fedele, D. et al. (Feb. 2010). "Timescale of mass accretion in pre-main-sequence stars." In: *A&A* 510, A72, A72. DOI: 10.1051/0004-6361/200912810. arXiv: 0911.3320 [astro-ph.SR].

Fellgett, P. (Apr. 1955). "A Proposal for a Radial Velocity Photometer." In: *Optica Acta* 2.1, pp. 9–16. DOI: 10.1080/713820996.

Fischer, D. A. et al. (June 2016). "State of the Field: Extreme Precision Radial Velocities." In: *PASP* 128.964, p. 066001. DOI: 10.1088/1538-3873/128/964/066001. arXiv: 1602.07939 [astro-ph.IM].

Ford, E. B. (May 2006). "Improving the Efficiency of Markov Chain Monte Carlo for Analyzing the Orbits of Extrasolar Planets." In: *ApJ* 642.1, pp. 505–522. DOI: 10.1086/500802.

Ford, E. B., B. Kozinsky, and F. A. Rasio (May 2000). "Secular Evolution of Hierarchical Triple Star Systems." In: *The Astrophysical Journal* 535.1, p. 385. DOI: 10.1086/308815. URL: https://dx.doi.org/10.1086/308815.

Foreman-Mackey, D. et al. (Mar. 2013). "emcee: The MCMC Hammer." In: *PASP* 125.925, pp. 306–312.

Foreman-Mackey, D. et al. (Nov. 2017). "Fast and Scalable Gaussian Process Modeling with Applications to Astronomical Time Series." In: *The Astronomical Journal* 154.6, p. 220. DOI: 10.3847/1538-3881/aa9332. URL: https://dx.doi.org/10.3847/1538-3881/aa9332.

Foreman-Mackey, D. et al. (May 2021). "exoplanet: Gradient-based probabilistic inference for exoplanet data & other astronomical time series." In: *arXiv e-prints*, arXiv:2105.01994, arXiv:2105.01994. arXiv: 2105.01994 [astro-ph.IM].

Fredslund Andersen, M. et al. (2019). "Oscillations in the Sun with SONG: Setting the scale for asteroseismic investigations." In: *A&A* 623, p. L9. DOI: 10.1051/0004-6361/201935175. URL: https://doi.org/10.1051/0004-6361/201935175.

Fu, G. et al. (Dec. 2022). "Water and an Escaping Helium Tail Detected in the Hazy and Methane-depleted Atmosphere of HAT-P-18b from JWST NIRISS/SOSS." In: *ApJL* 940.2, L35, p. L35. DOI: 10.3847/2041-8213/ac9977. arXiv: 2211.13761 [astro-ph.EP].

Fulton, B. J. and E. A. Petigura (May 2018). "The California Kepler Survey VII. Precise Planet Radii Leveraging Gaia DR2 Reveal the Stellar Mass Dependence of the Planet Radius Gap." In: *ArXiv e-prints*. arXiv: 1805.01453 [astro-ph.EP].

Fulton, B. J. et al. (Sept. 2017). "The California-Kepler Survey. III. A Gap in the Radius Distribution of Small Planets." In: *AJ* 154, 109, p. 109. DOI: 10.3847/1538-3881/aa80eb. arXiv: 1703.10375 [astro-ph.EP].

Fulton, B. J. et al. (Apr. 2018). "RadVel: The Radial Velocity Modeling Toolkit." In: *PASP* 130.986, p. 044504. DOI: 10.1088/1538-3873/aaaaa8. arXiv: 1801.01947 [astro-ph.IM].

Fulton, B. J. et al. (July 2021). "California Legacy Survey. II. Occurrence of Giant Planets beyond the Ice Line." In: *ApJS* 255.1, 14, p. 14. DOI: 10.3847/1538-4365/abfcc1. arXiv: 2105.11584 [astro-ph.EP].

Gaia Collaboration et al. (June 2023). "Gaia Data Release 3. Summary of the content and survey properties." In: *A&A* 674, A1, A1. DOI: 10.1051/0004-6361/202243940. arXiv: 2208.00211 [astro-ph.GA].

Galarza, J. Y. et al. (Mar. 2024). "TOI-1173 A *b*: The First Inflated Super-Neptune in a Wide Binary System." In: *arXiv e-prints*, arXiv:2403.06240, arXiv:2403.06240. DOI: 10.48550/arXiv.2403.06240. arXiv: 2403.06240 [astro-ph.EP].

Galle, J. G. (Nov. 1846). "Account of the discovery of Le Verrier's planet Neptune, at Berlin, Sept. 23, 1846." In: *MNRAS* 7, p. 153. DOI: 10.1093/mnras/7.9.153.

Gaudi, B. S. (Sept. 2012). "Microlensing Surveys for Exoplanets." In: *ARA&A* 50, pp. 411–453. DOI: 10.1146/annurev-astro-081811-125518.

Gelman, A. et al. (2003). *Bayesian Data Analysis*. 2nd ed. Chapman and Hall.

Gibson, R. K. (Feb. 2023). "PARVI: The Little Spectrograph That Could." PhD thesis. Columbia University. DOI: 10.7916/59b0-kp28.

Gibson, S. R. et al. (Aug. 2016). "KPF: Keck Planet Finder." In: *Ground-based and Airborne Instrumentation for Astronomy VI*. Ed. by C. J. Evans, L. Simard, and H. Takami. Vol. 9908. Society of Photo-Optical Instrumentation Engineers (SPIE) Conference Series, 990870, p. 990870. DOI: 10.1117/12.2233334.

Gibson, S. R. et al. (July 2018). "Keck Planet Finder: preliminary design." In: *Ground-based and Airborne Instrumentation for Astronomy VII*. Ed. by C. J. Evans, L. Simard, and H. Takami. Vol. 10702. Society of Photo-Optical Instrumentation Engineers (SPIE) Conference Series, 107025X, p. 107025X. DOI: 10.1117/12.2311565.

Gibson, S. R. et al. (Dec. 2020). "Keck Planet Finder: design updates." In: *Society of Photo-Optical Instrumentation Engineers (SPIE) Conference Series*. Vol. 11447. Society of Photo-Optical Instrumentation Engineers (SPIE) Conference Series, 1144742, p. 1144742. DOI: 10.1117/12.2561783.

Gibson, S. R. (Jan. 2013). “KiwiSpec: The Design and Performance of a High Resolution Echelle Spectrograph for Astronomy.” PhD thesis. University of Canterbury, New Zealand.

Giles, H. A. C., A. Collier Cameron, and R. D. Haywood (Dec. 2017). “A Kepler study of starspot lifetimes with respect to light-curve amplitude and spectral type.” In: *MNRAS* 472.2, pp. 1618–1627. DOI: 10.1093/mnras/stx1931. arXiv: 1707.08583 [astro-ph.SR].

Ginzburg, S., H. E. Schlichting, and R. Sari (Feb. 2018). “Core-powered mass-loss and the radius distribution of small exoplanets.” In: *Monthly Notices of the Royal Astronomical Society* 476.1, pp. 759–765. ISSN: 0035-8711. DOI: 10.1093/mnras/sty290. eprint: https://academic.oup.com/mnras/article-pdf/476/1/759/24215431/sty290.pdf. URL: https://doi.org/10.1093/mnras/sty290.

Goldreich, P. and S. Tremaine (Oct. 1980). “Disk-satellite interactions.” In: *ApJ* 241, pp. 425–441. DOI: 10.1086/158356.

Goldreich, P. and S. Soter (1966). “Q in the solar system.” In: *Icarus* 5.1, pp. 375–389. ISSN: 0019-1035. DOI: https://doi.org/10.1016/0019-1035(66)90051-0. URL: https://www.sciencedirect.com/science/article/pii/0019103566900510.

Gomes, R., R. Deienno, and A. Morbidelli (Jan. 2017). “The Inclination of the Planetary System Relative to the Solar Equator May Be Explained by the Presence of Planet 9.” In: *AJ* 153.1, 27, p. 27. DOI: 10.3847/1538-3881/153/1/27. arXiv: 1607.05111 [astro-ph.EP].

Gray, D. F. (2005). *The Observation and Analysis of Stellar Photospheres*. DOI: 10.1017/CBO9781316036570.

Griffin, R. (Jan. 1973). “On the possibility of determining stellar radial velocities to 0.01 km s^{-1}.” In: *MNRAS* 162, pp. 243–253. DOI: 10.1093/mnras/162.3.243.

Griffin, R. F. (May 1967). “A Photoelectric Radial-Velocity Spectrometer.” In: *ApJ* 148, p. 465. DOI: 10.1086/149168.

Grunblatt, S. K. et al. (Nov. 2017). “Seeing Double with K2: Testing Re-inflation with Two Remarkably Similar Planets around Red Giant Branch Stars.” In: *The Astronomical Journal* 154.6, p. 254. DOI: 10.3847/1538-3881/aa932d. URL: https://dx.doi.org/10.3847/1538-3881/aa932d.

Grundahl, F. et al. (Jan. 2006). “SONG: Stellar Oscillations Network Group . A global network of small telescopes for asteroseismology and planet searches.” In: *MmSAI* 77, p. 458.

Guerrero, N. M. et al. (June 2021). “The TESS Objects of Interest Catalog from the TESS Prime Mission.” In: *ApJS* 254.2, 39, p. 39. DOI: 10.3847/1538-4365/abefe1. arXiv: 2103.12538 [astro-ph.EP].

Guilluy, G. et al. (Aug. 2023). "DREAM. III. A helium survey in exoplanets on the edge of the hot Neptune desert with GIANO-B at TNG." In: *A&A* 676, A130, A130. DOI: 10.1051/0004-6361/202346419. arXiv: 2307.00967 [astro-ph.EP].

Gupta, A. and H. E. Schlichting (May 2019). "Sculpting the valley in the radius distribution of small exoplanets as a by-product of planet formation: the core-powered mass-loss mechanism." In: *Monthly Notices of the Royal Astronomical Society* 487.1, pp. 24–33. ISSN: 0035-8711. DOI: 10.1093/mnras/stz1230. eprint: https://academic.oup.com/mnras/article-pdf/487/1/24/28693821/stz1230.pdf. URL: https://doi.org/10.1093/mnras/stz1230.

Gupta, A. F. and M. Bedell (Mar. 2023). "Fishing for Planets: A Comparative Analysis of EPRV Survey Performance in the Presence of Correlated Noise." In: *arXiv e-prints*, arXiv:2303.14571, arXiv:2303.14571. DOI: 10.48550/arXiv.2303.14571. arXiv: 2303.14571 [astro-ph.EP].

Gupta, A. F. et al. (Mar. 2021). "Target Prioritization and Observing Strategies for the NEID Earth Twin Survey." In: *AJ* 161.3, 130, p. 130. DOI: 10.3847/1538-3881/abd79e. arXiv: 2101.11689 [astro-ph.EP].

Gupta, A. F. et al. (Dec. 2022). "Detection of p-mode Oscillations in HD 35833 with NEID and TESS." In: *AJ* 164.6, 254, p. 254. DOI: 10.3847/1538-3881/ac96f3. arXiv: 2210.00544 [astro-ph.SR].

Hale, S. J. et al. (Jan. 2016). "Performance of the Birmingham Solar-Oscillations Network (BiSON)." In: *SoPh* 291.1, pp. 1–28. DOI: 10.1007/s11207-015-0810-0. arXiv: 1510.07085 [astro-ph.SR].

Hall, R. D. et al. (Sept. 2018). "On the Feasibility of Intense Radial Velocity Surveys for Earth-Twin Discoveries." In: *MNRAS* 479.3, pp. 2968–2987. DOI: 10.1093/mnras/sty1464. arXiv: 1806.00518 [astro-ph.EP].

Halverson, S. et al. (May 2014). "Development of Fiber Fabry-Perot Interferometers as Stable Near-infrared Calibration Sources for High Resolution Spectrographs." In: *PASP* 126.939, p. 445. DOI: 10.1086/676649. arXiv: 1403.6841 [astro-ph.IM].

Halverson, S. et al. (June 2015). "An Efficient, Compact, and Versatile Fiber Double Scrambler for High Precision Radial Velocity Instruments." In: *ApJ* 806.1, 61, p. 61. DOI: 10.1088/0004-637X/806/1/61. arXiv: 1505.07463 [astro-ph.IM].

Halverson, S. et al. (Aug. 2016). "A comprehensive radial velocity error budget for next generation Doppler spectrometers." In: vol. 9908. SPIE, 99086P, 99086P. DOI: 10.1117/12.2232761. arXiv: 1607.05634 [astro-ph.IM].

Hamer, J. H. and K. C. Schlaufman (July 2022). “Evidence for the Late Arrival of Hot Jupiters in Systems with High Host-star Obliquities.” In: *AJ* 164.1, 26, p. 26. DOI: 10.3847/1538-3881/ac69ef. arXiv: 2205.00040 [astro-ph.EP].

Harvey, J. W. et al. (1996). “The Global Oscillation Network Group (GONG) Project.” In: *Science* 272.5266, pp. 1284–1286. DOI: 10.1126/science.272.5266.1284. eprint: https://www.science.org/doi/pdf/10.1126/science.272.5266.1284. URL: https://www.science.org/doi/abs/10.1126/science.272.5266.1284.

Hastings, W. K. (Apr. 1970). “Monte Carlo Sampling Methods using Markov Chains and their Applications.” In: *Biometrika* 57.1, pp. 97–109. DOI: 10.1093/biomet/57.1.97.

Haywood, R. D. et al. (July 2014). “Planets and stellar activity: hide and seek in the CoRoT-7 system.” In: *Monthly Notices of the Royal Astronomical Society* 443.3, pp. 2517–2531. ISSN: 0035-8711. DOI: 10.1093/mnras/stu1320. eprint: https://academic.oup.com/mnras/article-pdf/443/3/2517/4927775/stu1320.pdf. URL: https://doi.org/10.1093/mnras/stu1320.

Haywood, R. D. et al. (Apr. 2016). “The Sun as a planet-host star: proxies from SDO images for HARPS radial-velocity variations.” In: *MNRAS* 457.4, pp. 3637–3651. DOI: 10.1093/mnras/stw187. arXiv: 1601.05651 [astro-ph.EP].

Haywood, R. D. et al. (Aug. 2022). “Unsigned Magnetic Flux as a Proxy for Radial-velocity Variations in Sun-like Stars.” In: *ApJ* 935.1, 6, p. 6. DOI: 10.3847/1538-4357/ac7c12. arXiv: 2005.13386 [astro-ph.SR].

Haywood, R. D. (2016). “Stellar Activity as a Source of Radial-Velocity Variability.” In: *Radial-velocity Searches for Planets Around Active Stars*. Cham: Springer International Publishing, pp. 13–44. ISBN: 978-3-319-41273-3. DOI: 10.1007/978-3-319-41273-3_2. URL: https://doi.org/10.1007/978-3-319-41273-3_2.

Hebb, L. et al. (Mar. 2009). “WASP-12b: The Hottest Transiting Extrasolar Planet Yet Discovered.” In: *ApJ* 693.2, pp. 1920–1928. DOI: 10.1088/0004-637X/693/2/1920. arXiv: 0812.3240 [astro-ph].

Hébrard, G. et al. (2008). “Misaligned spin-orbit in the XO-3 planetary system?*.” In: *A&A* 488.2, pp. 763–770. DOI: 10.1051/0004-6361:200810056.

Hébrard, G. et al. (2010). “Observation of the full 12-hour-long transit of the exoplanet HD 80606 b - Warm-Spitzer photometry and SOPHIE spectroscopy.” In: *Å* 516, A95. DOI: 10.1051/0004-6361/201014327. URL: https://doi.org/10.1051/0004-6361/201014327.

Hedges, C. et al. (Dec. 2020). "Systematics-insensitive Periodogram for Finding Periods in TESS Observations of Long-period Rotators." In: *Research Notes of the AAS* 4.12, p. 220. DOI: 10.3847/2515-5172/abd106. URL: https://dx.doi.org/10.3847/2515-5172/abd106.

Heller, C. H. (May 1993). "Encounters with Protostellar Disks. I. Disk Tilt and the Nonzero Solar Obliquity." In: *ApJ* 408, p. 337. DOI: 10.1086/172591.

Hellier, C. et al. (Oct. 2012). "Seven transiting hot Jupiters from WASP-South, Euler and TRAPPIST: WASP-47b, WASP-55b, WASP-61b, WASP-62b, WASP-63b, WASP-66b and WASP-67b." In: *MNRAS* 426.1, pp. 739–750. DOI: 10.1111/j.1365-2966.2012.21780.x. arXiv: 1204.5095 [astro-ph.EP].

Henry, G. W. et al. (Jan. 2000). "A Transiting "51 Peg-like" Planet." In: *ApJL* 529.1, pp. L41–L44. DOI: 10.1086/312458.

Herschel, W. and D. Watson (Jan. 1781). "Account of a Comet. By Mr. Herschel, F. R. S.; Communicated by Dr. Watson, Jun. of Bath, F. R. S." In: *Philosophical Transactions of the Royal Society of London Series I* 71, pp. 492–501.

Hirano, T. et al. (Dec. 2011). "Improved Modeling of the Rossiter-McLaughlin Effect for Transiting Exoplanets." In: *ApJ* 742.2, 69, p. 69. DOI: 10.1088/0004-637X/742/2/69. arXiv: 1108.4430 [astro-ph.EP].

Hirano, T. et al. (Aug. 2020). "Limits on the Spin-Orbit Angle and Atmospheric Escape for the 22 Myr Old Planet AU Mic b." In: *ApJL* 899.1, L13, p. L13. DOI: 10.3847/2041-8213/aba6eb. arXiv: 2006.13243 [astro-ph.EP].

Hjorth, M. et al. (Feb. 2021). "A backward-spinning star with two coplanar planets." In: *Proceedings of the National Academy of Science* 118.8, e2017418118, e2017418118. DOI: 10.1073/pnas.2017418118. arXiv: 2102.07677 [astro-ph.EP].

Hoffman, M. and A. Gelman (2014). "The No-U-turn sampler: adaptively setting path lengths in Hamiltonian Monte Carlo." In: *J. Mach. Learn. Res.* 15, pp. 1593–1623.

Høg, E. et al. (Mar. 2000). "The Tycho-2 catalogue of the 2.5 million brightest stars." In: *A&A* 355, pp. L27–L30.

Hogg, D. W. and D. Foreman-Mackey (May 2018). "Data Analysis Recipes: Using Markov Chain Monte Carlo*." In: *The Astrophysical Journal Supplement Series* 236.1, p. 11. DOI: 10.3847/1538-4365/aab76e. URL: https://dx.doi.org/10.3847/1538-4365/aab76e.

Hojjatpanah, S. et al. (Sept. 2019). "Catalog for the ESPRESSO blind radial velocity exoplanet survey." In: *A&A* 629, A80, A80. DOI: 10.1051/0004-6361/201834729. arXiv: 1908.04627 [astro-ph.EP].

Holcomb, R. J. et al. (Sept. 2022). "SpinSpotter : An Automated Algorithm for Identifying Stellar Rotation Periods with Autocorrelation Analysis." In: *The Astrophysical Journal* 936.2, p. 138. DOI: 10.3847/1538-4357/ac8990. URL: https://dx.doi.org/10.3847/1538-4357/ac8990.

Holmgren, W. F., C. W. Hansen, and M. A. Mikofski (2018). "pvlib python: a python package for modeling solar energy systems." In: *Journal of Open Source Software* 3.29, p. 884. DOI: 10.21105/joss.00884. URL: https://doi.org/10.21105/joss.00884.

Holt, J. R. (Jan. 1893). "Spectroscopic Determination of Stellar Rotation." In: *Astronomy and Astro-Physics (formerly The Sidereal Messenger)* 12, p. 646.

Horne, K. (June 1986). "An optimal extraction algorithm for CCD spectroscopy." In: *PASP* 98, pp. 609–617. DOI: 10.1086/131801.

Hosokawa, Y. (Jan. 1953). "On the Rotation Effect of Velocity Curves in Eclipsing Binary Systems." In: *PASJ* 5, p. 88.

Howard, A. W. et al. (Sept. 2010a). "THE CALIFORNIA PLANET SURVEY. I. FOUR NEW GIANT EXOPLANETS." In: *ApJ* 721.2, pp. 1467–1481. DOI: 10.1088/0004-637x/721/2/1467.

Howard, A. W. et al. (Oct. 2010b). "The Occurrence and Mass Distribution of Close-in Super-Earths, Neptunes, and Jupiters." In: *Science* 330.6004, p. 653. DOI: 10.1126/science.1194854. arXiv: 1011.0143 [astro-ph.EP].

Howard, A. W. et al. (Aug. 2012). "Planet Occurrence within 0.25 AU of Solar-type Stars from Kepler." In: *ApJS* 201.2, 15, p. 15. DOI: 10.1088/0067-0049/201/2/15. arXiv: 1103.2541 [astro-ph.EP].

Howell, S. B. et al. (July 2011). "Speckle Camera Observations for the NASA Kepler Mission Follow-up Program." In: *AJ* 142.1, 19, p. 19. DOI: 10.1088/0004-6256/142/1/19.

Howell, S. B. et al. (Apr. 2014). "The K2 Mission: Characterization and Early Results." In: *PASP* 126.938, pp. 398–408. DOI: 10.1086/676406.

Hu, Q. et al. (Apr. 2024). "The PFS View of TOI-677 b: A Spin–Orbit Aligned Warm Jupiter in a Dynamically Hot System." In: *AJ* 167.4, 175, p. 175. DOI: 10.3847/1538-3881/ad2855. arXiv: 2402.07346 [astro-ph.EP].

Huang, C. X., C. Petrovich, and E. Deibert (Apr. 2017). "Dynamically Hot Super-Earths from Outer Giant Planet Scattering." In: *AJ* 153.5, p. 210. DOI: 10.3847/1538-3881/aa67fb.

Huber, D. et al. (2013). "Stellar Spin-Orbit Misalignment in a Multiplanet System." In: *Science* 342.6156, pp. 331–334. DOI: 10.1126/science.1242066. eprint: https://science.sciencemag.org/content/342/6156/331.full.pdf.

Huber, D. et al. (Aug. 2017a). "Asteroseismology and Gaia: Testing Scaling Relations Using 2200 Kepler Stars with TGAS Parallaxes." In: *ApJ* 844.2, 102, p. 102. DOI: 10.3847/1538-4357/aa75ca. arXiv: 1705.04697 [astro-ph.SR].

Huber, D. et al. (Aug. 2017b). "Asteroseismology and Gaia: Testing Scaling Relations Using 2200 Kepler Stars with TGAS Parallaxes." In: *ApJ* 844.2, 102, p. 102. DOI: 10.3847/1538-4357/aa75ca. arXiv: 1705.04697 [astro-ph.SR].

Hunter, J. D. (2007). "Matplotlib: A 2D Graphics Environment." In: *CSE* 9.3, pp. 90–95.

Husser, T. .-. et al. (May 2013). "A new extensive library of PHOENIX stellar atmospheres and synthetic spectra." In: *A&A* 553, A6, A6. DOI: 10.1051/0004-6361/201219058. arXiv: 1303.5632 [astro-ph.SR].

Hut, P. (Dec. 1980). "Stability of tidal equilibrium." In: *A&A* 92.1-2, pp. 167–170.

Hut, P. (June 1981). "Tidal evolution in close binary systems." In: *A&A* 99, pp. 126–140.

Hwang, H.-C., Y.-S. Ting, and N. L. Zakamska (May 2022). "The eccentricity distribution of wide binaries and their individual measurements." In: *MNRAS* 512.3, pp. 3383–3399. DOI: 10.1093/mnras/stac675. arXiv: 2111.01789 [astro-ph.SR].

Isaacson, H. and D. Fischer (Dec. 2010a). "Chromospheric Activity and Jitter Measurements for 2630 Stars on the California Planet Search." In: *ApJ* 725.1, pp. 875–885. DOI: 10.1088/0004-637X/725/1/875. arXiv: 1009.2301 [astro-ph.EP].

Isaacson, H. and D. Fischer (Dec. 2010b). "Chromospheric Activity and Jitter Measurements for 2630 Stars on the California Planet Search." In: *ApJ* 725.1, pp. 875–885. DOI: 10.1088/0004-637X/725/1/875. arXiv: 1009.2301 [astro-ph.EP].

Ito, T. and K. Ohtsuka (Nov. 2019). "The Lidov-Kozai Oscillation and Hugo von Zeipel." In: *Monographs on Environment, Earth and Planets* 7.1, pp. 1–113. DOI: 10.5047/meep.2019.00701.0001. arXiv: 1911.03984 [astro-ph.EP].

Ivshina, E. S. and J. N. Winn (Apr. 2022). "TESS Transit Timing of Hundreds of Hot Jupiters." In: *ApJS* 259.2, 62, p. 62. DOI: 10.3847/1538-4365/ac545b. arXiv: 2202.03401 [astro-ph.EP].

Jenkins, J. M. et al. (Aug. 2016). "The TESS science processing operations center." In: *Software and Cyberinfrastructure for Astronomy IV*. Vol. 9913. Proc. SPIE, 99133E, 99133E. DOI: 10.1117/12.2233418.

Jenkins, J. S. et al. (Jan. 2020). "An ultrahot Neptune in the Neptune desert." In: *Nature Astronomy* 4, pp. 1148–1157. DOI: 10.1038/s41550-020-1142-z. arXiv: 2009.12832 [astro-ph.EP].

Jentink, C. F. et al. (2022). "ABORAS: polarimetric, 10cm/s RV observations of the Sun as a star." In: vol. 12182. SPIE. SPIE, p. 1218231. DOI: 10.1117/12.2627113. URL: https://doi.org/10.1117/12.2627113.

Jurgenson, C. et al. (2016). "EXPRES: a next generation RV spectrograph in the search for earth-like worlds." In: *Ground-based and Airborne Instrumentation for Astronomy VI*. Ed. by C. J. Evans, L. Simard, and H. Takami. Vol. 9908. International Society for Optics and Photonics. SPIE, 99086T. DOI: 10.1117/12.2233002. URL: https://doi.org/10.1117/12.2233002.

Kamiaka, S. et al. (Mar. 2019). "The Misaligned Orbit of the Earth-sized Planet Kepler-408b." In: *The Astronomical Journal* 157.4, p. 137. DOI: 10.3847/1538-3881/ab04a9.

Kane, S. R. et al. (Sept. 2020). "A Volatile-poor Formation of LHS 3844b Based on Its Lack of Significant Atmosphere." In: *PSJ* 1.2, 36, p. 36. DOI: 10.3847/PSJ/abaab5. arXiv: 2007.14493 [astro-ph.EP].

Kanodia, S. and J. Wright (Jan. 2018). "Python Leap Second Management and Implementation of Precise Barycentric Correction (barycorrpy)." In: *Research Notes of the American Astronomical Society* 2.1, 4, p. 4. DOI: 10.3847/2515-5172/aaa4b7. arXiv: 1801.01634 [astro-ph.EP].

Kant, I. (1755). "Königsberg: Petersen".

Kempton, E. M. .-. et al. (Nov. 2018). "A Framework for Prioritizing the TESS Planetary Candidates Most Amenable to Atmospheric Characterization." In: *PASP* 130.993, p. 114401. DOI: 10.1088/1538-3873/aadf6f. arXiv: 1805.03671 [astro-ph.EP].

Kipping, D. M. (Nov. 2013). "Efficient, uninformative sampling of limb darkening coefficients for two-parameter laws." In: *MNRAS* 435, pp. 2152–2160. DOI: 10.1093/mnras/stt1435. arXiv: 1308.0009 [astro-ph.SR].

Kipping, D. and T. Jansen (Sept. 2020). "Detection of the Occultation of 55 Cancri e with TESS." In: *Research Notes of the American Astronomical Society* 4.9, 170, p. 170. DOI: 10.3847/2515-5172/abbc0f. arXiv: 2009.12601 [astro-ph.EP].

Kirk, J. et al. (Feb. 2020). "Confirmation of WASP-107b's Extended Helium Atmosphere with Keck II/NIRSPEC." In: *AJ* 159.3, p. 115. DOI: 10.3847/1538-3881/ab6e66.

Kiseleva, L. G., P. P. Eggleton, and S. Mikkola (Oct. 1998). "Tidal friction in triple stars." In: *MNRAS* 300.1, pp. 292–302. ISSN: 0035-8711. DOI: 10.1046/j.1365-8711.1998.01903.x. eprint: https://academic.oup.com/mnras/article-pdf/300/1/292/3920716/300-1-292.pdf.

Kjeldsen, H. and T. R. Bedding (Jan. 1995). "Amplitudes of stellar oscillations: the implications for asteroseismology." In: *A&A* 293, pp. 87–106. DOI: 10.48550/arXiv.astro-ph/9403015. arXiv: astro-ph/9403015 [astro-ph].

Kjeldsen, H. et al. (Dec. 2005). "Solar-like Oscillations in α Centauri B." In: *The Astrophysical Journal* 635.2, p. 1281. DOI: 10.1086/497530. URL: https://dx.doi.org/10.1086/497530.

Kjeldsen, H. et al. (Aug. 2008). "The Amplitude of Solar Oscillations Using Stellar Techniques." In: *ApJ* 682.2, p. 1370. DOI: 10.1086/589142. URL: https://dx.doi.org/10.1086/589142.

Knutson, H. A. et al. (Apr. 2014). "Friends of Hot Jupiters. I. A Radial Velocity Search for Massive, Long-period Companions to Close-in Gas Giant Planets." In: *ApJ* 785.2, 126, p. 126. DOI: 10.1088/0004-637X/785/2/126. arXiv: 1312.2954 [astro-ph.EP].

Kochukhov, O., V. Makaganiuk, and N. Piskunov (Dec. 2010). "Least-squares deconvolution of the stellar intensity and polarization spectra." In: *A&A* 524, A5, A5. DOI: 10.1051/0004-6361/201015429. arXiv: 1008.5115 [astro-ph.SR].

Kochukhov, O. et al. (Mar. 2020). "Hidden magnetic fields of young suns." In: *A&A* 635, A142, A142. DOI: 10.1051/0004-6361/201937185. arXiv: 2002.10469 [astro-ph.SR].

Kochukhov, O. (2016). "Doppler and Zeeman Doppler Imaging of Stars." In: *Lecture Notes in Physics, Berlin Springer Verlag*. Ed. by J.-P. Rozelot and C. Neiner. Vol. 914, p. 177. DOI: 10.1007/978-3-319-24151-7_9.

Kolbl, R. et al. (Jan. 2015). "Detection of Stars Within ~0.8 in of Kepler Objects of Interest." In: *AJ* 149.1, 18, p. 18. DOI: 10.1088/0004-6256/149/1/18. arXiv: 1412.5259 [astro-ph.SR].

Kopal, Z. (Apr. 1942). "The Calculation of Rotation Factors for Eclipsing Binary Systems." In: *Proceedings of the National Academy of Science* 28.4, pp. 133–140. DOI: 10.1073/pnas.28.4.133.

Kostov, V. B. et al. (Nov. 2016). "TATOOINE'S FUTURE: THE ECCENTRIC RESPONSE OFKEPLER'S CIRCUMBINARY PLANETS TO COMMON-ENVELOPE EVOLUTION OF THEIR HOST STARS." In: *ApJ* 832.2, p. 183. DOI: 10.3847/0004-637x/832/2/183.

Kovács, G., S. Zucker, and T. Mazeh (Aug. 2002). "A box-fitting algorithm in the search for periodic transits." In: *A&A* 391, pp. 369–377. DOI: 10.1051/0004-6361:20020802. eprint: astro-ph/0206099.

Kozai, Y. (Nov. 1962). "Secular perturbations of asteroids with high inclination and eccentricity." In: *AJ* 67, pp. 591–598. DOI: 10.1086/108790.

Kraft, R. P. (Nov. 1967). “Studies of Stellar Rotation. V. The Dependence of Rotation on Age among Solar-Type Stars.” In: *ApJ* 150, p. 551. DOI: 10.1086/149359.

Kraus, S. et al. (Sept. 2020a). “A triple-star system with a misaligned and warped circumstellar disk shaped by disk tearing.” In: *Science* 369.6508, pp. 1233–1238. DOI: 10.1126/science.aba4633. arXiv: 2004.01204 [astro-ph.SR].

Kraus, S. et al. (July 2020b). “Spin-Orbit Alignment of the β Pictoris Planetary System.” In: *ApJL* 897.1, L8, p. L8. DOI: 10.3847/2041-8213/ab9d27. arXiv: 2006.10784 [astro-ph.EP].

Kreidberg, L. (Nov. 2015). “batman: BAsic Transit Model cAlculatioN in Python.” In: *PASP* 127.957, p. 1161. DOI: 10.1086/683602. arXiv: 1507.08285 [astro-ph.EP].

Kreidberg, L. et al. (May 2018). “Water, High-altitude Condensates, and Possible Methane Depletion in the Atmosphere of the Warm Super-Neptune WASP-107b.” In: *ApJL* 858.1, p. L6. DOI: 10.3847/2041-8213/aabfce.

Kreidberg, L. et al. (Aug. 2019). “Absence of a thick atmosphere on the terrestrial exoplanet LHS 3844b.” In: *Nature* 573.7772, pp. 87–90. DOI: 10.1038/s41586-019-1497-4. arXiv: 1908.06834 [astro-ph.EP].

Kunovac Hodžić, V. et al. (Jan. 2021). “Orbital misalignment of the super-Earth π Men c with the spin of its star.” In: *MNRAS*. stab237. ISSN: 0035-8711. DOI: 10.1093/mnras/stab237.

Kürster, M. et al. (June 2003). “The low-level radial velocity variability in Barnard’s star (= GJ 699). Secular acceleration, indications for convective redshift, and planet mass limits.” In: *A&A* 403, pp. 1077–1087. DOI: 10.1051/0004-6361:20030396. arXiv: astro-ph/0303528 [astro-ph].

Lai, D. (June 2012). “Tidal dissipation in planet-hosting stars: damping of spin-orbit misalignment and survival of hot Jupiters.” In: *MNRAS* 423.1, pp. 486–492. DOI: 10.1111/j.1365-2966.2012.20893.x. arXiv: 1109.4703 [astro-ph.EP].

Lai, D. (Dec. 2016). “Solar Obliquity Induced by Planet Nine: Simple Calculation.” In: *AJ* 152.6, 215, p. 215. DOI: 10.3847/0004-6256/152/6/215. arXiv: 1608.01421 [astro-ph.EP].

Lai, D., F. Foucart, and D. N. C. Lin (Apr. 2011). “Evolution of spin direction of accreting magnetic protostars and spin-orbit misalignment in exoplanetary systems.” In: *MNRAS* 412.4, pp. 2790–2798. DOI: 10.1111/j.1365-2966.2010.18127.x. arXiv: 1008.3148 [astro-ph.EP].

Lakeland, B. S. et al. (Jan. 2024). “The magnetically quiet solar surface dominates HARPS-N solar RVs during low activity.” In: *MNRAS* 527.3, pp. 7681–7691. DOI: 10.1093/mnras/stad3723. arXiv: 2311.16076 [astro-ph.SR].

Langellier, N. et al. (June 2021). "Detection Limits of Low-mass, Long-period Exoplanets Using Gaussian Processes Applied to HARPS-N Solar Radial Velocities." In: *AJ* 161.6, 287, p. 287. DOI: 10.3847/1538-3881/abf1e0. arXiv: 2008.05970 [astro-ph.EP].

Laplace, P. S. (1796). "l'Imprimierie du Circle Social Paris".

Latham, D. W. et al. (May 1989). "The unseen companion of HD114762: a probable brown dwarf." In: *Nature* 339.6219, pp. 38–40. DOI: 10.1038/339038a0.

Le Verrier, U. J. (Oct. 1846). "Recherches sur les mouvements d'Uranus par U. J. Le Verrier (Fortsetzung)." In: *Astronomische Nachrichten* 25, p. 65.

Lee, E. J. (June 2019). "The Boundary between Gas-rich and Gas-poor Planets." In: *ApJ* 878.1, 36, p. 36. DOI: 10.3847/1538-4357/ab1b40. arXiv: 1904.10470 [astro-ph.EP].

Lee, E. J. and E. Chiang (Feb. 2016). "Breeding Super-Earths and Birthing Super-puffs in Transitional Disks." In: *ApJ* 817.2, 90, p. 90. DOI: 10.3847/0004-637X/817/2/90. arXiv: 1510.08855 [astro-ph.EP].

Leite, I. et al. (Dec. 2022). "Imaging sensors for PoET: a spatially resolved solar spectroscopy instrument." In: *Journal of Physics: Conference Series* 2407.1, p. 012020. DOI: 10.1088/1742-6596/2407/1/012020. URL: https://dx.doi.org/10.1088/1742-6596/2407/1/012020.

Li, G. and J. N. Winn (Feb. 2016). "Are Tidal Effects Responsible for Exoplanetary Spin&ndashOrbit Alignment?" In: *ApJ* 818.1, 5, p. 5. DOI: 10.3847/0004-637X/818/1/5. arXiv: 1511.05570 [astro-ph.EP].

Li, G. et al. (Apr. 2014). "Eccentricity Growth and Orbit Flip in Near-coplanar Hierarchical Three-body Systems." In: *ApJ* 785.2, 116, p. 116. DOI: 10.1088/0004-637X/785/2/116. arXiv: 1310.6044 [astro-ph.EP].

Liang, Y., J. N. Winn, and P. Melchior (Jan. 2024). "AESTRA: Deep Learning for Precise Radial Velocity Estimation in the Presence of Stellar Activity." In: *AJ* 167.1, 23, p. 23. DOI: 10.3847/1538-3881/ad0e01. arXiv: 2311.18326 [astro-ph.EP].

Lidov, M. (1962). "The evolution of orbits of artificial satellites of planets under the action of gravitational perturbations of external bodies." In: *Planet. Space Sci.* 9.10, pp. 719–759. ISSN: 0032-0633. DOI: https://doi.org/10.1016/0032-0633(62)90129-0.

Lienhard, F. et al. (July 2023). "Unsigned magnetic flux proxy from solar optical intensity spectra." In: *MNRAS* 522.4, pp. 5862–5878. DOI: 10.1093/mnras/stad1343. arXiv: 2305.03522 [astro-ph.EP].

Lightkurve Collaboration et al. (Dec. 2018). *Lightkurve: Kepler and TESS time series analysis in Python.* Astrophysics Source Code Library. ascl: 1812.013.

Lin, A. S. J. et al. (Mar. 2022). "Observing the Sun as a Star: Design and Early Results from the NEID Solar Feed." In: *AJ* 163.4, p. 184. DOI: 10.3847/1538-3881/ac5622. URL: https://dx.doi.org/10.3847/1538-3881/ac5622.

Lin, D. N. C., P. Bodenheimer, and D. C. Richardson (Apr. 1996). "Orbital migration of the planetary companion of 51 Pegasi to its present location." In: *Nature* 380.6575, pp. 606–607. DOI: 10.1038/380606a0.

Lin, D. N. C. and J. Papaloizou (Oct. 1986). "On the Tidal Interaction between Protoplanets and the Protoplanetary Disk. III. Orbital Migration of Protoplanets." In: *ApJ* 309, p. 846. DOI: 10.1086/164653.

Lopez, E. D. (Nov. 2017). "Born dry in the photoevaporation desert: Kepler's ultra-short-period planets formed water-poor." In: *MNRAS* 472, pp. 245–253. DOI: 10.1093/mnras/stx1558. arXiv: 1610.01170 [astro-ph.EP].

Lothringer, J. D. et al. (June 2021). "A New Window into Planet Formation and Migration: Refractory-to-Volatile Elemental Ratios in Ultra-hot Jupiters." In: *ApJ* 914.1, p. 12. DOI: 10.3847/1538-4357/abf8a9. URL: https://doi.org/10.3847/1538-4357/abf8a9.

Louden, E. M. et al. (Feb. 2021). "Hot Stars with Kepler Planets Have High Obliquities." In: *AJ* 161.2, 68, p. 68. DOI: 10.3847/1538-3881/abcebd. arXiv: 2012.00776 [astro-ph.EP].

Louden, E. M. et al. (May 2024). "A Larger Sample Confirms Small Planets Around Hot Stars Are Misaligned." In: *arXiv e-prints*, arXiv:2405.20035, arXiv:2405.20035. DOI: 10.48550/arXiv.2405.20035. arXiv: 2405.20035 [astro-ph.EP].

Lovis, C. and D. Fischer (2010). "Radial Velocity Techniques for Exoplanets." In: *Exoplanets*. Ed. by S. Seager. Tucson, AZ: University of Arizona Space Science Series, pp. 27–53.

Lovis, C. et al. (July 2011). "The HARPS search for southern extra-solar planets. XXXI. Magnetic activity cycles in solar-type stars: statistics and impact on precise radial velocities." In: *arXiv e-prints*, arXiv:1107.5325, arXiv:1107.5325. DOI: 10.48550/arXiv.1107.5325. arXiv: 1107.5325 [astro-ph.SR].

Lubin, J. et al. (Aug. 2021). "Stellar Activity Manifesting at a One-year Alias Explains Barnard b as a False Positive." In: *AJ* 162.2, 61, p. 61. DOI: 10.3847/1538-3881/ac0057.

Luger, R. et al. (Oct. 2021). "Mapping stellar surfaces III: An Efficient, Scalable, and Open-Source Doppler Imaging Model." In: *arXiv e-prints*, arXiv:2110.06271, arXiv:2110.06271. DOI: 10.48550/arXiv.2110.06271. arXiv: 2110.06271 [astro-ph.SR].

Luhn, J. K. et al. (Sept. 2022). "HD 166620: Portrait of a Star Entering a Grand Magnetic Minimum." In: *ApJL* 936.2, L23, p. L23. DOI: 10.3847/2041-8213/ac8b13. arXiv: 2207.00612 [astro-ph.SR].

Luhn, J. K. et al. (Mar. 2023). "Impact of Correlated Noise on the Mass Precision of Earth-analog Planets in Radial Velocity Surveys." In: *AJ* 165.3, 98, p. 98. DOI: 10.3847/1538-3881/acad08. arXiv: 2204.12512 [astro-ph.EP].

Lupton, W. F. and A. R. Conrad (Jan. 1993). "The Keck Task Library (KTL)." In: *Astronomical Data Analysis Software and Systems II*. Ed. by R. J. Hanisch, R. J. V. Brissenden, and J. Barnes. Vol. 52. Astronomical Society of the Pacific Conference Series, p. 315.

MacDougall, M. G. et al. (June 2023). "The TESS-Keck Survey. XV. Precise Properties of 108 TESS Planets and Their Host Stars." In: *The Astronomical Journal* 166.1, p. 33. DOI: 10.3847/1538-3881/acd557. URL: https://dx.doi.org/10.3847/1538-3881/acd557.

Maciejewski, G. (Sept. 2020). "Search for Planets in Hot Jupiter Systems with Multi-Sector TESS Photometry. I. No Companions in Planetary Systems KELT-18, KELT-23, KELT-24, Qatar-8, WASP-62, WASP-100, WASP-119, and WASP-126." In: *AcA* 70.3, pp. 181–202. DOI: 10.32023/0001-5237/70.3.2. arXiv: 2010.11977 [astro-ph.EP].

Mahadevan, S. et al. (Sept. 2012). "The habitable-zone planet finder: a stabilized fiber-fed NIR spectrograph for the Hobby-Eberly Telescope." In: *Ground-based and Airborne Instrumentation for Astronomy IV*. Ed. by I. S. McLean, S. K. Ramsay, and H. Takami. Vol. 8446. Society of Photo-Optical Instrumentation Engineers (SPIE) Conference Series, 84461S, 84461S. DOI: 10.1117/12.926102. arXiv: 1209.1686 [astro-ph.EP].

Malavolta, L. et al. (Mar. 2018). "An Ultra-short Period Rocky Super-Earth with a Secondary Eclipse and a Neptune-like Companion around K2-141." In: *AJ* 155, 107, p. 107. DOI: 10.3847/1538-3881/aaa5b5. arXiv: 1801.03502 [astro-ph.EP].

Mamajek, E. E. and L. A. Hillenbrand (Nov. 2008). "Improved Age Estimation for Solar-Type Dwarfs Using Activity-Rotation Diagnostics." In: *ApJ* 687.2, pp. 1264–1293. DOI: 10.1086/591785. arXiv: 0807.1686 [astro-ph].

Mann, A. W. et al. (Oct. 2020). "TESS Hunt for Young and Maturing Exoplanets (THYME). III. A Two-planet System in the 400 Myr Ursa Major Group." In: *AJ* 160.4, 179, p. 179. DOI: 10.3847/1538-3881/abae64. arXiv: 2005.00047 [astro-ph.EP].

Marchwinski, R. C. et al. (Jan. 2015). "Toward Understanding Stellar Radial Velocity Jitter as a Function of Wavelength: The Sun as a Proxy." In: *ApJ* 798.1, 63, p. 63. DOI: 10.1088/0004-637X/798/1/63. arXiv: 1410.7379 [astro-ph.SR].

Mardling, R. A. (Sept. 2010). "The determination of planetary structure in tidally relaxed inclined systems." In: *MNRAS* 407.2, pp. 1048–1069. ISSN: 0035-8711. DOI: 10.1111/j.1365-2966.2010.16814.x. eprint: https://academic.oup.com/mnras/article-pdf/407/2/1048/3899072/mnras0407-1048.pdf.

MAST (2021). *TESS Light Curves - All Sectors*. DOI: 10.17909/T9-NMC8-F686. URL: http://archive.stsci.edu/doi/resolve/resolve.html?doi=10.17909/t9-nmc8-f686.

Masuda, K., E. A. Petigura, and O. J. Hall (Mar. 2022). "Inferring the rotation period distribution of stars from their projected rotation velocities and radii: Application to late-F/early-G Kepler stars." In: *MNRAS* 510.4, pp. 5623–5638. DOI: 10.1093/mnras/stab3650. arXiv: 2112.07162 [astro-ph.SR].

Masuda, K. and J. N. Winn (Feb. 2020). "On the Inference of a Star's Inclination Angle from its Rotation Velocity and Projected Rotation Velocity." In: *AJ* 159.3, p. 81. DOI: 10.3847/1538-3881/ab65be.

Masuda, K., J. N. Winn, and H. Kawahara (Feb. 2020). "Mutual Orbital Inclinations between Cold Jupiters and Inner Super-Earths." In: *AJ* 159.2, 38, p. 38. DOI: 10.3847/1538-3881/ab5c1d. arXiv: 1912.00387 [astro-ph.EP].

Mawet, D. et al. (Sept. 2019). "High-resolution Infrared Spectrograph for Exoplanet Characterization with the Keck and Thirty Meter Telescopes." In: *Bulletin of the American Astronomical Society*. Vol. 51, 134, p. 134. DOI: 10.48550/arXiv.1908.03623. arXiv: 1908.03623 [astro-ph.IM].

Mayor, M. et al. (Dec. 2003). "Setting New Standards with HARPS." In: *The Messenger* 114, pp. 20–24.

Mayor, M. and D. Queloz (Nov. 1995). "A Jupiter-mass companion to a solar-type star." In: *Nature* 378.6555, pp. 355–359. DOI: 10.1038/378355a0.

Mazeh, T., T. Holczer, and S. Faigler (May 2016). "Dearth of short-period Neptunian exoplanets: A desert in period-mass and period-radius planes." In: *A&A* 589, A75, A75. DOI: 10.1051/0004-6361/201528065. arXiv: 1602.07843 [astro-ph.EP].

McLaughlin, D. B. (July 1924). "Some results of a spectrographic study of the Algol system." In: *ApJ* 60, pp. 22–31. DOI: 10.1086/142826.

McLeod, K. K. et al. (June 2017). "KELT-18b: Puffy Planet, Hot Host, Probably Perturbed." In: *AJ* 153.6, 263, p. 263. DOI: 10.3847/1538-3881/aa6d5d. arXiv: 1702.01657 [astro-ph.EP].

Metropolis, N. et al. (June 1953). "Equation of State Calculations by Fast Computing Machines." In: **??***jnlJChPh* 21.6, pp. 1087–1092. DOI: 10.1063/1.1699114.

Meunier, N., M. Desort, and A. .-. Lagrange (Mar. 2010). "Using the Sun to estimate Earth-like planets detection capabilities . II. Impact of plages." In: *A&A* 512, A39, A39. DOI: 10.1051/0004-6361/200913551. arXiv: 1001.1638 [astro-ph.EP].

Meunier, N. and Lagrange, A.-M. (2013). "Using the Sun to estimate Earth-like planets detection capabilities - IV. Correcting for the convective component." In: *A&A* 551, A101. DOI: 10.1051/0004-6361/201219917. URL: https://doi.org/10.1051/0004-6361/201219917.

Meunier, N. and Lagrange, A.-M. (2019). "Unexpectedly strong effect of supergranulation on the detectability of Earth twins orbiting Sun-like stars with radial velocities." In: *A&A* 625, p. L6. DOI: 10.1051/0004-6361/201935099. URL: https://doi.org/10.1051/0004-6361/201935099.

Meunier, N., Lagrange, A.-M., and Desort, M. (2010a). "Reconstructing the solar integrated radial velocity using MDI/SOHO." In: *A&A* 519, A66. DOI: 10.1051/0004-6361/201014199. URL: https://doi.org/10.1051/0004-6361/201014199.

Meunier, N., Lagrange, A.-M., and Desort, M. (2010b). "Reconstructing the solar integrated radial velocity using MDI/SOHO." In: *A&A* 519, A66. DOI: 10.1051/0004-6361/201014199. URL: https://doi.org/10.1051/0004-6361/201014199.

Meunier, N. et al. (2015). "Using the Sun to estimate Earth-like planet detection capabilities - VI. Simulation of granulation and supergranulation radial velocity and photometric time series." In: *A&A* 583, A118. DOI: 10.1051/0004-6361/201525721. URL: https://doi.org/10.1051/0004-6361/201525721.

Milbourne, T. W. et al. (Mar. 2019). "HARPS-N Solar RVs Are Dominated by Large, Bright Magnetic Regions." In: *The Astrophysical Journal* 874.1, p. 107. DOI: 10.3847/1538-4357/ab064a. URL: https://dx.doi.org/10.3847/1538-4357/ab064a.

Milbourne, T. W. et al. (Oct. 2021). "Estimating Magnetic Filling Factors from Simultaneous Spectroscopy and Photometry: Disentangling Spots, Plage, and Network." In: *ApJ* 920.1, 21, p. 21. DOI: 10.3847/1538-4357/ac1266. arXiv: 2105.09113 [astro-ph.SR].

Millholland, S., E. Petigura, and K. Batygin (June 2020). "Tidal Inflation Reconciles Low-density Sub-Saturns with Core Accretion." In: *ApJ* 897.1, p. 7. DOI: 10.3847/1538-4357/ab959c.

Millholland, S. C. and C. Spalding (Dec. 2020). "Formation of Ultra-short-period Planets by Obliquity-driven Tidal Runaway." In: *ApJ* 905.1, 71, p. 71. DOI: 10.3847/1538-4357/abc4e5. arXiv: 2010.15087 [astro-ph.EP].

Močnik, T. et al. (Apr. 2017). “Starspots on WASP-107 and pulsations of WASP-118.” In: *MNRAS* 469.2, pp. 1622–1629. ISSN: 0035-8711. DOI: 10.1093/mnras/stx972. eprint: https://academic.oup.com/mnras/article-pdf/469/2/1622/17571505/stx972.pdf.

Montet, B. T. et al. (Mar. 2020). “The Young Planet DS Tuc Ab Has a Low Obliquity.” In: *AJ* 159.3, 112, p. 112. DOI: 10.3847/1538-3881/ab6d6d. arXiv: 1912.03794 [astro-ph.EP].

Mortier, A. (Aug. 2016). “Tracking Magnetic Variability From High-Resolution Unpolarised Spectra.” In: *19th Cambridge Workshop on Cool Stars, Stellar Systems, and the Sun (CS19)*. Cambridge Workshop on Cool Stars, Stellar Systems, and the Sun, 134, p. 134. DOI: 10.5281/zenodo.59214.

Motalebi, F. et al. (Dec. 2015). “The HARPS-N Rocky Planet Search. I. HD 219134 b: A transiting rocky planet in a multi-planet system at 6.5 pc from the Sun.” In: *A&A* 584, A72, A72. DOI: 10.1051/0004-6361/201526822. arXiv: 1507.08532 [astro-ph.EP].

Murgas, F. et al. (Dec. 2022). “HD 20329b: An ultra-short-period planet around a solar-type star found by TESS.” In: *A&A* 668, A158, A158. DOI: 10.1051/0004-6361/202244459. arXiv: 2211.02547 [astro-ph.EP].

Murphy, M. T. et al. (Sept. 2007). “High-precision wavelength calibration of astronomical spectrographs with laser frequency combs.” In: *MNRAS* 380.2, pp. 839–847. DOI: 10.1111/j.1365-2966.2007.12147.x. arXiv: astro-ph/0703622 [astro-ph].

Murray-Clay, R. A., E. I. Chiang, and N. Murray (Mar. 2009). “Atmospheric Escape From Hot Jupiters.” In: *ApJ* 693.1, pp. 23–42. DOI: 10.1088/0004-637X/693/1/23. arXiv: 0811.0006 [astro-ph].

Naoz, S. (Sept. 2016). “The Eccentric Kozai-Lidov Effect and Its Applications.” In: *ARA&A* 54, pp. 441–489. DOI: 10.1146/annurev-astro-081915-023315. arXiv: 1601.07175 [astro-ph.EP].

Naoz, S. et al. (May 2011). “Hot Jupiters from secular planet-planet interactions.” In: *Nature* 473.7346, pp. 187–189. DOI: 10.1038/nature10076. arXiv: 1011.2501 [astro-ph.EP].

Naoz, S. et al. (Aug. 2013a). “Resonant Post-Newtonian Eccentricity Excitation in Hierarchical Three-body Systems.” In: *ApJ* 773.2, 187, p. 187. DOI: 10.1088/0004-637X/773/2/187. arXiv: 1206.4316 [astro-ph.SR].

Naoz, S. et al. (Mar. 2013b). “Secular dynamics in hierarchical three-body systems.” In: *Monthly Notices of the Royal Astronomical Society* 431.3, pp. 2155–2171. ISSN: 0035-8711. DOI: 10.1093/mnras/stt302. eprint: https://academic.oup.com/mnras/article-pdf/431/3/2155/4890577/stt302.pdf. URL: https://doi.org/10.1093/mnras/stt302.

Nardetto, N. et al. (July 2006). “High resolution spectroscopy for Cepheids distance determination. I. Line asymmetry.” In: *A&A* 453.1, pp. 309–319. DOI: 10.1051/0004-6361:20054333. arXiv: 0804.1321 [astro-ph].

NASA Exoplanet Archive (2019). *Confirmed Planets Table*. DOI: 10.26133/NEA1. URL: https://catcopy.ipac.caltech.edu/dois/doi.php?id=10.26133/NEA1.

Neal, R. M. (June 2012). “MCMC using Hamiltonian dynamics.” In: *arXiv e-prints*, arXiv:1206.1901, arXiv:1206.1901. arXiv: 1206.1901 [stat.CO].

Neumann, A. et al. (Sept. 2022). *pytransitions/transitions*. Version 0.9.0. DOI: 10.5281/zenodo.7043191. URL: https://doi.org/10.5281/zenodo.7043191.

Newman, P. D. et al. (Apr. 2023). “Simulations for Planning Next-generation Exoplanet Radial Velocity Surveys.” In: *AJ* 165.4, 151, p. 151. DOI: 10.3847/1538-3881/acad07. arXiv: 2204.13968 [astro-ph.EP].

Newville, M. et al. (Sept. 2014). *LMFIT: Non-Linear Least-Square Minimization and Curve-Fitting for Python*. Version 0.8.0. DOI: 10.5281/zenodo.11813. URL: https://doi.org/10.5281/zenodo.11813.

Ngo, H. et al. (Aug. 2016). “Friends of Hot Jupiters. IV. Stellar Companions Beyond 50 au Might Facilitate Giant Planet Formation, but Most are Unlikely to Cause Kozai-Lidov Migration.” In: *ApJ* 827.1, 8, p. 8. DOI: 10.3847/0004-637X/827/1/8. arXiv: 1606.07102 [astro-ph.EP].

Ogilvie, G. I. (Aug. 2014). “Tidal Dissipation in Stars and Giant Planets.” In: *ARA&A* 52, pp. 171–210. DOI: 10.1146/annurev-astro-081913-035941. arXiv: 1406.2207 [astro-ph.SR].

Oh, S. et al. (May 2017). “Comoving Stars in Gaia DR1: An Abundance of Very Wide Separation Comoving Pairs.” In: *The Astronomical Journal* 153.6, p. 257. DOI: 10.3847/1538-3881/aa6ffd. URL: https://dx.doi.org/10.3847/1538-3881/aa6ffd.

Oklopčić, A. and C. M. Hirata (Mar. 2018). “A New Window into Escaping Exoplanet Atmospheres: 10830 Å Line of Helium.” In: *ApJL* 855.1, p. L11. DOI: 10.3847/2041-8213/aaada9.

Orell-Miquel, J. et al. (Sept. 2023). “Confirmation of an He I evaporating atmosphere around the 650-Myr-old sub-Neptune HD 235088 b (TOI-1430 b) with CARMENES.” In: *A&A* 677, A56, A56. DOI: 10.1051/0004-6361/202346445. arXiv: 2307.05191 [astro-ph.EP].

Owen, J. E. and Y. Wu (Sept. 2017). “The Evaporation Valley in the Kepler Planets.” In: *ApJ* 847.1, 29, p. 29. DOI: 10.3847/1538-4357/aa890a. arXiv: 1705.10810 [astro-ph.EP].

Paegert, M. et al. (Aug. 2021). “TESS Input Catalog versions 8.1 and 8.2: Phantoms in the 8.0 Catalog and How to Handle Them.” In: *arXiv e-prints*, arXiv:2108.04778, arXiv:2108.04778. DOI: 10.48550/arXiv.2108.04778. arXiv: 2108.04778 [astro-ph.EP].

Palle, E. et al. (June 2020a). “A He I upper atmosphere around the warm Neptune GJ 3470 b.” In: *A&A* 638, A61, A61. DOI: 10.1051/0004-6361/202037719. arXiv: 2004.12812 [astro-ph.EP].

Palle, E. et al. (Nov. 2020b). “Transmission spectroscopy and Rossiter-McLaughlin measurements of the young Neptune orbiting AU Mic.” In: *A&A* 643, A25, A25. DOI: 10.1051/0004-6361/202038583. arXiv: 2006.13609 [astro-ph.EP].

Palumbo Michael L., I. et al. (Jan. 2022). “GRASS: Distinguishing Planet-induced Doppler Signatures from Granulation with a Synthetic Spectra Generator.” In: *AJ* 163.1, 11, p. 11. DOI: 10.3847/1538-3881/ac32c2. arXiv: 2110.11839 [astro-ph.SR].

Palumbo, M. and E. Ford (Feb. 2024). “Charting the Path Toward Mitigating Granulation-Driven RV Noise with Synthetic Spectra.” In: *American Astronomical Society Meeting Abstracts*. Vol. 56. American Astronomical Society Meeting Abstracts, 327.01D, p. 327.01D.

Paragas, K. et al. (Mar. 2021). “Metastable Helium Reveals an Extended Atmosphere for the Gas Giant HAT-P-18b.” In: *ApJL* 909.1, L10, p. L10. DOI: 10.3847/2041-8213/abe706. arXiv: 2102.08392 [astro-ph.EP].

Parviainen, H. (Feb. 2016). *PyDE: v1.5*. Version v1.5. DOI: 10.5281/zenodo.45602. URL: https://doi.org/10.5281/zenodo.45602.

Pepe, F. et al. (June 2002). “The CORALIE survey for southern extra-solar planets VII. Two short-period Saturnian companions to <ASTROBJ>HD 108147</ASTROBJ> and <ASTROBJ>HD 168746</ASTROBJ>.” In: *A&A* 388, pp. 632–638. DOI: 10.1051/0004-6361:20020433. arXiv: astro-ph/0202457 [astro-ph].

Pepe, F. et al. (Sept. 2013). “ESPRESSO — An Echelle SPectrograph for Rocky Exoplanets Search and Stable Spectroscopic Observations.” In: *The Messenger* 153, pp. 6–16.

Pepe, F. et al. (2004). “The HARPS search for southern extra-solar planets* - I. HD075A new "hot Jupiter".” In: *A&A* 423.1, pp. 385–389. DOI: 10.1051/0004-6361:20040389. URL: https://doi.org/10.1051/0004-6361:20040389.

Pepe, F. et al. (2021). “ESPRESSO at VLT - On-sky performance and first results.” In: *A&A* 645, A96. DOI: 10.1051/0004-6361/202038306. URL: https://doi.org/10.1051/0004-6361/202038306.

Perryman, M. et al. (Dec. 2014). "Astrometric Exoplanet Detection with Gaia." In: *ApJ* 797.1, 14, p. 14. DOI: 10.1088/0004-637X/797/1/14. arXiv: 1411.1173 [astro-ph.EP].

Petigura, E. A. et al. (Aug. 2017). "The California-Kepler Survey. I. High-resolution Spectroscopy of 1305 Stars Hosting Kepler Transiting Planets*." In: *The Astronomical Journal* 154.3, p. 107. DOI: 10.3847/1538-3881/aa80de. URL: https://dx.doi.org/10.3847/1538-3881/aa80de.

Petigura, E. A. (Jan. 2015). "Prevalence of Earth-size Planets Orbiting Sun-like Stars." PhD thesis. University of California, Berkeley.

Petrovich, C. (May 2015a). "Hot Jupiters from Coplanar High-eccentricity Migration." In: *ApJ* 805.1, 75, p. 75. DOI: 10.1088/0004-637X/805/1/75. arXiv: 1409.8296 [astro-ph.EP].

Petrovich, C. (Jan. 2015b). "Steady-state Planet Migration by the Kozai-Lidov Mechanism in Stellar Binaries." In: *ApJ* 799.1, 27, p. 27. DOI: 10.1088/0004-637X/799/1/27. arXiv: 1405.0280 [astro-ph.EP].

Petrovich, C. et al. (Oct. 2020). "A Disk-driven Resonance as the Origin of High Inclinations of Close-in Planets." In: *ApJL* 902.1, p. L5. DOI: 10.3847/2041-8213/abb952.

Phillips, D. F. et al. (June 2012). "Calibration of an astrophysical spectrograph below 1 m/s using a laser frequency comb." In: *Opt. Express* 20.13, pp. 13711–13726. DOI: 10.1364/OE.20.013711. URL: https://opg.optica.org/oe/abstract.cfm?URI=oe-20-13-13711.

Phillips, D. F. et al. (July 2016). "An astro-comb calibrated solar telescope to search for the radial velocity signature of Venus." In: *Advances in Optical and Mechanical Technologies for Telescopes and Instrumentation II*. Ed. by R. Navarro and J. H. Burge. Vol. 9912. SPIE, 99126Z, 99126Z. DOI: 10.1117/12.2232452.

Piaulet, C. et al. (Jan. 2021). "WASP-107b's Density Is Even Lower: A Case Study for the Physics of Planetary Gas Envelope Accretion and Orbital Migration." In: *AJ* 161.2, p. 70. DOI: 10.3847/1538-3881/abcd3c.

Piskunov, N. E. and J. A. Valenti (Apr. 2002). "New algorithms for reducing cross-dispersed echelle spectra." In: *A&A* 385, pp. 1095–1106. DOI: 10.1051/0004-6361:20020175.

Podgorski, W. et al. (July 2014). "A novel systems engineering approach to the design of a precision radial velocity spectrograph: the GMT-Consortium Large Earth Finder (G-CLEF)." In: *Ground-based and Airborne Instrumentation for Astronomy V*. Ed. by S. K. Ramsay, I. S. McLean, and H. Takami. Vol. 9147. Society of Photo-Optical Instrumentation Engineers (SPIE) Conference Series, 91478W, 91478W. DOI: 10.1117/12.2056329.

Pollack, J. B. et al. (Nov. 1996). "Formation of the Giant Planets by Concurrent Accretion of Solids and Gas." In: *Icarus* 124.1, pp. 62–85. DOI: 10.1006/icar.1996.0190.

Pont, F. et al. (Aug. 2009). "Spin-orbit misalignment in the HD 80606 planetary system." In: *A&A* 502.2, pp. 695–703. DOI: 10.1051/0004-6361/200912463. arXiv: 0906.5605 [astro-ph.EP].

Powell, M. J. D. (Jan. 1964). "An efficient method for finding the minimum of a function of several variables without calculating derivatives." In: *The Computer Journal* 7.2, pp. 155–162. ISSN: 0010-4620. DOI: 10.1093/comjnl/7.2.155.

Queloz, D. et al. (2000). "Detection of a spectroscopic transit by the planet orbiting the star HD 209458." In: *A&A* 359, p. L13. arXiv: astro-ph/0006213.

Queloz, D. et al. (2010). "WASP-8b: a retrograde transiting planet in a multiple system." In: *A&A* 517, p. L1. DOI: 10.1051/0004-6361/201014768.

Queloz, D. et al. (2009). "The CoRoT-7netary system: two orbiting super-Earths ***." In: *A&A* 506.1, pp. 303–319. DOI: 10.1051/0004-6361/200913096. URL: https://doi.org/10.1051/0004-6361/200913096.

Radzom, B. T. et al. (Apr. 2024). "Evidence for Primordial Alignment: Insights from Stellar Obliquity Measurements for Compact Sub-Saturn Systems." In: *arXiv e-prints*, arXiv:2404.06504, arXiv:2404.06504. DOI: 10.48550/arXiv.2404.06504. arXiv: 2404.06504 [astro-ph.EP].

Rafikov, R. R. (Sept. 2006). "Atmospheres of Protoplanetary Cores: Critical Mass for Nucleated Instability." In: *ApJ* 648, pp. 666–682. DOI: 10.1086/505695. eprint: astro-ph/0405507.

Rafikov, R. R. (Mar. 2005). "Can Giant Planets Form by Direct Gravitational Instability?" In: *ApJL* 621.1, pp. L69–L72. DOI: 10.1086/428899. arXiv: astro-ph/0406469 [astro-ph].

Rajpaul, V. et al. (Sept. 2015). "A Gaussian process framework for modelling stellar activity signals in radial velocity data." In: *MNRAS* 452.3, pp. 2269–2291. DOI: 10.1093/mnras/stv1428. arXiv: 1506.07304 [astro-ph.EP].

Rasio, F. A. et al. (Oct. 1996). "Tidal Decay of Close Planetary Orbits." In: *ApJ* 470, p. 1187. DOI: 10.1086/177941. arXiv: astro-ph/9605059 [astro-ph].

Rasio, F. A. and E. B. Ford (Nov. 1996). "Dynamical instabilities and the formation of extrasolar planetary systems." In: *Science* 274, pp. 954–956. DOI: 10.1126/science.274.5289.954.

Redman, S. L., G. Nave, and C. J. Sansonetti (Mar. 2014). "The Spectrum of Thorium from 250 nm to 5500 nm: Ritz Wavelengths and Optimized Energy Levels." In: *ApJS* 211.1, 4, p. 4. DOI: 10.1088/0067-0049/211/1/4. arXiv: 1308.5229 [astro-ph.IM].

Rein, H. and S.-F. Liu (2012). "REBOUND: an open-source multi-purpose N-body code for collisional dynamics." In: *A&A* 537, A128. DOI: 10.1051/0004-6361/201118085.

Rein, H. and D. Tamayo (July 2015). "whfast: a fast and unbiased implementation of a symplectic Wisdom–Holman integrator for long-term gravitational simulations." In: *MNRAS* 452.1, pp. 376–388. ISSN: 0035-8711. DOI: 10.1093/mnras/stv1257. eprint: https://academic.oup.com/mnras/article-pdf/452/1/376/4912268/stv1257.pdf.

Reiners, A. and J. H. M. M. Schmitt (2003). "Differential rotation in rapidly rotating F-stars." In: *A&A* 412.3, pp. 813–819. DOI: 10.1051/0004-6361:20034255. URL: https://doi.org/10.1051/0004-6361:20034255.

Ribas, I. et al. (Mar. 2005). "Evolution of the Solar Activity over Time and Effects on Planetary Atmospheres. I. High-Energy Irradiances (1-1700 Å)." In: *ApJ* 622.1, pp. 680–694. DOI: 10.1086/427977. arXiv: astro-ph/0412253 [astro-ph].

Rice, M., K. Gerbig, and A. Vanderburg (Mar. 2024). "The Orbital Geometries and Stellar Obliquities of Exoplanet-hosting Multistar Systems." In: *AJ* 167.3, 126, p. 126. DOI: 10.3847/1538-3881/ad1bed. arXiv: 2401.04173 [astro-ph.EP].

Rice, M., S. Wang, and G. Laughlin (Feb. 2022). "Origins of Hot Jupiters from the Stellar Obliquity Distribution." In: *ApJL* 926.2, L17, p. L17. DOI: 10.3847/2041-8213/ac502d. arXiv: 2201.11768 [astro-ph.EP].

Rice, W. K. M., P. J. Armitage, and D. F. Hogg (Mar. 2008). "Why are there so few hot Jupiters?" In: *MNRAS* 384.3, pp. 1242–1248. DOI: 10.1111/j.1365-2966.2007.12817.x. arXiv: 0712.0823 [astro-ph].

Ricker, G. R. et al. (Jan. 2015). "Transiting Exoplanet Survey Satellite (TESS)." In: *Journal of Astronomical Telescopes, Instruments, and Systems* 1, 014003, p. 014003. DOI: 10.1117/1.JATIS.1.1.014003.

Rimmele, T. R. et al. (Dec. 2020). "The Daniel K. Inouye Solar Telescope - Observatory Overview." In: *SoPh* 295.12, 172, p. 172. DOI: 10.1007/s11207-020-01736-7.

Rincon, F. and M. Rieutord (Sept. 2018). "The Sun's supergranulation." In: *Living Reviews in Solar Physics* 15.1, 6, p. 6. DOI: 10.1007/s41116-018-0013-5.

Rogers, T. M. and D. N. C. Lin (May 2013). "ON THE TIDAL DISSIPATION OF OBLIQUITY." In: *The Astrophysical Journal Letters* 769.1, p. L10. DOI: 10.1088/2041-8205/769/1/L10. URL: https://dx.doi.org/10.1088/2041-8205/769/1/L10.

Rogers, T. M. et al. (July 2013). "Internal Gravity Waves in Massive Stars: Angular Momentum Transport." In: *ApJ* 772.1, 21, p. 21. DOI: 10.1088/0004-637X/772/1/21. arXiv: 1306.3262 [astro-ph.SR].

Roguet-Kern, N., H. M. Cegla, and V. Bourrier (May 2022). "Optimal parameter space for detecting stellar differential rotation and centre-to-limb convective variations." In: *A&A* 661, A97, A97. DOI: 10.1051/0004-6361/202142380. arXiv: 2203.07151 [astro-ph.SR].

Rosenthal, L. J. et al. (July 2021). "The California Legacy Survey. I. A Catalog of 178 Planets from Precision Radial Velocity Monitoring of 719 Nearby Stars over Three Decades." In: *ApJS* 255.1, 8, p. 8. DOI: 10.3847/1538-4365/abe23c. arXiv: 2105.11583 [astro-ph.EP].

Rossiter, R. A. (July 1924). "On the detection of an effect of rotation during eclipse in the velocity of the brigher component of beta Lyrae, and on the constancy of velocity of this system." In: *ApJ* 60, pp. 15–21. DOI: 10.1086/142825.

Rouan, D. et al. (Nov. 2011). "The Orbital Phases and Secondary Transits of Kepler-10b. A Physical Interpretation Based on the Lava-ocean Planet Model." In: *ApJL* 741.2, L30, p. L30. DOI: 10.1088/2041-8205/741/2/L30. arXiv: 1109.2768 [astro-ph.EP].

Rowe, J. F. et al. (Mar. 2014). "Validation of Kepler's Multiple Planet Candidates. III. Light Curve Analysis and Announcement of Hundreds of New Multi-planet Systems." In: *ApJ* 784.1, 45, p. 45. DOI: 10.1088/0004-637X/784/1/45. arXiv: 1402.6534 [astro-ph.EP].

Rubenzahl, R. A. et al. (Mar. 2021). "The TESS-Keck Survey. IV. A Retrograde, Polar Orbit for the Ultra-low-density, Hot Super-Neptune WASP-107b." In: *The Astronomical Journal* 161.3, 119, p. 119. DOI: 10.3847/1538-3881/abd177. arXiv: 2101.09371 [astro-ph.EP].

Rubenzahl, R. A. et al. (Dec. 2023). "Staring at the Sun with the Keck Planet Finder: An Autonomous Solar Calibrator for High Signal-to-noise Sun-as-a-star Spectra." In: *Publications of the Astronomical Society of the Pacific* 135.1054, 125002, p. 125002. DOI: 10.1088/1538-3873/ad0b30. arXiv: 2311.05129 [astro-ph.IM].

Rubenzahl, R. A. et al. (May 2024a). "KPF Confirms a Polar Orbit for KELT-18 b." In: *Submitted to The Astronomical Journal*.

Rubenzahl, R. A. et al. (Apr. 2024b). "The TESS-Keck Survey. XII. A Dense 1.8 $R_\oplus$ Ultra-short-period Planet Possibly Clinging to a High-mean-molecular-weight Atmosphere after the First Gigayear." In: *The Astronomical Journal* 167.4, 153, p. 153. DOI: 10.3847/1538-3881/ad28bb. arXiv: 2402.07451 [astro-ph.EP].

Rupprecht, G. et al. (Sept. 2004). "The exoplanet hunter HARPS: performance and first results." In: *Ground-based Instrumentation for Astronomy*. Ed. by A. F. M. Moorwood and M. Iye. Vol. 5492. SPIE, pp. 148–159. DOI: 10.1117/12.551267.

Saar, S. H. and R. A. Donahue (Aug. 1997). "Activity-Related Radial Velocity Variation in Cool Stars." In: *ApJ* 485.1, p. 319. DOI: 10.1086/304392. URL: https://dx.doi.org/10.1086/304392.

Salvatier, J., T. V. Wiecki, and C. Fonnesbeck (2016). "Probabilistic programming in Python using PyMC3." In: *PeerJ Computer Science* 2. DOI: 10.7717/peerj-cs.55.

Sanchis-Ojeda, R. and J. N. Winn (Dec. 2011). "Starspots, Spin-Orbit Misalignment, and Active Latitudes in the HAT-P-11 Exoplanetary System." In: *ApJ* 743.1, 61, p. 61. DOI: 10.1088/0004-637X/743/1/61. arXiv: 1107.2920 [astro-ph.EP].

Sanchis-Ojeda, R. et al. (June 2011). "Starspots and Spin-orbit Alignment in the WASP-4 Exoplanetary System." In: *ApJ* 733.2, 127, p. 127. DOI: 10.1088/0004-637X/733/2/127. arXiv: 1103.4859 [astro-ph.EP].

Sanchis-Ojeda, R. et al. (Sept. 2013a). "KEPLER-63b: A GIANT PLANET IN A POLAR ORBIT AROUND A YOUNG SUN-LIKE STAR." In: *ApJ* 775.1, p. 54. DOI: 10.1088/0004-637x/775/1/54.

Sanchis-Ojeda, R. et al. (Sept. 2013b). "Transits and Occultations of an Earth-sized Planet in an 8.5 hr Orbit." In: *ApJ* 774.1, 54, p. 54. DOI: 10.1088/0004-637X/774/1/54. arXiv: 1305.4180 [astro-ph.EP].

Sanchis-Ojeda, R. et al. (May 2014). "A STUDY OF THE SHORTEST-PERIOD PLANETS FOUND WITH KEPLER." In: *The Astrophysical Journal* 787.1, p. 47. DOI: 10.1088/0004-637X/787/1/47. URL: https://dx.doi.org/10.1088/0004-637X/787/1/47.

Sanchis-Ojeda, R. et al. (Oct. 2015). "A Low Stellar Obliquity for WASP-47, a Compact Multiplanet System with a Hot Jupiter and an Ultra-short Period Planet." In: *ApJL* 812.1, L11, p. L11. DOI: 10.1088/2041-8205/812/1/L11. arXiv: 1509.05337 [astro-ph.EP].

Schlaufman, K. C. (Aug. 2010). "Evidence of Possible Spin-orbit Misalignment Along the Line of Sight in Transiting Exoplanet Systems." In: *ApJ* 719.1, pp. 602–611. DOI: 10.1088/0004-637X/719/1/602. arXiv: 1006.2851 [astro-ph.EP].

Schou, J. et al. (Jan. 2012). "Design and Ground Calibration of the Helioseismic and Magnetic Imager (HMI) Instrument on the Solar Dynamics Observatory (SDO)." In: *SoPh* 275.1-2, pp. 229–259. DOI: 10.1007/s11207-011-9842-2.

Schwab, C. et al. (2016). "Design of NEID, an extreme precision Doppler spectrograph for WIYN." In: *Ground-based and Airborne Instrumentation for Astronomy VI*. Ed. by C. J. Evans, L. Simard, and H. Takami. Vol. 9908. International Society for Optics and Photonics. SPIE, 99087H. DOI: 10.1117/12.2234411. URL: https://doi.org/10.1117/12.2234411.

Scott, N. J. et al. (Sept. 2021). "Twin High-resolution, High-speed Imagers for the Gemini Telescopes: Instrument description and science verification results." In: *Frontiers in Astronomy and Space Sciences* 8, 138, p. 138. DOI: 10.3389/fspas.2021.716560.

Seager, S. and G. Mallén-Ornelas (Mar. 2003). "A Unique Solution of Planet and Star Parameters from an Extrasolar Planet Transit Light Curve." In: *ApJ* 585.2, pp. 1038–1055. DOI: 10.1086/346105. arXiv: astro-ph/0206228 [astro-ph].

Sedaghati, E. et al. (Sept. 2023). "Orbital Alignment of the Eccentric Warm Jupiter TOI-677 b." In: *AJ* 166.3, 130, p. 130. DOI: 10.3847/1538-3881/acea84. arXiv: 2307.07598 [astro-ph.EP].

Seifahrt, A. et al. (July 2018). "MAROON-X: a radial velocity spectrograph for the Gemini Observatory." In: *Ground-based and Airborne Instrumentation for Astronomy VII*. Ed. by C. J. Evans, L. Simard, and H. Takami. Vol. 10702. Society of Photo-Optical Instrumentation Engineers (SPIE) Conference Series, 107026D, p. 107026D. DOI: 10.1117/12.2312936. arXiv: 1805.09276 [astro-ph.IM].

Shporer, A. and T. Brown (Apr. 2011). "THE IMPACT OF THE CONVECTIVE BLUESHIFT EFFECT ON SPECTROSCOPIC PLANETARY TRANSITS." In: *ApJ* 733.1, p. 30. DOI: 10.1088/0004-637x/733/1/30.

Sicilia, D. et al. (Apr. 2024). "The GAPS Programme at TNG. XXX: Characterization of the low-density gas giant HAT-P-67 b with GIARPS." In: *arXiv e-prints*, arXiv:2404.03317, arXiv:2404.03317. DOI: 10.48550/arXiv.2404.03317. arXiv: 2404.03317 [astro-ph.EP].

Siegel, J. C., J. N. Winn, and S. H. Albrecht (June 2023). "Ponderings on the Possible Preponderance of Perpendicular Planets." In: *ApJL* 950.1, L2, p. L2. DOI: 10.3847/2041-8213/acd62f. arXiv: 2305.13400 [astro-ph.EP].

Siegel, J. C. et al. (June 2022). "Into the Depths: A New Activity Metric for High-precision Radial Velocity Measurements Based on Line Depth Variations." In: *AJ* 163.6, 260, p. 260. DOI: 10.3847/1538-3881/ac609a. arXiv: 2204.05810 [astro-ph.SR].

Socrates, A. et al. (May 2012). "Super-eccentric Migrating Jupiters." In: *ApJ* 750.2, 106, p. 106. DOI: 10.1088/0004-637X/750/2/106. arXiv: 1110.1644 [astro-ph.EP].

Souami, D. and J. Souchay (July 2012). "The solar system's invariable plane." In: *A&A* 543, A133, A133. DOI: 10.1051/0004-6361/201219011.

Southworth, J. (Oct. 2011). "Homogeneous studies of transiting extrasolar planets – IV. Thirty systems with space-based light curves." In: *MNRAS* 417.3, pp. 2166–2196. ISSN: 0035-8711. DOI: 10.1111/j.1365-2966.2011.19399.x. eprint: https://academic.oup.com/mnras/article-pdf/417/3/2166/17331227/mnras0417-2166.pdf.

Spake, J. J. et al. (2018). "Helium in the eroding atmosphere of an exoplanet." In: *Nature* 557.7703, pp. 68–70. DOI: 10.1038/s41586-018-0067-5.

Spalding, C. (July 2019). "Stellar Winds As a Mechanism to Tilt the Spin Axes of Sun-like Stars." In: *ApJ* 879.1, 12, p. 12. DOI: 10.3847/1538-4357/ab23f5. arXiv: 1905.09094 [astro-ph.SR].

Spalding, C. and K. Batygin (Sept. 2015). "MAGNETIC ORIGINS OF THE STELLAR MASS-OBLIQUITY CORRELATION IN PLANETARY SYSTEMS." In: *ApJ* 811.2, p. 82. DOI: 10.1088/0004-637x/811/2/82.

Spalding, C. and J. N. Winn (Mar. 2022). "Tidal Erasure of Stellar Obliquities Constrains the Timing of Hot Jupiter Formation." In: *ApJ* 927.1, 22, p. 22. DOI: 10.3847/1538-4357/ac4993. arXiv: 2201.03653 [astro-ph.EP].

Stefansson, G. et al. (Oct. 2020). "The Habitable Zone Planet Finder Reveals a High Mass and Low Obliquity for the Young Neptune K2-25b." In: *AJ* 160.4, 192, p. 192. DOI: 10.3847/1538-3881/abb13a. arXiv: 2007.12766 [astro-ph.EP].

Stefánsson, G. et al. (Dec. 2020). "A Mini-Neptune and a Radius Valley Planet Orbiting the Nearby M2 Dwarf TOI-1266 in Its Venus Zone: Validation with the Habitable-zone Planet Finder." In: *AJ* 160.6, 259, p. 259. DOI: 10.3847/1538-3881/abbe19.

Stefànsson, G. et al. (June 2022). "The Warm Neptune GJ 3470b Has a Polar Orbit." In: *ApJL* 931.2, L15, p. L15. DOI: 10.3847/2041-8213/ac6e3c. arXiv: 2111.01295 [astro-ph.EP].

Strassmeier, K. G. et al. (May 2015). "PEPSI: The high-resolution échelle spectrograph and polarimeter for the Large Binocular Telescope." In: *Astronomische Nachrichten* 336.4, p. 324. DOI: 10.1002/asna.201512172. arXiv: 1505.06492 [astro-ph.IM].

Struve, O. (Oct. 1952). "Proposal for a project of high-precision stellar radial velocity work." In: *The Observatory* 72, pp. 199–200.

STScI (2018). *TESS Input Catalog and Candidate Target List*. DOI: 10.17909/FWDT-2X66. URL: http://archive.stsci.edu/doi/resolve/resolve.html?doi=10.17909/fwdt-2x66.

Szentgyorgyi, A. H. and G. Furész (June 2007). "Precision Radial Velocities for the Kepler Era." In: *Revista Mexicana de Astronomia y Astrofisica Conference Series*. Ed. by S. Kurtz. Vol. 28. Revista Mexicana de Astronomia y Astrofisica Conference Series, pp. 129–133.

Tamayo, D. et al. (Oct. 2019). "REBOUNDx: a library for adding conservative and dissipative forces to otherwise symplectic N-body integrations." In: *MNRAS* 491.2, pp. 2885–2901. ISSN: 0035-8711. DOI: 10.1093/mnras/stz2870. eprint: https://academic.oup.com/mnras/article-pdf/491/2/2885/31258091/stz2870.pdf.

Tayar, J. et al. (Mar. 2022). "A Guide to Realistic Uncertainties on the Fundamental Properties of Solar-type Exoplanet Host Stars." In: *ApJ* 927.1, 31, p. 31. DOI: 10.3847/1538-4357/ac4bbc. arXiv: 2012.07957 [astro-ph.EP].

Terrien, R. C. et al. (Mar. 2022). "Rotational Modulation of Spectroscopic Zeeman Signatures in Low-mass Stars." In: *ApJL* 927.1, p. L11. DOI: 10.3847/2041-8213/ac4fc8. URL: https://dx.doi.org/10.3847/2041-8213/ac4fc8.

Teyssandier, J. et al. (Dec. 2013). "Extreme Orbital Evolution from Hierarchical Secular Coupling of Two Giant Planets." In: *ApJ* 779.2, 166, p. 166. DOI: 10.1088/0004-637X/779/2/166. arXiv: 1310.5048 [astro-ph.EP].

Thompson, A. P. G. et al. (Apr. 2020). "The spectral impact of magnetic activity on disc-integrated HARPS-N solar observations: exploring new activity indicators." In: *Monthly Notices of the Royal Astronomical Society* 494.3, pp. 4279–4290. ISSN: 0035-8711. DOI: 10.1093/mnras/staa1010. eprint: https://academic.oup.com/mnras/article-pdf/494/3/4279/33155495/staa1010.pdf. URL: https://doi.org/10.1093/mnras/staa1010.

Thompson, S. J. et al. (Aug. 2016). "HARPS3 for a roboticized Isaac Newton Telescope." In: *Ground-based and Airborne Instrumentation for Astronomy VI*. Ed. by C. J. Evans, L. Simard, and H. Takami. Vol. 9908. Society of Photo-Optical Instrumentation Engineers (SPIE) Conference Series, 99086F, 99086F. DOI: 10.1117/12.2232111. arXiv: 1608.04611 [astro-ph.IM].

Tokovinin, A. and O. Kiyaeva (Dec. 2015). "Eccentricity distribution of wide binaries." In: *Monthly Notices of the Royal Astronomical Society* 456.2, pp. 2070–2079. ISSN: 0035-8711. DOI: 10.1093/mnras/stv2825. eprint: https://academic.oup.com/mnras/article-pdf/456/2/2070/18755561/stv2825.pdf. URL: https://doi.org/10.1093/mnras/stv2825.

Triaud, A. H. M. J. et al. (Dec. 2010). "Spin-orbit angle measurements for six southern transiting planets. New insights into the dynamical origins of hot Jupiters." In: *A&A* 524, A25, A25. DOI: 10.1051/0004-6361/201014525. arXiv: 1008.2353 [astro-ph.EP].

Tsantaki, M. et al. (Feb. 2018). "Atmospheric stellar parameters for large surveys using FASMA, a new spectral synthesis package." In: *MNRAS* 473.4, pp. 5066–5097. DOI: 10.1093/mnras/stx2564. arXiv: 1710.00260 [astro-ph.SR].

Tsantaki, M., D. Andreasen, and G. Teixeira (June 2020). "FASMA 2.0: A Python package for stellar parameters and chemical abundances." In: *The Journal of Open Source Software* 5.50, 2048, p. 2048. DOI: 10.21105/joss.02048.

Tu, L. et al. (May 2015). "The extreme ultraviolet and X-ray Sun in Time: High-energy evolutionary tracks of a solar-like star." In: *A&A* 577, L3, p. L3. DOI: 10.1051/0004-6361/201526146. arXiv: 1504.04546 [astro-ph.SR].

Upton, L. A. and D. H. Hathaway (2023). "Solar Cycle Precursors and the Outlook for Cycle 25." In: *Journal of Geophysical Research: Space Physics* n/a.n/a. e2023JA031681 2023JA031681, e2023JA031681. DOI: https://doi.org/10.1029/2023JA031681. eprint: https://agupubs.onlinelibrary.wiley.com/doi/pdf/10.1029/2023JA031681. URL: https://agupubs.onlinelibrary.wiley.com/doi/abs/10.1029/2023JA031681.

Valenti, J. A., R. P. Butler, and G. W. Marcy (Oct. 1995). "Determining Spectrometer Instrumental Profiles Using FTS Reference Spectra." In: *PASP* 107, p. 966. DOI: 10.1086/133645.

Valenti, J. A. and D. A. Fischer (July 2005). "Spectroscopic Properties of Cool Stars (SPOCS). I. 1040 F, G, and K Dwarfs from Keck, Lick, and AAT Planet Search Programs." In: *ApJSupplement Series* 159.1, pp. 141–166. DOI: 10.1086/430500.

Van Zandt, J. et al. (Feb. 2023). "TESS-Keck Survey. XIV. Two Giant Exoplanets from the Distant Giants Survey." In: *AJ* 165.2, 60, p. 60. DOI: 10.3847/1538-3881/aca6ef. arXiv: 2209.06958 [astro-ph.EP].

Vehtari, A. et al. (June 2021). "Rank-normalization, folding, and localization: An improved R-hat for assessing convergence of MCMC (with Discussion)." In: *Bayesian Analysis* 16.2, pp. 667–718. DOI: 10.1214/20-BA1221.

Vick, M., D. Lai, and K. R. Anderson (Apr. 2019). "Chaotic tides in migrating gas giants: forming hot and transient warm Jupiters via Lidov-Kozai migration." In: *MNRAS* 484.4, pp. 5645–5668. DOI: 10.1093/mnras/stz354. arXiv: 1812.05618 [astro-ph.EP].

Vick, M., Y. Su, and D. Lai (Feb. 2023). "High-eccentricity Migration with Disk-induced Spin-Orbit Misalignment: A Preference for Perpendicular Hot Jupiters." In: *ApJL* 943.2, L13, p. L13. DOI: 10.3847/2041-8213/acaea6. arXiv: 2211.09122 [astro-ph.EP].

Virtanen, P. et al. (2020). “SciPy 1.0: Fundamental Algorithms for Scientific Computing in Python.” In: *NatMe* 17, pp. 261–272. DOI: 10.1038/s41592-019-0686-2.

Vissapragada, S. et al. (Dec. 2022). “The Possible Tidal Demise of Kepler’s First Planetary System.” In: *ApJL* 941.2, L31, p. L31. DOI: 10.3847/2041-8213/aca47e. arXiv: 2212.09752 [astro-ph.EP].

Vissapragada, S. et al. (May 2024). “Helium in the Extended Atmosphere of the Warm Superpuff TOI-1420b.” In: *AJ* 167.5, 199, p. 199. DOI: 10.3847/1538-3881/ad3241. arXiv: 2403.05614 [astro-ph.EP].

Vogt, S. S. et al. (June 1994). “HIRES: the high-resolution echelle spectrometer on the Keck 10-m Telescope.” In: *Instrumentation in Astronomy VIII*. Ed. by D. L. Crawford and E. R. Craine. Vol. 2198. Society of Photo-Optical Instrumentation Engineers (SPIE) Conference Series, p. 362. DOI: 10.1117/12.176725.

Vogt, S. S. (Nov. 1987). “The Lick Observatory Hamilton echelle spectrometer.” In: *PASP* 99, pp. 1214–1228. DOI: 10.1086/132107.

Vogt, S. S. et al. (Apr. 2014). “APF—The Lick Observatory Automated Planet Finder.” In: *PASP* 126.938, p. 359. DOI: 10.1086/676120. arXiv: 1402.6684 [astro-ph.IM].

von Zeipel, H. (Mar. 1910). “Sur l’application des séries de M. Lindstedt à l’étude du mouvement des comètes périodiques.” In: *Astronomische Nachrichten* 183.22, p. 345. DOI: 10.1002/asna.19091832202.

Walker, G. A. H. et al. (Aug. 1995). “A search for Jupiter-mass companions to nearby stars.” In: *Icarus* 116.2, pp. 359–375. DOI: 10.1006/icar.1995.1130.

Wang, L. and F. Dai (June 2018). “Evaporation of Low-mass Planet Atmospheres: Multidimensional Hydrodynamics with Consistent Thermochemistry.” In: *ApJ* 860.2, 175, p. 175. DOI: 10.3847/1538-4357/aac1c0. arXiv: 1710.03826 [astro-ph.EP].

Weiss, L. M. and G. W. Marcy (Mar. 2014). “The Mass-Radius Relation for 65 Exoplanets Smaller than 4 Earth Radii.” In: *ApJL* 783.1, L6, p. L6. DOI: 10.1088/2041-8205/783/1/L6. arXiv: 1312.0936 [astro-ph.EP].

Weiss, L. M. et al. (Feb. 2021). “The TESS-Keck Survey. II. An Ultra-short-period Rocky Planet and Its Siblings Transiting the Galactic Thick-disk Star TOI-561.” In: *AJ* 161.2, 56, p. 56. DOI: 10.3847/1538-3881/abd409. arXiv: 2009.03071 [astro-ph.EP].

Wildi, F. et al. (2010). “A Fabry-Perot calibrator of the HARPS radial velocity spectrograph: performance report.” In: *Ground-based and Airborne Instrumentation for Astronomy III*. Ed. by I. S. McLean, S. K. Ramsay, and H. Takami. Vol. 7735. International Society for Optics and Photonics. SPIE,

p. 77354X. DOI: 10.1117/12.857951. URL: https://doi.org/10.1117/12.857951.

Winn, J. N. et al. (Oct. 2005). "Measurement of Spin-Orbit Alignment in an Extrasolar Planetary System." In: *The Astrophysical Journal* 631.2, p. 1215. DOI: 10.1086/432571. URL: https://dx.doi.org/10.1086/432571.

Winn, J. N. et al. (July 2010a). "HOT STARS WITH HOT JUPITERS HAVE HIGH OBLIQUITIES." In: *ApJL* 718.2, pp. L145–L149. DOI: 10.1088/2041-8205/718/2/l145.

Winn, J. N. et al. (Oct. 2010b). "THE OBLIQUE ORBIT OF THE SUPER-NEPTUNE HAT-P-11b." In: *ApJL* 723.2, pp. L223–L227. DOI: 10.1088/2041-8205/723/2/l223.

Winn, J. N. et al. (Nov. 2010c). "The Oblique Orbit of the Super-Neptune HAT-P-11b." In: *ApJL* 723.2, pp. L223–L227. DOI: 10.1088/2041-8205/723/2/L223. arXiv: 1009.5671 [astro-ph.EP].

Wolszczan, A. and D. A. Frail (Jan. 1992). "A planetary system around the millisecond pulsar PSR1257 + 12." In: *Nature* 355.6356, pp. 145–147. DOI: 10.1038/355145a0.

Wright, J. T. and J. D. Eastman (Sept. 2014). "Barycentric Corrections at 1 cm s^{-1} for Precise Doppler Velocities." In: *PASP* 126.943, p. 838. DOI: 10.1086/678541. arXiv: 1409.4774 [astro-ph.IM].

Wright, J. T. et al. (Mar. 2009). "Ten New and Updated Multiplanet Systems and a Survey of Exoplanetary Systems." In: *ApJ* 693.2, pp. 1084–1099. DOI: 10.1088/0004-637X/693/2/1084. arXiv: 0812.1582 [astro-ph].

Wright, J. T. et al. (July 2012). "The Frequency of Hot Jupiters Orbiting nearby Solar-type Stars." In: *ApJ* 753.2, 160, p. 160. DOI: 10.1088/0004-637X/753/2/160. arXiv: 1205.2273 [astro-ph.EP].

Wright, J. T. and S. Kanodia (Sept. 2020). "Barycentric Corrections for Precise Radial Velocity Measurements of Sunlight." In: *PSJ* 1.2, 38, p. 38. DOI: 10.3847/PSJ/ababa4. arXiv: 2008.00915 [astro-ph.EP].

Wu, Y. and N. Murray (May 2003). "Planet Migration and Binary Companions: The Case of HD 80606b." In: *ApJ* 589.1, pp. 605–614. DOI: 10.1086/374598. arXiv: astro-ph/0303010 [astro-ph].

Wu, Y. (Mar. 2018). "Diffusive Tidal Evolution for Migrating Hot Jupiters." In: *AJ* 155.3, 118, p. 118. DOI: 10.3847/1538-3881/aaa970. arXiv: 1710.02542 [astro-ph.EP].

Wu, Y. and Y. Lithwick (July 2011). "Secular Chaos and the Production of Hot Jupiters." In: *ApJ* 735.2, 109, p. 109. DOI: 10.1088/0004-637X/735/2/109. arXiv: 1012.3475 [astro-ph.EP].

Xuan, J. W. and M. C. Wyatt (July 2020). "Evidence for a high mutual inclination between the cold Jupiter and transiting super Earth orbiting π Men." In: *MNRAS* 497.2, pp. 2096–2118. ISSN: 0035-8711. DOI: 10.1093/mnras/staa2033. eprint: https://academic.oup.com/mnras/article-pdf/497/2/2096/33565925/staa2033.pdf.

Xue, Y. et al. (Mar. 2014). "TIDAL EVOLUTION OF THE SPIN–ORBIT ANGLE IN EXOPLANETARY SYSTEMS." In: *The Astrophysical Journal* 784.1, p. 66. DOI: 10.1088/0004-637X/784/1/66. URL: https://dx.doi.org/10.1088/0004-637X/784/1/66.

Ycas, G. G. et al. (Mar. 2012). "Demonstration of on-sky calibration of astronomical spectra using a 25 GHz near-IR laser frequency comb." In: *Opt. Express* 20.6, pp. 6631–6643. DOI: 10.1364/OE.20.006631. URL: https://opg.optica.org/oe/abstract.cfm?URI=oe-20-6-6631.

Yee, S. W., E. A. Petigura, and K. von Braun (Feb. 2017). "Precision Stellar Characterization of FGKM Stars using an Empirical Spectral Library." In: *ApJ* 836, 77, p. 77. DOI: 10.3847/1538-4357/836/1/77. arXiv: 1701.00922 [astro-ph.SR].

Yee, S. W. et al. (May 2018). "HAT-P-11: Discovery of a Second Planet and a Clue to Understanding Exoplanet Obliquities." In: *AJ* 155.6, p. 255. DOI: 10.3847/1538-3881/aabfec.

Yee, S. W. et al. (Jan. 2020). "The Orbit of WASP-12b Is Decaying." In: *ApJL* 888.1, L5, p. L5. DOI: 10.3847/2041-8213/ab5c16. arXiv: 1911.09131 [astro-ph.EP].

Yoshida, S. et al. (Nov. 2023). "TESS Spots a Super-puff: The Remarkably Low Density of TOI-1420b." In: *AJ* 166.5, 181, p. 181. DOI: 10.3847/1538-3881/acf858. arXiv: 2309.09945 [astro-ph.EP].

Zanazzi, J. J., J. Dewberry, and E. Chiang (Mar. 2024). "Damping Obliquities of Hot Jupiter Hosts by Resonance Locking." In: *arXiv e-prints*, arXiv:2403.05616, arXiv:2403.05616. DOI: 10.48550/arXiv.2403.05616. arXiv: 2403.05616 [astro-ph.EP].

Zeeman, P. (Feb. 1897). "The Effect of Magnetisation on the Nature of Light Emitted by a Substance." In: *Nature* 55.1424, p. 347. DOI: 10.1038/055347a0.

Zeng, L., D. D. Sasselov, and S. B. Jacobsen (Mar. 2016). "Mass-Radius Relation for Rocky Planets Based on PREM." In: *ApJ* 819, 127, p. 127. DOI: 10.3847/0004-637X/819/2/127. arXiv: 1512.08827 [astro-ph.EP].

Zhang, M. et al. (Feb. 2022). "Escaping Helium from TOI 560.01, a Young Mini-Neptune." In: *AJ* 163.2, 67, p. 67. DOI: 10.3847/1538-3881/ac3fa7. arXiv: 2110.13150 [astro-ph.EP].

Zhang, M. et al. (Feb. 2023). "Detection of Atmospheric Escape from Four Young Mini-Neptunes." In: *AJ* 165.2, 62, p. 62. DOI: 10.3847/1538-3881/aca75b. arXiv: 2207.13099 [astro-ph.EP].

Zhao, L. L. et al. (Feb. 2021). "Excalibur: A Nonparametric, Hierarchical Wavelength Calibration Method for a Precision Spectrograph." In: *AJ* 161.2, 80, p. 80. DOI: 10.3847/1538-3881/abd105. arXiv: 2010.13786 [astro-ph.IM].

Zhao, L. L. et al. (Apr. 2022). "The EXPRES Stellar Signals Project II. State of the Field in Disentangling Photospheric Velocities." In: *AJ* 163.4, 171, p. 171. DOI: 10.3847/1538-3881/ac5176. arXiv: 2201.10639 [astro-ph.EP].

Zhao, L. L. et al. (Feb. 2023a). "Measured spin-orbit alignment of ultra-short-period super-Earth 55 Cancri e." In: *Nature Astronomy* 7, pp. 198–205. DOI: 10.1038/s41550-022-01837-2. arXiv: 2212.03953 [astro-ph.EP].

Zhao, L. L. et al. (Sept. 2023b). "The Extreme Stellar-Signals Project III. Combining Solar Data from HARPS, HARPS-N, EXPRES, and NEID." In: *arXiv e-prints*, arXiv:2309.03762, arXiv:2309.03762. DOI: 10.48550/arXiv.2309.03762. arXiv: 2309.03762 [astro-ph.EP].

Zhao, Y. and X. Dumusque (Mar. 2023). "SOAP-GPU: Efficient spectral modeling of stellar activity using graphical processing units." In: *A&A* 671, A11, A11. DOI: 10.1051/0004-6361/202244568. arXiv: 2301.04259 [astro-ph.SR].

Zhou, G. et al. (Apr. 2020). "A Well-aligned Orbit for the 45 Myr-old Transiting Neptune DS Tuc Ab." In: *ApJL* 892.2, L21, p. L21. DOI: 10.3847/2041-8213/ab7d3c. arXiv: 1912.04095 [astro-ph.EP].

Zieba, S. et al. (Aug. 2022). "K2 and Spitzer phase curves of the rocky ultra-short-period planet K2-141 b hint at a tenuous rock vapor atmosphere." In: *A&A* 664, A79, A79. DOI: 10.1051/0004-6361/202142912. arXiv: 2203.00370 [astro-ph.EP].